The Application of RASS in Urban Boundary Layer Meteorology

by

Guy Potvin

Department of Atmospheric and Oceanic Sciences
McGill University, Montreal, Quebec.

Submitted to the Faculty of Graduate Studies and Research in partial fulfillment of the requirements for the degree of Doctor of Philosophy.

October, 1998

0-612-44556-9

Abstract

This thesis describes the application of a Radio-Acoustic Sounding System (RASS) at an urban site, and proposes a Rank-Order Signal Processing Algorithm (ROSPA) to overcome the problems associated with that type of application. The main problem is clutter of many kinds contaminating the clear-air profiler measurements. ROSPA uses primarily order statistics, and operates in two main stages. The first stage operates on the clear-air Doppler velocity spectra by using a threshold minimum filter on the successive spectral power values at a given Doppler velocity bin for several spectra at a given altitude. The threshold minimum filter is a variant of the minimum filter. The second stage operates on the time-height mean Doppler clear-air velocity data by imposing a median filter. It is shown using theoretical models that the minimum and median filters possess the properties required to eliminate intermittent clutter, namely their insensitivity with respect to outliers. A profiler/RASS at an urban site, another at a rural site, and an airplane flying over mainly rural terrain, are used to study the urban boundary layer on the clear and convective early afternoon of June 28, 1996. The rural profiler/RASS data are free of clutter and show an initially stable rural boundary layer becoming convective in the middle of the observation period, and attaining a depth of about 1 km at the end of the period. The urban profiler/RASS data are treated with ROSPA to eliminate the severe intermittent clutter contamination and show a convective urban boundary layer over the entire observation period, with a depth increasing from 1.5 to 1.8 km. The heat flux profile of the second half of the rural RASS data agrees well with the airplane profile up to about 0.6 km. The surface heat flux estimated by airplane measurements is 146 $\pm$ 0.77 W/m^2, while the urban RASS measurements yield 523 $\pm$ 239 W/m^2. This result, along with comparisons of the vertical velocity variance profiles, is consistent with the differences between urban and rural boundary layers. It is concluded that the results indicate the usefulness of the profiler/RASS in urban boundary layer studies, and it is suggested that the anomalies in the urban heat and vertical velocity variance flux profiles may be due to factors independent of ROSPA.

MCGILL UNIVERSITY

Date: **October, 1998**

Author: **Guy Potvin**

Title: **The Application of RASS in Urban Boundary Layer Meteorology**

Department: **Atmospheric and Oceanic Sciences**

Degree: **Ph.D.** Convocation: **Fall** Year: **1998**

Signature of Author

MCGILL UNIVERSITY
DEPARTMENT OF
ATMOSPHERIC AND OCEANIC SCIENCES

The undersigned hereby certify that they have read and recommend to the Faculty of Graduate Studies and Research for acceptance a thesis entitled "**The Application of RASS in Urban Boundary Layer Meteorology**" by **Guy Potvin** in partial fulfillment of the requirements for the degree of **Doctor of Philosophy**.

Date: ____________

External Examiner: ______________________________

Research Supervisor: ______________________________
Prof. R. R. Rogers

Examing Committee: ______________________________

____

Cette thèse est dédiée à mon père. Robert.

ainsi qu'à ma mère. Colette.

Résumé

Cette thèse décrit l'application du RASS (Radio-Acoustic Sounding System) en milieu urbain. Afin d'éliminer les échos du sol et les échos parasites des mesures de vélocité verticale de l'air, l'algorithme ROSPA (Rank Order Signal Processing Algorithm) est proposé. ROSPA fait usage des statistiques de rang, tel le minimum ou la médiane d'un ensemble fini de variables aléatoires, et opère principalement en deux étapes. La première étape consiste à trouver l'enveloppe minimum des spectres Doppler de l'air clair en utilisant la puissance minimale, à chaque composante de vélocité Doppler et à chaque altitude, de plusieurs spectres Doppler d'affilée, créant ainsi des spectres Doppler presque sans échos parasites. La seconde étape consiste à utiliser la médiane d'un groupe de vélocités moyennes de l'air clair, regroupées dans le temps et l'altitude, ce qui élimine les échos parasites restants. Un RASS se trouvant sur un site urbain, un autre sur un site rural, et un avion instrumenté survolant un terrain rural, ont été déployés afin d'étudier la couche limite urbaine lors de l'après-midi ensoleillé du 28 juin 1996. Les mesures d'air clair du RASS rural ne comportent aucune contamination d'échos du sol ou parasites, et démontrent une couche limite initialement stable devenant convective au milieu de la période d'observation pour atteindre une épaisseur de 1 km à la fin de la période. Les mesures d'air clair du RASS urbain sont traitées avec ROSPA afin d'éliminer les échos parasites, et présentent une couche limite convective durant toute la période d'observation avec une épaisseur allant de 1.5 km au début à 1.8 km à la fin. Le profil de flux de chaleur de la seconde moitié des mesures du RASS rural est en bon accord avec le profil mesuré par l'avion, du sol jusqu'à 0.6 km d'altitude. Le flux de chaleur au sol, évalué à partir du profil mesuré par l'avion, est de 146 $\pm$ 0.77 W/m^2, alors que le RASS urbain nous donne 523 $\pm$ 239 W/m^2. Ce résultat, ainsi que les profils de variance de la vélocité verticale, sont compatibles avec les différences attendues entres les couches limites urbaines et rurales. Nous affirmons que le RASS est un outil valable pour l'étude de la couche limite urbaine, et que les anomalies des profils de flux de chaleur et de flux de variance urbains sont causées par des facteurs indépendants de ROSPA.

Statement of Originality

The signal processing algorithm presented in this thesis (ROSPA) is wholly original. Minimum and median filters are known, and have been used in other applications, including, to a certain extent, profiler applications. Indeed, medians have been used in profiler/RASS applications as a means of smoothing contaminated data, mainly for presentation purposes, or as a means of finding a robust central value estimate of part or all of a time series, for the purpose of eliminating outliers. But this is the first time that these filters have been used as signal processing steps in their own right, with a view towards estimating turbulence statistics. ROSPA is, therefore, the application of minimum and median filters specifically for estimating second-order statistics from continuous, and contaminated, profiler/RASS data. In addition, the use of RASS acoustic velocity data to calibrate ROSPA is also original, while the use of Gaussian white noise statistics and hypothesis tests for white noise suppression is, if not original, at least uncommon. Most important of all, the various turbulent statistics of the urban boundary layer taken by the profiler/RASS, the purpose of ROSPA, is original. In particular, the profiles of heat and vertical air velocity variance flux using the eddy-correlation method with ROSPA treated urban profiler/RASS data is unprecedented.

Acknowledgements

The author would like to gratefully acknowledge the contribution and unwavering support of Prof. R. R. Rogers to the research and writing of this thesis. In addition, special thanks are due to J. I. MacPherson at the National Research Council of Canada (NRC), N. R. Donaldson and J. W. Strapp at the Cloud Physics Research Division (CPRD) of the Atmospheric Environment Service of Canada (AES), and J. Mailhot and S. Bélair at the Recherche en Prévision Numérique (RPN) of the AES, who made the use of the St-Anicet and aircraft data possible. Thanks are also due to Dr. William Brown for his helpful comments and ideas. A. Bourque at the Centre Météorologique du Québec (CMQ) is thanked for providing the surface station data. This thesis was also made possible by the financial support of the Natural Sciences and Engineering Research Council of Canada (NSERC), AES, and the U.S. Office of Naval Research.

Contents

List of Tables

List of Figures

Chapter 1

Introduction

The precursor to the Radio-Acoustic Sounding System (RASS), known as the electromagnetic-acoustic (EMAC) probe, was invented in the late 1950's. The EMAC probe, using the same physical principles as the RASS, was designed to measure wind velocity (see Smith and Fetter (1989) for an historical review of the EMAC probe). The potential of EMAC probe technology for temperature measurements was first suggested by Atlas (1962), and the first successful RASS temperature profiles were obtained by North *et al.* (1973). Ever since the early 1970's, the RASS has been continually improved, and used to study a variety of boundary-layer and tropospheric meteorological phenomena. Among them, we note the use of RASS for studying mesoscale and synoptic scale weather systems (Neiman *et al.*, 1991; Neiman *et al.*, 1992; Cohn *et al.*, 1996); tropospheric and stratospheric temperature evolution (Matuura *et al.*, 1986; Tsuda *et al.*, 1989; Tsuda *et al.*, 1994); and boundary-layer inversions (Bonino *et al.*, 1981) and momentum and virtual heat fluxes (Peters *et al.*, 1985; Angevine *et al.*, 1993a; Angevine *et al.*, 1993b; Angevine, 1994; Peters and Kirtzel, 1994).

However, to the best of the author's knowledge, RASS was never used to study the urban boundary layer. This leaves open important questions about the urban boundary layer concerning the vertical structure and evolution of the turbulent kinetic energy and virtual potential temperature, among others. In particular, no attempt was made to estimate profiles of vertical turbulent flux in an urban boundary layer using RASS. This requires simultaneous measurements of the profiles of temperature and vertical air velocity, which in principle may be obtained from a combined wind profiler-RASS system. Reasons may be that the opportunity never presented itself or that profiler measurements of vertical air motion at an urban site can be severely contaminated by many kinds of clutter. The clutter can compromise the quality of the vertical air velocity measurements, which are essential if the eddy-correlation method is to be used to estimate the fluxes. And yet, the profiler/RASS combination has certain advantages over aircraft and towers. Less expensive than an aircraft, the profiler/RASS also provides better resolution in height over longer times. Indeed, the continuous time-height data of air motion and temperature of the profiler/RASS is comparable to tower data. However, the profiler/RASS can, under certain meteorological conditions, provide a greater height coverage than any tower. In addition, a profiler/RASS can be designed in such a way as to be transportable, which is not easily done for a tower.

There are good reasons, therefore, to remove the clutter from the clear-air profiler measurements, particularly in an urban boundary layer. A very complex environment, the urban boundary layer is also difficult to probe on account of restrictions on aircraft flight paths and on the type and location of ground-based instruments. The urban boundary layer, therefore, is still a relatively unexplored environment, certainly as compared with the rural boundary layer. Reliable profiler/RASS data would undoubtedly be a valuable addition to the study of that environment.

The goals of this thesis are twofold: first, to develop a signal processing algorithm capable of adequately eliminating the clutter from the clear-air velocity measurements; second, to analyze and compare the structure of a convective urban boundary

Figure 1.1: A view of the downtown core of Montreal centered on the campus of McGill University.

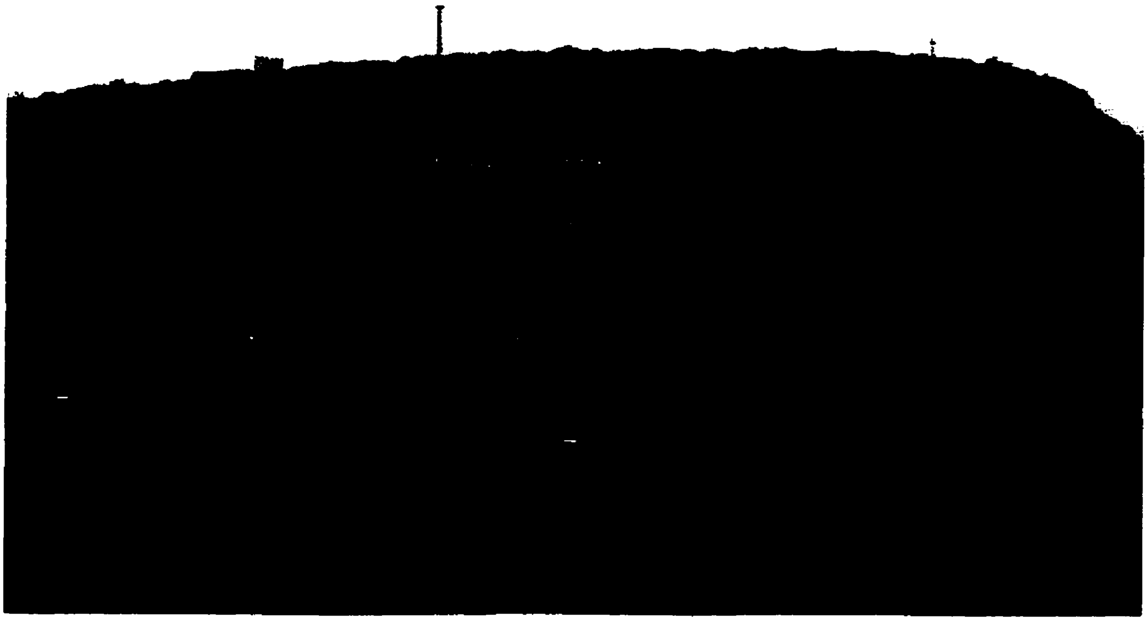

Figure 1.2: The array of instruments on the roof of Burnside Hall, on the campus of McGill University in downtown Montreal. The profiler is in the center, surrounded by four RASS acoustic speakers (cylinders).

layer with that of a rural convective boundary layer. The second goal will be accomplished using data taken by a profiler/RASS located at an urban site, by another profiler/RASS located at a rural site, and by an instrumented airplane flying between the two, over largely rural terrain. The urban site is the roof of Burnside Hall, located on the campus of McGill University in downtown Montreal. The campus and its environs are shown in Fig. 1.1, and the profiler, along with the RASS acoustic speakers, are shown in Fig. 1.2.

Chapter 2 begins by explaining the physical principles of the clear-air profiler and acoustic RASS measurements, along with the technical characteristics of the profiler/RASS used here, and ends with the spectral statistics of Gaussian white noise. Chapter 3 will review the different types of clutter affecting profiler measurements and various methods used to suppress them. Afterwards, Chapter 3 will explain the different steps used in the signal processing. At each step, we will eplain the theoretical principles involved. Chapter 4 will review the essential physical aspects of the urban boundary layer. In Chapter 5, we will start with an overview of the conditions on the day of a special boundary layer experiment: June 28, 1996. Then, we examine in detail the data from the rural profiler/RASS and the airplane. The data from the urban profiler/RASS will be treated with the signal processing algorithm, which first needs to be calibrated. The calibration procedure will be explained, and the urban boundary layer will be analyzed using the treated profiler/RASS data. Topics relating to the treatment of the data, errors on the profiler/RASS measurements, aircraft-RASS comparisons, and the differences between rural and urban turbulent flux profiles, will be examined in Chapter 5 and, in a more general way, in the discussion in Chapter 6. We summarize our conclusions in Chapter 7.

Chapter 2

The Profiler/RASS

In order to understand the profiler/RASS measurements presented in chapter 5, it is necessary first to explain the physical principles involved. This will give us some idea of which physical processes in the atmosphere correspond to what characteristics of the measurements. It will also give us an understanding of the limitations and qualities of the profiler/RASS system. First, we will focus on profiler measurements of clear air reflectivity, mean Doppler velocity, and spectral width. Second, we will look at RASS measurements of quantities related to an acoustic wave propagating in the atmosphere. Finally, we will review the effect of Gaussian white noise on the discrete-time signal processing relevant to profiler/RASS measurements.

2.1 Clear-Air Radar Measurements

The literature on all aspects of clear-air measurements by Doppler radars is vast. Therefore, we will not cite all the relevant references on this topic. Suffice it to say that the basic theory of radar wave and clear air interactions can be found in Tatarski (1961), while a comprehensive account of the theoretical aspects of Doppler radar measurements of clear air can be found in Doviak and Zrnić (1993). Additional material regarding clear-air returned power, mean Doppler velocity, and spectral width, can be found in Ottersten (1969), Gage and Balsley (1978), Gage *et al.* (1980), Hocking (1983), Gossard and Strauch (1983), and Muschinski (1998).

The general equation describing the detected electric field from refractive index fluctuations for a vertically-pointing pulsed Doppler radar (profiler), is

$$E_p(n, r_0) = \frac{k^2}{2\pi r_0^2} \int_{\phi=0}^{2\pi} \int_{\theta=0}^{\pi/2} \int_{r=r_0-L/2}^{r_0+L/2} |\vec{A}(\theta, \phi)|^2 e^{i(2k_0 r_p - \omega_0 T_{\mathrm{ipp}} n)} \eta(r, \theta, \phi, nT_{\mathrm{ipp}} + r_0/c - r_p/c) \mathrm{d}V_p \tag{2.1}$$

where $E_p(n, r_0)$ is the detected electric field, with n is the pulse number, r_0 is the range, k is the wavenumber of the returned field, $|\vec{A}(\theta, \phi)|^2$ is proportional to the angular transmitted power distribution of the profiler antenna about the main lobe ($\theta = 0$), ω_0 is the angular frequency of the profiler ($k_0 = \omega_0/c$), T_{ipp} is the interpulse period (IPP), $\eta(r, \theta, \phi, t)$ is the field of refractive index fluctuations of air, V_p is the resolution volume, and $r_p = r - r_0$. A derivation of this equation can be found in Appendix A.

Note that Eq. 2.1 is expressed using spherical coordinates because they coincide with the emitted radar waves. However, if we concentrate on the main lobe only, and if we assume that its beamwidth is sufficiently small, then we can neglect the curvature of the radar wavefronts within the main lobe. It is then convenient to express Eq. 2.1 in cartesian coordinates with the origin centered in the resolution volume ($\vec{x}_p$). For the moment, we will assume that the resolution volume is a rectangular parallelepiped where $-r_0\Delta\theta/2 \le x_p \le r_0\Delta\theta/2$, $-r_0\Delta\theta/2 \le y_p \le r_0\Delta\theta/2$, and $-L/2 \le z_p \le L/2$, where $\Delta\theta$ is the profiler beamwidth. We will further assume that the profiler illuminates the entire volume equally: $|\vec{A}(\vec{x}_p)|^2$ = constant. All this gives us the equation

$$E_p(n, r_0) = \frac{k^2 |\vec{A}|^2}{2\pi r_0^2} \int_{V_p} e^{i(2k_0 z_p - \omega_0 T_{\mathrm{ipp}} n)} \eta(\vec{x}_p, nT_{\mathrm{ipp}} + r_0/c - z_p/c) \mathrm{d}V_p \tag{2.2}$$

where we have dropped the limits of integration, and we have set $z_p = z - r_0$. We will now make use of the Fourier transform of the refractive index fluctuation field,

$\Phi_\eta(\vec{k}_\eta, \omega_\eta)$:

$$\eta(\vec{x}_p, t) = \frac{1}{(2\pi)^4} \int_{-\infty}^{\infty} \Phi_\eta(\vec{k}_\eta, \omega_\eta) e^{-i(\vec{k}_\eta \cdot \vec{x}_p - \omega_\eta t)} \mathrm{d}^3 k_\eta \mathrm{d}\omega_\eta \tag{2.3}$$

where $\vec{k}_\eta = (k_\eta, l_\eta, m_\eta)$ and ω_η are the wavenumbers and angular frequencies of the clear-air refractive index fluctuations. Also note that we abbreviate by showing only one integral sign instead of four, a convention we will use from now on unless stated otherwise. We place Eq. 2.3 in Eq. 2.2 to obtain

$$\begin{aligned} E_p(n, r_0) = \frac{k^2 |\vec{A}|^2}{(2\pi)^5 r_0^2} \int_{-\infty}^{\infty} \Phi_\eta(\vec{k}_\eta, \omega_\eta) e^{i\omega_\eta r_0/c} \left[\int_{-L/2}^{L/2} e^{i(2k_0 - m_\eta - \omega_\eta/c) z_p} \mathrm{d}z_p \right] \\ \left[\int_{-r_0\Delta\theta/2}^{r_0\Delta\theta/2} e^{-i(k_\eta x_p)} \mathrm{d}x_p \right] \left[\int_{-r_0\Delta\theta/2}^{r_0\Delta\theta/2} e^{-i(l_\eta y_p)} \mathrm{d}y_p \right] e^{i(\omega_\eta - \omega_0) T_{\mathrm{ipp}} n} \mathrm{d}^3 k_\eta \mathrm{d}\omega_\eta. \end{aligned} \tag{2.4}$$

The integrals in square brackets can be easily integrated to give

$$\begin{aligned} E_p(n, r_0) = \frac{k^2 V_p |\vec{A}|^2}{(2\pi)^5 r_0^2} \int_{-\infty}^{\infty} \Phi_\eta(\vec{k}_\eta, \omega_\eta) e^{i\omega_\eta r_0/c} \,\mathrm{sinc}[(2k_0 - m_\eta - \omega_\eta/c) L/2] \\ \mathrm{sinc}(k_\eta r_0 \Delta\theta/2)\, \mathrm{sinc}(l_\eta r_0 \Delta\theta/2)\, e^{i(\omega_\eta - \omega_0) T_{\mathrm{ipp}} n}\, \mathrm{d}^3 k_\eta \mathrm{d}\omega_\eta \end{aligned} \tag{2.5}$$

where $\mathrm{sinc}(x) = \sin(x)/x$ is a function with a main lobe at $x = 0$ ($\mathrm{sinc}(0) = 1$), with side lobes on both sides, and attaining zero at $x = \pm\pi, \pm 2\pi, \pm 3\pi$, etc. In fact, it can be shown that, $a \cdot \mathrm{sinc}(ax) \to \pi\delta(x)$, where δ is the Dirac delta function, as $a \to \infty$ (Arfken, 1985). In what follows, we will drop the ω_η/c term in the first sinc function, because we assume that $|\Phi_\eta(\vec{k}_\eta, \omega_\eta)|^2$ has power only where $m_\eta \gg \omega_\eta/c$. In other words, any realistic atmospheric phase velocity is very much less than the speed of light, $|\omega_\eta/m_\eta| \ll c$. The discrete-time Fourier transform (see Appendix B: Eq. B.2) of $E_p(n, r_0)$, is

$$\begin{aligned} H_p(\omega, r_0) = \frac{k^2 V_p |\vec{A}|^2}{(2\pi)^4 r_0^2} \int_{-\infty}^{\infty} \Phi_\eta(\vec{k}_\eta, \omega_\eta) e^{i\omega_\eta r_0/c} \,\mathrm{sinc}[(2k_0 - m_\eta) L/2]\, \mathrm{sinc}(k_\eta r_0 \Delta\theta/2) \\ \mathrm{sinc}(l_\eta r_0 \Delta\theta/2) \left[\sum_{k=-\infty}^{\infty} \delta(T_{\mathrm{ipp}}(\omega - \omega_\eta + \omega_0) + 2\pi k) \right] \mathrm{d}^3 k_\eta \mathrm{d}\omega_\eta \end{aligned} \tag{2.6}$$

where we used equation B.11 to introduce the delta functions. Before we integrate with respect to ω_η, we perform the transformation $\omega \to \omega - \omega_0$. This is because the profiler emits a wave with angular frequency ω_0 and detects one with angular frequency $\omega_0 - \omega_\eta$, namely, a wave with the atmospheric frequency 'riding' on the profiler frequency. It is convenient to remove the carrier frequency from the returned signal. The result is

$$H_p(\omega, r_0) = \frac{k^2 V_p |\vec{A}|^2}{(2\pi)^4 r_0^2 T_{\rm ipp}} \int_{-\infty}^{\infty} \left[\sum_{k=-\infty}^{\infty} \Phi_\eta(\vec{k}_\eta, \omega + 2\pi k/T_{\rm ipp}) e^{i(\omega + 2\pi k/T_{\rm ipp}) r_0/c} \right]$$
$$\mathrm{sinc}[(2k_0 - m_\eta)L/2]\ \mathrm{sinc}(k_\eta r_0 \Delta\theta/2) \mathrm{sinc}(l_\eta r_0 \Delta\theta/2)\ \mathrm{d}^3 k_\eta. \qquad (2.7)$$

We will assume that the IPP (interpulse period) is chosen so that all the atmospheric spectral power is contained within the angular frequency interval $[-\pi/T_{\rm ipp}, \pi/T_{\rm ipp}]$, where $\omega_N = \pi/T_{\rm ipp}$ is the Nyquist angular frequency defined by the IPP. This means that only the term $k = 0$ in the summation is not zero, giving

$$H_p(\omega, r_0) = \frac{k^2 V_p |\vec{A}|^2}{(2\pi)^4 r_0^2 T_{\rm ipp}} \int_{-\infty}^{\infty} \Phi_\eta(\vec{k}_\eta, \omega) e^{i\omega r_0/c} \mathrm{sinc}[(2k_0 - m_\eta)L/2]$$
$$\mathrm{sinc}(k_\eta r_0 \Delta\theta/2) \mathrm{sinc}(l_\eta r_0 \Delta\theta/2)\ \mathrm{d}^3 k_\eta. \qquad (2.8)$$

At this point, it is important to mention that the turbulent refractive index fluctuations are modelled by a stationary random field with zero mean. In other words, not only is the ensemble mean zero, $\overline{\eta} = 0$, but the covariance function depends only on the space and time lags between the two points:

$$\overline{\eta(\vec{x}_1, t_1)\eta(\vec{x}_2, t_2)} = \mathrm{Cov}(\vec{x}_2 - \vec{x}_1, t_2 - t_1). \qquad (2.9)$$

If the refractive index fluctuation field is random, then so is $\Phi(\vec{k}_\eta, \omega_\eta)$ and $H_p(\omega, r_0)$. Also, given a stationary random refractive index fluctuation field, it can be shown that

$$\overline{\Phi(\vec{k}_\eta, \omega_\eta)\Phi^*(\vec{k}'_\eta, \omega'_\eta)} = (2\pi)^4 S_\eta(\vec{k}_\eta, \omega_\eta)\ \delta(\vec{k}_\eta - \vec{k}'_\eta)\delta(\omega_\eta - \omega'_\eta) \qquad (2.10)$$

where $S_\eta(\vec{k}_\eta, \omega_\eta)$ is the power spectrum of η. Equation 2.10 is an important result in the theory of random fields (Panchev, 1971; Vanmarcke, 1983). The power spectrum represents the contribution of each frequency and wavenumber to the variance of the random field. In this case, we have

$$\sigma_\eta^2 = \frac{1}{(2\pi)^4}\int_{-\infty}^{\infty} S_\eta(\vec{k}_\eta, \omega_\eta)\mathrm{d}^3k_\eta \mathrm{d}\omega_\eta. \tag{2.11}$$

It also follows that the power spectrum of the returned signal is

$$S_p(\omega, r_0) = \frac{1}{2\pi}\int_{-\infty}^{\infty} \overline{H_p(\omega, r_0)\cdot H_p^*(\omega', r_0)}\,\mathrm{d}\omega'. \tag{2.12}$$

We place Eq. 2.8 into Eq. 2.12, we use Eq. 2.10 when we integrate with respect to the primed wavenumber and frequency coordinates, to obtain

$$S_p(\omega, r_0) = \frac{k^4 V_p^2|\vec{A}|^4}{(2\pi)^5 r_0^4 T_{\mathrm{ipp}}^2}\int_{-\infty}^{\infty} S_\eta(\vec{k}_\eta, \omega)\ \mathrm{sinc}^2[(2k_0 - m_\eta)L/2]$$
$$\mathrm{sinc}^2(k_\eta r_0\Delta\theta/2)\ \mathrm{sinc}^2(l_\eta r_0 \Delta\theta/2)\ \mathrm{d}^3k_\eta \tag{2.13}$$

which is a relationship between the profiler Doppler spectrum and the power spectrum of the clear-air refractive index fluctuations. If the resolution volume is large enough so that the sinc functions can be approximated as delta functions, we can approximate Eq. 2.13 as

$$S_p(\omega, r_0) \approx \frac{k^4 V_p|\vec{A}|^4}{32\pi^2 r_0^4 T_{\mathrm{ipp}}^2} S_\eta(0, 0, 2k_0, \omega). \tag{2.14}$$

Here, the profiler essentially singles out the wavenumber vector $\vec{k}_\eta = (0, 0, 2k_0)$. It is the clear-air refractive index fluctuations with a vertical wavelength half the profiler wavelength ($\lambda_\eta = \lambda_0/2$, a condition known as *Bragg matching*) that contributes the most to the detected spectral power. As we will see, Bragg matching also plays an essential role in RASS measurements. We can simplify further by using the expression $V_p = r_0^2(\Delta\theta)^2 L$, to find

$$S_p(\omega, r_0) \approx \frac{\Lambda}{r_0^2} S_\eta(0, 0, 2k_0, \omega) \tag{2.15}$$

where we defined the constant $\Lambda = k^4(\Delta\theta)^2 L|\vec{A}|^4/(32\pi^2 T_{\mathrm{ipp}}^2)$, and where we can see the r_0^{-2} dependence that must be taken into account when measuring clear-air reflectivity.

The range-normalized detected power is defined as

$$P_{RN}(r_0) = r_0^2 \int_{-\infty}^{\infty} S_p(\omega, r_0)\mathrm{d}\omega \approx \Lambda \int_{-\infty}^{\infty} S_\eta(0, 0, 2k_0, \omega)\mathrm{d}\omega. \tag{2.16}$$

Furthermore, if the turbulence causing the refractive index fluctuations is stationary, locally homogeneous, isotropic and in the inertial range, the structure function of $\eta(\vec{x}, t)$ is

$$\overline{[\eta(\vec{x} + \Delta\vec{x}, t) - \eta(\vec{x}, t)]^2} = C_n^2 |\Delta\vec{x}|^{2/3} \tag{2.17}$$

where C_n^2 is the refractivity turbulence structure parameter, which is a measure of the intensity of the turbulence (Gage *et al.*, 1980). The corresponding spectrum is given by $S_\eta \propto |\vec{k}_\eta|^{-11/3}$. In that case, and if the profiler wavelength is within the inertial range (which is usually the case), we can say that

$$P_{RN}(r_0) \propto C_n^2 k_0^{1/3} \tag{2.18}$$

which means that the range-normalized detected clear-air power is proportional to the intensity of the turbulence (Ottersten, 1969; Doviak and Zrnić, 1993).

If the radial component of the wind within the resolution volume has a mean value of zero, then it is reasonable to assume that the covariance function satisfies the condition: $\mathrm{Cov}(\Delta\vec{x}, \Delta t) = \mathrm{Cov}(\Delta\vec{x}, -\Delta t)$, and consequently the power spectrum: $S_\eta(\vec{k}_\eta, \omega_\eta) = S_\eta(\vec{k}_\eta, -\omega_\eta)$. These properties reflect the fact that with a zero mean wind, the motion of the eddies will, on average, cancel each other out. They also imply that the first-order spectral moments will vanish: $\int_{-\infty}^{\infty} S_\eta(0, 0, 2k_0, \omega_\eta)\omega_\eta \mathrm{d}\omega_\eta = \int_{-\infty}^{\infty} S_p(\omega, r_0)\omega \mathrm{d}\omega = 0$. We can introduce a mean advection by performing the substitution $\vec{x} \rightarrow \vec{x} - \vec{U}t$, where $\vec{U} = (u, v, w)$ is the advection velocity. That substitution implies others, namely: $\mathrm{Cov}(\Delta\vec{x}, \Delta t) \rightarrow \mathrm{Cov}(\Delta\vec{x} - \vec{U}\Delta t, \Delta t)$ and $S_\eta(\vec{k}_\eta, \omega_\eta) \rightarrow S_\eta(\vec{k}_\eta, \omega_\eta - \vec{U} \cdot \vec{k}_\eta)$ (see Potvin (1993) for a similar analysis applied to rainfall fields). Using that substitution, the mean Doppler frequency, defined as

$$\omega_D(r_0) = \frac{\int_{-\infty}^{\infty} S_p(\omega, r_0)\omega \mathrm{d}\omega}{\int_{-\infty}^{\infty} S_p(\omega, r_0)\mathrm{d}\omega} \tag{2.19}$$

becomes

$$\omega_D(r_0) \approx \frac{\int_{-\infty}^{\infty} S_\eta(0,0,2k_0,\omega - 2wk_0)\omega \mathrm{d}\omega}{\int_{-\infty}^{\infty} S_\eta(0,0,2k_0,\omega - 2wk_0)\mathrm{d}\omega}. \tag{2.20}$$

Using the spectral symmetry mentioned earlier, $S_\eta(0,0,2k_0,\omega - 2wk_0) = S_\eta(0,0,2k_0,-\omega + 2wk_0)$, it follows that

$$\omega_D \approx 2k_0 w \tag{2.21}$$

and consequently, the vertical air velocity measured by the profiler is taken to be $w_D = \omega_D/(2k_0)$. This analysis depends on the rather artificial division of atmospheric motion into turbulent small-scale eddies and constant large-scale motion advecting the eddies. Of course, the large-scale motions can be just as turbulent as the small-scale eddies, particularly in the boundary layer. The profiler measures the mean Doppler velocity over a finite integration time. The constant motion $\vec{U}$ can therefore be seen as the average of the turbulent motions over the resolution volume and the integration time.

The standard deviation of the Doppler velocity about its mean is defined by

$$\sigma_D(r_0) = \left[\frac{\int_{-\infty}^{\infty} S_p(\omega, r_0)(\omega - \omega_D)^2 \mathrm{d}\omega}{\int_{-\infty}^{\infty} S_p(\omega, r_0)\mathrm{d}\omega}\right]^{1/2} \tag{2.22}$$

and it describes the broadening of the power spectrum. By convention, the spectral width, μ_D, is sometimes defined by $\mu_D = 2\sigma_D$, which is twice the standard deviation of the Doppler velocity. To a first approximation, the spectral width is twice the value of the root mean square (rms) vertical velocity of eddies with sizes ranging from the smallest scales present to either the resolution length of the profiler or the largest scale of the turbulence, whichever is smaller (Hocking, 1983). However, other factors, such as the finite resolution volume and integration time (windowing effects, see Appendix B), and the uneven illumination within the resolution volume, affect the spectral width (Doviak and Zrnić, 1993). In addition, spectral broadening is also caused by the cross-beam wind component (Hocking, 1983; Doviak and Zrnić, 1993; Leblanc, 1994; Rogers *et al.*, 1996). That effect is not obvious from our previous development since we ignored the curvature of the radar wavefronts. Also, the profiler side lobes are inclined with respect to the vertical. The lobe inclined in the direction of the horizontal wind will measure an incoming Doppler velocity, while that inclined in the opposite direction will measure an outgoing Doppler velocity. These Doppler velocities contribute to increasing the spectral width.

2.2 RASS Measurements

Mathematical descriptions of various aspects of the RASS are numerous in the literature. For instance, Lataitis (1992) estimated the returned power; Nalbandyan (1976a; 1976b), Kon and Tatarski (1980), and May *et al.* (1990) examined the Doppler spectrum; attenuation of sound by turbulence was examined by Clifford and Wang (1977) and Makarova (1980); temperature errors were investigated by Lataitis (1993), Peters (1994b; 1994a) and Peters and Angevine (1996); altitude coverage by Masuda (1988), Takahashi *et al.* (1988), and Bauer and Peters (1993); and finally, a general description of RASS was given by Nalbandyan (1977) and Lataitis (1993).

The main difference between RASS and clear-air measurement is the origin of the refractive index fluctuations. Unlike the random refractive index fluctuations due to turbulence, the RASS creates and detects an acoustic wave, which induces refractive index fluctuations by the compression and rarefaction of the air. For the moment, we will assume the acoustic wave to be perfectly deterministic, with the form of a plane wave within the resolution volume

$$\eta(\vec{x}, t) = N_0 \exp[-i(\vec{k}_a \cdot \vec{x} - \omega_a t)] \tag{2.23}$$

where $\vec{k}_a = (k_a, l_a, m_a)$ and ω_a are, respectively, the acoustic wavenumber and angular frequency. Also, the dispersion relation for the acoustic wave is $\omega_a = c_a|\vec{k}_a| + \vec{U} \cdot \vec{k}_a$, where $\vec{U} = (u, v, w)$ is the motion of the air inside the resolution volume, $c_a = \sqrt{(\gamma R T_v)}$ is the speed of sound in still air, $\gamma = 1.4$ is the ratio of the specific heats at constant pressure and constant volume, $R = 287$ m^{2}s^{-2}K^{-1} is the gas constant of dry air, and T_v is the virtual temperature of the air (K). The wind velocity appears in the dispersion relation because acoustic waves are advected by it, unlike radar waves. In what follows, we will assume that the atmospheric flow is laminar and stationary. Acoustic wave propagation in a stratified atmosphere, such that $\vec{U} = (u(z), v(z), 0)$ and $c_a = c_a(z)$, which does not vary much over an acoustic wavelength (i.e. the limit of *geometrical acoustics*: $|\partial\vec{U}/\partial z|\lambda_a \to 0$ and $|\partial c_a/\partial z|\lambda_a \to 0$) is a well known problem in atmospheric acoustics (Rayleigh, 1896; Bateman, 1918; Milne, 1921; Pridmore-Brown, 1962; Lighthill, 1978). Furthermore, we will not discuss the attenuation of sound in air, although it can be a major factor in the altitude limitation of RASS (May *et al.*, 1988). Suffice it to say that the molecular attenuation of sound in air is a complicated function of acoustic frequency, air temperature and relative humidity, as shown by Harris (1966). In general, the attenuation increases with acoustic frequency, and dry cold air and moist hot air have low attenuation values.

Since the acoustic wave described in Eq. 2.23 is a plane wave, its spectrum is $\Phi_\eta(\vec{k}_\eta, \omega_\eta) = (2\pi)^4 N_0 \delta(\vec{k}_\eta - \vec{k}_a)\delta(\omega_\eta - \omega_a)$, which we place in Eq. 2.8 to find the detected Doppler spectrum of RASS. After performing the integration with respect to the wavenumber coordinates, we obtain

$$H_p(\omega, r_0) = \frac{k^2 V_p N_0 |\vec{A}|^2}{r_0^2 T_{\text{ipp}}} \delta(\omega - \omega_a) e^{i\omega r_0/c} \text{sinc}[(2k_0 - m_a)L/2] \\ \text{sinc}(k_a r_0 \Delta\theta/2)\text{sinc}(l_a r_0 \Delta\theta/2). \tag{2.24}$$

Here, we see that the detected signal has the same angular frequency as the acoustic wave, $\omega = \omega_a$, but the power will depend on how close the acoustic wavenumber $\vec{k}_a$ is to the vector $(0, 0, 2k_0)$. If the acoustic wave propagates vertically, then the maximum detected power is reached when the Bragg matching condition is satisfied, $m_a = 2k_0$, in which case the mean Doppler frequency is $\omega_D = 2k_0(c_a + w)$, and the measured RASS velocity is $c_R = c_a + w$.

We can now identify two problems with RASS measurements. First, in order to obtain a reasonably strong detected power, the acoustic frequency must be such that Bragg matching is satisfied ($\omega_a \approx 2k_0 c_a$). The proper frequency therefore depends on the speed of sound, which, in turn, is a function of the virtual temperature. But the virtual temperature is not known prior to measurement. The acoustic speakers of the RASS must therefore emit acoustic waves over a range of frequencies sufficiently wide to contain the proper Bragg match frequency. As we shall see, the RASS used in our experiments emits acoustic waves with a frequency that varies over a preset bandwidth. The detected power spectrum is not, therefore, a sharp peak at a single frequency, but a wider Gaussian shape with a maximum at the Bragg match frequency. The second problem is the contribution of the vertical air velocity to the RASS velocity, which is the principal source of error in RASS temperature estimates. This error can be removed if we possess accurate vertical air velocity measurements. However, the clear-air power spectra might suffer from contamination, making the vertical air velocity values unreliable. Chapter 3 will deal with such an eventuality.

Another source of error is the misalignment of the acoustic wavenumber vector with respect to the radar wavenumber vector. Such a misalignment has a variety of causes: the displacement of the acoustic source with respect to the profiler, the horizontal displacement of the spherical acoustic wavefronts by wind advection, the deformation of the acoustic wavefronts by turbulent eddies (mainly horizontal shear of vertical air velocity) and temperature fluctuations. If we assume no wind, $\vec{U} = 0$, and an inclined acoustic wavenumber vector, $\vec{k}_a = (|\vec{k}_a| \sin\phi, 0, |\vec{k}_a| \cos\phi)$, where ϕ is small, then the acoustic frequency that gives the highest detected power according to Eq. 2.24 is, to a first approximation:

$$\omega = \frac{2k_0 c_a \cos\phi}{\cos^2\phi + \beta^2 \sin^2\phi} \tag{2.25}$$

where $\beta = r_0 \Delta\theta / L$ is the aspect ratio of the resolution volume. The corresponding

RASS velocity is

$$c_R = \frac{c_a \cos\phi}{\cos^2\phi + \beta^2 \sin^2\phi}. \tag{2.26}$$

At low altitudes, $\beta^2 \ll 1$ and $c_R \approx c_a \sec\phi$, which means that the RASS measures a artificially high velocity, $c_R - c_a \approx c_a(\sec\phi - 1) \approx c_a\phi^2/2 \geq 0$, or an artificially warm temperature. At altitudes where the resolution volume is as wide as it is high, $\beta^2 \approx 1$, the RASS measures a velocity $c_R \approx c_a \cos\phi$, which is too low with respect to the speed of sound, $c_R - c_a \approx c_a(\cos\phi - 1) \approx -c_a\phi^2/2 \leq 0$. Alternatively, using small angle approximations, we can state that $c_R - c_a \approx c_a(1/2 - \beta^2)\phi^2$, which means that the RASS is insensitive to leading-order misalignment errors at $r_0 = (\sqrt{2})^{-1} L/\Delta\theta$. The aspect ratio of the resolution volume appears in Eqs. 2.25 and 2.26, because finding the peak of Eq. 2.24 implies maximizing the product of two competing sinc functions. That is, the vertical function $\text{sinc}[(2k_0 - |\vec{k}_a|\cos\phi)L/2]$ has a maximum at $|\vec{k}_a| = 2k_0 \sec\phi$, while the horizontal function $\text{sinc}[(r_0\Delta\theta/2)|\vec{k}_a|\sin\phi]$ attains a maximum at $|\vec{k}_a| = 0$. Which function predominates depends on the height of the resolution volume, L, relative to its width, $r_0\Delta\theta$, such that if $L \gg r_0\Delta\theta$, then the vertical sinc function has a much sharper maximum than the horizontal sinc function, and so the vertical sinc function determines the frequency of the maximum.

As mentioned previously, Eq. 2.24 does not take into account the spherical nature of the radar wavefronts, or the uneven illumination within the resolution volume. Moreoever, it does not take into account the spherical form of the acoustic wavefronts, the uneven distribution of acoustic power within the resolution volume, or interference effects that may be created by multiple acoustic speakers. Indeed, in many treatments of RASS, such as Lataitis (1992; 1993), the spherical shape of the wavefronts plays a major role. The curvature and position of the acoustic wavefronts relative to the radar wavefronts are assumed to focus or diffuse the returning power to the profiler. Most important, though, is the assumption of a constant misalignment over the entire resolution volume. In fact, the action of turbulent eddies deforms the propagating acoustic wavefronts, causing a variable misalignment throughout the volume.

Turbulence interacts with sound in many ways. Turbulent eddies can emit acoustic waves of their own (Lighthill. 1952). but this sound has little power and a low frequency. and so does not interfere with RASS measurements. Turbulent eddies also scatter propagating acoustic waves (Lighthill. 1953: Kraichnan. 1953: Tatarski. 1961: Monin. 1962: Clifford and Brown. 1970). There appear to be two types of scattering mechanisms: the turbulent eddies proper. and turbulent temperature fluctuations (Howe. 1973). For the turbulent eddies. only the cases where the acoustic wavelength is either much longer or much shorter than the eddy size are well understood. while the intermediate case poses some difficulty (Lighthill. 1972). There is. on average. a net loss of acoustic energy to the turbulence. From this. we can define an attenuation of sound due to turbulence. not accounted for by molecular attenuation. According to Ingard (1953). attenuation due to atmospheric turbulence can be stronger than any other type of attenuation (molecular. fog. rain or ground). while Brown and Clifford (1976) claim that other factors not related to the atmosphere. such as beamwidth and beam orientation. can be just as important.

The effect of turbulence on the acoustic wave is usually described using Rytov's form (Chernov. 1960: Tatarski. 1961: Ishimaru. 1978). which is

$$\eta'(\vec{x},t) = \eta(\vec{x},t)\exp[\chi(\vec{x},t) + i\psi(\vec{x},t)] \tag{2.27}$$

where $\eta'(\vec{x},t)$ is the perturbed acoustic wave. $\eta(\vec{x},t)$ is the unperturbed incident acoustic wave. described in Eq. 2.23. and $\chi = \ln(|\eta'|/|\eta|)$ and ψ are. respectively. the turbulent fluctuations of the log-amplitude and phase of the incident wave. The acoustic wave, $\eta'(\vec{x},t)$, is therefore random, rather than deterministic. According to Peters and Angevine (1996), the amplitude fluctuations are negligible compared to the effect of the phase fluctuations. Indeed, it is the phase fluctuations, $\psi(\vec{x},t)$, that create 'correlation patches', zones of more or less constant inclination, independent of one another, within the resolution volume. It is the aspect ratio of these patches, β_T, that now should appear in Eq. 2.26. Also, according to Tatarski (1961), and Clifford and Wang (1977), the acoustic wave is much more coherent along the direction of propagation than perpendicular to it (or along the wavefronts). This means that the correlation patches are elongated along the acoustic wavenumber vector, $\vec{k}_a = (0, 0, |\vec{k}_a|)$, which implies that $\beta_T \ll 1$ for all altitudes. A more accurate aspect ratio, however, should be

$$\beta_T = \frac{\min(r_0 \Delta\theta, L_\perp)}{\min(L, L_\parallel)} \tag{2.28}$$

where $L_\parallel$ is the length of the correlation patch along $\vec{k}_a$, and $L_\perp$ is the length perpendicular to it. But $L_\parallel \approx r_0$, and $L_\perp \propto r_0^{-3/5}$ so that, in general, we assume $\beta_T = L_\perp / L < 1$. Of course, the inclination angle of each correlation patch, φ, is itself a random variable. According to Peters and Angevine (1996), if we assume homogeneous turbulence and a mean wind with a value of zero, the overall error is $c_R - c_a \approx (1/4) c_a \overline{\varphi^2}$, where $\overline{\varphi^2}$ is the variance of the inclination angle.

Apart from the vertical air velocity, horizontal wind, and turbulence, other sources of error exist (Angevine and Ecklund, 1994). Among them, we find errors in range: that is, the acoustic attenuation and the horizontal winds may cause an uneven vertical distribution of acoustic energy within the resolution volume, meaning that the measured temperature is not an unweighted average over the volume. In addition, slight deviations from the formula, $c_a = \sqrt{(\gamma R T_v)}$, due to a weak dependence on atmospheric variables other than the virtual temperature, such as pressure, humidity or CO_2 concentration (Harris, 1971; Cramer, 1993) may cause errors. RASS-radiosonde comparisons (May *et al.*, 1989; Angevine and Ecklund, 1994; Moran and Strauch, 1994; Peters and Angevine, 1996; Riddle *et al.*, 1996), as well as RASS-tower comparisons (Angevine *et al.*, 1998) show that, overall, the RASS measurements have random and systematic errors in the order of 1°C, without any correction. The systematic error is negative close to the ground (< 250 m AGL) and positive at higher altitudes. If we take into account the vertical air velocity, the random error can be reduced to about 0.2°C, depending on the meteorological conditions and the quality of the velocity measurements.

2.3 Examples of Profiler and RASS Observations

The technical characteristics of the particular profiler/RASS system determine the kinds of measurements that can be performed with acceptable accuracy. In this section, we will list the technical and signal processing characteristics of the McGill profiler/RASS, examine its capabilities, and show some examples of profiler and RASS data.

Table 2.1: The characteristics of the profiler (top) and RASS (bottom) components.

Frequency	915 MHz
Wavelength	32.8 cm
Peak power	500 W
Antenna aperture	1.8 m × 1.8 m
Antenna type	64 element array
Number of beams	5
Pointing directions	Vertical; 21° zenith angle at cardinal points
Beamwidth	9°
Pulse duration	0.7 μs (typical)
Pulse length	105 m (typical)
Acoustic power	30 W (nominal)
Acoustic frequency	2 kHz (typical)
Acoustic bandwidth	120 Hz (typical)
Acoustic wavelength	16 cm (typical)
Freq. selection	random
Acoustic Dwell time	15 ms
Speaker diameter	1.2 m
Speaker beamwidth	10°

The radar wind profiler is the prototype of the Radian model LAP-3000 built for McGill University by the Aeronomy Laboratory of the U.S. National Oceanic and

Atmospheric Administration. Its main characteristics are: wavelength 33 cm, peak power 500 W, beamwidth 9° and, in the examples shown, pulse duration 0.7 μs. In the RASS mode, the acoustic signal is transmitted continuously with its frequency changed every 15 ms and selected randomly from the interval 2025-2130 Hz, corresponding to a temperature interval of 5-35°C. The fundamental vertical resolution in the examples, as determined by the radar pulse duration, was 105 m, though the RASS signals were sampled at an interval of 0.4 μs to give a spacing in altitude of 60 m. To reduce the signal-to-noise ratio, nine consecutive detected pulses were coherently integrated to form one element in a 2048-point time series. The average was removed from the time series (DC filtering), and a Hanning window was imposed on it. A Fast Fourier Transform (FFT, see Appendix B) was performed on the time series, producing a power spectrum extending over the Doppler velocity interval $\pm$396 m/s. Twenty-four such power spectra were then averaged. The time resolution, determined by the amount of coherent and spectral integration, was 22 s. The characteristics of the profiler/RASS are summarized in Table 2.1 and described by Angevine *et al.* (1994b). The signal processing parameters are listed in Table 2.2.

Table 2.2: The signal processing parameters of the profiler operating in RASS mode.

Interpulse period	23 μs
Unambiguous range limit	3.45 km
Sampling interval	0.4 μs
Sampling resolution	60 m
Coherent integration	9
DC filtering	yes
Windowing	Hanning
Spectral integration	24
Number of spectral points	2048
Pulse coding	none
Nyquist Doppler velocity	396 m/s

Figure 2.1 shows an example of profiler clear-air measurements, taken over McGill

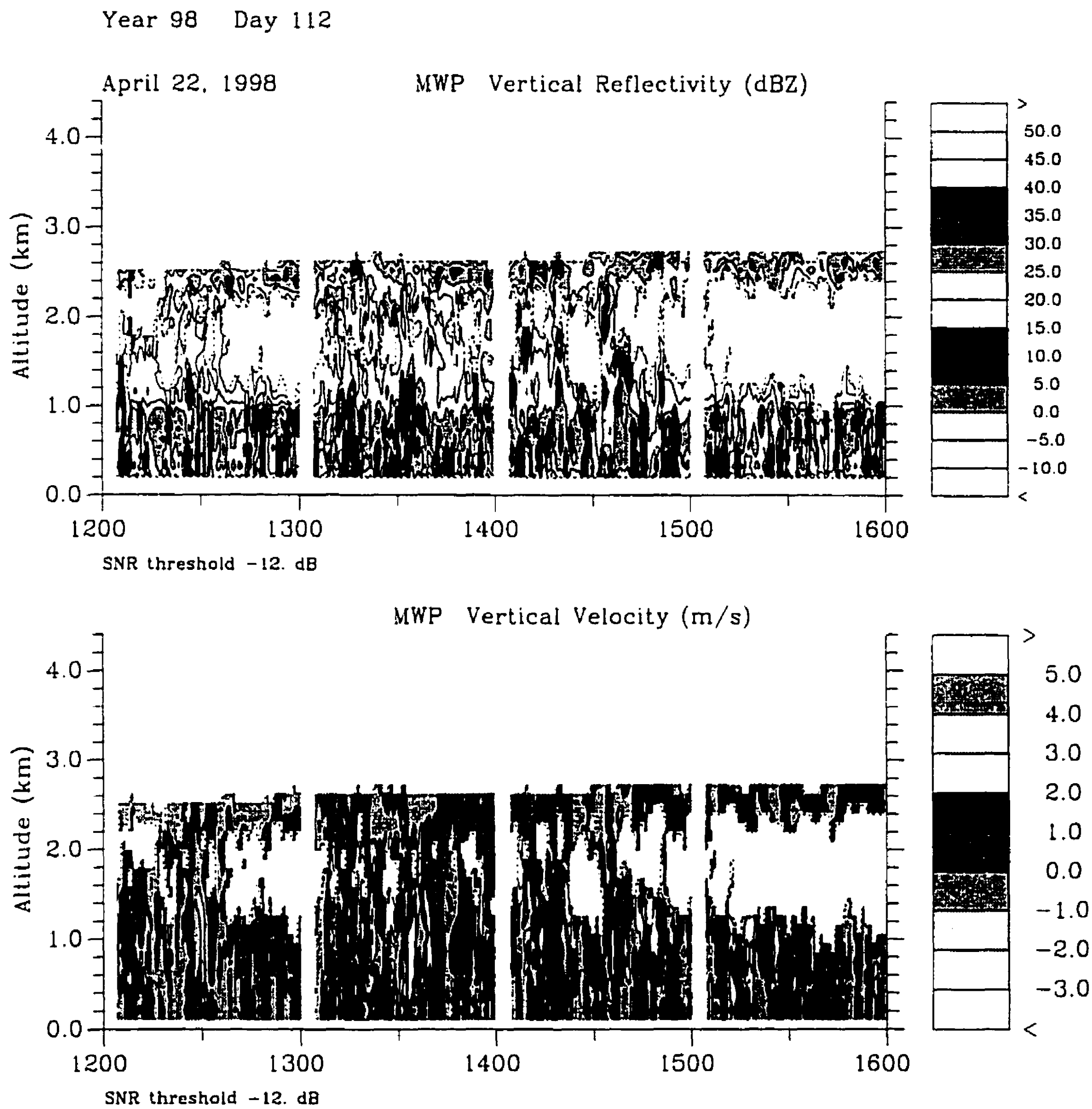

Figure 2.1: An example of time-height profiler data of clear-air reflectivity (top) and mean Doppler velocity (bottom). The sign convention is that positive Doppler velocity indicates motion towards the radar.

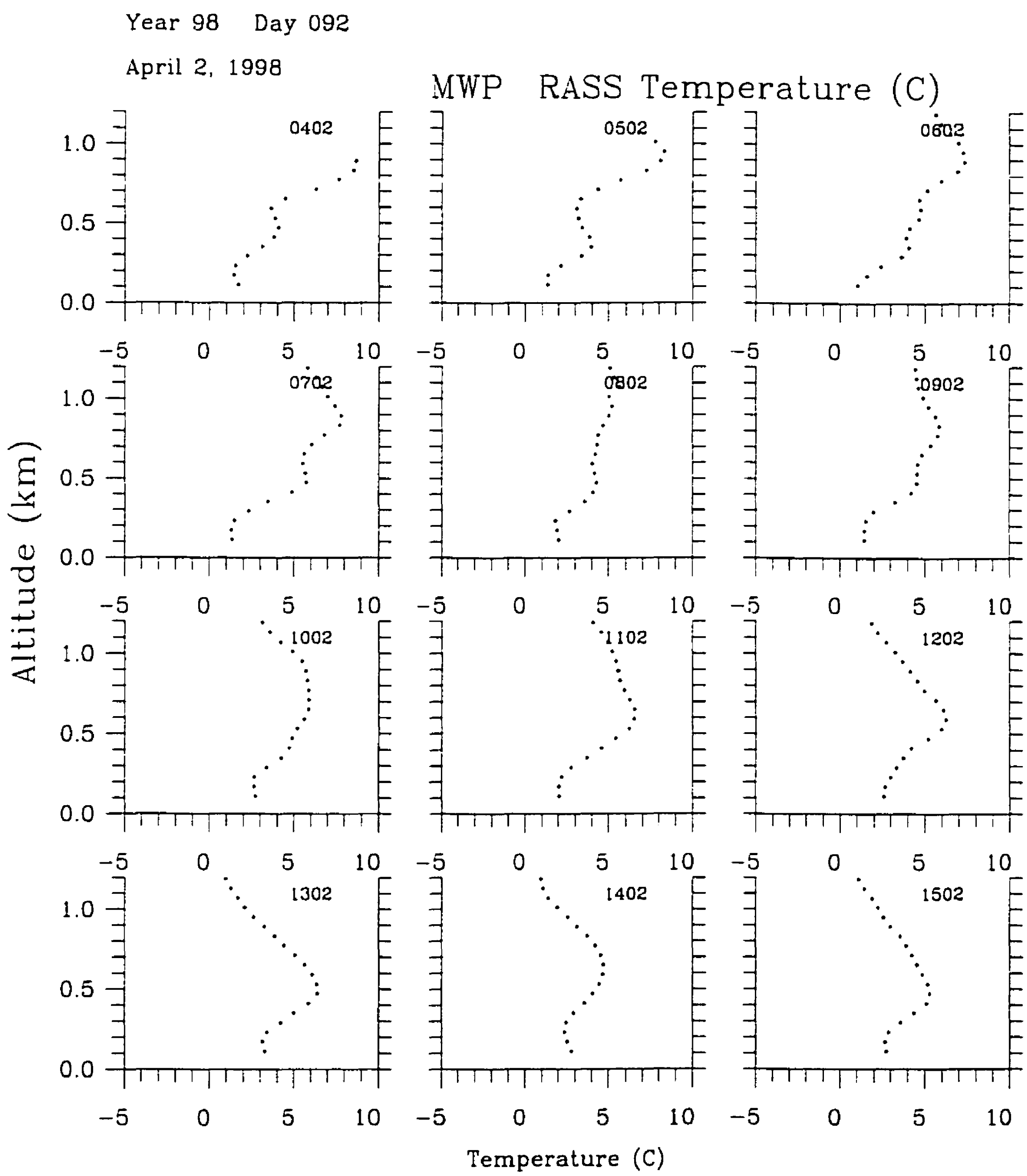

Figure 2.2: An example of RASS virtual temperature profiles. The profiles are consensus averages over 4 minutes (7-8 measurements), at the start of every hour.

on April 22, 1998. An inversion layer persists over the entire 4-hour period at 2.5 km AGL. The layer is visible because of the shear-driven turbulence mixing the air above and below the layer, with different potential temperature and humidity values, causing the necessary refractive index fluctuations. Inside the layer, there is a more or less regular oscillation between upward and downward motion, possibly the result of gravity waves. Between 1 km AGL and the inversion layer, we see the occasional outburst of convection, particularly from 1200 to 1240 and from 1300 to 1500 Eastern Standard Time (EST). See Rogers *et al.* (1993; 1994) for an analysis of similar profiler data. Of particular importance to us, however, is the persistent detected power from the ground to about 1 km AGL. That signal is mainly clutter from the ground, or flying objects (the dark patches in the reflectivity plot), contaminating the clear-air data. Describing the different types of clutter, and eliminating them, is the central topic of Chapter 3.

Figure 2.2 shows a series of RASS virtual temperature profiles from 0400 to 1500 EST, on April 2, 1998. At the start of every hour, RASS measurements were taken over a 4-minute period, yielding 7-8 measurements at each height. The virtual temperature measurements were averaged using a consensus averaging algorithm, which is designed to eliminate outliers from a dataset prior to averaging. First described by Strauch *et al.* (1984), consensus averaging is used for obtaining reliable horizontal wind profiles from profiler data. The hourly profiles in Fig. 2.2 begin at 0400 EST, when there are two stable layers (one from 0.2 to 0.4 km AGL, and the other from 0.6 to 1 km AGL). The lower stable layer persists until the last profile at 1500 EST. The upper stable layer is progressively weakened, until it disappears completely by 1200 EST, leaving behind a mildly stable layer from about 0.5 to 1.2 km AGL.

2.4 Effects of Gaussian White Noise

All measurements include a random error, whether large or small with respect to the measured value, due to imperfections in the instrument. Profiler/RASS measurements are certainly no exception. Unlike contamination which may or may not be present, the random error is present in every measurement. Any signal processing algorithm must, therefore, be able to deal with this type of error. It is thus important to understand the effect of these errors on the profiler/RASS Doppler spectra so that we can take them into account in the signal processing.

Noise usually designates a random error that affects each member in a time series and is independent of all other members. The noise component of a discrete-time time series is given as $z[n]$, which is composed of independent and identically distributed (iid) random variables z such that: (i) z has an average of zero ($\bar{z} = 0$); (ii) $z[i]$ is independent of $z[j]$ for all $i \neq j$. The square brackets are used to denote a discrete argument. Also, for convenience, we assume that z is complex, $z = z_r + i\, z_i$, where the real and imaginary parts are iid with a Gaussian probability density function (also called a normal probability density function) with a mean $\mu = 0$ and a variance σ^2:

$$f_r(z_r) = \frac{1}{\sigma\sqrt{(2\pi)}} \exp\left[-\frac{z_r^2}{2\sigma^2}\right] \qquad f_i(z_i) = \frac{1}{\sigma\sqrt{(2\pi)}} \exp\left[-\frac{z_i^2}{2\sigma^2}\right]. \tag{2.29}$$

Next, we consider a time series only N points long, such that $n = 0, \ldots, N-1$, and, for the sake of generality, we impose a window $w[n]$ on the time series. The DFT (see Appendix B) of this time series is then

$$Z[k] = \sum_{n=0}^{N-1} w[n] z[n] e^{-i(2\pi kn/N)}. \tag{2.30}$$

The real and imaginary parts of $Z[k]$ are

$$Z_r[k] = \sum_{n=0}^{N-1} w[n]\{z_r[n]\cos(2\pi kn/N) + z_i[n]\sin(2\pi kn/N)\} \tag{2.31}$$

$$Z_i[k] = \sum_{n=0}^{N-1} w[n]\{z_i[n]\cos(2\pi kn/N) - z_r[n]\sin(2\pi kn/N)\} \tag{2.32}$$

where $w[n]$ is assumed to be real. Equations 2.31 and 2.32 are sums of normally distributed random variables. Given N normally distributed random variables, with means μ_n and variances σ_n^2, it is well known that the sum of these random variables is a normally distributed random variable with a mean $\mu_s = \sum_{n=0}^{N-1} \mu_n$ and a variance $\sigma_s^2 = \sum_{n=0}^{N-1} \sigma_n^2$. Furthermore, suppose $y = az$, where z is a normally distributed random variable with a mean μ and a variance σ^2 and a is a real constant. It is not hard to see that y is a normally distributed random variable with a mean $a\mu$ and a variance $a^2\sigma^2$. It follows then that $Z_r[k]$ is a normally distributed random variable with a zero mean, $\mu_r = 0$, and a variance $\sigma_r^2 = \sum_{n=0}^{N-1} \sigma^2 w^2[n]\{\cos^2(2\pi kn/N) + \sin^2(2\pi kn/N)\} = \sigma^2 \sum_{n=0}^{N-1} w^2[n]$. The same applies for $Z_i[k]$: $\mu_i = 0$ and $\sigma_i^2 = \sigma^2 \sum_{n=0}^{N-1} w^2[n]$. Note that these parameters do not depend on k. The joint probability density function of Z_r and Z_i is

$$g(Z_r, Z_i) = \frac{1}{2\pi\sigma_s^2} \exp\left[-\frac{Z_r^2 + Z_i^2}{2\sigma_s^2}\right] \tag{2.33}$$

where $\sigma_s = \sigma_r = \sigma_i$. We now express $g(Z_r, Z_i)$ in a polar representation, $Z = Re^{i\phi}$. Using the fact that $\mathrm{d}Z_r\mathrm{d}Z_i = R\mathrm{d}R\mathrm{d}\phi$ and $R^2 = Z_r^2 + Z_i^2$, we find

$$g(R, \phi) = \frac{R}{2\pi\sigma_s^2} \exp\left[-\frac{R^2}{2\sigma_s^2}\right]. \tag{2.34}$$

Since Eq. 2.34 does not depend on ϕ, it is convenient to find the marginal density function, $g(R) = \int_0^{2\pi} g(R, \phi)\mathrm{d}\phi$,

$$g(R) = \frac{R}{\sigma_s^2} \exp\left[-\frac{R^2}{2\sigma_s^2}\right]. \tag{2.35}$$

However, we are only interested in the spectral power $E = Z^*Z = R^2$. We obtain the probability density function of the spectral power by using $R\mathrm{d}R = \frac{1}{2}\mathrm{d}E$ in Eq. 2.35,

$$g(E) = \lambda \exp[-\lambda E] \tag{2.36}$$

where $\lambda = (2\sigma_s^2)^{-1}$. The probability density function of the spectral power value of Gaussian white noise is therefore exponential for any value of k. The signal processing algorithm of a profiler/RASS may average m power spectra together. It is well known that the average of m exponentially distributed random variables is a random variable with a gamma probability density function (Marshall and Hitschfeld, 1953; Wallace, 1953; Feller, 1971); that is,

$$g_a(E_a) = \frac{(\lambda m)^m E_a^{m-1}}{(m-1)!} \exp[-\lambda m E_a], \tag{2.37}$$

where

$$E_a = \frac{1}{m} \sum_{j=0}^{m-1} E_j. \tag{2.38}$$

From Eq. 2.37, we also know that $\overline{E}_a = 1/\lambda$, which is the noise level of the spectrum. Equation 2.37 will therefore be used as a model to estimate the probabilities of the spectral power of white noise. Note that the coherent integration of the white noise time series, $z_l[n] = \sum_{j=0}^{l-1} z[ln - j]$, would not change the preceding development since $z_l[n]$ would still be a Gaussian noise time series. It should be noted, however, that the scatter from turbulence leads to spectral power components that are also exponentially distributed (Doviak and Zrnić, 1993). But while the spectral components that contain power due to turbulence have the same type of distribution as those with only noise, it is more than reasonable to assume that the value of the parameters will be very different (for instance, $\overline{E}_{\mathrm{turb}} >> \overline{E}_{\mathrm{noise}}$). It is this difference that will be exploited in subsection 3.2.3 on noise suppression.

In conclusion, we can say that Eq. 2.37 gives us a general description of the probability density function of white noise spectral power. This density function will enable us to eliminate white noise in a way based on its statistics. We will therefore be able to express the elimination of spectral white noise in probabilistic terms.

Chapter 3

Signal Processing

The promise of the RASS is only fully realized when an accurate and reliable estimation of the vertical air velocity is available. In an urban environment, this is problematic given the type of clutter affecting the clear-air Doppler spectra at close range. An appropriate signal processing algorithm is therefore essential. In this chapter, we present such an algorithm based on *order statistics*. These are statistics referring to the sorting of random data into ascending or descending order. The minimum, maximum and median of a finite number of individual measurements are examples of order statistics. We begin by describing the types of clutter in an urban setting near the ground, and review various methods of clutter reduction used by others. In the second section, we explain the various steps involved in the signal processing algorithm.

3.1 The Problem of Clutter

Clutter, in all its forms, is the bane of profilers, particularly at low altitudes and for sites like the one at McGill University, in which the profiler is located atop a high building in the center of a city. In this section, we will start by identifying the different types of clutter along with their causes and characteristics. Next, we will examine some other methods designed to deal with the problem of clutter.

3.1.1 Types of Clutter

By *clutter*, we mean any radio wave source, reflective object, or other cause, that creates a power spectrum in the Doppler profiler data which is not related to the atmospheric signal spectrum, and may make its identification difficult, if not impossible. Note, however, that we do not consider white noise to be clutter.

Ground Clutter

Ground clutter is the power obtained by the backscattering of energy in the antenna sidelobes off the ground or objects on the ground. Consequently, nearly all the spectral power of ground clutter is concentrated in or near the zero Doppler velocity bin. The presence of mobile objects on the ground, notably swaying trees, may introduce some spectral power close to, and on either side of the zero Doppler velocity bin. Indeed, since mobile objects are equally likely to move towards as away from the profiler, we expect the ground clutter spectrum to be symmetric on average with respect to the zero Doppler velocity bin. Furthermore, windowing effects may also cause some of spectral power in the zero Doppler velocity bin to leak into lobes on both sides of the bin. Overall, though, the ground clutter spectrum tends to be very narrow, with a spectral width < 1 m/s (Keeler and Passarelli, 1990), and tends to decrease in intensity at higher altitudes.

Ground clutter also tends to be much worse in urban areas than in rural areas, given the presence of many high-rise buildings in the vicinity. While the McGill profiler in downtown Montreal is placed on the roof of a fourteen story building, there are many taller buildings in the neighborhood. These are an obvious source of ground clutter, possibly even causing multiple reflections of side lobe energy. The ground clutter spectrum can be a steady feature, remaining unchanged over long periods. Occasionally, the ground clutter spectrum 'flares up', that is it suddenly gains a lot of power (as much as 40 dB) over a wide range of Doppler velocities (about 10 m/s) and over periods of about 1 min, but sometimes as long as 5 min.

It is not clear what causes this phenomenon, or even if it is really ground related. Nevertheless, we will classify it as a ground clutter phenomenon.

Intermittent Clutter

Intermittent clutter is defined here as a brief (usually less than a minute) but intense surge in reflected power, independent of ground clutter, noise and atmospheric signal and fairly well localized in altitude (usually less than 200 m wide). This is accounted for by the backscattering of main or side lobe energy off flying objects, mainly birds and aircraft. As a consequence, intermittent clutter tends to be short lived, usually less than 30 s, approximately. The lifetime depends, of course, on the velocity of the flier and the width of the profiler beam at that altitude. For birds flying in a straight line across the profiler beam (with a beamwidth of 9°, for example), with a velocity of about 7 m/s (typical for migrating birds (Merritt, 1995)) at an altitude of 1 km, the intermittent clutter lifetime will be approximately 22 s. Some birds may linger over the profiler, of course, causing a longer intermittent clutter lifetime.

Intermittent clutter also can be much more powerful than the atmospheric signal, particularly clear-air signals, causing it to dominate the spectrum. This need not always be the case, however, and so it is inappropriate to use a fixed spectral power threshold to distinguish intermittent clutter from the atmospheric signal since both have a very wide dynamic range.

Radio Frequency Interference

Radio Frequency Interference (RFI) is power received from sources emitting near the profiler frequency and over a fairly narrow bandwidth. Cellular phones are one such example. Contrary to ground or intermittent clutter, RFI is not the result of scattering of the profiler emitted power. Since the profiler emits finite pulses but receives a continuous RFI signal, RFI is seen as a signal at all altitudes but over a narrow Doppler velocity interval (about 3 m/s). The RFI tends to move slowly across the Doppler velocity axis. RFI episodes usually last a few minutes, rarely more than ten. However, RFI episodes also tend to cluster, where on certain days many episodes rapidly succeed one another.

3.1.2 Review of Clutter Suppression Methods

Most clutter suppression methods are directed towards ground clutter. Some involve directly modifying the power spectrum (Passarelli *et al.*, 1981; Ohsaki and Masuda, 1996), while others analyze the form of the corresponding autocorrelation function (Passarelli, 1981; Sato and Woodman, 1982). The spectral methods sometimes involve eliminating the spectral power in bins at or close to zero Doppler velocity. The choice of bins is either predetermined or variable according to the shape of the spectrum. After the power in those bins has been eliminated, they are replaced by some interpolated values from the unaffected bins. Other spectral methods assume a ground clutter spectrum that is symmetric about the zero Doppler velocity bin, and exploit that symmetry in some way. All these methods run the risk of eliminating too much or to little of the original spectrum. In the present work, a symmetry-based spectral method will be adopted (see subsection 3.2.4), mainly because of its simplicity.

The autocorrelation methods rest on assumptions about the ground clutter and atmospheric signal spectra (symmetric, Gaussian, etc.) which are designed to restrict the degrees of freedom of the autocorrelation function. This means that the entire autocorrelation function may be specified by a few parameters (mean Doppler velocity, spectral width, etc.), according to the assumptions. The theoretical autocorrelation function which best fits the measured autocorrelation is found and the corresponding parameters are taken to be the truth. The autocorrelation methods require, therefore, that the assumptions and the parameters sought be specified ahead of time, unlike the spectral methods which, if properly done, theoretically allow the estimation of any number of spectral moments.

It is well worth mentioning the Statistical Averaging Method (SAM) by Merritt (1995), because it uses order statistics. SAM is basically a spectral averaging method that excludes spectral power values containing intermittent clutter by performing tests on the distribution of these values. It is assumed that noise and atmospheric signal spectral power values are exponentially distributed, while the intermittent clutter values have a very different kind of distribution. For a given Doppler velocity bin, the successive spectral power values are sorted in ascending order. It is also assumed that the noise and atmospheric spectral power values are much weaker than the intermittent clutter power values, so that the lowest values are likely not to contain intermittent clutter. Starting from the two smallest values, several tests are performed to see if those values are consistent with an exponential distribution. If the tests fail, then only the smallest value is used. If the tests do not fail, then they are performed on the three lowest values, and on the four lowest and so on, until either the tests fail or all the power values are accepted. The spectral averaging is performed solely with the accepted power values. This method operates on the unaveraged spectra and works best with a large number of them. It also assumes that the dwell time (the total coherent and spectral integration time) is longer than the duration of the intermittent clutter event, so that at least some of the spectral power values are free of clutter. If birds are the cause of the clutter, then the necessary dwell time increases with altitude due to the spreading of the profiler beam. Merritt recommends dwell times of 1-2 min to assure some clean spectral power values. However, in the present study we only have access to the averaged spectra, which, given the integration time of about 22 s, severly limits the number of spectra available. We must then use the most efficient method possible for eliminating intermittent clutter. As we shall see in chapter 5, some on-line spectral averaging programs for profilers use SAM to eliminate intermittent clutter (see, for example, Angevine (1997)).

If one has access to the time series of the returned radar signal, then additional methods are available. Jordan *et al.* (1997), for instance, use wavelet transforms to analyze the profiler time series. Ground and intermittent clutter are easier to separate from the clear-air signal using wavelet transforms because, unlike Fourier transforms, they do not suffer from windowing effects and we are free to use a wavelet form specifically chosen to identify ground and/or intermittent clutter. Once the ground and intermittent clutter are identified in the wavelet transforms, their energies are reduced to match the clear-air levels using an interpolation scheme. Hocking (1997) removes ground clutter by fitting a polynomial to the time series and removing it, while May and Strauch (1998) propose using a digital filter on the time series to remove ground clutter. The subsequent Fourier transform shows much less ground clutter. What remains is removed using a 'notch filter' around the zero Doppler velocity bin. Intermittent clutter due to aircraft may also be reduced by an algorithm operating on the profiler time series. However, the returned radar signal time series is not available to us, and so we will restrict ourselves to spectral data.

Cornman *et al.* (1998) use fuzzy logic to identify the clear-air spectra in the presence of all types of clutter. The method is applied mainly to spectral power fields in Doppler velocity-height coordinates, $S(v,h)$, at a given time. For every point, local properties of the spectral power field, $S(v,h)$, are found, such as its curvature, gradient and others. For each of these properties, membership functions are consulted and the membership value is found for that property. The membership functions vary from 0 to 1 and express the degree to which that property value belongs to the set of clear-air property values (1 means that the value belongs to the clear-air set, 0 means it does not). The membership values for each property for every point are then weighted and added together, creating a total membership function, $M_T(v,h)$, that varies between 0 and 1, and expresses the degree to which that point is a clear-air spectral component. The total membership function is further modified in such a way as to enhance coherent features and suppress isolated points. Finally, the points that are used in the spectral moment calculations are those whose membership values exceed a certain threshold value. Issues regarding the determination of the membership functions and the threshold value aside, the membership values do not tell us how much of the spectral power at a given point is due to clear air. Therefore, this method may have difficulty handling cases where different kinds of spectra are overlayed on top of one another. While Cornman *et al.* do not use order statistics, there is no reason why they cannot be incorporated into this method. However, in order to incorporate them in a fuzzy logic algorithm, their properties must first be understood. Therefore, we will restrict ourselves to using order statistics only.

Since the membership functions represent the beliefs of a human expert, the fuzzy logic algorithm attempts to mimic the pattern recognition ability of a human expert. A similar thing is done by Clothiaux *et al.* (1994) using a neural network. Simply put, the local maxima of spectral power of clear-air Doppler spectra are identified for each range gate. From these, all possible wind profiles are constructed by linking together a local maximum at each range gate to form a profile. A human analyst then rates each profile according to how closely it resembles a real atmospheric profile. This information is then used to 'train' a neural network to identify real atmospheric profiles. The neural network is then used to identify atmospheric wind profiles from profiler data taken in meteorological conditions similar to those of the data used to train it. Neural networks are, however, beyond the scope of this thesis.

Finally, we mention what we describe as simple threshold methods, used by Lataitis (1993), Angevine (1994), Angevine *et al.* (1994a; 1994b; 1994c), Lippmann *et al.* (1996). Usually, the methods start by evaluating some central tendency statistic over the entire contaminated time series, either the mean or median, followed by its standard deviation (Angevine, 1994; Angevine *et al.*, 1994a). Only those points that fall within an interval consisting of the mean or median, plus or minus some multiple of the standard deviation, are accepted. This is done for the clear-air Doppler velocity, spectral width, and the signal-to-noise ratio time series in parallel, over periods of one to two hours (with 20-30 seconds between measurements). A given point must fall within every interval in order to be accepted. These methods use the statistics of the entire time series to identify outliers, with no attempt to treat the data prior to compiling these statistics. The outliers may make the standard deviations of the time series too large which in turn may cause the simple threshold method to accept too many outliers. Also, this method does nothing to remove points near the mean or median which are still suspect because they are discontinuous with respect to their immediate neighbors.

Alternatively, a relatively short running window may be imposed on the mean Doppler velocity time series, and those data points within the window that 'cluster' sufficiently are accepted (Lataitis, 1993; Lippmann *et al.*, 1996). The clustering is determined for a given point by finding the number of points that fall within the interval consisting of its data value plus or minus a predetermined threshold length. If this number of points, normalized with respect to the total number of points within the window, is above a certain threshold, then the point is accepted. Presumably, an outlier stands out by virtue of its extreme value, and so few points will fall within the interval centered about its data value. However, should the outliers within a window cluster sufficiently, which may happen in the case of ground clutter for instance, they will also be accepted.

3.2 The Ranked-Order Signal Processing Algorithm (ROSPA)

Here, we introduce, explain and analyze the processing algorithm used to treat the urban RASS data, called ROSPA. ROSPA is a sequence of filters and operations applied principally to the clear-air spectral data measured by a profiler in RASS mode. As we shall see, the acoustic velocity data is not only interesting by itself, but is also valuable in calibrating ROSPA for treatment of the clear-air Doppler velocities.

3.2.1 The Minimum Filter

Definition

The *minimum filter* is a type of ranked-order filter described by Heygster (1982), Kim and Yaroslavskii (1986), Pitas and Venetsanopoulos (1990), and by Astola and Kuosmanen (1997). Given an input discrete-time time series, $x[i]$ where the square brackets are used to indicate that the argument is discrete, the minimum filter imposes a moving window an odd number of points long, $2n+1$, with n points on either side of the center point i. The output time series, $y[i]$, is simply the minimum value of the points within the window. Mathematically, we have

$$y[i] = \min(x[i-n], x[i-n+1], \ldots, x[i+n-1], x[i+n]) \tag{3.1}$$

where $x[i]$ is the input time series, and $y[i]$ is the output time series. Figure 3.1 demontrates the minimum filter.

Theory

We will now evaluate the effect of the minimum filter on an input time series, $x[i]$, which is random and characterized as follows: (i) $x[i]$ and $x[j]$ are independent for all $i \neq j$; (ii) $x[i] = z[i]$, where $z[i]$ is a series of independent identically distributed (iid) random variables with a probability density function $f(z)$; (iii) for any given time i, an error $\xi[i]$, also iid with density function $g(\xi)$ and independent of $z[i]$, is added to the time series, $x[i] = z[i] + \xi[i]$, with a probability of occurrence p. Also, (iv) the error is always positive, $g(\xi) = 0$ for all $\xi \leq 0$. In essence, $x[i]$ is a series of iid random variables with a positive *impulsive noise* added to it. Unlike white noise, which affects every member of a time series equally, impulsive noise only affects certain members and not others. In this case, which members are affected is determined randomly by a probability of occurrence, p. Impulsive noise is interpreted here as representing a malfunction or disruption of the normal process of measurement, caused by factors physically unrelated to the quantity of interest. For a profiler measuring

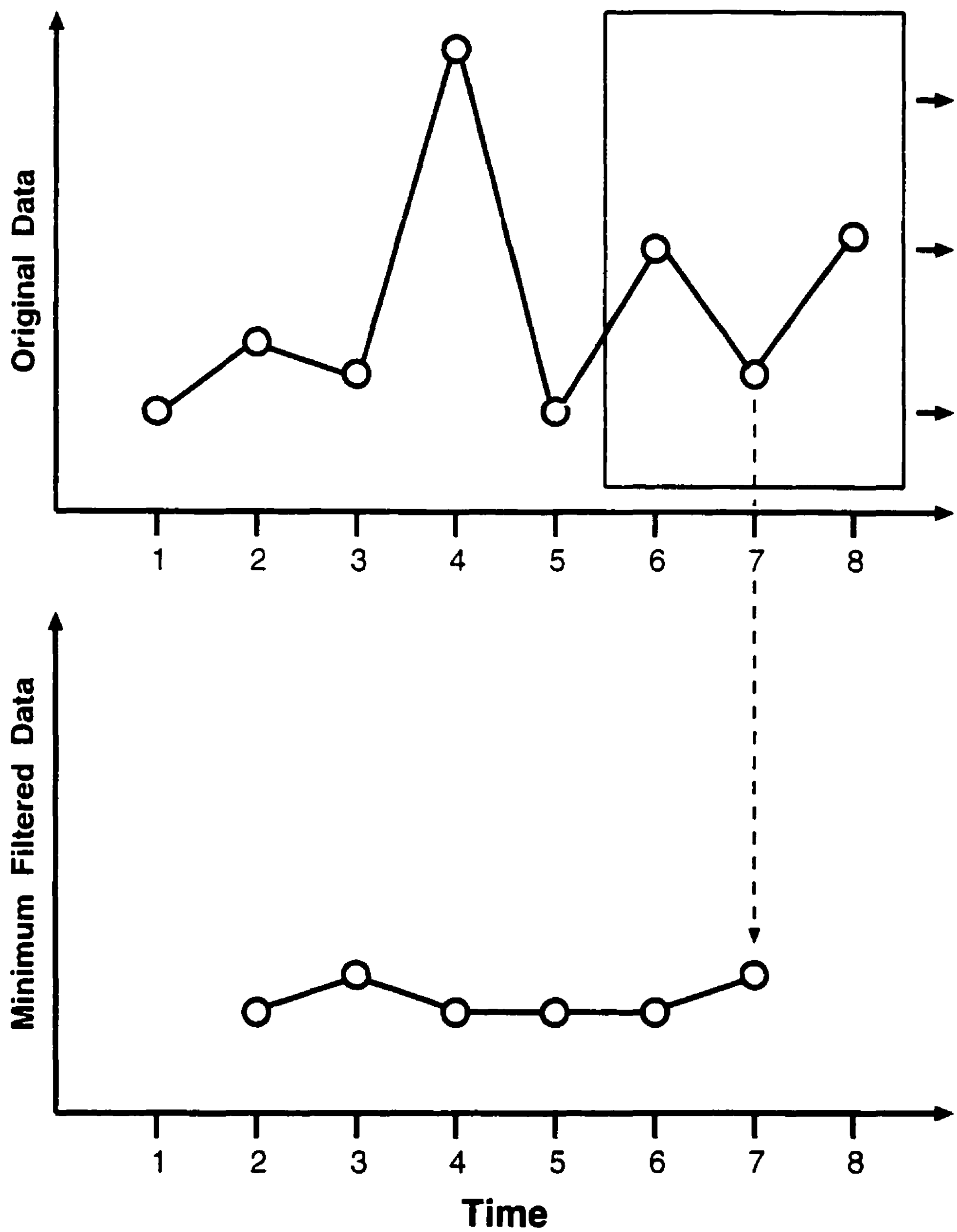

Figure 3.1: Schematic demonstration of the minimum filter. The upper plot shows the original data, with the three-point wide window (box) going from left to right. At each window position, the minimum value of the points inside the window is found and given to the corresponding point in the lower plot.

clear-air reflectivity, for instance, the power returned due to refractive index fluctuations represents a normal measurement, while the power returned by a bird or aircraft represents a disruption. In this model, the random variable ξ represents a disruption. The random variable z represents a normal measurement, which we will also call the *signal* to emphasize its usefulness.

For convenience, we introduce the random variable $a = z + \xi$, with the probability density function $h(a) = \int_0^\infty g(\xi)f(a-\xi)\mathrm{d}\xi$. The overall probability density function for a given point of the input time series, $\rho_i(x)$, is given by

$$\rho_i(x) = (1-p)f(x) + ph(x). \tag{3.2}$$

Furthermore, we introduce the input cumulative probability distribution function, $R_i(x) = \int_x^\infty \rho_i(x')\mathrm{d}x'$, which equals

$$R_i(x) = (1-p)F(x) + pH(x) \tag{3.3}$$

where $F(x) = \int_x^\infty f(z)\mathrm{d}z$ and $H(x) = \int_x^\infty h(a)\mathrm{d}a$ are the distribution functions of the uncontaminated and contaminated points respectively. The average $\overline{x} = \int_{-\infty}^\infty \rho_i(x)x\mathrm{d}x$, is given by

$$\overline{x} = (1-p)\overline{z} + p\overline{a} \tag{3.4}$$

where $\overline{z} = \int_{-\infty}^\infty f(z)z\,\mathrm{d}z$, and $\overline{a} = \int_{-\infty}^\infty h(a)a\,\mathrm{d}a$. However, because $\overline{a} = \overline{z} + \overline{\xi}$, where $\overline{\xi} = \int_0^\infty g(\xi)\xi\,\mathrm{d}\xi$, we have

$$\overline{x} = \overline{z} + p\overline{\xi}. \tag{3.5}$$

Since the error is undesirable and $\overline{\xi} \geq 0$, we have an average positive bias of $\overline{x} - \overline{z} = p\overline{\xi}$, from the correct average $\overline{z}$. The effect of the error is to create a longer tail on the positive side of the probability density function $f(z)$.

Now, we determine the characteristics of the output time series, $y[i]$, of an m-point minimum filter. Note that these characteristics are only valid for the particular input time series $x[i]$. A general theory of rank-order filters is not possible since these filters are nonlinear. We must therefore specify the characteristics of the input before we can say anything about the output. Since the probability that a point may be contaminated with an error is independent of all the other points, the probability that an m-point window may contain $n \leq m$ contaminated points follows a binomial distribution.

$$P_{m,p}[n] = \frac{m!}{n!(m-n)!}(1-p)^{m-n}p^{n} \tag{3.6}$$

For a given n, the conditional probability density function of the minimum y, $\rho_{min}(y|n)$ is

$$\rho_{min}(y|n) = (m-n)F^{m-n-1}(y)H^{n}(y)f(y) + nF^{m-n}(y)H^{n-1}(y)h(y). \tag{3.7}$$

The first term in Eq. 3.7 represents the case when one of the $m-n$ uncontaminated points has the minimum value. The factor $(m-n)$ is there to take into account the fact that any of the uncontaminated points may have the minimum value. The second term represents the same thing for the contaminated points. The overall output probability density function, $\rho_o(y)$, is then

$$\rho_o(y) = \sum_{n=0}^{m} P_{m,p}[n]\rho_{min}(y|n). \tag{3.8}$$

It is now useful to partition $\rho_o(y)$ into.

$$\rho_o(y) = f_{min}(y) + h_{min}(y) \tag{3.9}$$

where

$$f_{min}(y) = \sum_{n=0}^{m}(m-n)\frac{m!}{n!(m-n)!}(1-p)^{m-n}p^{n}F^{m-n-1}(y)H^{n}(y)f(y). \tag{3.10}$$

and

$$h_{min}(y) = \sum_{n=0}^{m} n\frac{m!}{n!(m-n)!}(1-p)^{m-n}p^{n}F^{m-n}(y)H^{n-1}(y)h(y). \tag{3.11}$$

Here, we have two types of data points in the time series: those that do not contain an error (*good* points), and those that do (*bad* points). When we find the minimum in a given window, that point can be good or bad. Therefore, $f_{min}(y)$ represents the contribution to the overall probability density function of the good points. When a good point is the minimum, we call this event a *correct reconstruction*, following Pitas and Venetsanopoulos (1990) in their discussion of the median filter. We will adopt this terminology. Conversely, when a bad point is the minimum, this is an *incorrect reconstruction* and its contribution is represented by $h_{min}(y)$. We can use the fact that $f(z) = -F'(z)$ and $h(a) = -H'(a)$, where the prime denotes differentiation with respect to the argument, to rewrite Eqs. 3.10 and 3.11 as,

$$f_{min}(y) = -\sum_{n=0}^{m} \frac{m!}{n!(m-n)!}(1-p)^{m-n}p^n H^n(y)\frac{\mathrm{d}}{\mathrm{d}y}(F^{m-n}(y)). \tag{3.12}$$

$$h_{min}(y) = -\sum_{n=0}^{m} \frac{m!}{n!(m-n)!}(1-p)^{m-n}p^n F^{m-n}(y)\frac{\mathrm{d}}{\mathrm{d}y}(H^n(y)). \tag{3.13}$$

which, if used in Eq. 3.9, lead to,

$$\rho_o(y) = -\sum_{n=0}^{m} \frac{m!}{n!(m-n)!}(1-p)^{m-n}p^n \frac{\mathrm{d}}{\mathrm{d}y}(F^{m-n}(y)H^n(y)). \tag{3.14}$$

Alternatively, if we define $R_o(y) = \int_y^\infty \rho_o(y')\mathrm{d}y'$, or $\rho_o(y) = -R_o'(y)$, we can transform Eq. 3.14 into

$$R_o(y) = \sum_{n=0}^{m} \frac{m!}{n!(m-n)!}(1-p)^{m-n}p^n F^{m-n}(y)H^n(y). \tag{3.15}$$

To go further, we must now attribute a specific form to $f(z)$ and $g(\xi)$. We assume that $g(\xi)$ and $f(z)$ are gamma density functions,

$$\begin{aligned} g(\xi) &= \frac{(v\alpha)^v \xi^{v-1}}{(v-1)!}e^{-v\alpha\xi} \qquad 0 < \xi < \infty \\ &= 0 \qquad\qquad\qquad\qquad -\infty < \xi \le 0 \end{aligned} \tag{3.16}$$

and,

$$f(z) = \frac{(w\lambda)^w z^{w-1}}{(w-1)!} e^{-w\lambda z} \qquad 0 < z < \infty$$
$$= 0 \qquad -\infty < z \leq 0 \tag{3.17}$$

where w and v are integer parameters, and λ and α are real parameters, to be set later. The density $f(z)$ is a gamma function so as to simulate the spectral power of Gaussian white noise for a fixed frequency bin (see section 2.4). The time series $z[i]$ represents successive values of the spectral power for that bin for white noise spectra. The density $g(\xi)$ is a gamma function for computational simplicity. The distribution function $F(y)$ takes the form,

$$F(y) = \left[\sum_{i=0}^{w-1} \frac{(w\lambda y)^i}{i!}\right] e^{-w\lambda y} \qquad 0 < y < \infty$$
$$= 1 \qquad -\infty < y \leq 0. \tag{3.18}$$

As for $H(y)$, we have,

$$H(y) = \int_y^\infty h(a)\mathrm{d}a \tag{3.19}$$

$$= \int_y^\infty \left\{ \int_0^\infty g(\xi) f(a-\xi)\mathrm{d}\xi \right\} \mathrm{d}a \tag{3.20}$$

$$= \int_0^\infty g(\xi) F(y-\xi)\mathrm{d}\xi \tag{3.21}$$

where the order of integration has been reversed to obtain this result. The function $H(y)$ will be evaluated numerically. Before we can do this, however, we must choose some values of the parameters. We postulate that an error, when it occurs, is huge relative to the average value of the good points, namely $\overline{\xi} = 1000\,\overline{z}$. The average of a gamma density function is

$$\overline{z} = 1/\lambda, \tag{3.22}$$

$$\overline{\xi} = 1/\alpha. \tag{3.23}$$

We set $w = 24$, because we wish to simulate the white noise spectrum as measured by the profiler using RASS settings, where typically 24 spectra are averaged together

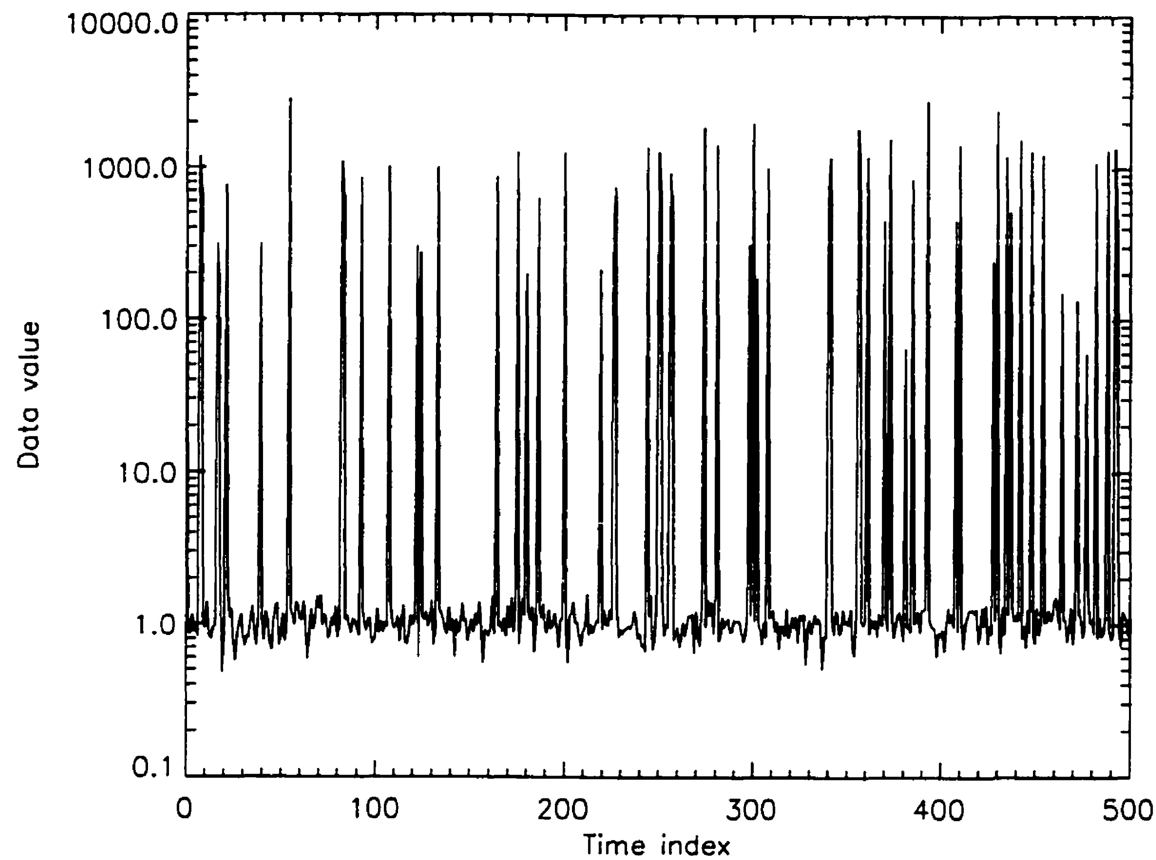

Figure 3.2: An artificially generated input time series for the minimum filter, using the specifications described in the text.

(see section 2.4). Also, we set $\lambda = 1$ so that $\bar{z} = 1$. We want a relatively broad error density function, $v = 2$. Finally, given our constraint on the means, we set $\alpha = 0.001$ so that $\bar{\xi} = 1000$. Note that if the errors were caused by reflections off birds, then a log-normal error density function would be more appropriate (Konrad *et al.*, 1968), but we choose a gamma function instead for computational convenience. We further assume that an error is relatively rare, $p = 0.1$. Figure 3.2 shows an example of such a time series.

Figure 3.3 shows graphically the results of the model described previously. The

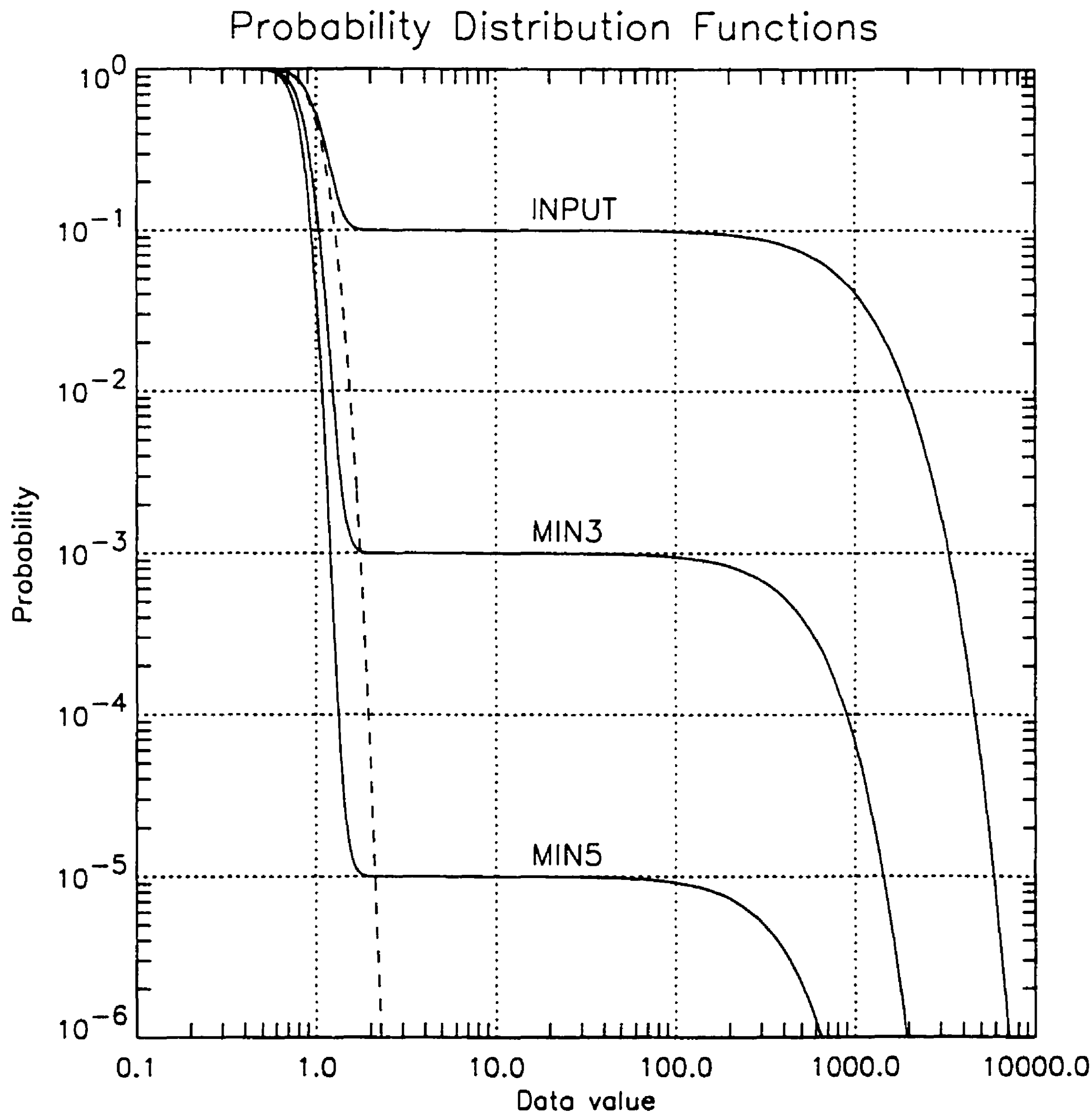

Figure 3.3: Theoretical probability distributions of the input $R_i(x)$ (the solid line labeled INPUT), the output of a 3-point minimum filter (the solid line labeled MIN3), and the output of a 5-point minimum filter (the solid line labeled MIN5). The dashed line is the probability distribution function of the uncontamined data $F(z)$.

line labeled INPUT is the input probability distribution function $R_i(x)$, and the dashed line is the uncontaminated probability distribution function $F(z)$. We can see that the input distribution function has a sharp drop at about unity, then, beyond 1, has a plateau with a probability value of about 0.1. The plateau represents the approximately 10% of the points that are bad. The initial drop, which follows the dashed line reasonably well, represents the approximately 90% of the points that are good. The output of the 3-point minimum filter (MIN3) shows a plateau with a probability value of about 0.001. This is because the MIN3 output may reach a value greater than about 2 only if there is an incorrect reconstruction, which can only happen if all the points within the window are bad. Since the probability of occurrence of an error is 0.1, then the probability of three bad points in a row is $0.1 \times 0.1 \times 0.1 = 0.001$. The same reasoning applies for the plateau on the 5-point minimum filter (MIN5) output distribution. We also see that both the MIN3 and MIN5 output distributions initially fall faster than the dashed line, such that the probability that the MIN3 and MIN5 outputs reach or surpass the threshold value of 1, is less than that for the uncontaminated distribution. This is explained by the fact that if all the points within the window are good, then the process of finding the minimum will necessarily induce a bias towards smaller values.

Application

The minimum filter, applied to clear-air spectra, takes the form,

$$S_{min}[k,j,i] = \min(S[k,j,i-n],\ldots,S[k,j,i+n]) \tag{3.24}$$

where $S[k,j,i]$ is the spectral power for the Doppler velocity bin index k, at altitude index j and time index i, and $S_{min}[k,j,i]$ is the spectral minimum of a sequence of $2n+1$ spectra. The sequence in time of power values for a fixed Doppler velocity bin and altitude is used as an input time series, $x_{\alpha,\beta}[i] = S[k=\alpha, j=\beta, i]$. It is this time series which is treated with a minimum filter; the output is then used to create a new set of clear-air spectra, $S_{min}[k=\alpha, j=\beta, i] = y_{\alpha,\beta}[i]$. To see how well the minimum filter works, we must first examine the time structure of the spectra. The clear-air spectra can be decomposed in the following way:

$$S[k,j,i] = A[k,j,i] + N[k,j,i] + G[k,j,i] + I[k,j,i] \tag{3.25}$$

where $A[k,j,i]$ is the atmospheric signal spectrum, $N[k,j,i]$ is a white noise spectrum, $G[k,j,i]$ is the ground clutter, and $I[k,j,i]$ is the intermittent clutter. The atmospheric spectrum, the white noise, and the ground clutter are relatively constant within a timescale of about 1 minute (approximately 3 spectral integration times). The intermittent clutter, on the other hand, varies greatly from one integration time to the next.

Figure 3.4(a) shows an example of the spectral power time series for a fixed Doppler velocity bin and altitude, $x_{\alpha,\beta}[i]$. Note that the power is expressed as a power-to-noise ratio (PNR), which is the total spectral power (signal + noise) divided by the noise level ($\overline{N}$). The PNR is more convenient than the signal-to-noise ratio (SNR) because occasionally the power falls below the noise level, causing the SNR to go to minus infinity on a logarithmic scale. The spikes in Fig. 3.4(a) probably indicate intermittent clutter. The spikes appear to be placed on top of a slowly varying signal, which we assume is the atmospheric signal. Figure 3.4(b) is the output of a 3-point minimum filter applied to the time series in (a). Most of the spikes have been eliminated, but some still persist. Also, we can discern the atmospheric signal better. Figure 3.4(c) is the output of a 5-point minimum filter applied to the time series in (a). Essentially all the spikes are gone but the atmospheric signal appears to have suffered some power depletion.

Figure 3.5 shows an example of a 3-point ($n = 1$) minimum spectral filter on the vertical pattern of clear-air spectral data. All of the first three plots ((a) to (c))show signs of intermittent clutter contamination. The intermittent clutter appears as a region of very high power, extending about 150 m in height and 3 m/s in Doppler velocity and usually accompanied by lobes regularly spaced along the Doppler velocity

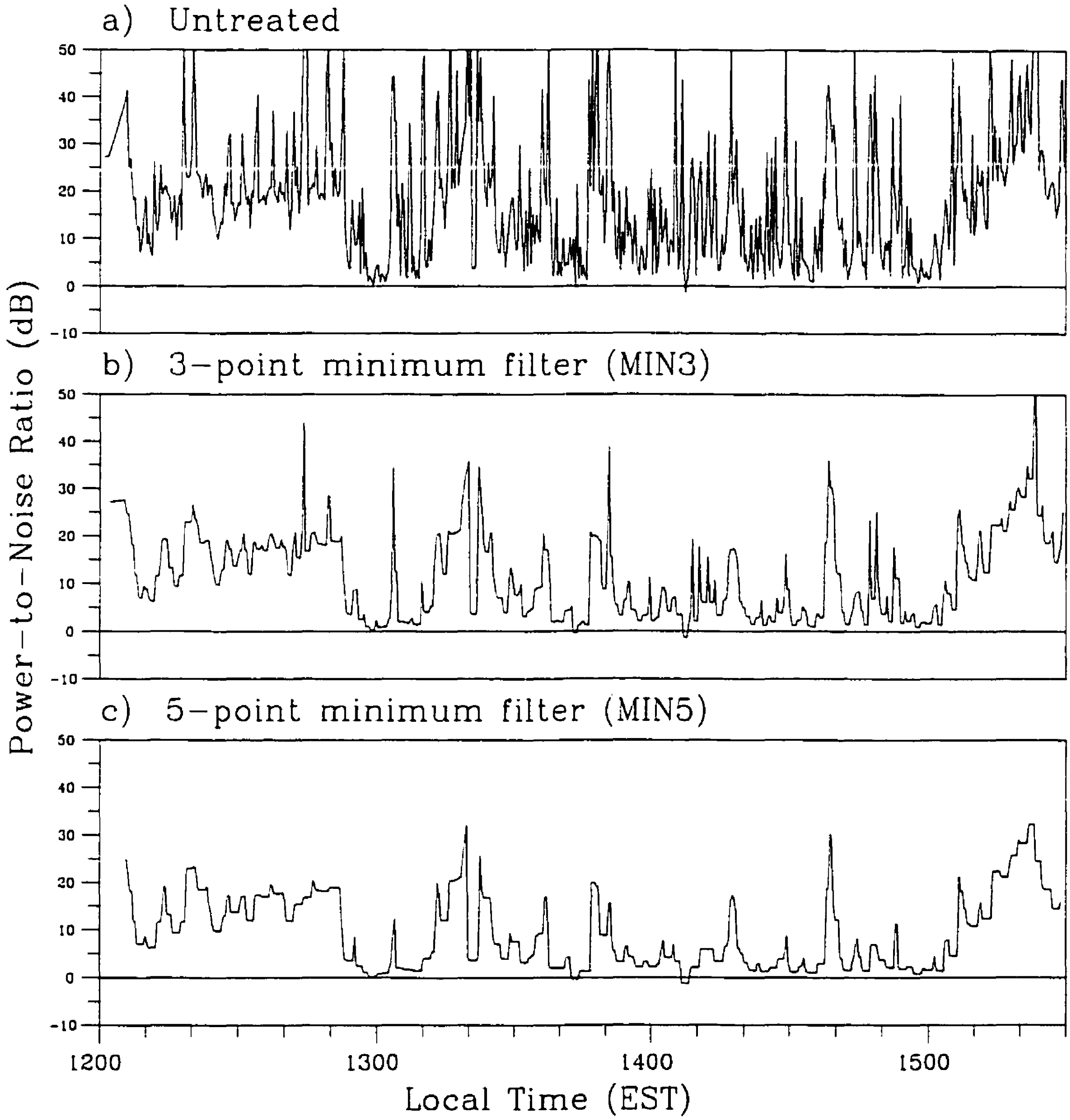

Figure 3.4: The application of 3-point (b) and 5-point (c) minimum filters to the clear-air spectral power-to-noise ratio (in decibels) time series (a) of the 2.7 m/s Doppler velocity bin, at 345 m AGL on June 28, 1996, over the McGill campus. Note that the line at 0 dB represents the noise level.

axis. Intermittent clutter events usually last only one integration time, such as the one at 0.6 km in Fig. 3.5(a). However, intermittent clutter events occasionally last longer, such as the one at 0.2 km in Figs. 3.5(b) and (c). Nonetheless, the 3-point minimum filter in Fig. 3.5(d) eliminates much of the clutter and produces a ridge of high power that forms an arc extending from 0.1 to 1.2 km in height, on the positive Doppler velocity side. The ridge most likely represents an updraught. Secondary peaks and the spread of power (as evident from the 5 and 15 dB contours) imply that the intermittent clutter has not been completely eliminated in this case. A weak ridge along the zero velocity line can also be seen (examine the 5 dB contour), which is a manifestation of ground clutter.

Intuitively, then, we can see that if intermittent clutter events are sufficiently short-lived to affect only one spectrum, and if they are sufficiently rare so that at least one spectrum within a 3 or 5 point window is free of intermittent clutter, and given that spectral power is always positive, then the minimum is likely to be the spectral power value that does not include the intermittent clutter. Moreover, if intermittent clutter events persist for more than one spectral integration time, then the performance of minimum filter would not be seriously affected as long as the lifetime of the individual events is shorter than the window length.

3.2.2 The Threshold Minimum Filter

Unfortunately, we cannot use the spectral power $S_{min}[k, j, i]$, given by Eq. 3.24, to estimate the mean Doppler velocity for purposes of heat flux and vertical air velocity variance estimation. The reason is that the minimum filter modifies the correlation between successive Doppler velocity estimates, which is undesirable if we wish to reliably eliminate the random error variance from estimates of vertical air velocity variance. To reduce this effect, the estimate $S_{min}[k, j, i]$ will be used as a reliable lower bound on the estimation of spectral power at that bin, altitude and time, in

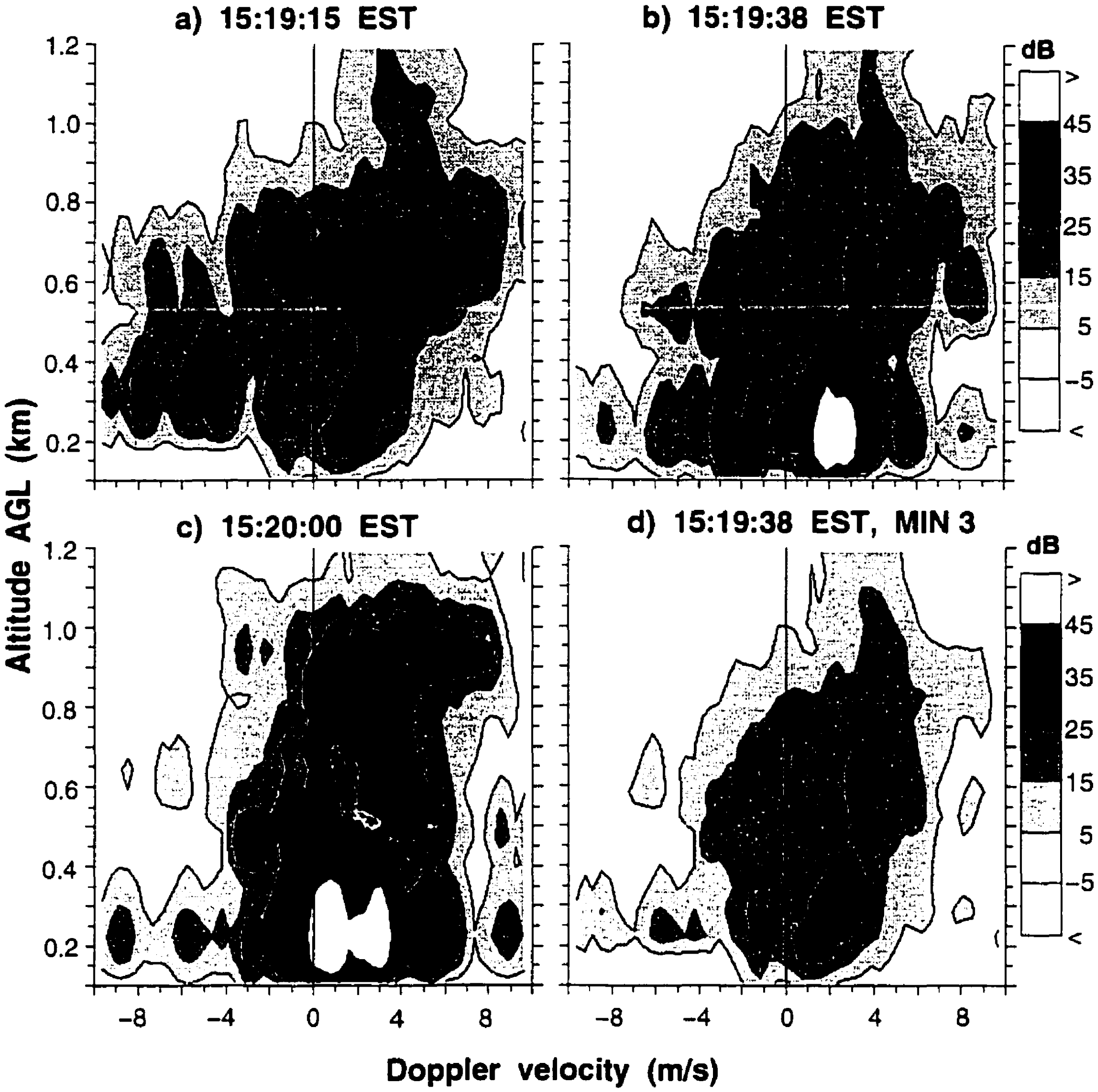

Figure 3.5: Doppler spectral contours of the clear-air spectral power-to-noise ratio, expressed in decibels, measured by the profiler using the RASS settings, at the McGill campus, on June 28, 1996. Figures (a), (b) and (c) show three consecutive untreated spectral plots. Figure (d) shows the minimum of the three previous plots at each point.

what is known as a *decision-based filter* (Astola and Kuosmanen, 1997), which we will call a *threshold minimum filter.*

Definition

Given the outputs of a series of $m = 2n + 1$ point minimum filters, $y_{min(2n+1)}[i]$, where $n = 0, 1, ..., N$, and the input time series, $x[i]$, where $y_{min(2N+1)}[i] \leq y_{min(2N-1)}[i] \leq ... \leq y_{min3}[i] \leq x[i]$, and a threshold factor, $\tau > 1$, from which we create a theshold time series, $\Gamma[i] = \tau y_{min(2N+1)}[i]$, we can define a threshold minimum filter denoted by TMIN[2N+1]:

$$\begin{aligned} y_{tmin(2N+1)}[i] &= x[i] && \text{if} \quad (x[i] \leq \Gamma[i]) \\ &= y_{min3}[i] && \text{if } (y_{min3}[i] \leq \Gamma[i] < x[i]) \\ &= y_{min5}[i] && \text{if } (y_{min5}[i] \leq \Gamma[i] < y_{min3}[i]) \\ &\dots \\ &= y_{min(2N+1)}[i] && \text{if } (\Gamma[i] < y_{min(2N-1)}[i]). \end{aligned} \tag{3.26}$$

In other words, the output of a $(2N+1)$-point minimum filter, $y_{min(2N+1)}[i]$, is used as a reliable baseline: that is a baseline assumed to be completely unaffected by intermittent clutter. For this, the window must be long enough to include at least one point which is clutter free. But since the baseline might also be too rigid, we would like to include points from the input time series, $x[i]$, that are reasonably close to the baseline, and are therefore assumed to be good. We introduce a threshold for each point which is some multiple of the baseline, $\Gamma[i] = \tau y_{min(2N+1)}[i]$. If the input time series is less or equal to the threshold, $x[i] \leq \Gamma[i]$, at that point, then it is accepted. If not, then the 3-point minimum filter output is tested: $y_{min3}[i] \leq \Gamma[i]$. If it passed the theshold test for that point, then it is accepted; if not then the same thing is done for the MIN5 output, and so on until we reach the baseline itself. The end result will therefore be a composite of the input time series and the outputs of minimum filters with various window sizes (but no larger than $(2N+1)$).

In those regions where the input time series is relatively smooth, most of the output points will simply be the original input points. In those regions where the input time series is highly contaminated by intermittent clutter, the output will be minimum filter output points with a window just large enough to adequately eliminate the clutter. The threshold is a multiple of the baseline because we assume that the good points obey a gamma probability density function, where all the moments are proportional to the corresponding power of the mean. If the minimum of a group of good points is, on average, also proportional to the mean, then the moments also scale with respect to the minimum. A multiple of the minimum is therefore the best way to account for the change in statistics as a function of time. We will explore this issue in more detail in the theory on threshold minimum filters. Of course, there remains the question of the appropriate threshold factor, which will be discussed later.

Theory

The theory of threshold minimum filters deals essentially with the choice of a given threshold factor value, τ. Indeed, the decisions described in Eq. 3.26 are in fact a series of hypothesis tests (see Appendix C for a description of hypothesis tests). We will use the same model input time series used for the theory of the minimum filter, in subsection 3.2.1, to compute the significance level α of the tests. In particular, we will concentrate on the test on the input time series, $x[i] \leq \Gamma[i]$. Also, we will limit ourselves to the case where either all of the points within the window are good (the null hypothesis H_0), or they are all good except the middle one, which is contaminated (the alternative hypothesis H_1).

We start by introducing the joint distribution of two order statistics (see David (1970)). Given $m = 2n + 1$ iid random variables, $x[i-n], x[i-n+1], ..., x[i+n-1], x[i+n]$, with distribution $F(x)$, described by Eq. 3.18, we sort them in ascending order, $x_{(1)}, x_{(2)}, ..., x_{(m)}$, where the subscripts denote the order. The joint probability density function for the random variables $x_{(r)}$ and $x_{(s)}$, where $1 \leq r < s \leq m$ and

$x_{(r)} < x_{(s)}$, is then

$$f_{r,s}(x,y) = \frac{m!}{(r-1)!(s-r-1)!(m-s)!}[1-F(x)]^{r-1}f(x) \cdot [F(x)-F(y)]^{s-r-1}f(y)F^{m-s}(y) \tag{3.27}$$

where $f(x)$ is the probability density function of the good points (see Eq. 3.17). Note that we adopt the convention that $f_{r,s}(x,y)$ denotes the joint probability density function of $x_{(r)} = x$ and $x_{(s)} = y$. And of course, when $r = s$, then we set $f_{r,s}(x,y) = f_r(x)\delta(x-y)$. The baseline is $x_{(1)}$. The point in the middle of the window, $x[i]$, has an equal chance of having any rank: $x[i] = x_{(s)}$, where $s = 1,\ldots,m$ with equal probability. This is because all the points within the window are iid. Therefore, the joint probability density function of the baseline, $x_{(1)} = x$, and the middle point, $x[i] = y$, is

$$f_{1,i}(x,y) = \frac{1}{m}\sum_{s=1}^{m} f_{1,s}(x,y). \tag{3.28}$$

The significance level, α, of the first hypothesis test is therefore

$$\alpha(\tau) = \int_{x=0}^{\infty}\left[\int_{y=\tau x}^{\infty} f_{1,i}(x,y)\mathrm{d}y\right]\mathrm{d}x \tag{3.29}$$

which is the probability that the first test fails when H_0 is true (a type *I* error), as a function of the threshold factor.

Alternatively, if H_1 is true, then the middle point is contaminated and obeys the probability distribution function $H(x)$, described by Eq. 3.21. In this case, the middle point has a greater probability of possessing a higher rank than a lower one. From Eq. 3.27, we can deduce that the joint probability density function of $x = x_{(1)}$, and $y = x_{(s)}$, where $s > 1$, and where y is also a bad point, is

$$g_{1,s}(x,y) = \frac{m!}{(s-2)!(m-s)!}f(x)[F(x)-F(y)]^{s-2}h(y)F^{m-s}(y). \tag{3.30}$$

From this, we can formulate the counterpart to Eq. 3.28:

$$g_{1,i}(x,y) = \frac{1}{m}\sum_{s=1}^{m} g_{1,s}(x,y) \tag{3.31}$$

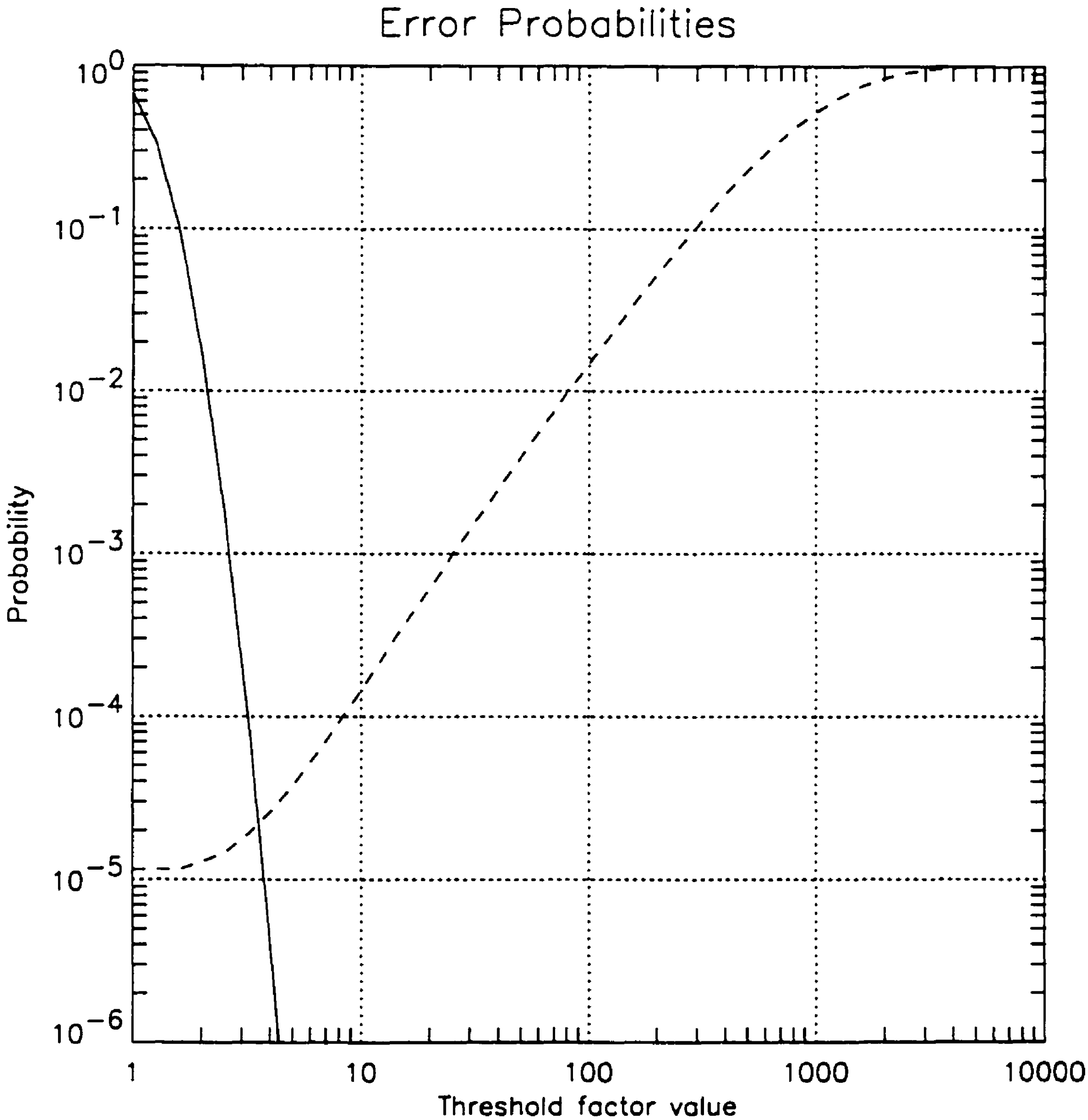

Figure 3.6: A plot of the probabilities of a type *I* error, α, (solid line) and of a type *II* error, β, (dashed line) of the threshold minimum filter hypothesis test, as a function of the threshold factor, τ, for a 3-point window (TMIN3).

where $g_{1,1}(x,y) = mF^{m-1}(x)h(x)\delta(x-y)$, is the probability that the bad point is the minimum. The probability, β, of accepting H_0 when H_1 is true (a type *II* error), is

$$\beta(\tau) = \int_{x=0}^{\infty}\left[\int_{y=x}^{\tau x} g_{1,i}(x,y)\mathrm{d}y\right]\mathrm{d}x \tag{3.32}$$

which is also expressed as a function of the threshold factor τ.

Figure 3.6 shows the $\alpha(\tau)$ and $\beta(\tau)$ functions for the case $m = 3$, where there is only one hypothesis test to perform. The solid line represents $\alpha(\tau)$, which starts at $\alpha(1) = 2/3$, meaning that there is a 1/3 probability that the middle point is the minimum, and drops very rapidly with increasing τ, meaning that the good points are closely grouped together and that a threshold factor of $\tau \approx 10$ essentially includes all good points. The dashed line in Fig. 3.6 represents $\beta(\tau)$. It starts at $\beta(1) \approx 10^{-5}$, which is the probability that the bad middle point is the minimum, and ends at $\beta(\infty) = 1$, which means that for a large enough τ, the bad point will certainly pass the hypothesis test. As expected, we see that as α decreases, β increases. Also, there is fairly wide range, $3 \leq \tau \leq 80$, where both error probabilities are acceptably small, α and $\beta \leq 1\%$. This is because the probability density functions of the good and bad points are fairly well separated in this model, which may not be the case for real data. Note that as τ increases beyond $\tau = 80$, not only does the probability of accepting a bad point become significant, but the magnitude of these bad points also increases, giving us a good reason to limit the size of the threshold factor as much as possible without eliminating too many good points.

The analysis is much more complicated if we include the possibility of more than one bad point within the window, or a window size that requires more than one hypothesis test. Nevertheless, the previous example demonstrates the main points of the threshold minimum filter, namely that the threshold factor must be large enough to include most good points, and small enough to exlude most bad points, particularly those with very large values. It is reasonable to assume that the optimal value of the threshold factor is a function of the ratio of the window period, $m\Delta$ (Δ is the time between measurements), and the timescale of the uncontaminated time series, T, such that if $\gamma = m\Delta/T$ is small, then the variation of the good points within the window is also small, thereby requiring a small threshold factor value. Also of concern is the average size of an error, $\bar{\xi}$, as this controls the size of the threshold factor which would admit too many bad points.

Application

The application here is the same for the minimum filter (subsection 3.2.1), that is,

$$S_{tmin}[k,j,i] = \mathrm{TMIN}(S[k,j,i-n],\ldots,S[k,j,i+n] \mid \zeta) \tag{3.33}$$

where $\zeta = 10\log(\tau)$ is the theshold factor in decibels. Figure 3.7 shows an example of a TMIN7 filter application with a 10 dB threshold factor ($\tau = 10$). Graph (b) shows the output of a MIN7 filter, which eliminates the spikes from the input but is too correlated over short time lags and suffers from power depletion. Graph (c) shows the output of a TMIN7 filter with a 10 dB threshold, which is less correlated over short lags and does not suffer as much from power depletion, while still excluding the obviously bad spikes. However, it is not hard to see in Fig. 3.7 that as the threshold increases, more and more spikes are admitted to the output. Therefore, we need a way to find the optimal threshold factor value, one that allows enough good points for a reasonable reconstruction of the spectra while exluding most if not all of the bad points. This issue will be discussed in greater detail in the chapter on data analysis.

3.2.3 Spectral Noise Suppression

Every bin in the spectrum includes a power contribution from white noise. We want to identify those bins that also include power from something other than noise. This is done by performing a hypothesis test on each bin (see Appendix C for a description of hypothesis tests). The null hypothesis, H_0, in this case is the statement that the power in a given bin is due only to white noise ($S = N$). Conversely, we define the alternative hypothesis, H_1, as the statement that the power in a given bin is due to

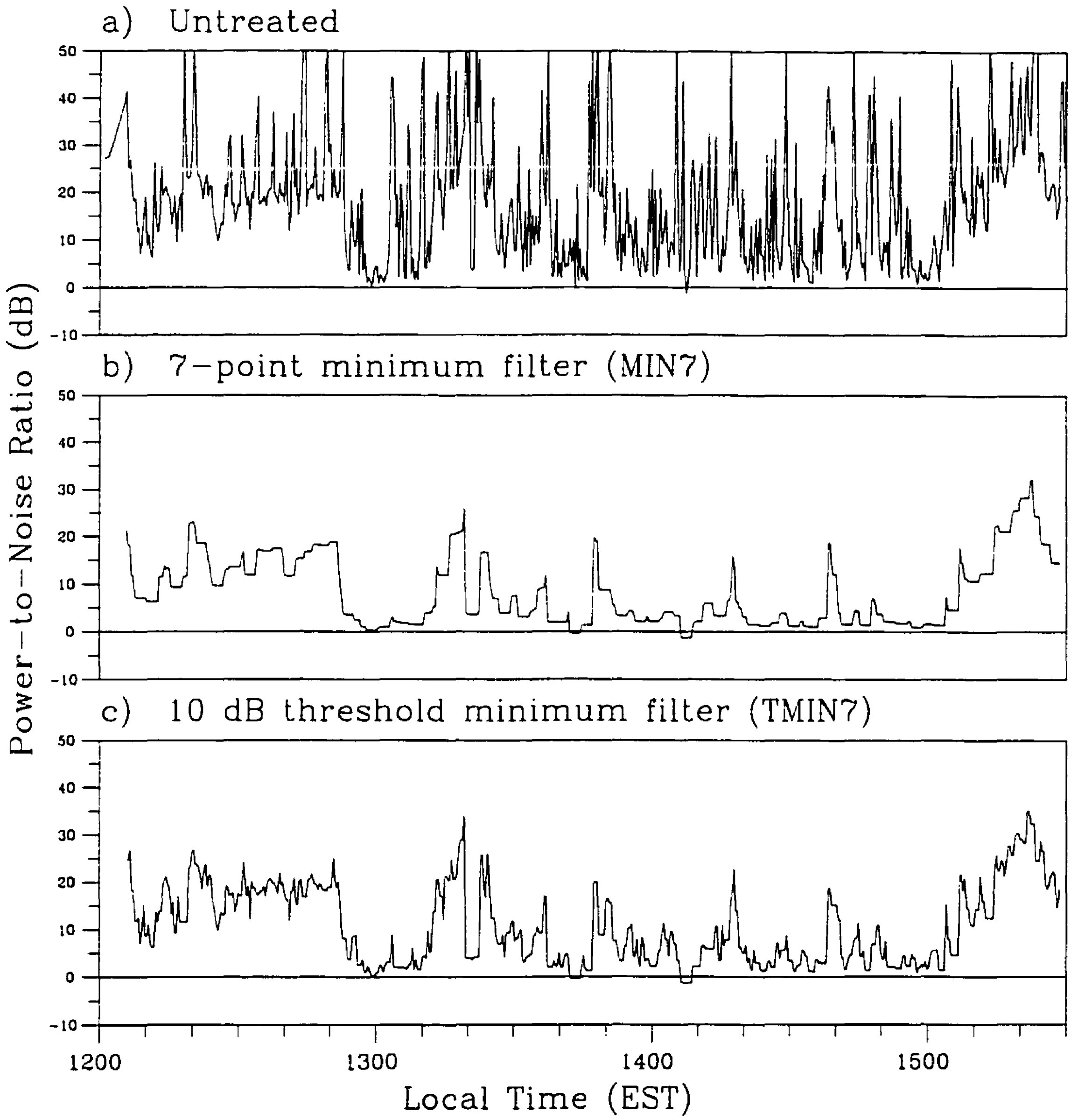

Figure 3.7: The application of a 7-point minimum filter (b) and a 7-point threshold minimum filter with a 10 dB threshold (c) to the clear-air spectral power-to-noise ratio (in decibels) time series (a) of the 2.7 m/s Doppler velocity bin, at 345 m AGL on June 28, 1996, over the McGill campus.

something other than white noise, in addition to the noise component ($S = N$+other).

If H_0 is true, then we can postulate a reasonable probability density function for the power value using the results from section 2.4 on white noise. Therefore, we know that the value of white noise spectral power has a probability density function described by Eq. 2.37, and a probability distribution function given by Eq. 3.18. The distribution function is thus

$$F_0(N) = \left[\sum_{i=0}^{w-1} \frac{(w\lambda N)^i}{i!}\right] e^{-w\lambda N} \tag{3.34}$$

for $N \geq 0$ ($F_0(N) = 1$ otherwise), where w is the number of spectral averages, and the average white noise spectral power (noise level), $\overline{N}$, is $\overline{N} = 1/\lambda$. In our work, w is ordinarily 24. The noise level is determined using the method by Hildebrand and Sekhon (1974), applied to the RASS power spectrum. The function $F_0(N)$ appeared as the dashed line in Fig. 3.3. The critical region C, which is the set of values of S where H_0 is rejected (and H_1 accepted), is defined using a threshold N_T, where C is $N_T < S < \infty$. Conversely, the region of acceptance is where H_0 is accepted (and H_1 rejected) and is defined as $0 \leq S \leq N_T$.

Since rejecting the null hypothesis when it is in fact true is often considered serious, α is usually made small. In our case, we will fix the significance level at 1%, or $\alpha = 0.01$. This corresponds to a threshold value of about $N_T = 1.534\lambda^{-1}$, or $N_T = 1.534\overline{N}$. If H_1 is true, then we do not know exactly the form of the probability distribution of the spectral power ($F_1(S)$) other than it must favour greater values of S ($F_1(S) \geq F_0(S)$, for all S) because, in this case, there is a random power value added to the white noise spectral power. The probability of a type *II* error, $\beta = 1 - F_1(N_T)$, is also unknown, except that $\beta \leq 1-\alpha$. In general, when we decrease α, we increase β. This seems to be the case here, since decreasing α increases N_T, which may increase β (as we saw in subsection 3.2.2 on the threshold minimum filter). On average, an atmospheric signal must have a spectral power (A) greater than $N_T - \overline{N}$ in order for H_1 to be accepted and for that bin to be used in spectral moment calculations. In

SNR units, we require $A/\overline{N} > (N_T - \overline{N})/\overline{N}$, or $A/\overline{N} > -2.72$ dB, on average, at the 1% significance level. This requirement is easily satisfied for most bins at low altitudes for a strong returned signal, meaning a low β for this kind of spectrum. For weak signals at high altitudes, however, there is a possibility that even the peak of the power spectrum may not satisfy the requirement, meaning that the entire spectrum may be mistaken for noise and that β is quite high. When a given bin is ruled to be only noise, the power value for that bin is replaced with $\overline{N}$, which serves as a flag to omit this bin in spectral moment calculations.

3.2.4 Ground Clutter Removal

Our strategy for eliminating ground clutter is based on the assumption that the ground clutter spectrum is symmetric about the zero Doppler velocity bin. We therefore expect the symmetry

$$G[k,j,i] = G[-k,j,i] \tag{3.35}$$

to hold, where $k = 0$ is taken to be the zero Doppler velocity bin. Following the work of Ohsaki and Masuda (1996), the symmetric part of the spectrum is identified and removed. Our first estimate of the ground clutter spectrum $\tilde{G}'[k,j,i]$ is taken to be

$$\tilde{G}'[k,j,i] = \tilde{G}'[-k,j,i] = \min(S[k,j,i], S[-k,j,i]) - \overline{N}, \qquad k > 0. \tag{3.36}$$

Here, we assume that $S[k,j,i]$ has already undergone minimum filtering and spectral noise suppression, which means that $\tilde{G}'[k,j,i]$ is sometimes exactly zero but never negative. In an effort to produce as conservative an estimate of ground clutter as possible, we will ensure that the final estimate, $\tilde{G}[k,j,i]$, decreases monotonically with increasing $|k|$:

$$\begin{aligned} \tilde{G}[1,j,i] &= \tilde{G}[-1,j,i] = \tilde{G}'[1,j,i] \\ \tilde{G}[k,j,i] &= \tilde{G}[-k,j,i] = \min(\tilde{G}'[1,j,i], \ldots, \tilde{G}'[k,j,i]), \qquad k > 1. \end{aligned} \tag{3.37}$$

Our estimate of the atmospheric signal at the zero Doppler velocity bin, $\tilde{A}[0,j,i]$, will always be interpolated from the values of the estimated atmospheric signal spectrum on either side of the zero Doppler velocity bin ($\tilde{A}[\pm1,j,i]$, $\tilde{A}[\pm2,j,i]$, ...), which in our case is

$$\tilde{A}[0,j,i] = -\frac{1}{6}\tilde{A}[-2,j,i] + \frac{2}{3}\tilde{A}[-1,j,i] + \frac{2}{3}\tilde{A}[1,j,i] - \frac{1}{6}\tilde{A}[2,j,i] \tag{3.38}$$

where the estimates $\tilde{A}[\pm1,j,i]$ and $\tilde{A}[\pm2,j,i]$, depend on the values of $\tilde{G}[1,j,i]$ and $\tilde{G}[2,j,i]$, respectively. We use these coefficients as they allow for the possibility of a local maximum or minimum at the zero Doppler velocity bin, as opposed to a simple linear interpolation. Therefore, we will not attempt to evaluate $\tilde{G}[0,j,i]$, since it has no effect on our estimate of $\tilde{A}[0,j,i]$. The treatment described in Eq. 3.37 may be too conservative, however, because the windowing effect may give the ground clutter secondary lobes on either side of the $k = 0$ bin. Equation 3.37 would not attribute these lobes to the ground clutter estimate. We will accept this risk, though, rather than allow the ground clutter estimate to potentially include far too much power. Note that if the atmospheric signal spectrum should be centered about zero velocity (no overall vertical air motion), then the ground clutter estimate would include most of the atmospheric signal power, thereby causing a very unreliable estimate of vertical air velocity. This is a common problem for ground clutter estimation methods.

3.2.5 Peak Identification

In the event of a spectrum with separated, nonoverlapping multiple peaks, it is necessary to identify one as the proper one, isolate it and ignore the other peaks. As we shall see in the next subsection, it is better to run the risk of choosing the wrong peak, and getting a completely wrong Doppler velocity value, than to use all the peaks and obtain a partially wrong Doppler velocity value. The peak identification algorithm used here is very similar to one proposed by May and Strauch (1989). We start by finding the spectral component with the most power, $S_{max} = S[k_{max}]$. From the spectral component k_{max}, the algorithm proceeds outwards in both directions until it encounters a spectral component with a power value less than the noise threshold N_T, from subsection 3.2.3 on spectral noise suppression. Mathematically, we have

$$\begin{aligned} S_{PI}[k] &= S[k] - N_T, \qquad a \le k \le b \\ &= 0, \qquad\qquad \text{elsewhere} \end{aligned} \tag{3.39}$$

where $a \le k_{max} \le b$ and $S[k] \ge N_T$ for all k belonging to the interval (a, b). However, if two or more peaks overlap sufficiently, then the trough between the peaks may not descend below the threshold value, in which case the peak identification algorithm may include more than one peak.

3.2.6 The Median Filter

After the clear-air spectra have been treated with a minimum filter, noise suppression, ground clutter removal, and the highest peak isolated, the mean Doppler velocities of these spectra are estimated. The resulting time series of the mean Doppler velocity, however, may still exhibit obvious bad points. The median filter is therefore used at this stage to eliminate these points.

Definition

The *median filter* is identical to the minimum filter except that the median, rather than the minimum, of the points within the window, is used. Mathematically, the median filter is expressed as,

$$y[i] = \text{med}(x[i-n], x[i-n+1], \ldots, x[i+n-1], x[i+n]) \tag{3.40}$$

where the conventions are the same as for Eq. 3.1 in section 3.2.1 on minimum filters. If the window is an odd number of points long, $m = 2n + 1$, the median is simply the value which exceeds those for n points and is exceeded by those for the other n points. The median is readily defined for an odd number of points, but not for an even number. Therefore, we will use windows with an odd number of points exclusively.

Figure 3.8 demonstrates the median filter.

The median filter can be extended to two dimensions as well. In this case, the window must also be two dimensional. In mathematical terms, we have,

$$y[i,j] = \mathrm{med}(x[i+r, j+s]; (r,s) \in A) \tag{3.41}$$

where A is the set of acceptable values of r and s. The only constraint that we require on the set A is that it contain an odd number of points. Moreover, A can assume a variety of shapes, such as squares (3×3 for instance), rectangles, crosses (+ or X shaped), or others. The appropriate shape depends strongly on the specific application.

Theory

The median filter is the best known and the most widely used of the rank-order filters. Median filters were pioneered in the 1970's (Rabiner *et al.*, 1975; Jayant, 1976; Mosteller and Tukey, 1977; Tukey, 1977). Initially, they served in speech processing to smooth over bad data points. During the 1980's, they were used in image processing (Heygster, 1982; Reeves, 1982; Kim and Yaroslavskii, 1986). It was also during this period that the theory and some statistical properties of the median filter were investigated (Kuhlmann and Wise, 1981; Ataman *et al.*, 1981; Gallagher and Wise, 1981; Nodes and Gallagher, 1982; Nodes and Gallagher, 1984; Arce *et al.*, 1986). Median filters are a special case of filters based on order statistics, such as ranked-order or trimmed mean filters. These, as well as other types of filters are described by Pitas and Venetsanopoulos (1990), and by Astola and Kuosmanen (1997).

The theory presented here on median filters will deal only with one-dimensional time series, but an extension to two dimensions is straightforward. We start by constructing a simple model for the input, just as we did for the minimum filter. Because we are considering smoothly varying signals, we assume that the signal in the absence

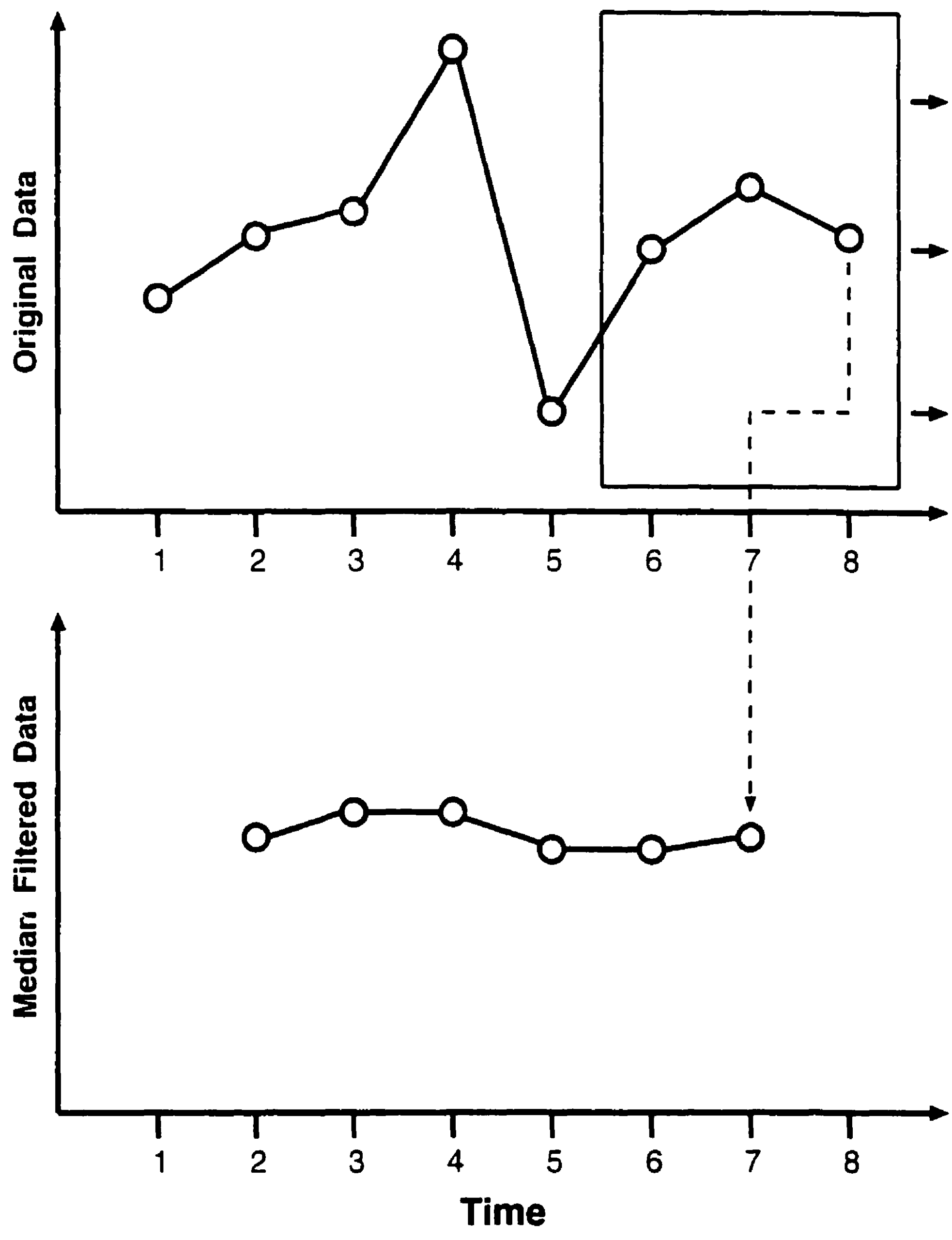

Figure 3.8: Schematic demonstration of the median filter. The upper plot shows the original data, with the three-point wide window (box) going from left to right. At each window position, the median value of the points inside the window is found and given to the corresponding point in the lower plot.

of intermittent clutter is perfectly correlated with itself over the length of the window. In other words, if $z[i]$ is the signal time series and m is the window length, we assume that $z[i] = z[i+1] = ... = z[i+m-1]$ with probability 1. The signal value z, constant within the window, is a random variable with a probability density function $f(z)$. However, each point of the input time series, $x[i]$, has a probability p of being intermittent clutter ζ, which is itself a random variable with a probability density function $g(\zeta)$. The intermittent clutter here is an impulsive noise much like the kind considered for the minimum filter, except that ζ may be negative and, more importantly, the value of ζ is not added to the signal but rather replaces it altogether. The impulsive noise here is not additive but rather substitutive.

To justify these assumptions, we recall Eq. 3.25 but we assume that the noise and ground clutter spectra have been completely eliminated:

$$S[k] = A[k] + I[k] \tag{3.42}$$

where $A[k]$ is the atmospheric signal spectrum, and $I[k]$ is the intermittent clutter spectrum that got through the minimum filter. Note that we omit the i and j indices for now. The mean Doppler velocity of $S[k]$ is

$$v_S = \Delta v \frac{\sum S[k]k}{\sum S[k]} \tag{3.43}$$

where Δv is the Doppler velocity increment. It is easy to see that

$$v_S = P_A v_A + P_I v_I \tag{3.44}$$

where $v_A = \Delta v(\sum A[k]k)/(\sum A[k])$ is the atmospheric signal Doppler velocity (vertical air velocity), $v_I = \Delta v(\sum I[k]k)/(\sum I[k])$ is the intermittent clutter Doppler velocity, $P_A = (\sum A[k])/(\sum\{A[k] + I[k]\})$ is the ratio of the atmospheric signal power to the total power, and similarly $P_I = (\sum I[k])/(\sum\{A[k] + I[k]\})$. It is obvious that $P_A + P_I = 1$, and that v_S may be identified as the input time series x, v_A as the signal time series z and v_I as the intermittent clutter ξ. Clearly then, v_I may be positive or negative. When intermittent clutter is not present, then $P_I = 0$, but when it is present, it is usually much more powerful than the atmospheric signal, so that $P_I \gg P_A$. It is not clear, though, if this is still the case after the spectra have been treated with the threshold minimum filter. However, as we have seen in subsection 3.2.5, the mean Doppler velocity algorithm we use starts by identifying the peak of the spectrum, then attempts to identify the spectrum associated with it. Therefore, if the spectra of the atmospheric signal and intermittent clutter are sufficiently far apart, there will be little or no overlap between them and the algorithm will choose one or the other.

The assumption of perfect correlation is used mainly to simplify the following development. If that assumption is relaxed, then the theoretical results are valid in the limit $\overline{(\zeta - z_m)^2} \gg \overline{(z[i] - z_m)^2}$, where $z_m = m^{-1} \sum_{l=0}^{m-1} z[l]$ is the average of the signal points within the window. In other words, if the deviation of the clutter from the window averaged signal value is much greater than the variation of the signal within the window, then the perfect correlation assumption is valid. Note that the perfect correlation assumption implies $\overline{(z[i] - z_m)^2} = 0$.

The probability density function for the input is

$$\rho_i(x) = (1-p)f(x) + pg(x). \tag{3.45}$$

As before, the probability of having n intermittent clutter points within an m-point window follows a binomial distribution (see Eq. 3.6). Note that from here on, we will consider only the case where $m = 5$. Next, we evaluate the conditional probability density function of the median for a given n, $\rho_{med}(y|n)$. As Fig. 3.9 shows, when $n = 0, 1, 2$ the median must be a signal point due to its perfect correlation within the window. Therefore, we have

$$\rho_{med}(y|n) = f(y) \qquad \text{for} \qquad n = 0, 1, 2. \tag{3.46}$$

For the case $n = 3$,

$$\begin{aligned}\rho_{med}(y|3) = &\frac{3!}{1!2!}\Big[G^2(y)(1-G(y)) + G(y)(1-G(y))^2\Big]f(y)\\ &+\frac{3!}{1!2!}\Big[F(y)(1-G(y))^2 + (1-F(y))G^2(y)\Big]g(y)\end{aligned} \tag{3.47}$$

where $F(y) = \int_y^\infty f(z)\mathrm{d}z$ and $G(y) = \int_y^\infty g(\zeta)\mathrm{d}\zeta$. The factorial coefficients take into account all possible permutations of the clutter and signal points. For the case $n = 4$,

$$\begin{aligned}\rho_{med}(y|4) = &\frac{4!}{2!2!}(1-G(y))^2G^2(y)f(y)\\ &+\frac{4!}{1!1!2!}\Big[G(y)(1-G(y))^2F(y) + G^2(y)(1-G(y))(1-F(y))\Big]g(y).\end{aligned} \tag{3.48}$$

And finally, for $n = 5$,

$$\rho_{med}(y|5) = \frac{5!}{1!2!2!}(1-G(y))^2G^2(y)g(y). \tag{3.49}$$

The overall output probability density function, $\rho_o(y)$, is completely analogous to the minimum filter case, Eq. 3.8,

$$\rho_o(y) = \sum_{n=0}^{5} P_{m,p}[n]\rho_{med}(y|n). \tag{3.50}$$

As before, we partition $\rho_o(y)$ into correct reconstruction, $f_{med}(y)$, and incorrect reconstruction, $g_{med}(y)$, segments,

$$\rho_o(y) = f_{med}(y) + g_{med}(y), \tag{3.51}$$

where

$$\begin{aligned}f_{med}(y) = &\left[\sum_{n=0}^{2}\frac{5!}{n!(5-n)!}(1-p)^{5-n}p^n\right]f(y)\\ &+\frac{5!}{1!2!2!}(1-p)^2p^3\Big[(1-G(y))G^2(y) + (1-G(y))^2G(y)\Big]f(y)\\ &+\frac{5!}{1!2!2!}(1-p)p^4(1-G(y))^2G^2(y)f(y),\end{aligned} \tag{3.52}$$

and

$$g_{med}(y) = \frac{5!}{1!2!2!}(1-p)^2p^3\Big[F(y)(1-G(y))^2 + (1-F(y))G^2(y)\Big]g(y)$$
$$+ \frac{5!}{1!1!1!2!}(1-p)p^4\Big[G(y)(1-G(y))^2F(y) + G^2(y)(1-G(y))(1-F(y))\Big]g(y)$$
$$+ \frac{5!}{1!2!2!}p^5(1-G(y))^2G^2(y)g(y). \quad (3.53)$$

Of course, the total probability of a correct reconstruction is

$$P_z = \int_{-\infty}^{\infty} f_{med}(y)\mathrm{d}y \quad (3.54)$$

and for an incorrect reconstruction

$$P_\zeta = \int_{-\infty}^{\infty} g_{med}(y)\mathrm{d}y. \quad (3.55)$$

We must now specify reasonable shapes for the probability density functions. Figure 3.10 shows the forms assumed for the intermittent clutter (ζ) density function (a fourth order polynomial) and the signal (z) density function (a Gaussian with tapered tails). Since we wish to model the profiler vertical air velocity measurements, we choose random variables with a finite domain (from -10 to 10) and with zero means, $\bar{z} = \bar{\zeta} = 0$. Figure 3.11 shows the input probability density functions, $\rho_i(x)$, described by Eq. 3.45 and where $p = 0.1$ (solid line) and $p = 0.4$ (dashed line). The obvious effect of the intermittent clutter contamination is to broaden the tails and flatten the peak of the density function. The output of the 5-point median filter is shown in Fig. 3.12, where we see that the output density function (solid line), $\rho_o(y)$, looks much like the signal density function in Fig. 3.10. However, the tails, while much reduced with respect to the input density function, are still slightly broader than those of the signal density function. This is due to incorrect reconstructions in those windows where $n \geq 3$. The total probability of a correct reconstruction, P_z, is plotted as a function of the input signal probability $q = 1 - p$ in Fig. 3.13. The upward deviation from the diagonal of this plot indicates that the median filter

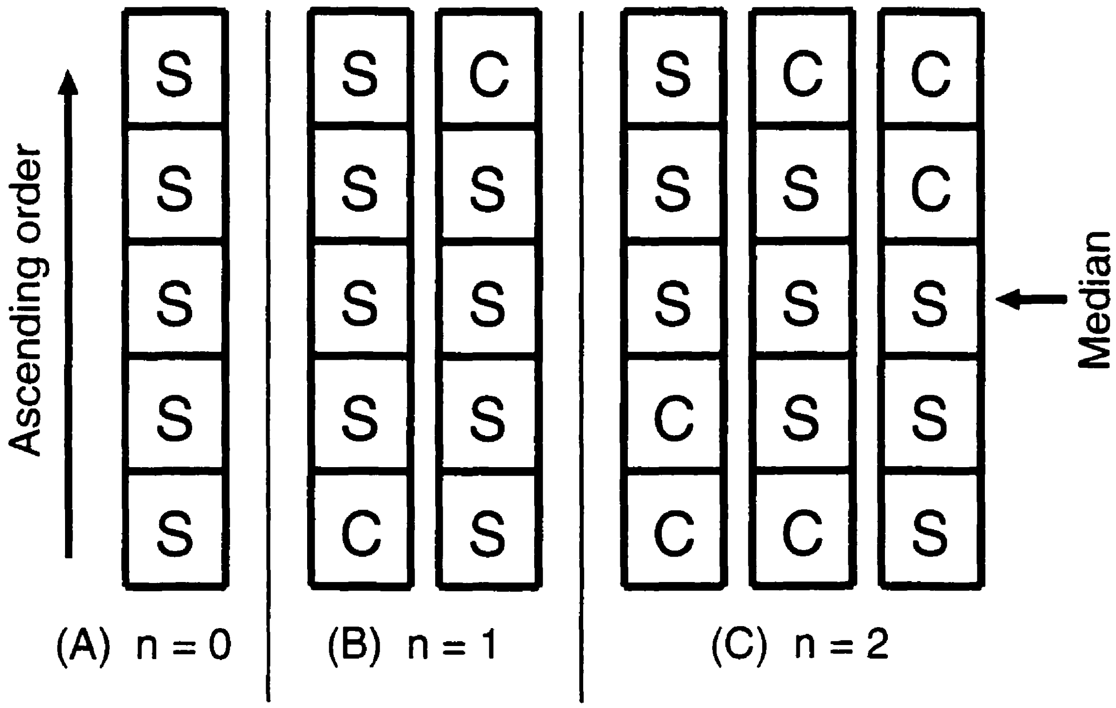

Figure 3.9: The possible configurations when the points within the window are sorted in ascending order. 'S' signifies a signal point and 'C' a clutter point. The signal points, being perfectly correlated, are always grouped together. The clutter points have values that are greater or less than the signal points. We neglect the case where the value of a clutter point is exactly equal to the signal value. (A) shows the case when there are no clutter points, (B) when there is one clutter point, and (C) when there are two clutter points. In all cases, the signal is the median.

MED5 has a better chance of selecting signal points for the output than if we simply passed the input through unaltered (diagonal), and this is true for all values of q. The median filter therefore has a propensity for selecting the signal points in this case.

Application

Our application of the median filter on real time-height vertical air velocity data uses a two-dimensional X-shaped window shown in Fig. 3.14. Given the shape of the window and the number of input points within it, we call this application an XMED5 filter. Mathematically, this filter is expressed as:

$$v_o[j,i] = \mathrm{med}(v[j+1,i-1], v[j-1,i-1], v[j,i], v[j+1,i+1], v[j-1,i+1]) \tag{3.56}$$

where $v[j,i]$ is the input time-height vertical air velocity data, $v_o[j,i]$ is the output, j is the height index and i is the time index. The reasons for this window configuration are closely linked to the characteristics of the profiler/RASS system described in section 2.3, and the desired properties of the output. We do not want to induce artificially strong correlation between points adjacent in time, which is why the input points $v[j,i-1]$ and $v[j,i+1]$ were excluded from the window. The reasons for this are the same stated for the threshold minimum filter, that is we must be able to eliminate the random error variance from the vertical air velocity variance estimate. Also, since the pulse length of the profiler is 105 m, and the sampling resolution is 60 m in RASS mode (see Tables 2.1 and 2.2), there is considerable overlap of the resolution volumes for measurements adjacent in height. The overlap increases the correlations between time series adjacent in height. Therefore, we assume that points adjacent in height are well correlated, and that the data directly above and below a given point should resemble its data value. Although these may be used in a median filter, a bad value at a given point will also be present at the points directly above and below, and so we must exclude the points $v[j+1,i]$ and $v[j-1,i]$ from the window, thereby resulting in its X-shape.

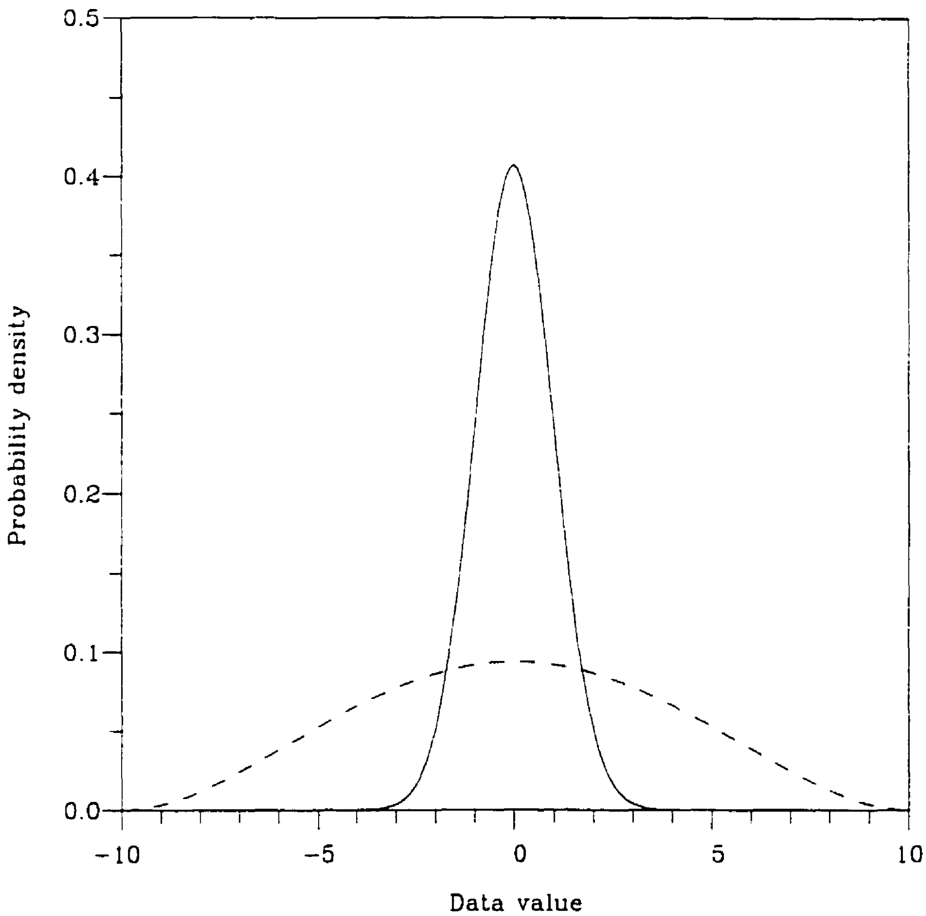

Figure 3.10: The solid line is the hypothetical signal probability density function. The dashed line is the hypothetical probability density function for intermittent clutter.

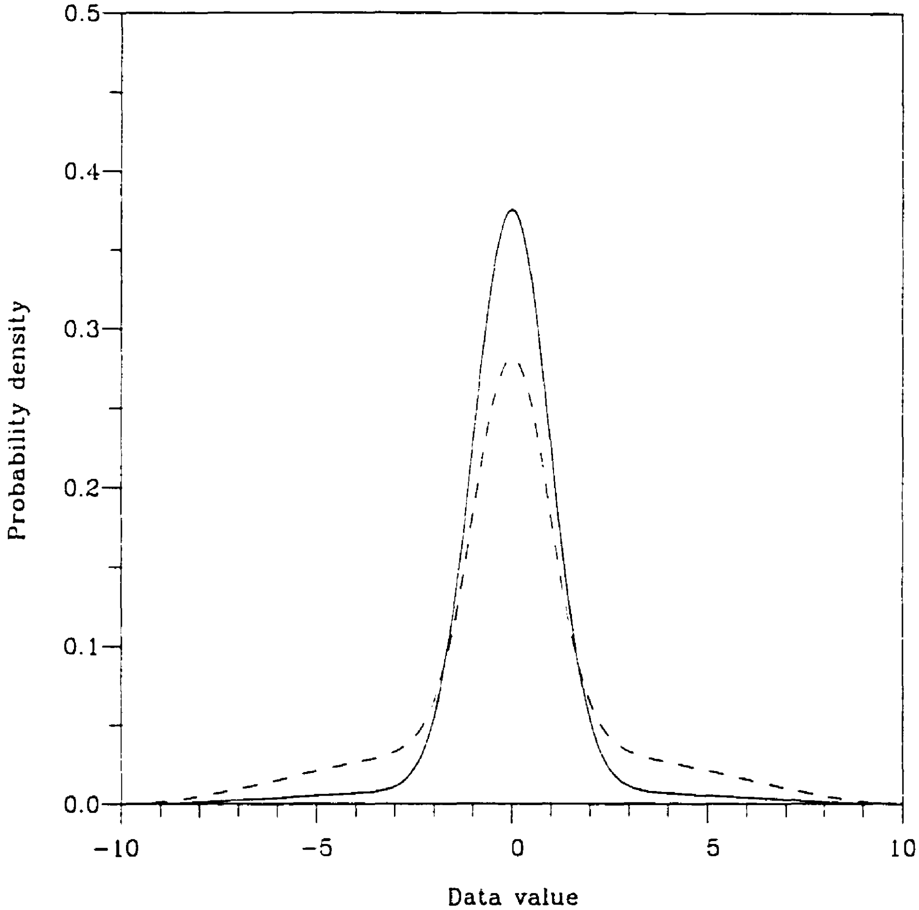

Figure 3.11: The solid line is the input probability density function for $p = 0.1$. The dashed line is the input probability density function for $p = 0.4$.

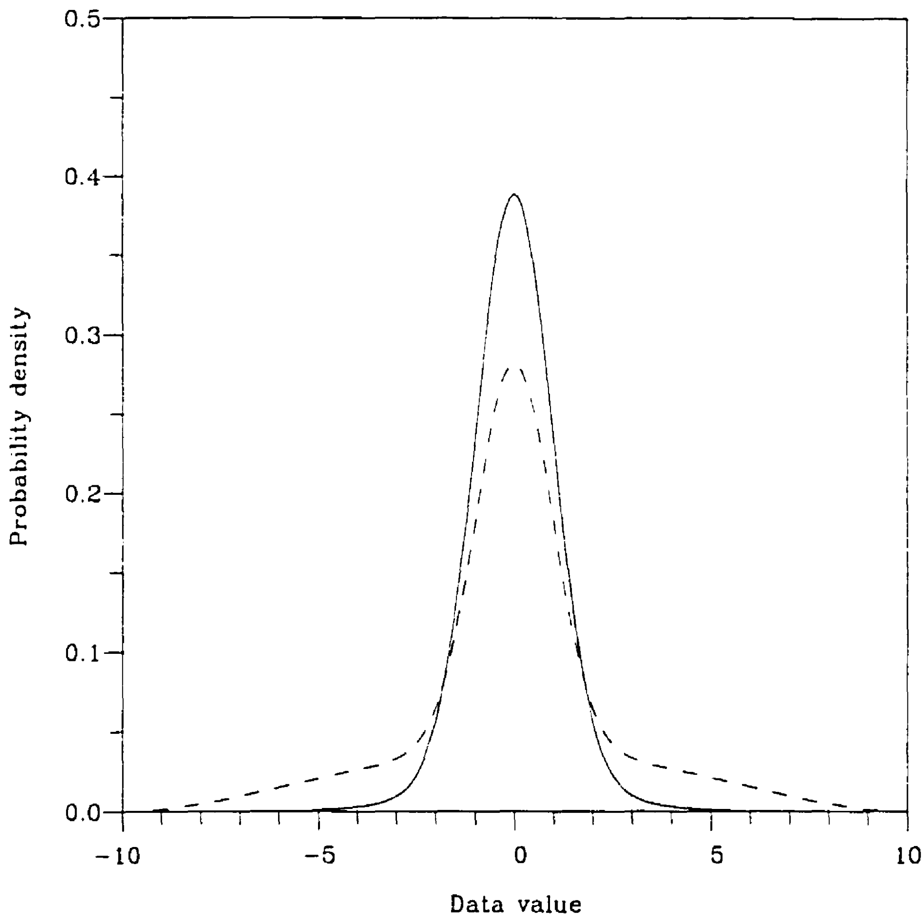

Figure 3.12: The dashed line represents the input density function with $p = 0.4$. The solid line is the output of a 5-point median filter (MED5).

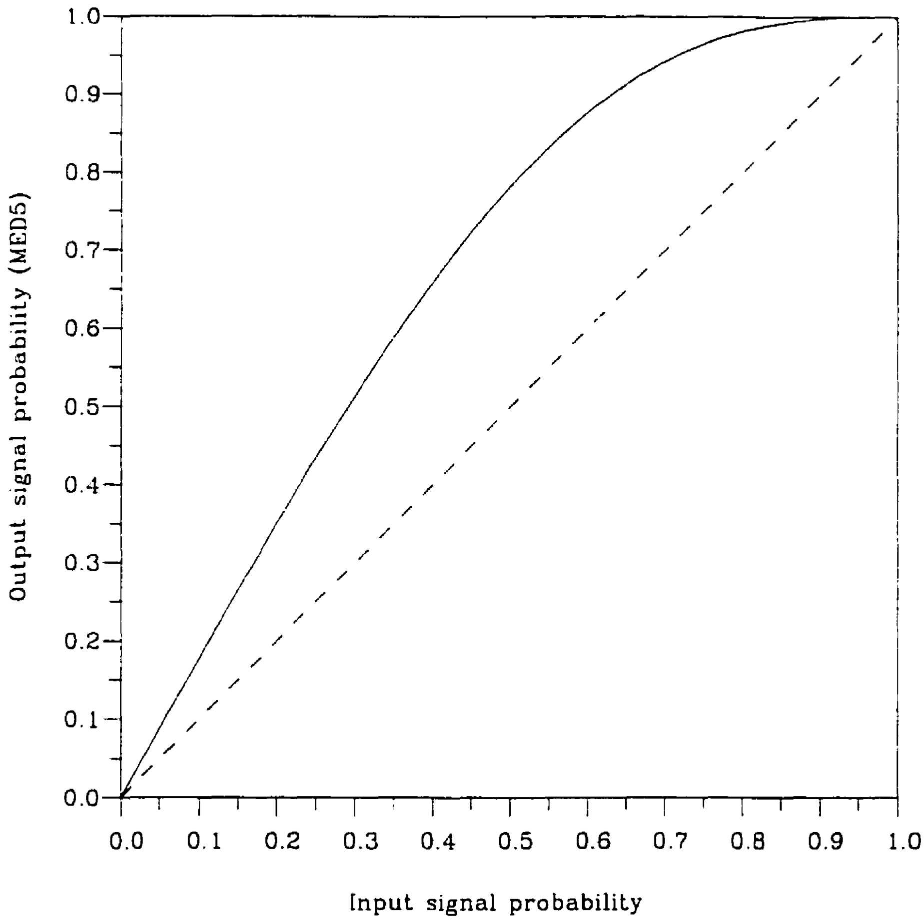

Figure 3.13: The solid line is the total probability of a correct reconstruction of the 5-point median filter (MED5), as a function of the input signal probability $(1-p)$. The dashed line is the diagonal plotted for comparison. It represents a null result.

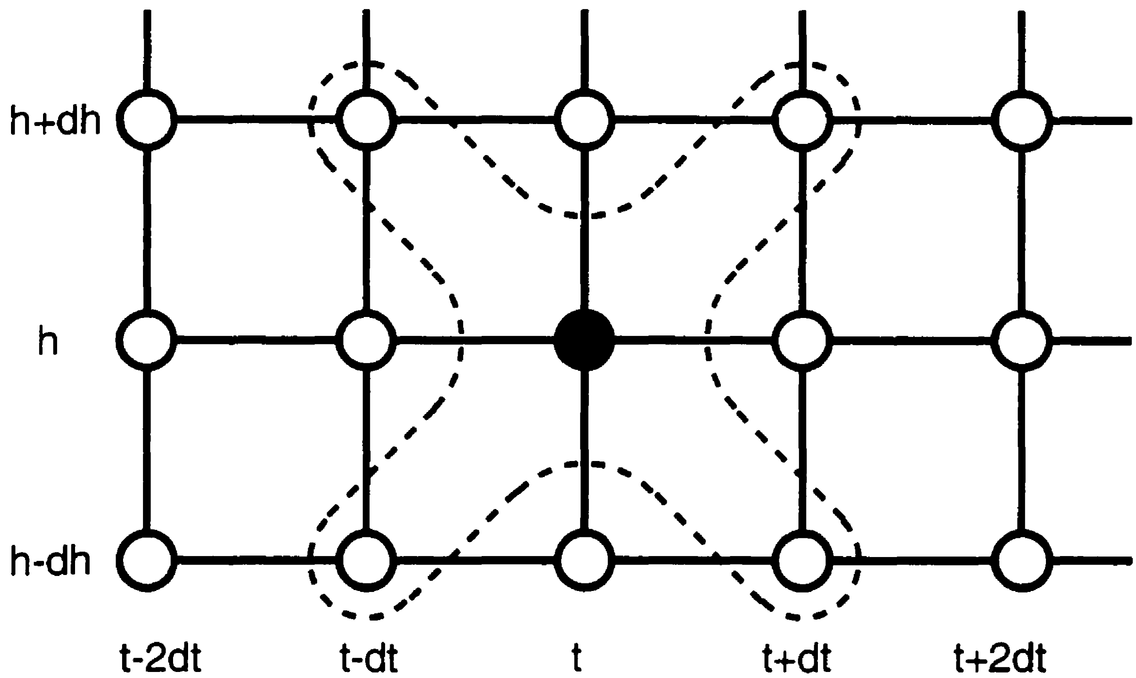

Figure 3.14: The dashed contour indicates the window in height and time for a XMED5 filter. The input points within the window are used to evaluate the median value, which is then placed at the center of the window (black circle) for the output time-height data.

Figure 3.15 offers an overview of the main points of ROSPA. The untreated vertical air velocity in Fig. 3.15(a) is heavily contaminated with intermittent clutter. The vertical air velocity is then treated with a 7.5 dB TMIN7 filter, followed by spectral noise suppression, ground clutter removal and peak identification. The resulting time series, in Fig. 3.15(b), shows significant improvement with only a few remaining bad points, which are subsequently eliminated by the XMED5 filter (Fig. 3.15c). Though not present in Fig. 3.15(c), there might still be a few outliers remaining at this stage. A method for detecting outliers is therefore needed.

3.2.7 Outlier Detection

The central problem of outlier detection is how we justify our expectations of what good data should look like (Barnett and Lewis, 1978). In other words, if we have a set of data where most of the members cluster around a central value with a given variance, and a few members deviate from the central value by an amount far in excess of the variance, then the clustered data conditions our expectations of what good data should look like, and the few extreme members produce a sense of 'surprise' with respect to these expectations. The extreme members are assumed to be the result of a disruption or malfunction of the measurement process and consequently obey a probability distribution different from that of the clustered data. However, unless the disruption or malfunction can be confirmed independently, we can never be sure if the clustered and extreme points are produced by different processes. They may come from the same measurement process and therefore be equally good, while conforming to a very wide probability distribution. Furthermore, without independent confirmation, there is no way of being sure if some of the clustered members are not the result of a faulty measurement process that happens to agree with the good points by accident.

Nevertheless, we will identify outliers using a hypothesis test similar to that used in subsection 3.2.2 on the threshold minimum, in a process we will call a threshold

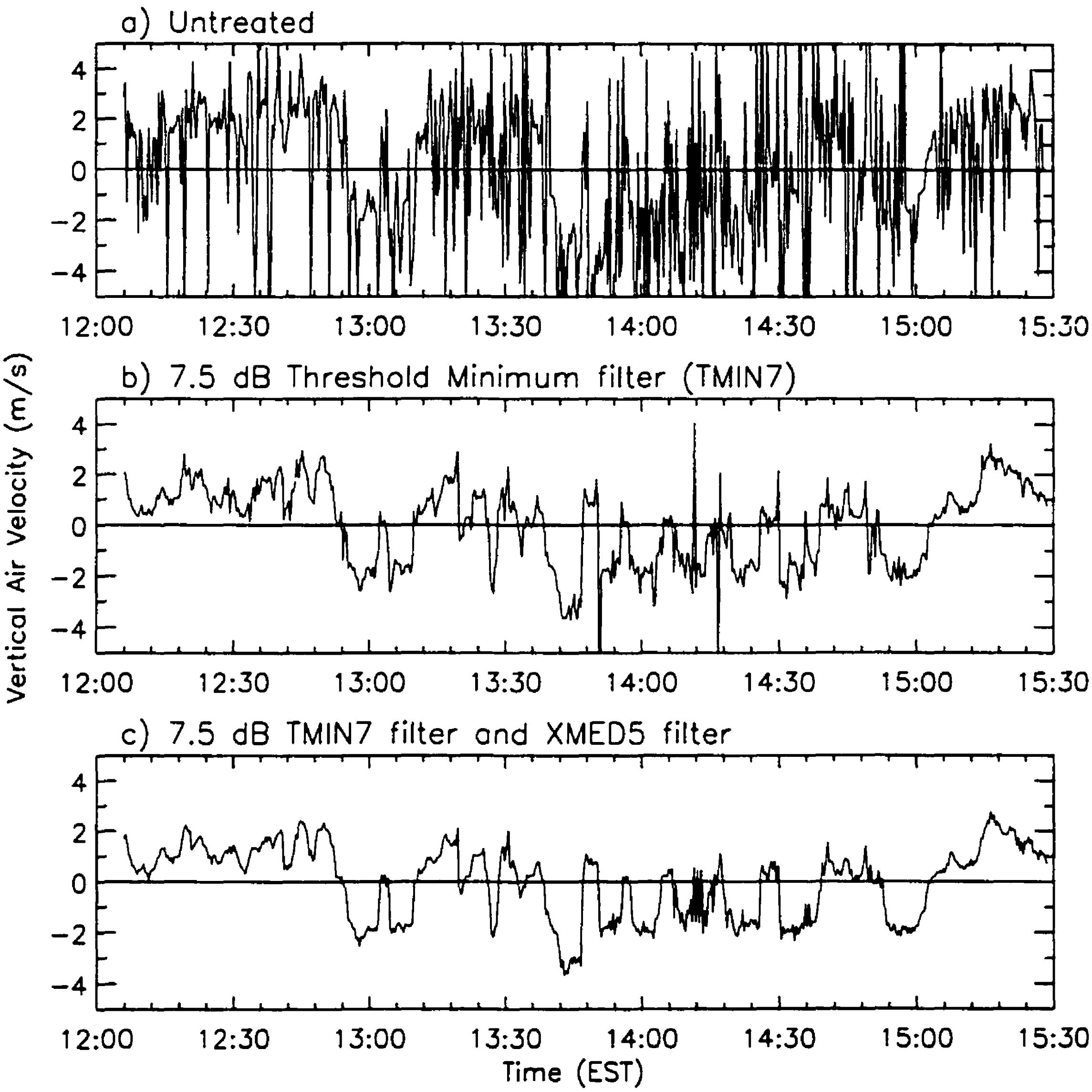

Figure 3.15: The main stages of ROSPA. The top curve (a) is the untreated vertical air velocity at 405 m over McGill, on June 28, 1996. The middle curve (b) is the vertical air velocity treated with a 7.5 dB TMIN7 filter, followed by spectral noise suppression, ground clutter removal and peak identification. The bottom curve (c) is the output of curve (b) treated with a XMED5 filter.

median (TMED), and which is very similar to a method used by Peters and Kirtzel (1994) for treating RASS data. Note that, contrary to the threshold minimum, only one test will be performed and those points that fail will simply be excluded from the dataset from which we compile statistics. The idea is that by this stage, the time series of vertical air velocity will contain relatively few outliers. TMED is therefore seen as a means of 'cleaning up' the data just prior to compiling statistics, rather than as a signal processing procedure in its own right. Just as for the threshold minimum, we must construct a statistically robust baseline from which we will identify the outliers. Rather than using the output of a median filter, which may have sharp edges which may cause the magnitude of the residual between it and the good input points to be slightly too high, we will constuct a smoother baseline with the use of a *template*.

Creating a Template

The template is a device for identifying the 'good' points of a discrete time series. It takes the form of a vector of logical variables as long as the time series it represents, $L[i]$. The first step consists of initializing all points of the template to 'false'. Then, a running window is passed over the time series. At each window position, the median point of the set of points inside the window is found. This point is tagged as 'good' by setting the corresponding position (of the point, not the window) on the template to 'true'.

Note that the window is an odd number of points long, $m = 2n + 1$, and the window length must be short enough so that the signal points are well correlated with one another, but long enough so that the clutter points are likely to cancel each other when estimating the median. Three is too short because a clutter point is too likely to be the median. Five gives acceptable results, and since seven yields essentially the same results, the window length will be set to five. The template is then a series

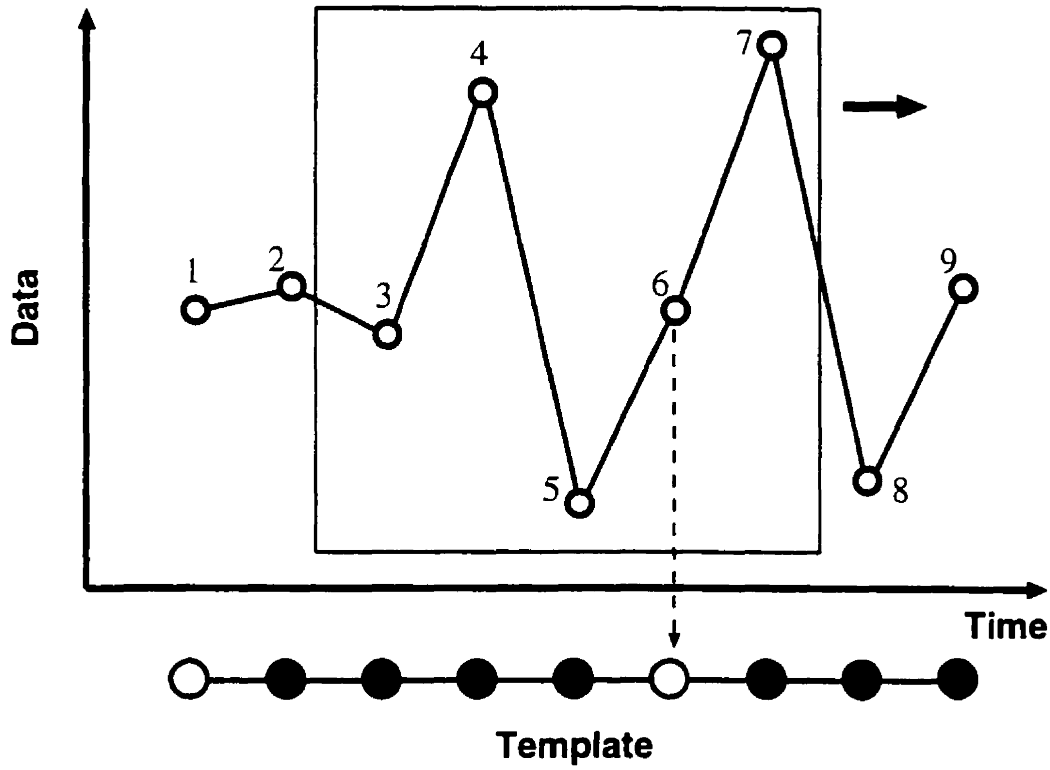

Figure 3.16: A demonstration of the template forming algorithm. The box represents the window going from left to right over the time series. The template is shown as the series of circles under the graph. A white circle indicates a 'true' point, black a 'false' point. Here, data point 6 is the median of the set of points inside the window. The corresponding position on the template is set to 'true'.

of logical variables identifying as 'true' every point in the time series that was the median of at least one window (out of 5 windows) which included it.

Figure 3.16 demonstrates the aforementioned procedure. In it, we see that the algorithm accepts points 1 and 6, which we expect are valid, and rejects points 4, 5 and 7, which we suspect are clutter. However, points 2 and 3 were also rejected, which appear to be valid. The baseline $\Gamma[i]$ takes on the value of the input time series, $x[i]$, if the corresponding point on the template, $L[i]$, is true. If $L[i]$ is false, then the baseline is the linear interpolation of the two nearest 'good' points: $\Gamma[i] = x[j] + (i-j)\cdot(x[k]-x[j])/(k-j)$, where $j < i < k$ and $L[j] = L[k] = \text{true}$.

Definition

Given the baseline $\Gamma[i]$, and a normalized threshold $\nu > 0$, we define the threshold median as the following test:

$$\begin{array}{lll} \text{if} & \Gamma[i] - \nu\sigma_b \le x[i] \le \Gamma[i] + \nu\sigma_b, & \text{then accept} \\ & \text{otherwise,} & \text{reject} \end{array} \tag{3.57}$$

where σ_b is the standard deviation of the baseline. We used the standard deviation of the baseline time series rather than of the input time series because we want to avoid outliers producing a standard deviation that is too large. Note that since $\Gamma[i] = x[i]$ where $L[i] = \text{true}$, there is a subset of the input points that will pass the test for any value of the normalized threshold. If the baseline was produced using a 5-point median filter, this subset is typically 50 - 70 % of the input time series.

We will omit describing in detail the theory of the threshold median, except to say that it is very similar to that of the threshold minimum. As for the threshold minimum, the optimal choice of ν is a balance between accepting as many good points as possible while rejecting as many bad points as possible. In addition, we can also assume that the best value of the normalized threshold is a function of the ratio of the window period and the timescale of the uncontaminated time series, $\gamma = m\Delta/T$ (the symbols are the same as in subsection 3.2.2 on the threshold minimum). That is, when γ is small, the normalized variation of the good points within the window is accordingly small, and so ν can also be small. However, by this stage, whatever outliers remain tend to be a few isolated spikes, which means that the good and bad points are reasonably well separated and that the choice of ν is not critical. We need only insure that the value of ν accepts all good points.

Application

The application of the threshold median is done by creating an input time series for each height, $x_\beta[i] = v[j = \beta, i]$, where $v[j, i]$ is the input time-height vertical air velocity data, j is the height index and i is the time index. Then, for every height, we create a baseline $\Gamma_\beta[i]$ from $x_\beta[i]$. Using ν and $\Gamma_\beta[i]$, we perform the test described in Eq. 3.57 on the corresponding input time series $x_\beta[i]$, which we repeat for every value of β. For every point in $x_\beta[i]$ which is rejected, we also reject the corresponding point in the time-height vertical air velocity data, $v[j = \beta, i] = x_\beta[i]$. The rejected points in $v[j, i]$ are then omitted from statistical estimates.

It is worth noting that the threshold median is the only procedure used on the RASS acoustic velocity data. The acoustic velocity data are not subject to ground or intermittent clutter, and RFI usually does not occur. That means that the fall of returned power below its noise level at distant range, i.e. the sudden loss of returned power from the acoustic wave, are mainly responsible for outliers in RASS acoustic velocity data, and usually near the highest measurable RASS altitude. If the outliers are sufficiently rare at a given height, such that the threshold median eliminates only 10% or less of the time series, then that height is used in statistical estimates. If, on the other hand, the threshold median rejects more than 10% of the points at a given height, then it is considered too contaminated and the RASS data at that height and higher are not used in statistical estimates. Obviously, if the lack of returned power is the cause of outliers, then minimum filters, threshold or not, are useless since they can only reduce the spectral power in the Doppler velocity bins. The XMED5 filter is not used on RASS data because we wish to limit the amount of signal processing done to the acoustic velocity data. We will limit ourselves to either eliminating bad points at a given height, or not using that height at all if too contaminated.

In this chapter, we have seen the various signal processing steps that make up ROSPA. We have tried to devise a signal processing algorithm especially suited for profiler/RASS clear-air measurements strongly contaminated with various types of clutter. ROSPA is intended to be robust and based on relatively simple principles. Both the threshold minimum and median filters are based on creating a robust baseline using order statistics, and accepting or modifying data points according to some threshold based on the baseline, and the XMED5 filter is simply a two-dimensional median filter. Other signal processing methods based on these principles are possible, of course, which may be more efficient than ROSPA. Nevertheless, we will settle on this particular combination of steps as we estimate it to be both reasonably effective and simple.

Next, we will examine the environment under study itself, namely the urban boundary layer, and how it differs from the rural boundary layer. This will give us some idea of the kind of results to expect over a city centre, and, consequently, some way of estimating the credibility of the profiler/RASS measurements using ROSPA.

Chapter 4

The Urban Boundary Layer

This thesis, because of its emphasis on the RASS, which is limited to approximately the lowest kilometer of the atmosphere, will focus mainly on the mixed layer portion of the urban boundary layer. Nevertheless, to provide a background for interpreting the observations, the horizontal and vertical structure of the urban boundary layer will be described, from the ground to the entrainment layer.

4.1 The Urban Heat Island

Most cities are sources of heat and pollution. Indeed, the production, dispersion, and radiative properties of aerosols are major problems in urban meteorology (Summers, 1964; Yap, 1969; Bergstrom and Viskanta, 1973a; Bergstrom and Viskanta, 1973b; Rouse *et al.*, 1973; Takeda and Iwasaka, 1982). Also, the downtown cores of cities are predominantly covered by asphalt and concrete. These materials are dry, water-proof, and possess albedoes and heat capacities that convert and store incoming radiation into sensible heat better than the surrounding countryside. As a consequence, the surface air temperatures in the city cores are usually warmer than the temperatures in the surrounding rural areas. Figure 4.1 illustrates the effect. The warmer isotherms tend to form closed loops around the city core. The pattern thus formed resembles the topographic contours of an island, hence the use of the term *urban heat island*

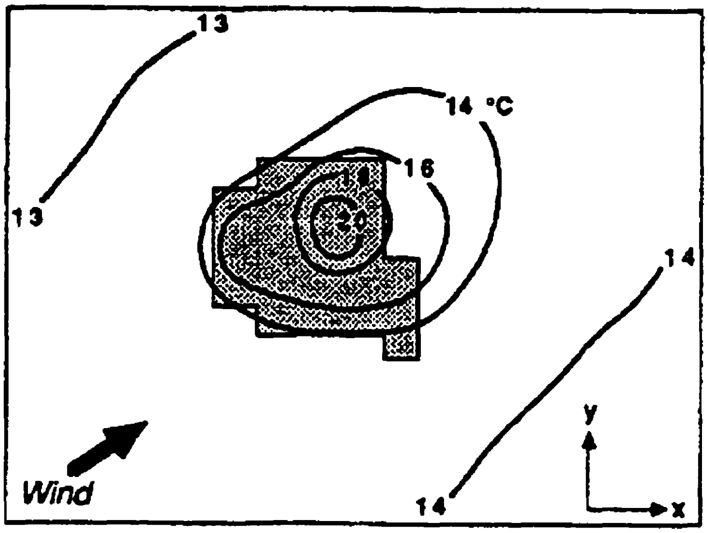

Figure 4.1: Idealized isotherm heat island pattern over an urban area (shaded) (from Stull (1988)).

to describe it. Howard (1833) was the first to find evidence of the heat island effect. Since then this effect has been very well studied, though mainly in midlatitude cities (for instance, Renou (1862), or Hammon and Duenchel (1902)). For reviews regarding the urban heat island effect, and urban climatology in general, one may consult Oke (1982; 1988), Lee (1984) or Stull (1988). A good bibliography of material regarding urban meteorology can be found in Oke (1990).

Furthermore, rural areas tend to cool more at night than do urban areas (see Fig. 4.2). The urban heat island effect is therefore strongest at this time. This is because during the day, the urban area was able to store more sensible heat than the surrounding rural areas, thus requiring more time to release it into the boundary layer and thereby causing a smaller cooling rate in the city at night (Oke and Maxwell, 1975). The difference in temperature between the urban and rural areas has a maximum in the order of 2 to 3°C for towns with a population of about 1000, while cities of a

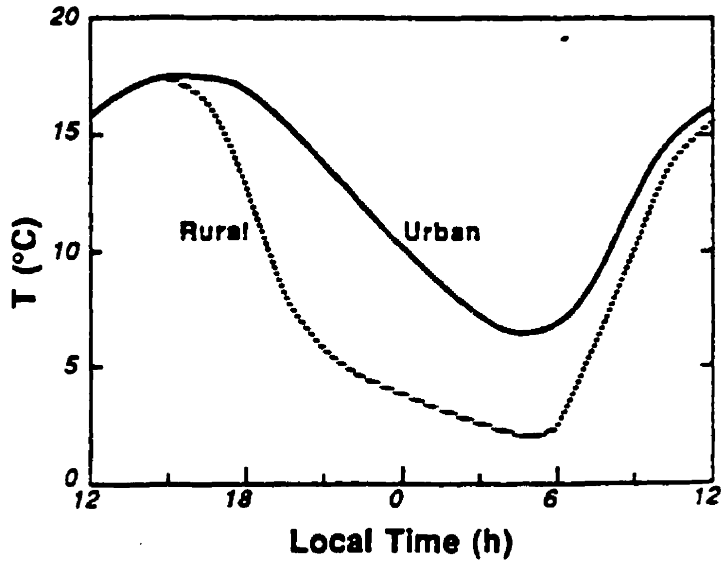

Figure 4.2: Idealized diurnal surface air temperature cycles for urban and rural areas (from Stull (1988)).

million or more can generate temperature excesses of 8 to 12°C (Oke. 1982). During the month of January, at night, the downtown core of Montreal can be as much as 5°C warmer than the surrounding rural areas (Environment Canada, 1987). At about midday, the urban heat island is almost undetectable at the surface. High winds, precipitation, and cloud cover are significant weather related factors that reduce the *heat island intensity*, defined as the difference in temperature (Oke and Maxwell, 1975) or potential temperature (Oke, 1982) between an urban and a rural area. In some cases, the rural temperature lapse rate close to the ground can be strongly correlated with the nighttime heat island intensity (Ludwig, 1970). Geographical factors include the proximity of water bodies, topographical features (Wanner and Filliger, 1989) and the nature of soils, vegetation and land use in the region (for example, see Katsoulis and Theoharatos (1985) for Athens; Oke and Hannell (1970) for Hamilton, Ontario; or Bornstein (1968) for New York City).

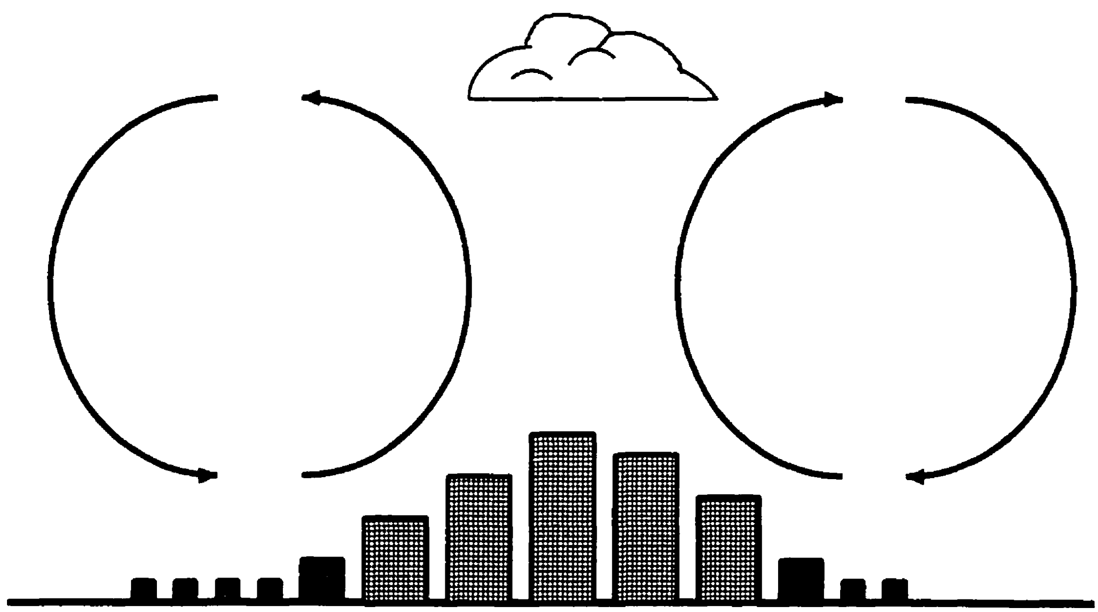

Figure 4.3: Local circulations induced by a warm city during calm ambient flow.

4.2 The Urban Plume

Now we look at the vertical structure of the urban boundary layer. If there is little or no wind, the thermal modification of the city extends upward as a self-contained urban heat 'dome', accompanied by a closed mesoscale circulation around the city. Figure 4.3 shows an idealized diagram of the mesoscale circulation. The heat island of the city produces warm rising air above it, which in turn causes horizontal convergence close to the surface layer along with a horizontal divergence near the top of the boundary layer, completed by descending air around the city (Stull, 1988). The rising air may cause condensation, producing clouds and a limited but real urban precipitation anomaly (Lee, 1984). This circulation pattern has also been observed in laboratory (Giovannoni, 1987) and numerical (Delage and Taylor, 1970) simulations.

However, it is more common that winds will carry away the warm, dry, and polluted city air (with significant concentrations of ozone and nitrogen oxides (Trainer *et al.*, 1995)), forming an *urban plume* (Oke, 1982). Figure 4.4 shows an example of an urban plume. During the day (Fig. 4.4(a)), the advection of the rural boundary layer over the city creates an *internal boundary layer*; that is, the roughness and warmer temperature (mainly in the morning and afternoon) of the city modifies the air that flows over it, thus creating a boundary layer extending from the city surface to the rural boundary layer air aloft (see Garratt (1990) for a review of internal boundary layers). The depth of the urban boundary layer increases as the day progresses, along with that of the rural boundary layer. However, a slight doming of the mixed layer over the city may be evident (by up to about 0.25 km (Spangler and Dirks, 1974), Fig. 4.4(a)), slightly downwind of the city core (Godowitch *et al.*, 1987). Similarly, another internal boundary layer forms as the air flows from the urban to the rural areas. The effect of the wind can also be seen in Fig. 4.1, where the isotherms are closer together along the upwind side than along the downwind side of the heat island.

The nighttime urban plume, Fig. 4.4(b-d), is noteworthy because of the surface mixed layer that is retained over the city. The rural areas have no mixed layers due to the surface-based radiative inversions. But as the stable rural air is advected over the city, the warmth and roughness of the city eliminates its stability up to 100-300 m (Fig. 4.4(c))(DeMarrais, 1961; Yap *et al.*, 1969), and an elevated warm plume appears on the lee side of the city (Oke and East, 1971). A plot of the heat island intensity with height for the city centre (Fig. 4.4(d)) shows the potential temperature excess declining rapidly with height until it becomes negative (rural warmer than urban) near the top of the urban boundary layer in the *cross-over effect* (Duckworth and Sandberg, 1954; Bornstein, 1968).

4.3 Convection and Fluxes

Before we can discuss the convection in an urban boundary layer, we must first describe the different sublayers within it. Figure 4.5 shows the divisions of the urban

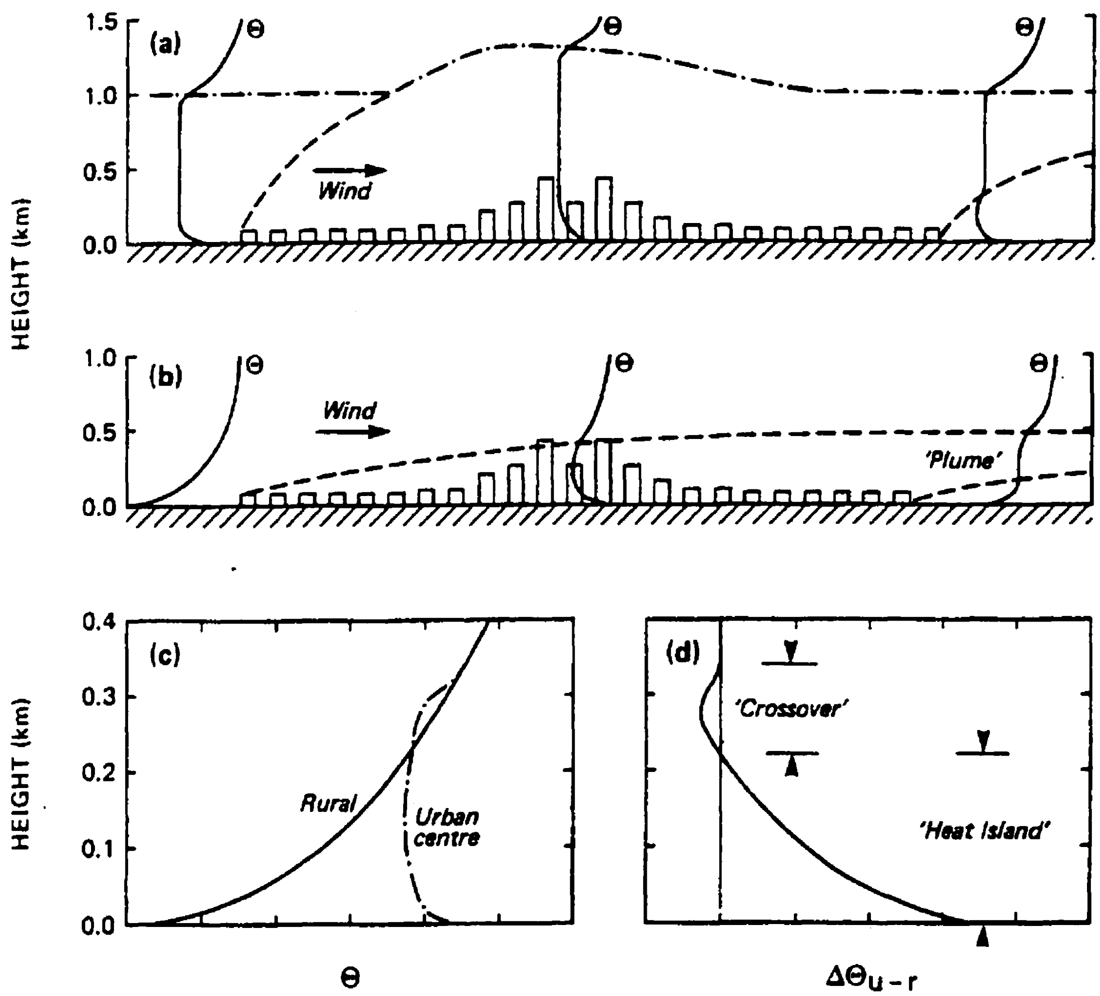

Figure 4.4: General form of the urban boundary layer in a large mid-latitude city during clear summer weather (a) by day, including profiles of potential temperature (θ) and the depths of the urban and rural internal boundary layers (dashed) and the daytime mixed layer (dot-dashed) and (b) at night. Comparison of (c) rural and urban potential temperature profiles and (d) the resulting profile of heat island intensity in the city centre at night (from Oke (1982)).

boundary layer according to Oke (1988) or Stull (1988). The *urban canopy layer* is defined as the layer that extends from the ground to about rooftop height (Oke, 1976; Oke, 1988; Lee, 1984; Stull, 1988). Analogous to a plant canopy layer (Garratt, 1992; Kaimal and Finnigan, 1994), the urban canopy layer is subject to microscale effects such as multiple reflections of radiation and ducting of airflow by buildings, affecting, among other things, the Reynolds stress profile within it (Rotach, 1993). It is in this layer that most traditional urban observations have been concentrated (i.e. surface stations, instrumented automobiles, etc). The urban canopy layer is most clearly defined in areas of high building density. It may be discontinuous or absent in less densely developed suburban areas. Above it is the *turbulent wake layer* (also known as the *roughness layer* (Oke, 1988)), where the wakes and the internal boundary layers from the individual buildings and surface patterns can still be felt. The depth of the turbulent wake layer (typically about 20-90 m in cities) is two to three times the average horizontal spacing of the dominant roughness elements (Oke, 1988). Higher still is the *surface layer*, where the individual wakes are not important, but where the momentum and heat budgets feel the average effect of the urban area.

Finally the *urban mixed layer* extends from the top of the surface layer to the top of the urban boundary layer. It is dominated by convective motions that penetrate through the entire layer, and has mostly uniform wind, humidity and potential temperature profiles. The convective motions have been observed by lidar (Kunkel *et al.*, 1977), tetroons (Angell *et al.*, 1973), echosounder (Melling and List, 1980), Doppler sodar (Casadio *et al.*, 1996), and instrumented aircraft (Hildebrand and Ackerman, 1984; Godowitch, 1986).

Figure 4.6 shows idealized profiles for a mixed layer over flat terrain. The controlling parameters in the mixed layer are the surface potential temperature flux, $Q_0 = \overline{w'\theta'}|_s$, and the convective boundary layer (CBL) height, z_i (McBean, 1976;

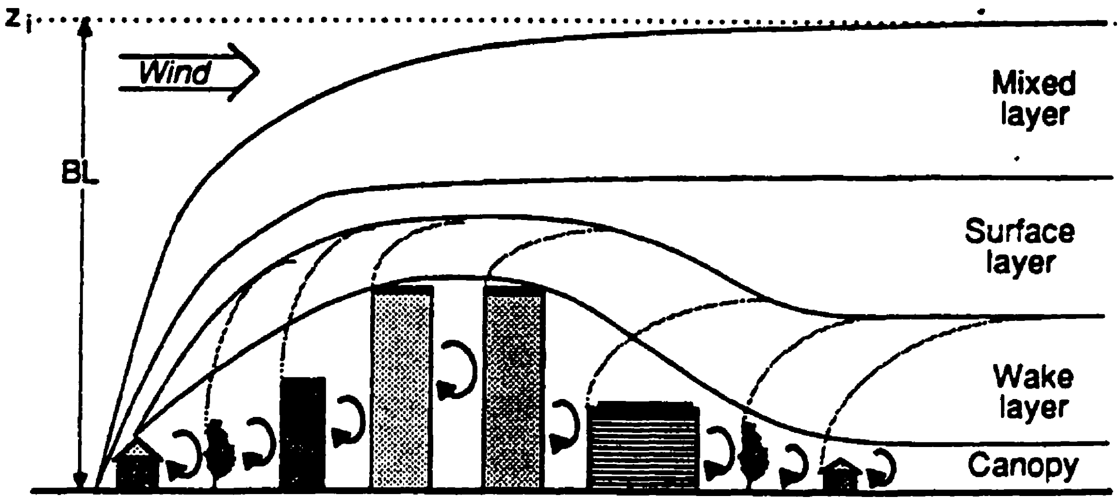

Figure 4.5: The different layers within the urban boundary layer (from Stull (1988)).

Garratt, 1992; Wyngaard, 1992; Kaimal and Finnigan, 1994). From these parameters, a scaling velocity is defined by

$$w_* = \left[\frac{gQ_0 z_i}{\overline{\theta}}\right]^{1/3} \tag{4.1}$$

where g is gravity, $\overline{\theta}$ is the average potential temperature through the mixed layer, and θ_* is a scaling temperature defined by

$$\theta_* = Q_0/w_*. \tag{4.2}$$

Note that the profiles in Fig. 4.6 are normalized with respect to these scales. Occasionally, variants of Eq. 4.1 are used to define the scaling velocity (Kaimal *et al.*, 1976; Lenschow and Stankov, 1986), but the values of w_* and θ_* turn out to be almost the same.

By and large, the normalized profiles for flat terrain are still valid in the urban boundary layer. In particular, the normalized potential temperature flux profile is valid in the urban boundary layer; only the parameters z_i and Q_0 are greater (Q_0 is 2-4 times greater) (Hildebrand and Ackerman, 1984). We must bear in mind, however,

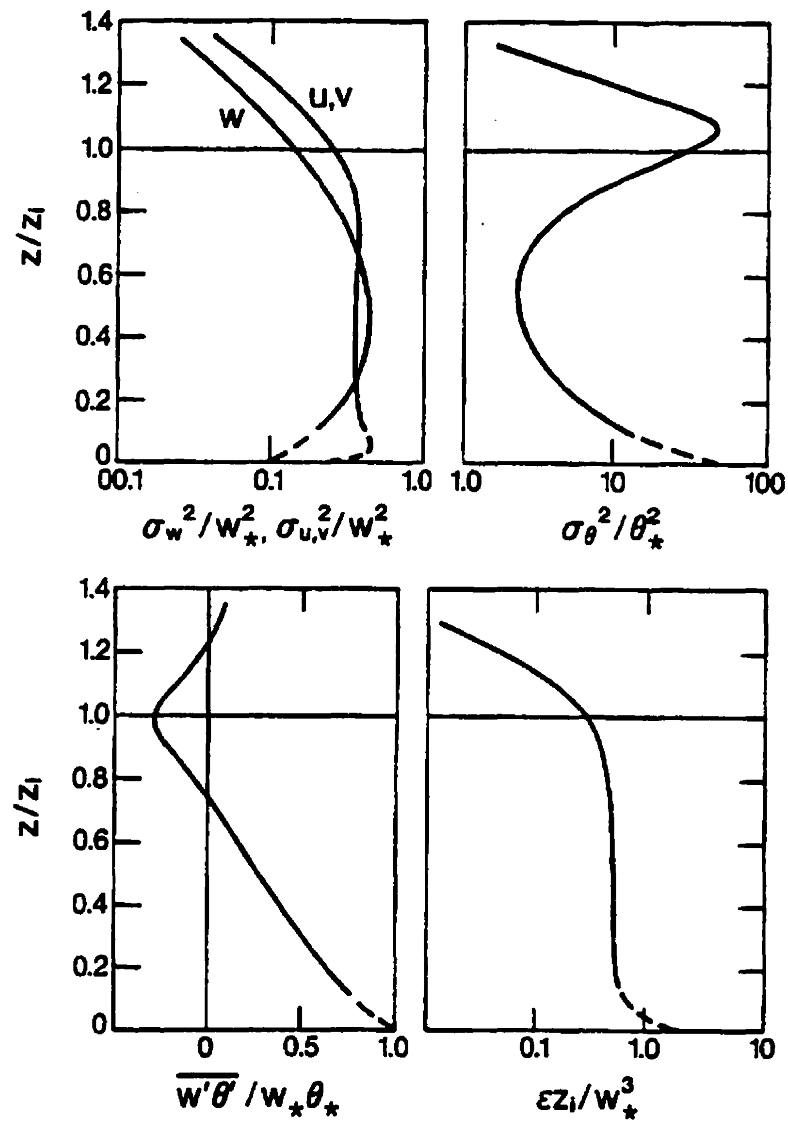

Figure 4.6: Idealized boundary layer profiles of (clockwise, from top left plot) vertical velocity variance, σ_w^2, and horizontal velocity variance, $\sigma_{u,v}^2$ (u is parallel to the mean wind, v is perpendicular); potential temperature variance, σ_θ^2; energy dissipation rate, ε; and potential temperature flux, $\overline{w'\theta'}$, for a boundary layer over flat terrain. Dashed portions of the curves imply extrapolations through the surface layer (from Kaimal and Finnigan (1994)).

that temperature advections caused by air moving over terrain with a large temperature gradient, which are not unusual in and around a city, can have a significant impact on the heat flux profiles as well (Ching *et al.*, 1983). Cold air advection from a rural area to a urban area, for instance, can increase the vertical heat flux over a city. Melling and List (1980) claim that the normalized urban vertical velocity variance profiles agree well with the flat terrain case for $z/z_i > 0.4$. However, Hildebrand and Ackerman (1984) maintain that the urban normalized vertical velocity variance profiles are consistently larger than their rural counterparts, particularly near the top of the boundary layer. Also, the peak value of the normalized urban vertical velocity variance profiles is located at a higher normalized altitude than for the rural profile. Moreover, vertical velocity variance values are typically 2-3 times greater in the urban boundary layer than in the rural (Hildebrand and Ackerman, 1984). Nevertheless, the profiles shown in Fig. 4.6 may be regarded as reasonably good approximations for urban profiles.

4.4 Spectra and Cospectra

Now we examine the form of power spectra and cospectra of winds and temperature in the boundary layer. Figure 4.7 shows the idealized form of power spectra of a stable surface layer over flat terrain (Kaimal, 1973). The power spectra of the quantity α, which can stand for u, v, w, or θ, are multiplied by the frequency f and divided by the corresponding variance σ_α^2, producing a dimensionless function of f. Note that we will be using this type of normalization often when presenting power spectra. The basic form of the curve in Fig. 4.7 is quite general and most of the power spectra we are likely to encounter in the mixed layer should conform to it to one degree or another. Indeed, in the mixed layer, the power spectra of u, v, and w retain that shape; the only difference with respect to the surface layer is a change in the scaling parameters, namely, Q_0 and z/z_i (Kaimal *et al.*, 1976). The potential temperature power spectra in the mixed layer cannot be easily generalized,

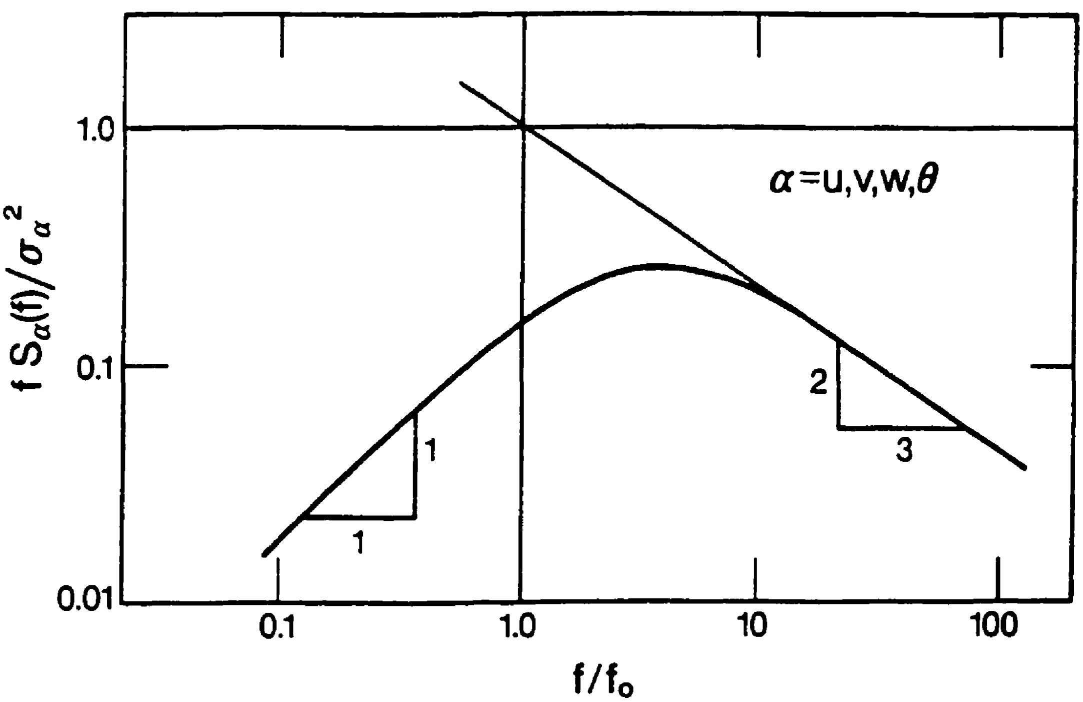

Figure 4.7: Normalized stable surface layer power spectrum for winds (u, v, w), and θ. The abscissa is normalized by the frequency f_0 where the inertial subrange slope intercepts the $fS_\alpha(f)/\sigma_\alpha^2 = 1$ line, as shown in the figure (from Kaimal and Finnigan (1994)).

particularly in the upper half of the mixed layer, due to entrainment effects. At high frequency, the effect of inertial subrange turbulence is felt, resulting in $S_\alpha(f) \propto f^{-5/3}$, or $fS_\alpha(f) \propto f^{-2/3}$ and a slope of -2/3 in log-log coordinates. Note that the -2/3 slope at the high frequency end should be apparent all through the mixed layer, and for all types of spectra (u, v, w, θ) (Kaimal *et al.*, 1976). At low frequency, $fS_\alpha(f) \propto f$, or $S_\alpha(f) = \text{const.}$, because at those scales the turbulence is directly coupled to a forcing mechanism (such as thermal plumes), and is no longer inertial. In the surface layer, the cospectrum of w and θ (heat flux cospectrum) shows a -7/3 power-law in the inertial subrange: $S_{w\theta}(f) \propto f^{-7/3}$ or $fS_{w\theta}(f) \propto f^{-4/3}$ (Kaimal *et al.*, 1972; Kaimal, 1973). However, there is no universal form for the heat flux cospectrum in the mixed layer (Kaimal *et al.*, 1976), although individual cospectra might be very useful in identifying the predominant heat transport mechanism, such as thermals with a low characteristic frequency.

Roth *et al.* (1989), Oke *et al.* (1989) and Roth and Oke (1993) present spectral and cospectral measurements taken close to the junction between the turbulent wake layer and the surface layer over a suburban surface. The w and θ spectra and cospectra show good agreement with their counterparts over a smooth surface, with a few minor differences. Namely, the peak of the power spectrum of w is slightly shifted towards lower frequencies and the power spectrum of θ is slightly shifted towards higher frequencies. Therefore, the general characteristics of spectra and cospectra over smooth surfaces may serve as an approximate model for urban boundary layers.

While much more can be said about the urban boundary layer, the overview in this chapter adequately covers those aspects of it measurable by a profiler/RASS. This, along with our understanding of the workings of ROSPA, gives us what we need to evaluate profiler/RASS measurements taken at the McGill University Campus site in downtown Montreal, which is an important topic in the next chapter.

Chapter 5

The June 28, 1996 Experiment

5.1 Overview of MERMOZ

In the MERMOZ project of the summer of 1996 (Montreal Experiment on Regional Mixing and Ozone), the Atmospheric Environment Service of Canada (AES) operated a UHF boundary-layer wind profiler, similar to the one at McGill, at a field station at a rural site 70 km southwest of Montreal (see Fig. 5.1). Equipped with a RASS, the radar was used mainly in a five-beam mode for routine wind profiling. However, during a 3-hour period (1045 to 1400 EST) in the early afternoon of June 28, the profiler was used for continuous RASS observations, producing a record of virtual temperature profiles up to 1 km with a height resolution of 60 m and a time resolution of 22 s. Clean and free of clutter or interference, the record is suitable for analysis of temperature and vertical velocity fluctuations and for estimation of the profile of vertical heat flux. A research aircraft of the National Research Council of Canada (NRC) was flying nearby during the same time, measuring along with other quantities the air temperature, humidity, and vertical velocity. In addition, the McGill profiler/RASS located in downtown Montreal, was also used continuously for RASS observations over a 3-hour period (1200 to 1530 EST). See section 2.3 for a description of the profiler/RASS equipment. To support the observations, a radiosonde was launched from the St-Anicet site at 1347 EST, followed by another at 1850 EST.

See Mailhot *et al.* (1998) for an detailed account of MERMOZ.

The AES and NRC cosponsored and co-directed the aircraft operations in MERMOZ. The aircraft, a DeHavilland DHC-6 Twin Otter, flew 24 flights, recording atmospheric state and radiometric data, and measuring the vertical fluxes of sensible and latent heat, CO_2, ozone, momentum, and turbulent kinetic energy. The aircraft uses a noseboom-mounted Rosemount 858 5-hole pressure probe and a Litton-90-100 Inertial Reference System to measure the three orthogonal components of atmospheric motion over a frequency range of 0-10 Hz (MacPherson, 1990). In post-processing, the accuracy of the measured winds is improved to better than 0.2 m s^{-1} utilizing a Kalman filtering technique that corrects the inertial velocities using GPS navigational data (Leach and MacPherson, 1991). Temperature is sensed by a heated Rosemount 102DJ1CG fast-response probe and corrected for dynamic heating using pressures measured by the noseboom. Humidity is measured by a fast-response LI-COR LI-6262 infrared CO_2/H_2O gas analyzer. Fluxes are calculated using the technique of eddy correlation after removing trends in the time histories. Data are digitally recorded at 32 Hz after anti-alias filtering at 10 Hz; at a typical airspeed of about 55 m s^{-1}, the along-track resolution of the data is approximately 5 m.

The early afternoon of June 28, 1996, was clear, cloudless with light winds, due to a synoptic-scale high pressure system dominating the region. As Fig 5.2 shows, the winds were predominantly from the east. The CBL height for profile A was about 500 m, and about 1 km for profile B, as we shall see in subsection 5.3.1. Figure 5.2 therefore shows that the winds were mostly ≤ 2 m/s within the CBL, and approximately 5 m/s above the CBL for profile A, which is consistent with the wind profile of a CBL described by Kaimal and Finnigan (1994). A ground fog had formed over the region early in the morning, starting at about 0030 EST and dissipating over McGill by about 0600 EST, and over St-Anicet by 0900 EST. The fog was at most 300 m thick. Figure 5.3 shows relatively cool temperatures early in the morning, especially

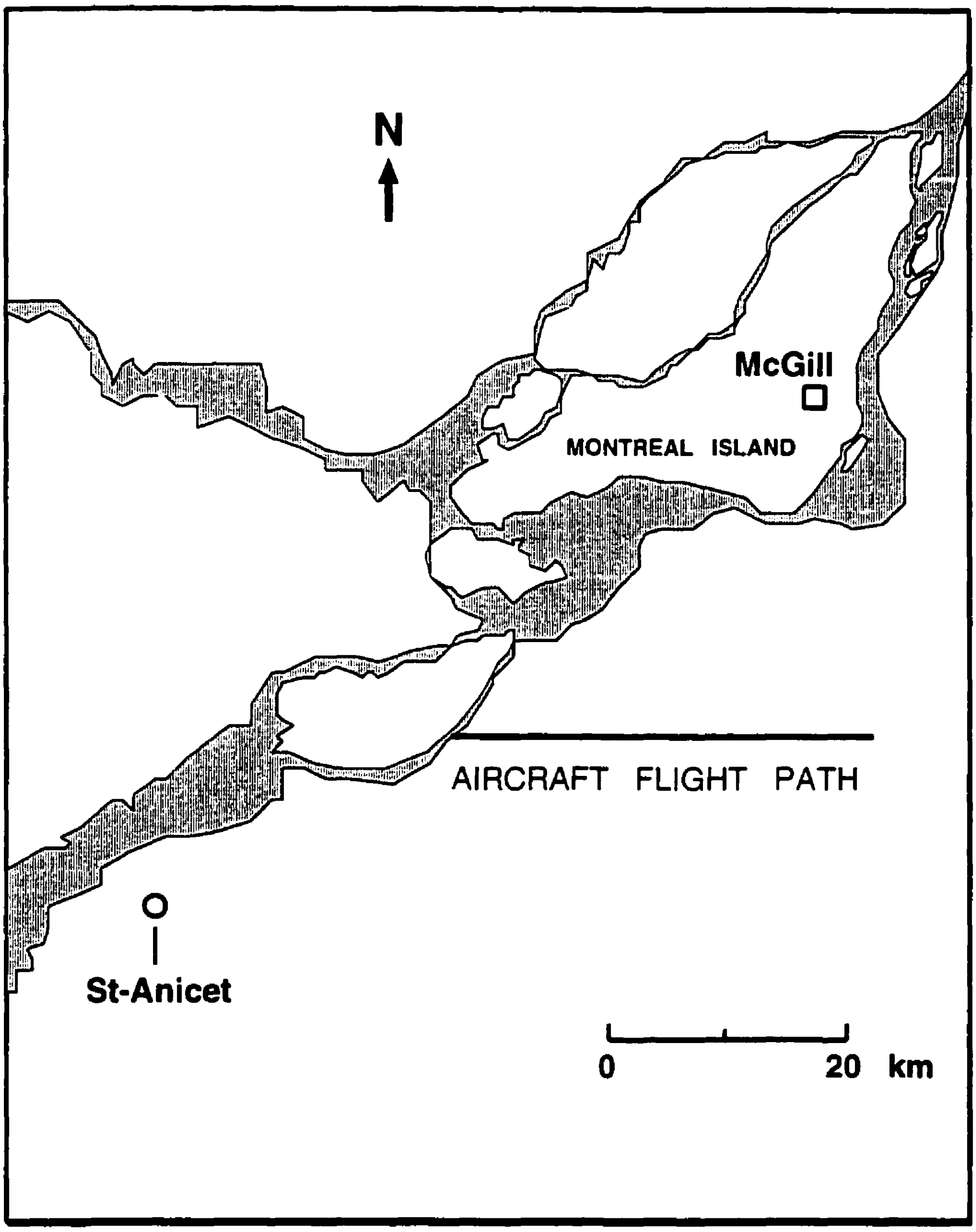

Figure 5.1: Map of the Montreal region showing the location of the aircraft flight path, the profiler/RASS and surface stations at St-Anicet (circle) and at the downtown McGill campus (square).

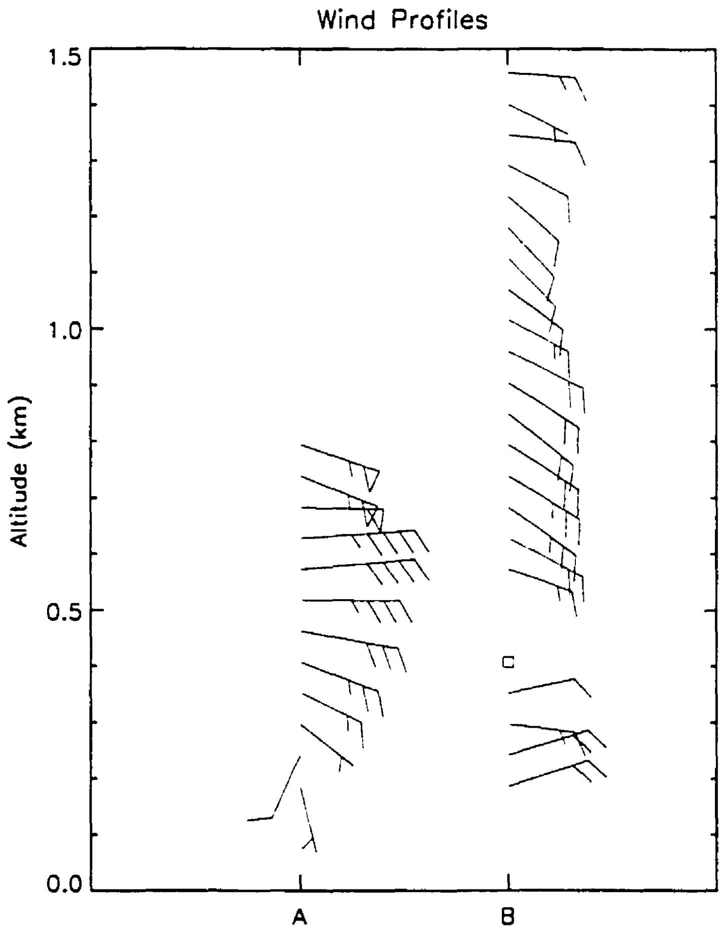

Figure 5.2: Wind profiles over St-Anicet taken by the profiler. Profile *A* is a consensus average the half-hour period preceding the continuous RASS measurements (1015 to 1045 EST), while *B* is for the half-hour following the RASS measurements (1400 to 1430 EST). A half barb represents 0.5 m/s, a full barb 1 m/s, and a triangle 5 m/s.

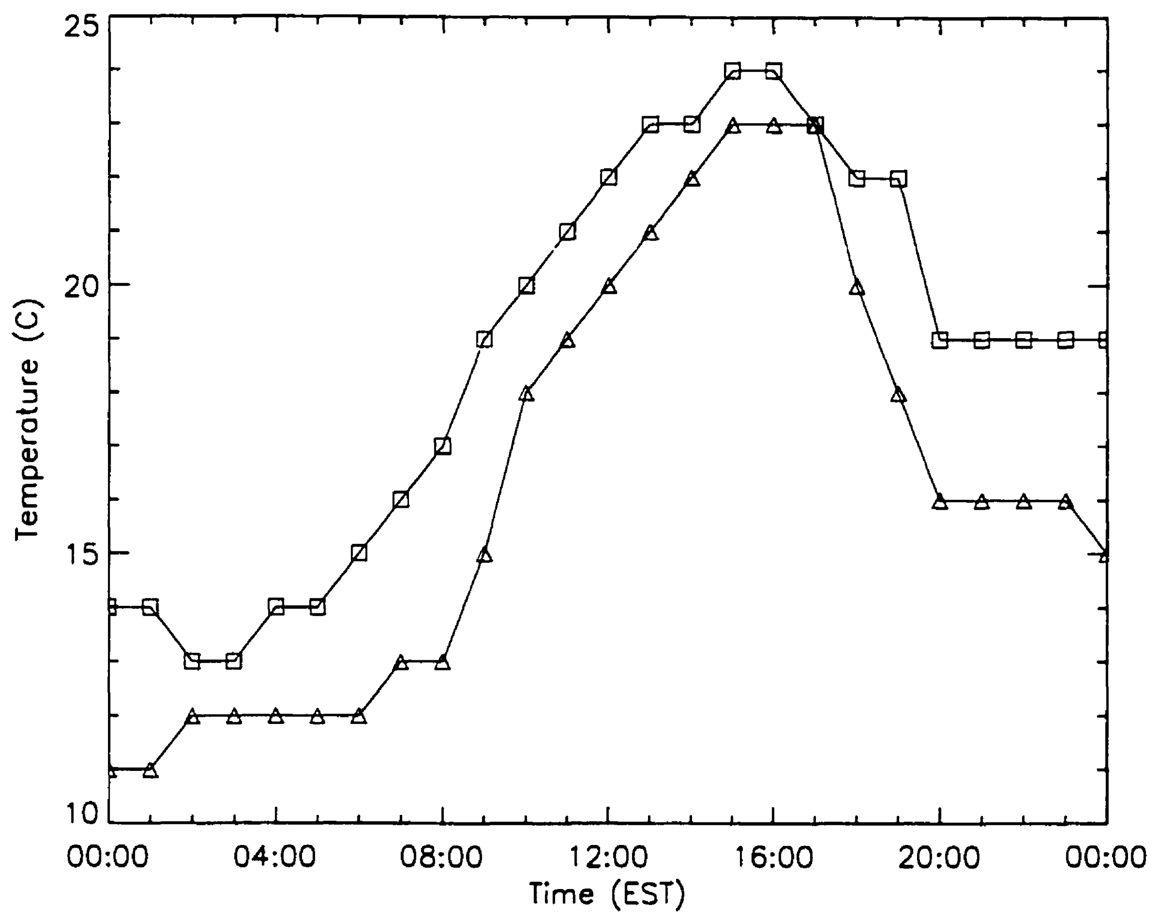

Figure 5.3: Plot of the hourly surface air temperature measurements at St-Anicet (triangles) and McGill (squares) on June 28, 1996.

at St-Anicet where the air at the surface was saturated with a temperature of about 11° to 12° C. Also note the resemblance of Fig. 5.3 with Fig. 4.2. The surface temperatures at McGill were generally warmer than those at St-Anicet: as much as 3° C warmer after sundown, an obvious urban effect.

Figures 5.4 and 5.5 show the potential temperature, virtual potential temperature, and water vapor mixing ratio profiles, taken by radiosonde over St-Anicet at 1347 and 1850 EST, respectively. The potential temperature profile in Fig. 5.4 is approximately constant at 293 K from the ground up to about 1 km, where a capping stable layer (also called an *inversion layer*) begins, followed by the free atmosphere, starting at about 1.1 km. This kind of potential temperature profile is typical of a CBL with a height of 1 km (see, for instance, Fig. 4.4(a), or consult Stull (1988), Garratt (1992), or Kaimal and Finnigan (1994)). The mixing ratio profile in Fig. 5.4 is also typical of a CBL, where we see a more or less constant value within the CBL (about 5 g/kg), and a noticeable decrease above the CBL (down to about 2 g/kg in the free atmosphere) (Garratt, 1992; Wyngaard, 1992). The drop in mixing ratio tends to reduce the increase in virtual potential temperature between the CBL and the free atmosphere. However, as Emanuel (1994) showed, it is the vertical gradient of the virtual potential temperature that determines the static stability of moist unsaturated air. The inversion layer is therefore less stable than the potential temperature profile would suggest, because it is the virtual potential temperature profile which is important for a moist unsaturated CBL. The erratic fluctuations in the potential temperature, virtual potential temperature and mixing ratio profiles between 0.7 and 1 km, may be due to the mixing between the CBL and the free atmosphere in that layer.

The radiosonde sounding at 1850 EST in Fig 5.5, on the other hand, shows no sign of a CBL. Instead, the free atmosphere appears to start at 200 m, below which is what looks like the beginnings of a *nocturnal inversion layer*, that is, a layer of air made stable by cooling from the bottom due to the ground. Indeed, as Fig. 5.3 shows, the surface air temperature at St-Anicet falls 8° C between 1700 and 2000 EST. This may mean that the ground is radiating more energy than it is receiving from the sun after 1700 EST, which in turn implies that after that time the surface virtual heat flux drops significantly, thereby inhibiting convection. It is also possible that the weakness of the inversion layer at 1347 EST favoured the entrainment of the free atmosphere into the CBL.

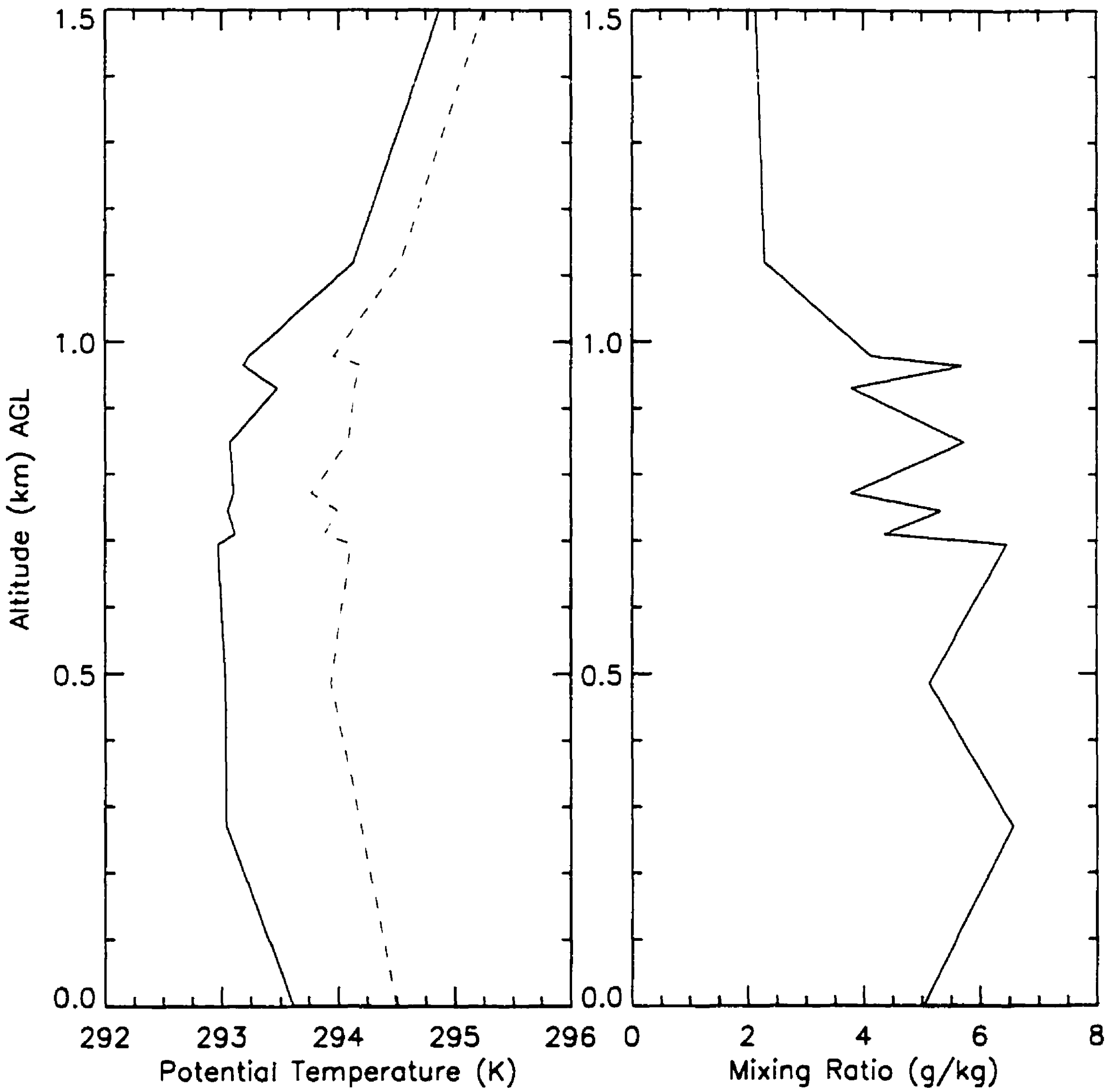

Figure 5.4: Profiles of potential temperature (solid line) and virtual potential temperature (dashed line) on the left, and the water vapor mixing ratio profile on the right, taken from a radiosonde lauched at St-Anicet, 1347 EST on June 28, 1996.

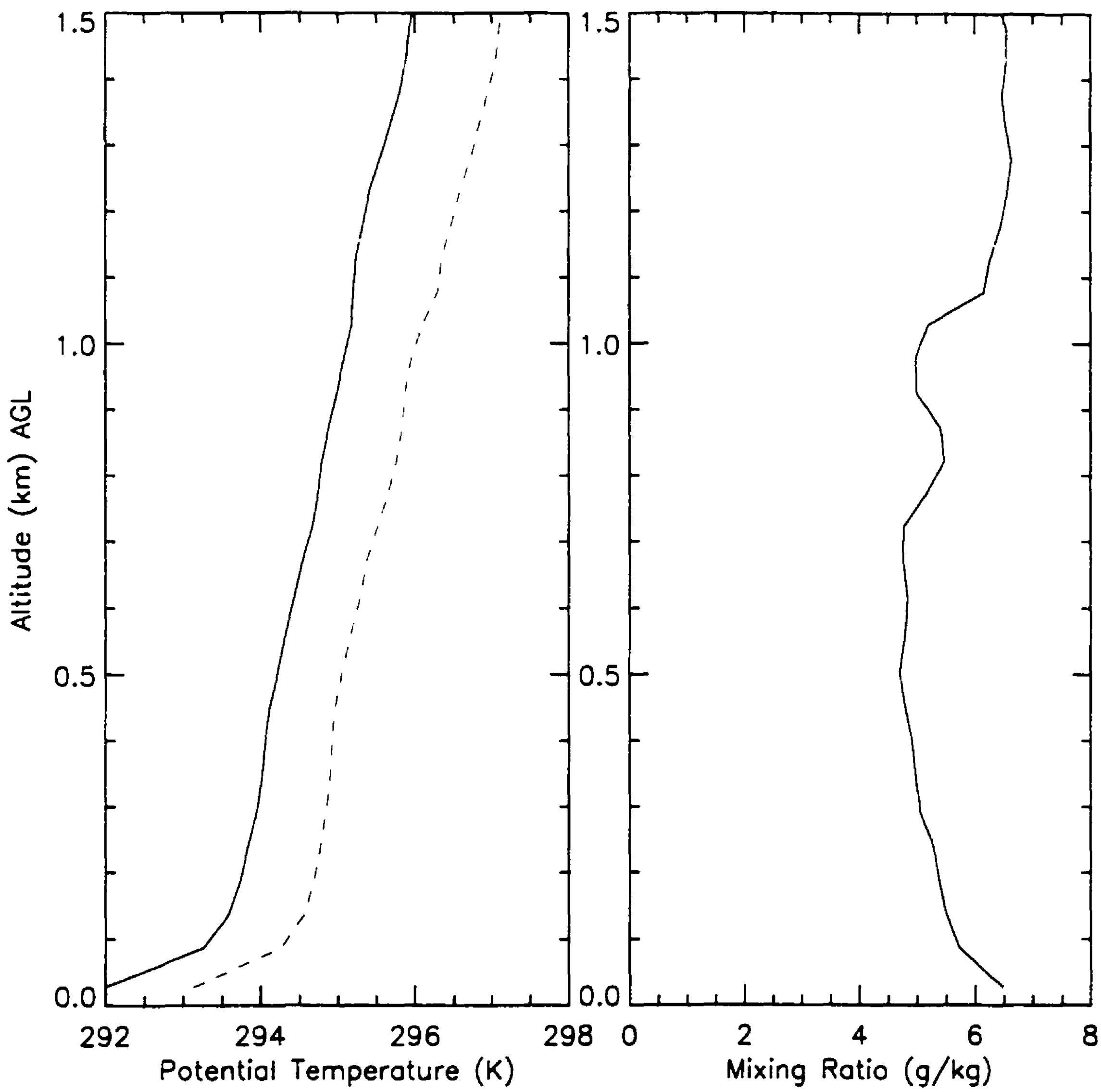

Figure 5.5: Same as in Fig. 5.4, but for a radiosonde lauched at St-Anicet, 1850 EST on June 28, 1996.

5.2 The Aircraft Data

Figure 5.6 shows the vertical velocity, virtual temperature, and virtual heat flux trace from the aircraft measurements at one altitude. The vertical air velocity and the virtual temperature fluctuations were high-pass filtered to remove trends caused by instrument effects or large scale gradients. The high-pass filter strongly attenuated any signal component with a wavelength of 12 km or greater. Figure 5.7 shows power spectra and the cospectrum of vertical velocity and virtual temperature for the aircraft measurements. These were smoothed at low wavenumbers by a running average over 5 wavenumber bins. At higher wavenumbers, however, the wavenumber bins appear closer and closer together in the logged wavenumber coordinates. Therefore, at high wavenumbers, if the interval in the logged coordinate between two wavenumbers five bins apart falls below 0.05, we average over all the wavenumber bins inside a 0.05 wide window in the logged wavenumber coordinate. Prior to the Fourier transform, a Hamming window (Kaimal and Finnigan, 1994; Oppenheim and Schafer, 1989) was applied to the data to reduce leakage between wavenumbers or frequencies. The power spectra were then multiplied by the wavenumber and divided by the variance of the time series with the Hamming window applied to it. This normalization produces a power spectrum with an area under the curve in linear-log coordinates equal to 1. For spectra so normalized, and when plotted as here on log-log coordinates, a slope of -2/3 is expected in the inertial subrange of homogeneous, isotropic turbulence (Caughey, 1984; Kaimal and Finnigan, 1994; Kaimal *et al.*, 1976). The cospectra are multiplied by the wavenumber, the density of the air $\rho = 1.2$ kg m^{-3}, and the specific heat of dry air at constant pressure $c_p = 1005$ m^{2}s^{-2}K^{-1}. This normalization produces a cospectrum with area under the curve in linear-log coordinates equal to the virtual heat flux.

The velocity power spectrum, Fig. 5.7(a) solid line, has most of its energy between 3×10^{-4} and 10^{-3} m^{-1} (or between 1 and 3.3 km wavelengths), and an inertial subrange, approximately the -2/3 law, extending from about 0.003 m^{-1} (330 m) to

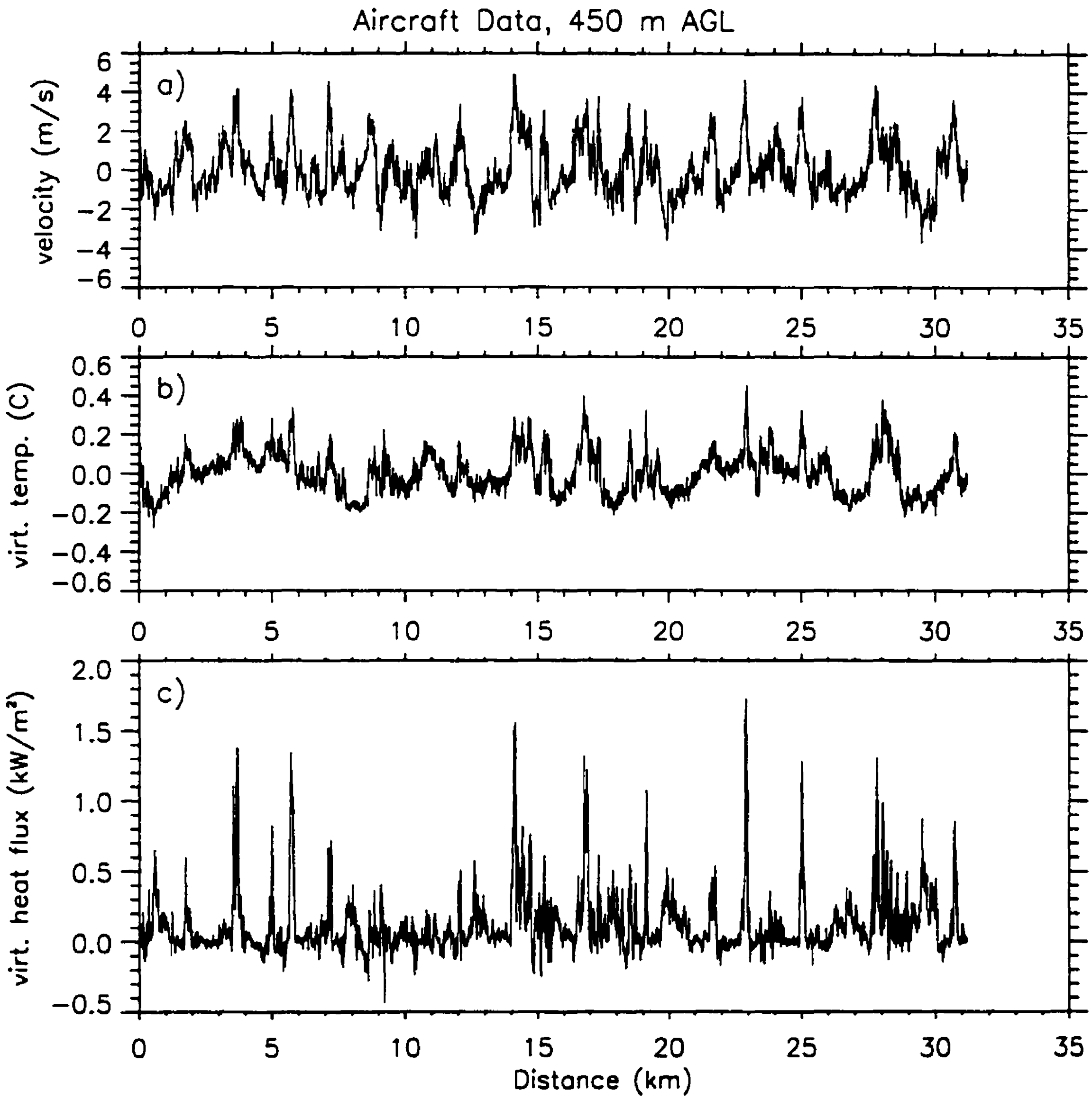

Figure 5.6: Distribution along a line of (a) vertical velocity fluctuations, (b) virtual temperature fluctuations, and (c) virtual heat flux trace, taken from an aircraft run at 450 m AGL, for 9 min starting at 1322 EST.

smaller scales. The temperature power spectrum, Figure 5.7(a) dotted line. has its peak at slightly lower wavenumbers, 3×10^{-4} to 6×10^{-4} m^{-1} (1.7 to 3.3 km). However, at high wavenumbers the -2/3 slope is not well obeyed. This is possibly due to noise contaminating the signal, as the initial small drop in the temperature autocorrelation function (Figure 5.8(a)) would suggest. Noise would appear as a line with a slope of +1 in the spectral plots. The aircraft cospectrum, Figure 5.7(b), demonstrates a sharp peak at 4×10^{-4} m^{-1} (2.5 km), in accord with the velocity and temperature peaks, and falls rapidly to zero over the inertial range, almost vanishing at scales less than 100 m, thereby demonstrating that the inertial subrange does not contribute much to the overall heat flux.

5.3 The Profiler/RASS Data

In this section, we will examine the data from the profiler/RASS at both locations. However, we begin by examining the data from St-Anicet given the absence of ground and intermittent clutter at that location. Next, we calibrate ROSPA using the St-Anicet and McGill data. The clean St-Anicet data will then be used as a guide for evaluating the treated McGill data.

5.3.1 St-Anicet Data

We must point out that the spectral averaging for the profiler at St-Anicet was performed using SAM (Statistical Averaging Method), an on-line intermittent clutter rejection algorithm by Merritt (1995), which we described in subsection 3.1.2. The clean and clutter free profiler data is probably due in part to the use of SAM. However, it also seems likely that the St-Anicet site itself was in part responsible for the quality of the profiler data. First, the St-Anicet clear-air spectra show no sign of ground clutter, something which SAM does not eliminate. Second, the time resolution of 22 s is probably too short to allow SAM to effectively eliminate all of the

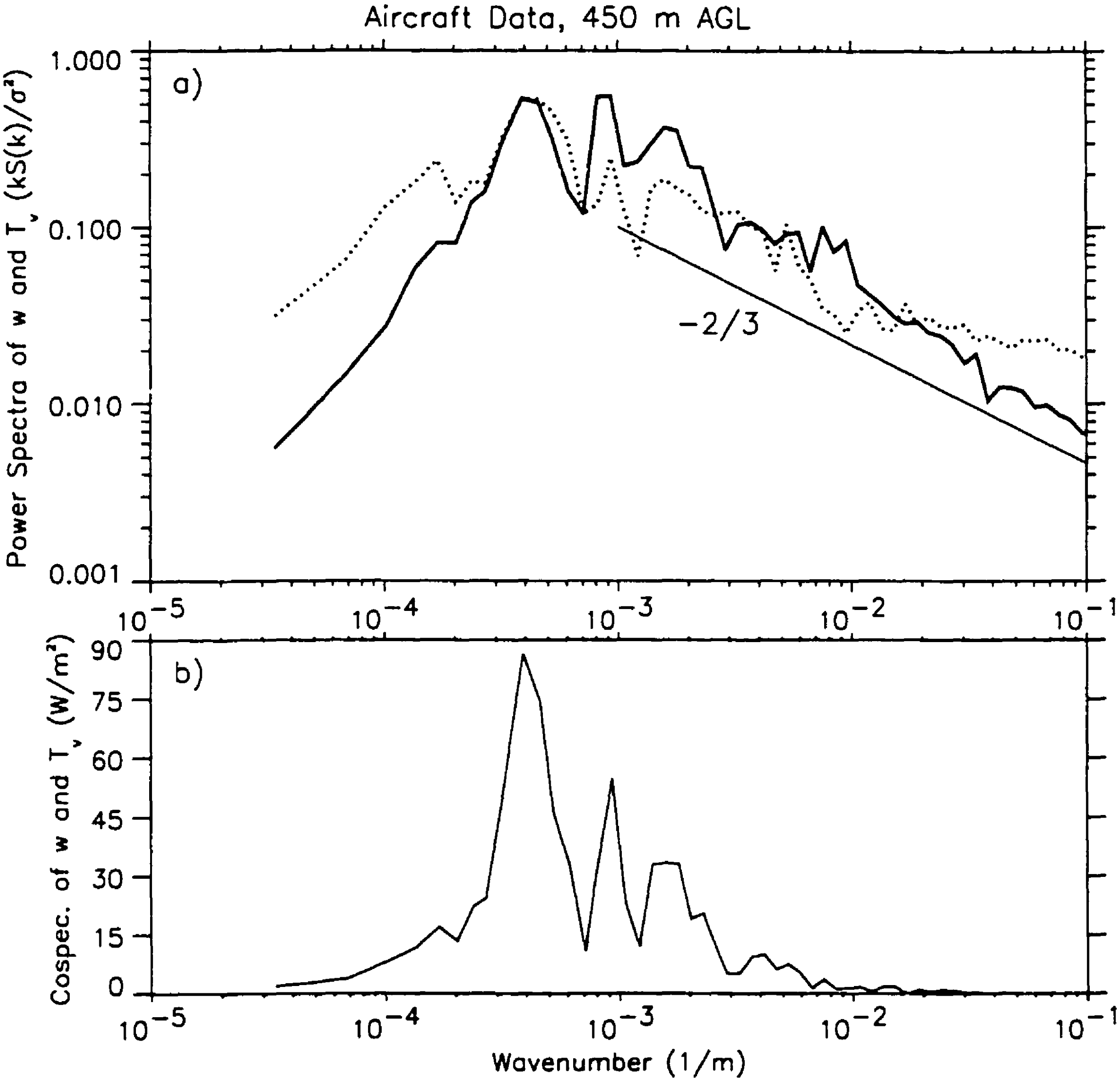

Figure 5.7: Power spectra and cospectrum of the data in Fig. 5.6. Graph (a) shows the power spectra of the vertical velocity (solid line), and the virtual temperature (dashed line), multiplied by the wavenumber and divided by the variance, that is, $(kS(k)/\sigma^2)$. Graph (b) shows the cospectrum of the vertical velocity and the virtual temperature, multiplied by the density, specific heat, and wavenumber, that is, $(\rho c_p k S_{wT}(k))$.

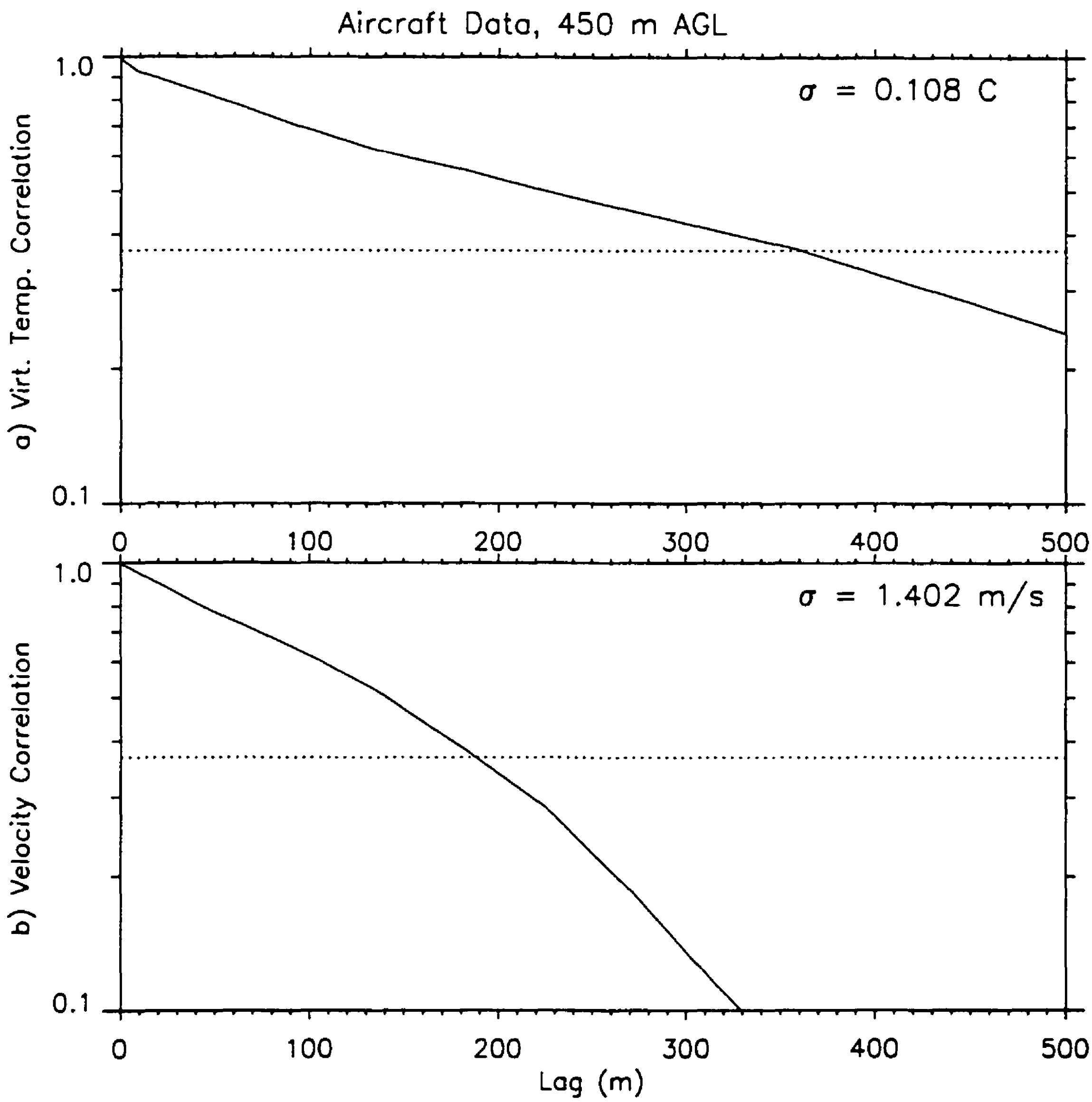

Figure 5.8: Virtual temperature (a) and vertical velocity (b) autocorrelation function for aircraft data at 450 m AGL. Note the corresponding standard deviations, σ, in the upper righthand corners. The dotted line represents the $1/e$ value (0.3679) of the correlation.

intermittent clutter, had that type of contamination been severe. It therefore seems likely that the clutter contamination at the St-Anicet site was not very serious.

Structure and Evolution of the CBL

Figure 5.9 shows a plot of the range-normalized signal-to-noise ratio of the clear-air signal measured by the profiler. Angevine *et al.* (1994c) explain that the altitude of the maximum of this quantity serves as a good approximation to the inversion height. The figure shows that the thickness of the boundary layer is approximately constant at 0.6 km AGL until about 1230 EST, when the buildup of the CBL begins. This kind of sudden growth has been observed previously by Carson (1973).

Figure 5.10 shows the virtual potential temperature obtained by imposing a half-hour running average (or about 80 measurements, 22 seconds apart) on RASS virtual temperature data and assuming a hydrostatic condition for obtaining pressure by upwards integration using surface pressure data. Although the reach of the RASS on this day was excellent, the raw data contained some outliers due to occasional weakness of the RASS signal at high altitudes. They were removed prior to averaging by applying a median filter with a 5-point window, to the raw data. Figure 5.10 shows a strong gradient of virtual potential temperature (a stable layer) at about 0.6 km initially (from 1100 to approximately 1130 EST) and at about 1 km towards the end of the observation period (the last hour). These stable layers inhibit convection at those altitudes, thereby capping the thermal plumes. In the middle of the period the height of the stable layer is not well defined, probably due to the rapid evolution of the CBL at this time. The warming of the CBL is evident from the downward slant of the virtual potential temperature contours. In particular, the 289 and 290 K contours show a sudden descent into the ground, indicating a rapid heating of the initial 0.6 km deep CBL, resulting in the weakening of the statically stable layer capping it and the subsequent release of convection up to 1 km starting at about 1230 EST.

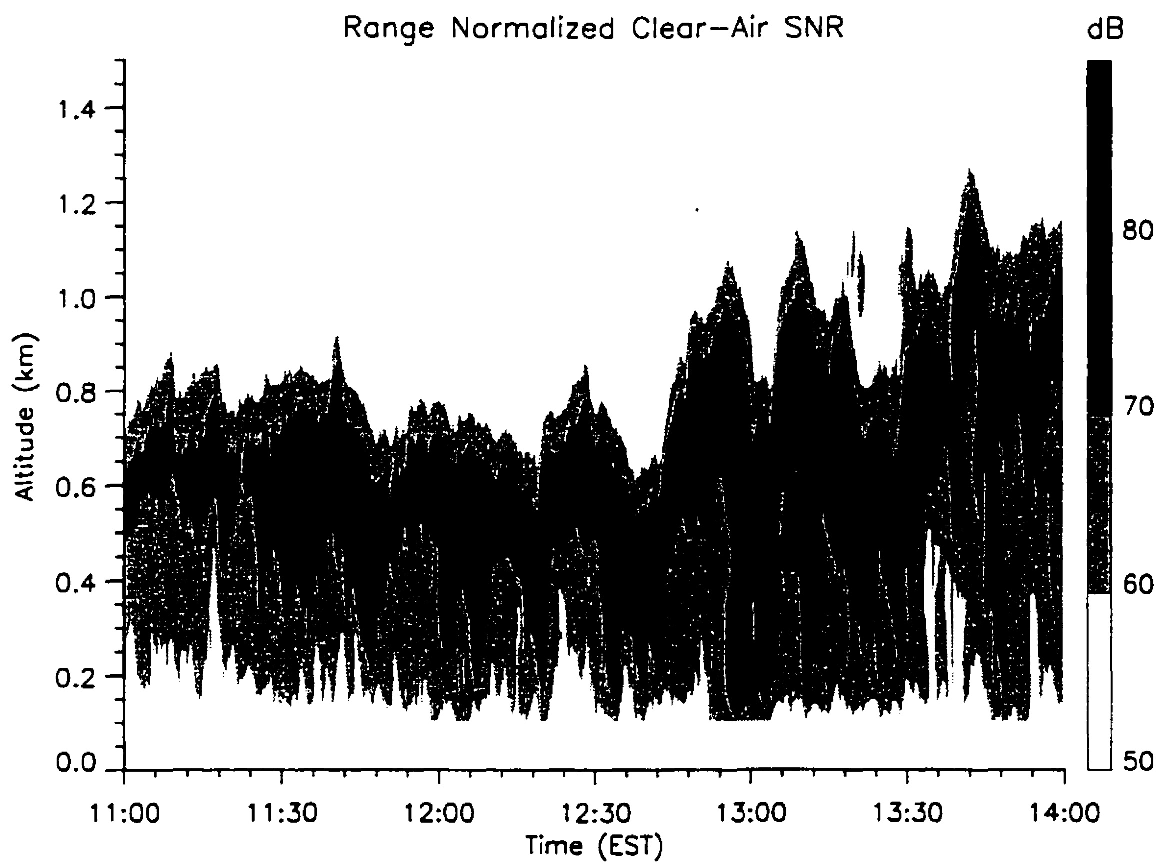

Figure 5.9: Time-height plot of the range normalized clear-air signal-to-noise ratio over St-Anicet on June 28, 1996.

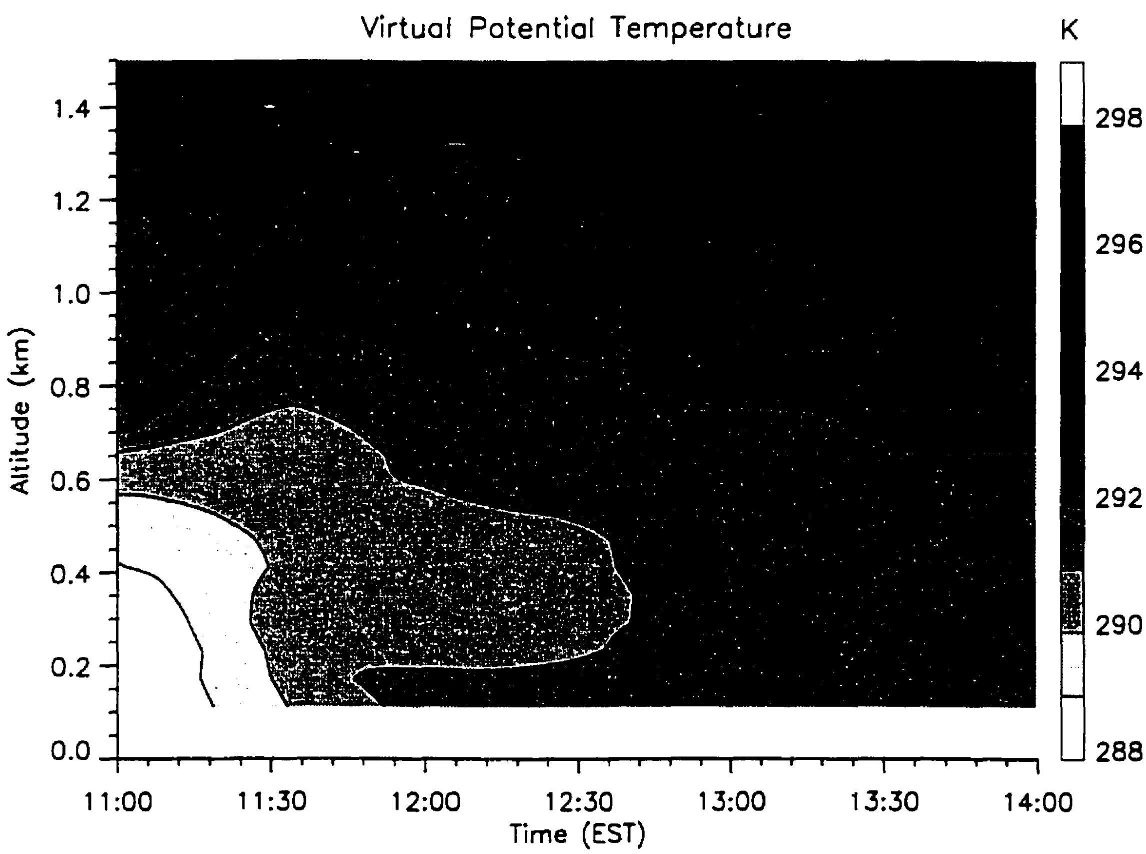

Figure 5.10: Same as Fig. 5.9, but for virtual potential temperature.

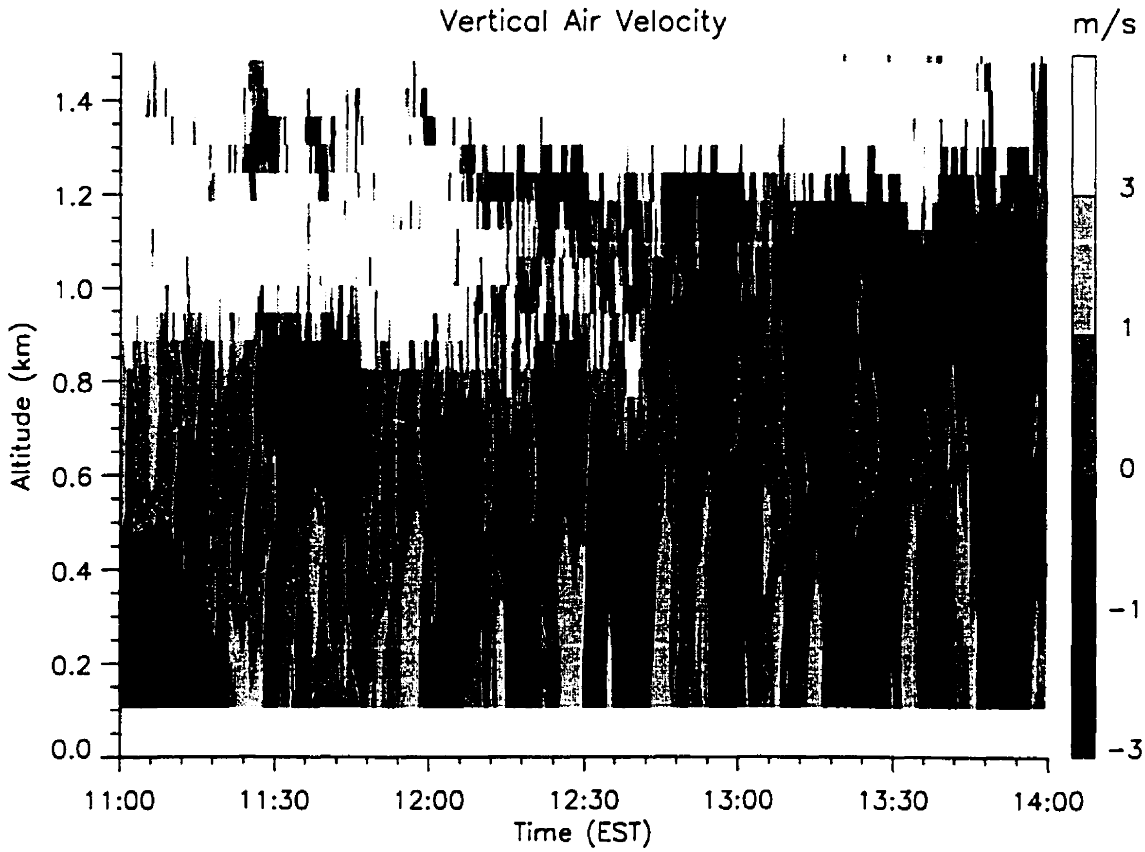

Figure 5.11: Same as Fig. 5.9, but for the vertical air velocity. Note that the solid line is the zero velocity contour.

Finally, Fig. 5.11 shows the vertical air velocity measured by the profiler. It indicates the presence of plumes and reveals their vertical structure, mainly in the second half of the period, when columns of rising and descending air are clearly visible. Such a structure of vertical air motion is consistent with the descriptions of Carson (1973) and Wyngaard (1992) and the observations of Kaimal *et al.* (1976) of the thermal plumes in a CBL. The time averaged vertical velocity over the entire period was removed from the velocities shown in Fig. 5.11 for each height, to eliminate any possible instrumental bias in the vertical velocity measurements (Angevine, 1997).

Data and Heat Flux Analysis

Here, we analyse the data and demonstrate certain difficulties in estimating the virtual heat flux. Figure 5.12 shows time series of measured and derived RASS quantities at one particular altitude (412 m). The uncorrected virtual temperature (curve a) includes the effect of vertical air velocity (curve b), which explains why these traces resemble each other. The interdependence of these quantities follows from

$$R = c + w \tag{5.1}$$

where R is the velocity of the acoustic wave measured by the RASS, w is the vertical velocity of the air, measured by the profiler, and c is the speed of sound in still air. Given that $c = \sqrt{\gamma R_a T_v}$, where $\gamma = 1.4$ is the ratio of specific heats of air, $R_a = 287$ m^{2}s^{-2}K^{-1} is the gas constant of air, and T_v is the virtual temperature in K, we may convert Eq. 5.1 to

$$T_R = T_v + 2w\sqrt{\frac{T_v}{\gamma R_a}} + \frac{w^2}{\gamma R_a} \tag{5.2}$$

where $T_R = R^2/(\gamma R_a)$ is the uncorrected temperature measured by the RASS and displayed in curve (a). The corrected temperature (curve c) has the effect of vertical air motion removed. From Eq. 5.2, this quantity is given by

$$T_v = T_R - 2w\sqrt{\frac{T_R}{\gamma R_a}} + \frac{w^2}{\gamma R_a}. \tag{5.3}$$

The smooth line in curve (c) is the quadratic least-squares fit to the data. It indicates the general warming trend during the observing period and is taken to represent the non-stationary mean temperature. Deviations of the corrected temperature from this line are taken to be the turbulent fluctuations used in heat flux calculations. The detrending necessary to obtain the corrected temperature fluctuations is the only correction for nonstationarity used on the RASS data. Because RASS measures virtual temperature, the product of the deviations from this line and the vertical air velocity gives the buoyancy flux, which when multiplied by the product of air density and specific heat gives the virtual heat flux trace (curve d). Notable in the trace are bursts of heat flux, sometimes exceeding 1000 W/m^2, which become more frequent as time increases. The virtual heat flux trace as plotted is in fact the average of two estimates of the flux: (1) the trace produced with the velocity time series moved ahead one time step with respect to the temperature time series and (2) that with the temperature time series moved ahead one time step with respect to the velocity time series. That is,

$$F[i] = \frac{\rho c_p}{2}(w'[i+1]T_v'[i] + w'[i]T_v'[i+1]) \tag{5.4}$$

where $\rho = 1.2$ kg m^{-3} is the density of air, $c_p = 1005$ m^{2}s^{-2}K^{-1} is the specific heat of dry air at constant pressure, F is the virtual heat flux in W/m^2, i is the discrete time index, and the primes denote fluctuations from the mean. The time average of the resulting trace is mathematically equivalent to a method of heat flux calculation used by Peters *et al.* (1985).

The reason for the time shift in Eq. 5.4 is to eliminate a systematic bias. This is made clear when we consider Eq. 5.3 and assume that T_R and w both carry errors, η_R and η_w respectively. These errors are assumed random, with zero means and variances σ_R^2 and σ_w^2. Also, we assume that η_R is independent of η_w and that the error at one time is independent of the errors at other times. Therefore, if there were no time shift in the definition of the heat flux trace ($F[i] = \rho c_p w'[i]T_v'[i]$), then Eq. 5.3 tells us that the errors η_w would combine in such a way as to produce an constant average bias in the heat flux estimation,

$$\text{bias} = -2\rho c_p \sigma_w^2 \sqrt{\frac{\overline{T_R}}{\gamma R_a}} \tag{5.5}$$

where the overbar denotes a time average. Eq. 5.5 shows that the bias is always negative. By time shifting, this bias is avoided although the heat flux may be slightly underestimated (Peters *et al.*, 1985).

The turbulent fluctuations of virtual temperature shown for one altitude in Fig. 5.12(c) are plotted in time-height coordinates in Fig. 5.13. These fluctuations have a

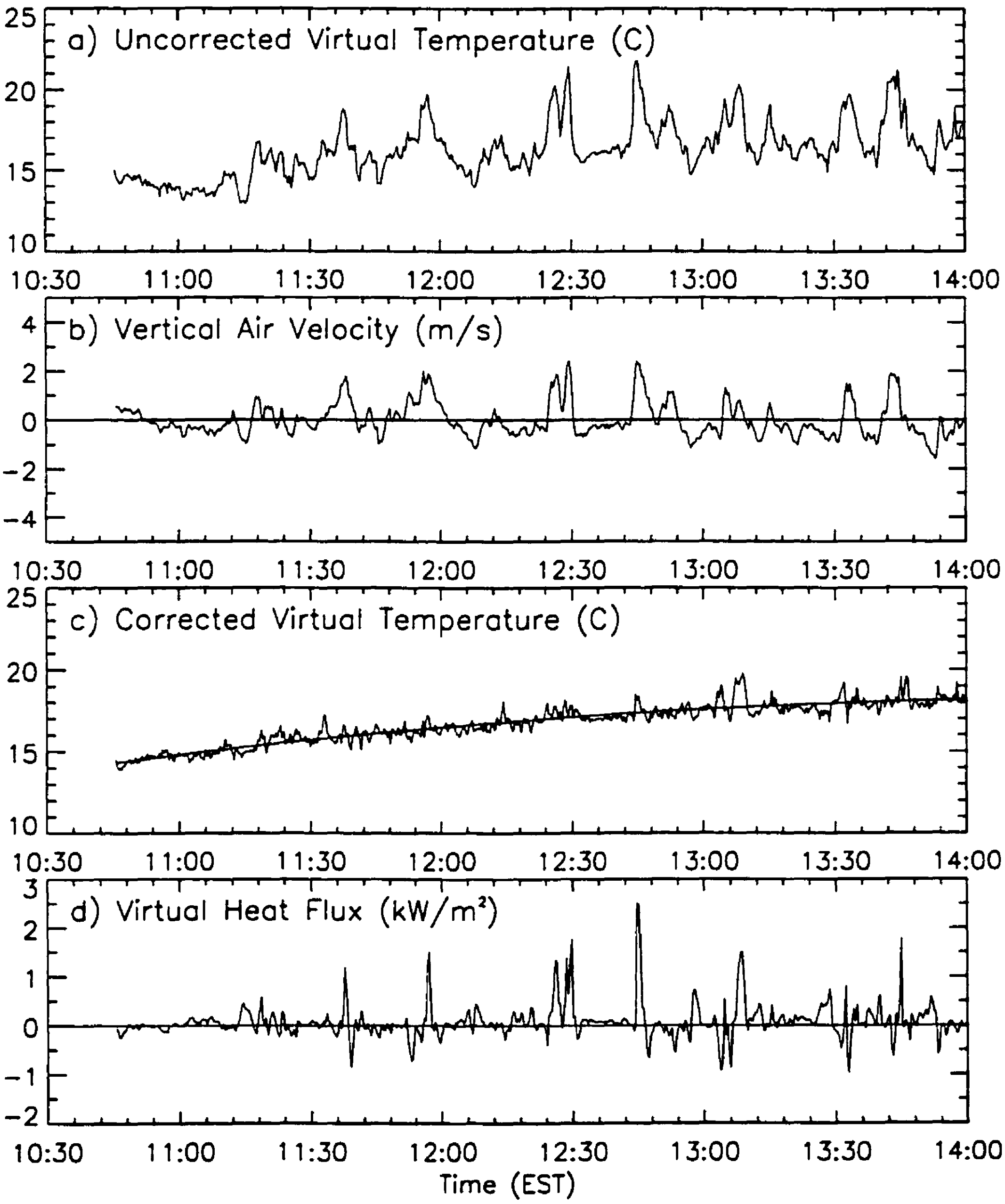

Figure 5.12: Time series of (a) uncorrected RASS temperature, (b) vertical air velocity, (c) corrected temperature, (d) virtual heat flux, at 412 m AGL over St-Anicet on June 28, 1996.

structure resembling that of the vertical velocity fluctuations in Fig. 5.11, but with generally shorter durations. There is also a predominance of positive temperature fluctuations between 0.8 and 1.2 km and from 1230 EST onwards. This coincides with a net preponderance of downwards motion in the same region (Fig. 5.11). An entrainment of potentially warm air from the free atmosphere downwards into the mixed layer is therefore suggested. Figure 5.14 shows the virtual heat flux. There is a predominance of positive heat flux in the lower part of the CBL, particularly towards the end of the period. Conversely, there is a predominance of negative heat flux around the top of the CBL (compare with Fig. 5.9).

Figure 5.15 shows a quadrant analysis of the heat flux, similar to the kind used by Kroon and Bink (1996) or Grant *et. al.* (1986), except that rather than compiling statistics, a time-height contour plot is used. This analysis partitions the flux into upwards and downwards motion and cool and warm currents. In the second half of the period, there are vertical columns of predominantly warm rising air with regions of mainly cool descending air. This structure is consistent with the picture of regions of descending cool air separated by thin walls of rising warm air, described by Schmidt and Schumann (1989) using a large-eddy simulation. The entrainment of warm air from the free atmosphere to the mixed layer is seen once again by the predominance of the positive downward (PD) quadrant at the top of the CBL.

Figures 5.16 to 5.19 demonstrate the spectral and correlation structure of the RASS data. The smoothing of the spectra and cospectra is identical to what was done to the aircraft spectra, except that at low frequencies the spectra and cospectra were averaged over three bins only. The RASS data were split into two parts, 1048 to 1224 EST and 1224 to 1400 EST, to show explicitly the nonstationarity. The first part has a CBL top relatively constant at about 0.6 km. The second part contains a CBL whose height grows rapidly from 0.6 km to about 1 km. Figure 5.16 shows the first part. The broad maximum of the velocity spectrum extends from 6×10^{-4} to

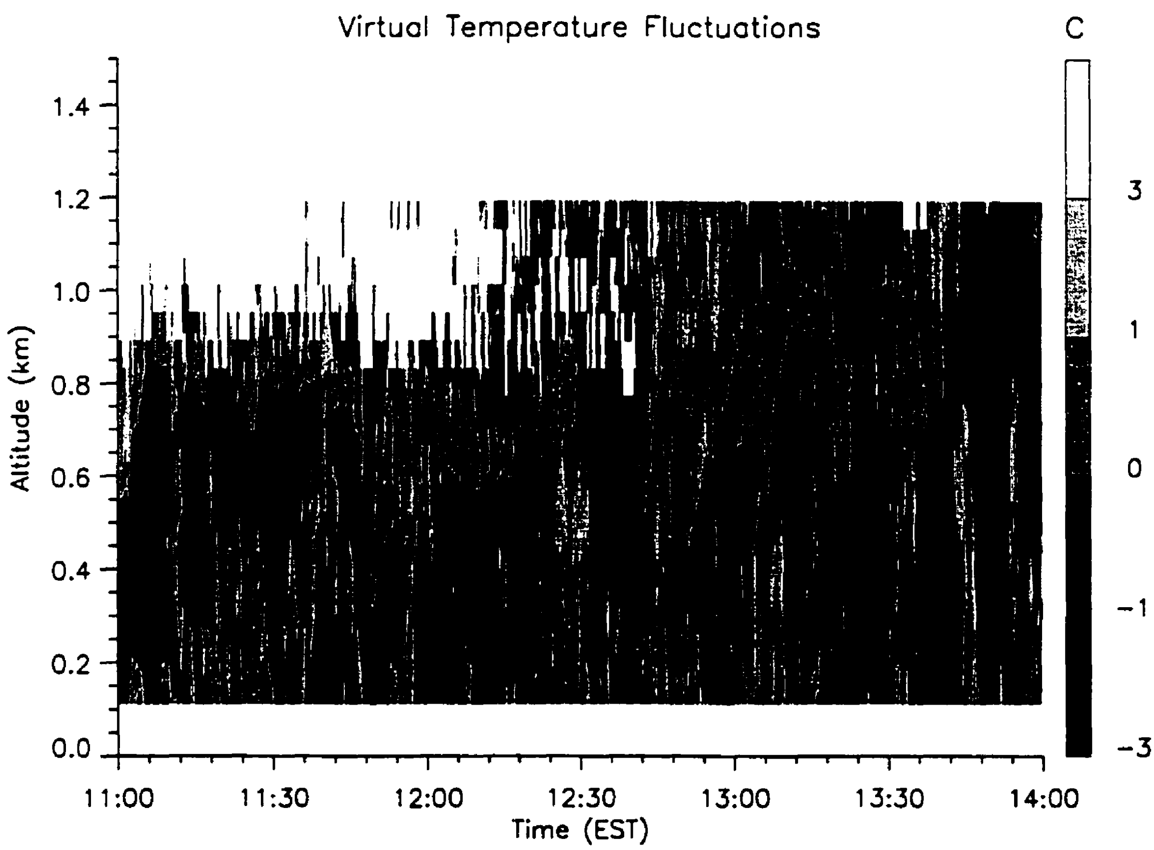

Figure 5.13: Time-height plot of virtual temperature fluctuations over St-Anicet, on June 28, 1996. Note that the solid line represents the zero value contour.

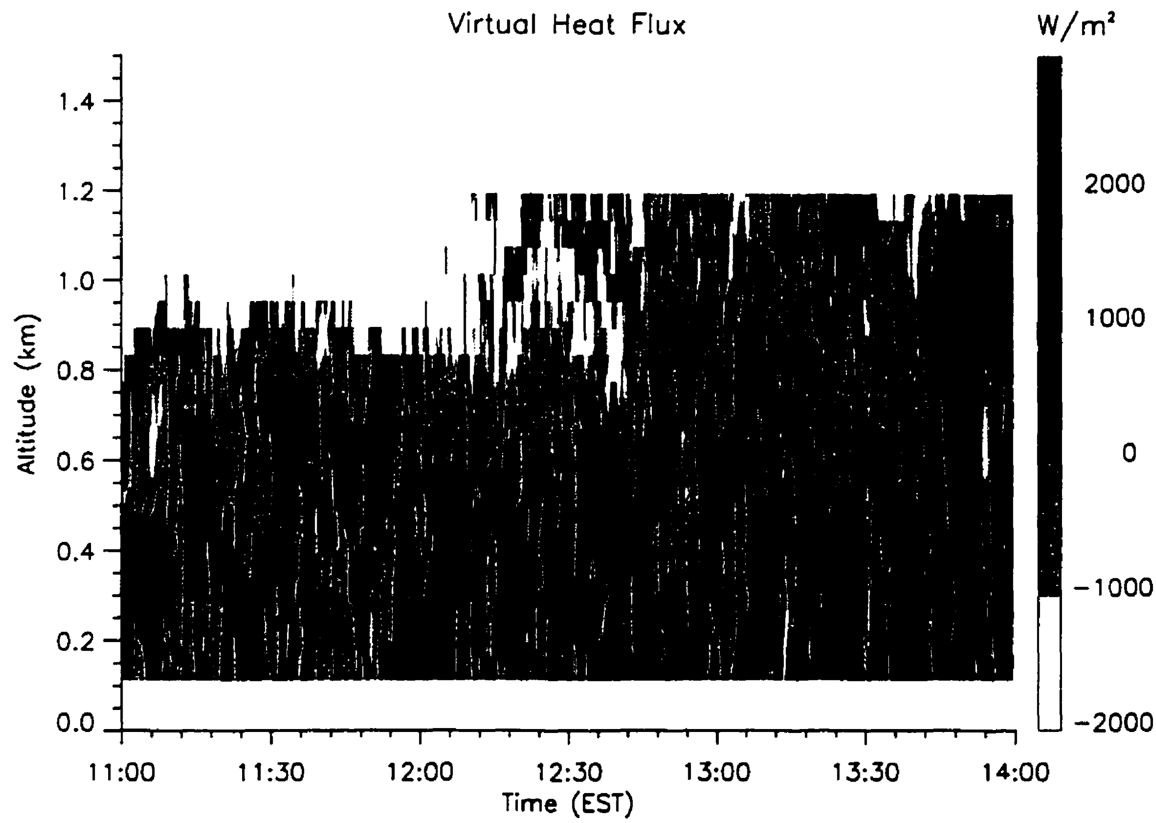

Figure 5.14: Same as in Fig. 5.13, but for the virtual heat flux. Note that the solid line represents the zero value contour.

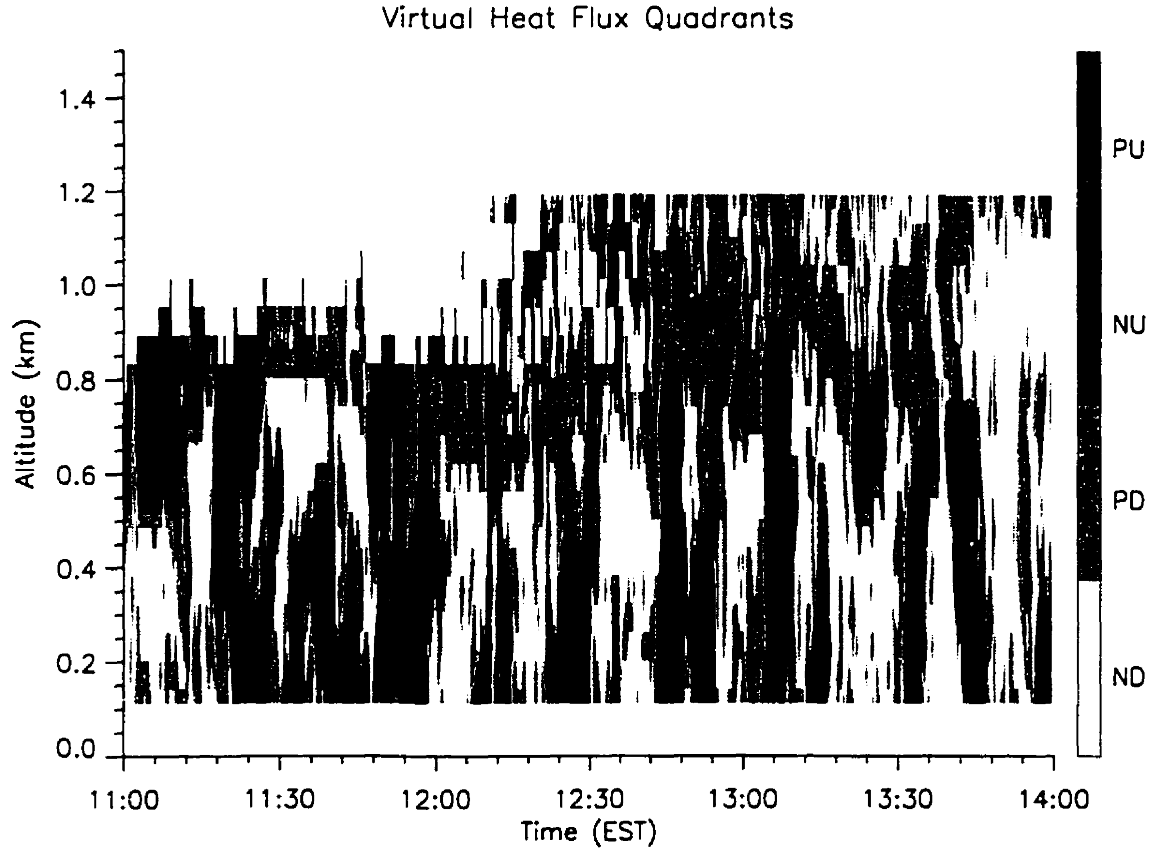

Figure 5.15: Same as in Fig. 5.13, but for the virtual heat flux quadrants. Note that, PU = positive virtual temperature fluctuation and upward vertical velocity fluctuation, NU = negative-upward, PD = positive-downward, and ND = negative-downward.

1.2×10^{-3} Hz (14 to 28 min) with a maximum at about 17 min. The slope at high frequencies seems steeper than 2/3, possibly due to a low-pass filter effect induced by the size of the profiler pulse volume. Eddies smaller than the pulse volume are averaged out, leaving the larger eddies which may have lifetimes greater than the integration time of the profiler. A low-pass filter effect may also be induced by the horizontal wind advecting eddies through the pulse volume over the integration time, thereby extending the effective averaging volume. The velocity spectrum in Fig. 5.17(a) has a similar structure with a peak at about 9 min and a high frequency slope steeper than 2/3.

The temperature power spectra in Figs. 5.17(a) and especially 5.16(a) appear to be strongly contaminated by a kind of measurement error (which tends to induce a slope of +1), making the identification of a peak unreliable. However, as Figs. 5.16(b) and 5.17(b) show, only the spectral components with periods ranging from 5 to 15 min, approximately, contribute significantly to the heat flux. Although the temperature spectral peaks at those periods may be obscured by the measurement errors, they still contribute, on average, to the cospectrum as though there were no measurement errors. The measurement errors can, however, increase the uncertainty of the heat flux estimates. White noise is suggested by the rapidly decreasing temperature autocorrelation functions in Figs. 5.18(a) and 5.19(a), although it is difficult to estimate the signal-to-noise ratio confidently due to the uncertainty in extrapolating the signal autocorrelation function to zero lag. The white noise is probably caused by errors in the estimation of temperature due to factors other than the vertical air velocity, such as small-scale turbulence, horizontal winds, and others (Angevine and Ecklund, 1994). These errors represent an inherent limit to the accuracy of RASS temperature measurements independent of the presence of clutter or interference in the vertical air velocity measurements. Therefore, the temperature white noise may not be reduced by the vertical air velocity low-pass filter effect. The heat flux cospectra, Figs. 5.16(b) and 5.17(b), have greater peaks, 170 and 200 W/m^2 respectively, than the aircraft cospectrum, 85 W/m^2, along with substantial negative components.

Figures 5.20 and 5.21 show profiles of vertical air velocity variance, while Figs. 5.22 and 5.23 show profiles of vertical air velocity variance flux (the third order moment of the vertical velocity, $\overline{(w-\overline{w})^3}$), for both wind profiler/RASS and aircraft measurements. The error bars for these and subsequent quantities were estimated using the methods described by Lenschow *et al.* (1993; 1994). For the variance of the estimation of the average of a time series, Lenschow *et al.* propose

$$\varepsilon_1^2 = 2\sigma^2\tau/T \tag{5.6}$$

where ε_1 is the standard deviation of the estimate of the average (which we also call the error on the estimate), σ is the standard deviation of the time series, $\tau = \int_0^\infty \rho(\Delta)d\Delta$ is the integral timescale of the time series ($\rho(\Delta)$ is the autocorrelation function of a stationary time series), and T is the duration of the time series. For the error on the estimate of the variance, we use

$$\varepsilon_2^2 = 2\sigma^4\tau/T \tag{5.7}$$

and for the error on the third-order moment

$$\varepsilon_3^2 = 4\sigma^6\tau/T. \tag{5.8}$$

Also note that the vertical air velocity variance for the profiler measurements is in fact the statistic $\overline{(w[i]-\overline{w})(w[i+1]-\overline{w})}$, that is, the autocovariance function at lag 1. This is done to avoid any bias that might result due to random and independent errors (noise) on the profiler measurements. The profiler measures vertical air velocity averaged over the resolution volume and the integration time, which reduces the contribution of small eddies. It is therefore not surprising that the aircraft measures a greater variance than the profiler in Figs. 5.20 and 5.21, given its finer resolution. The dashed lines in Figs. 5.20 and 5.21 represent the sum of the variance and the average clear-air spectral variance. The spectral variance is defined as the

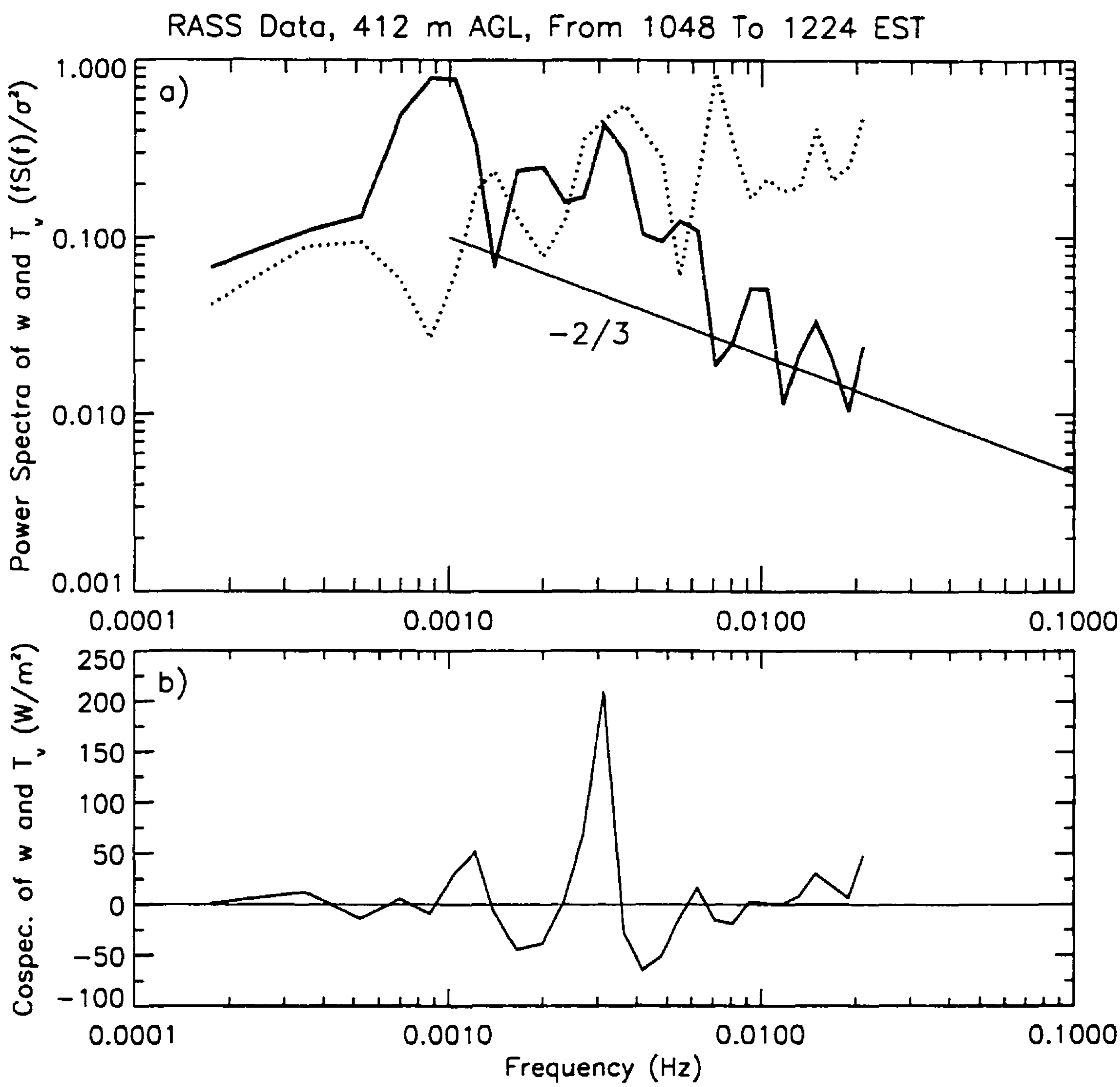

Figure 5.16: Power spectra and cospectrum of the RASS data at 412 m AGL from 1048 to 1224 EST. Graph (a) shows the power spectra of the vertical velocity (solid line), and the virtual temperature (dashed line), multiplied by the frequency and divided by the variance, that is, $fS(f)/\sigma^2$. Graph (b) shows the cospectrum of the vertical velocity and the virtual temperature, multiplied by the density, specific heat, and frequency, that is, $\rho c_p f S_{wT}(f)$.

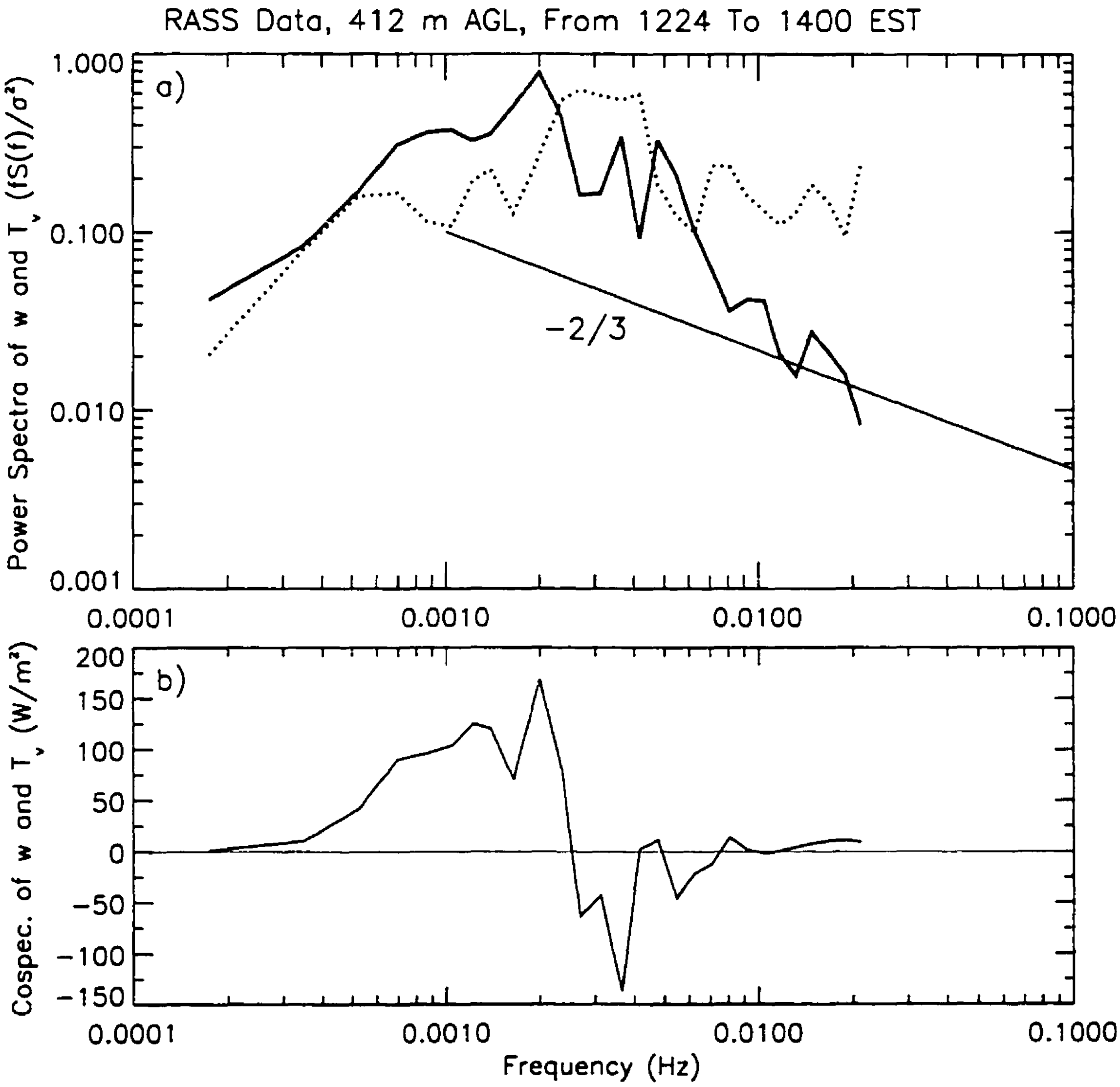

Figure 5.17: Same as in Fig. 5.16, but for RASS data at 412 m AGL from 1224 to 1400 EST.

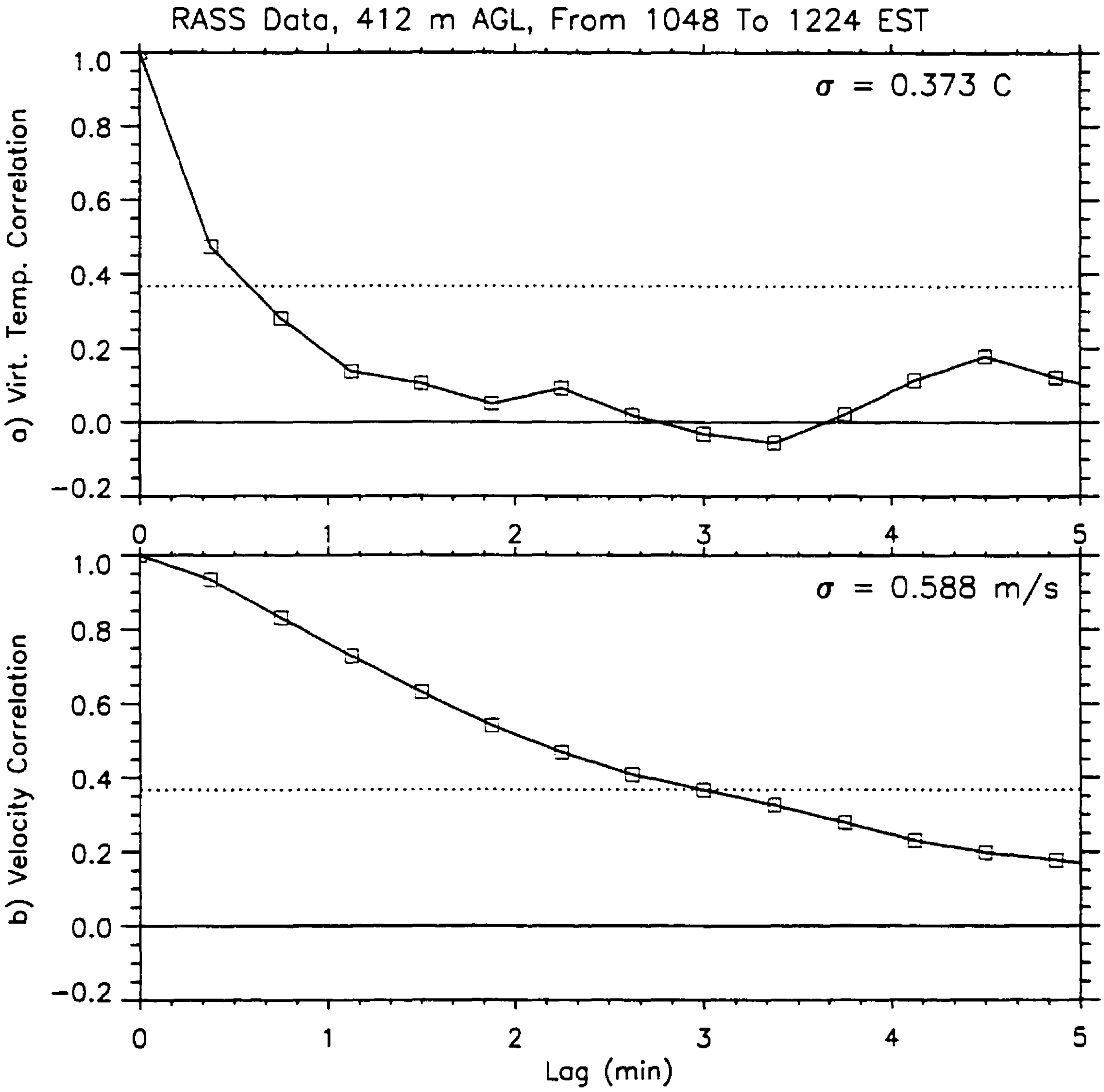

Figure 5.18: Virtual temperature (a) and vertical velocity (b) autocorrelation function for RASS data at 412 m AGL from 1048 to 1224 EST. Note the the corresponding stantard deviations, σ, in the upper righthand corners. The squares represent the discrete lags, 22 s apart, and the dotted line represents the $1/e$ value (0.3679) of the correlation.

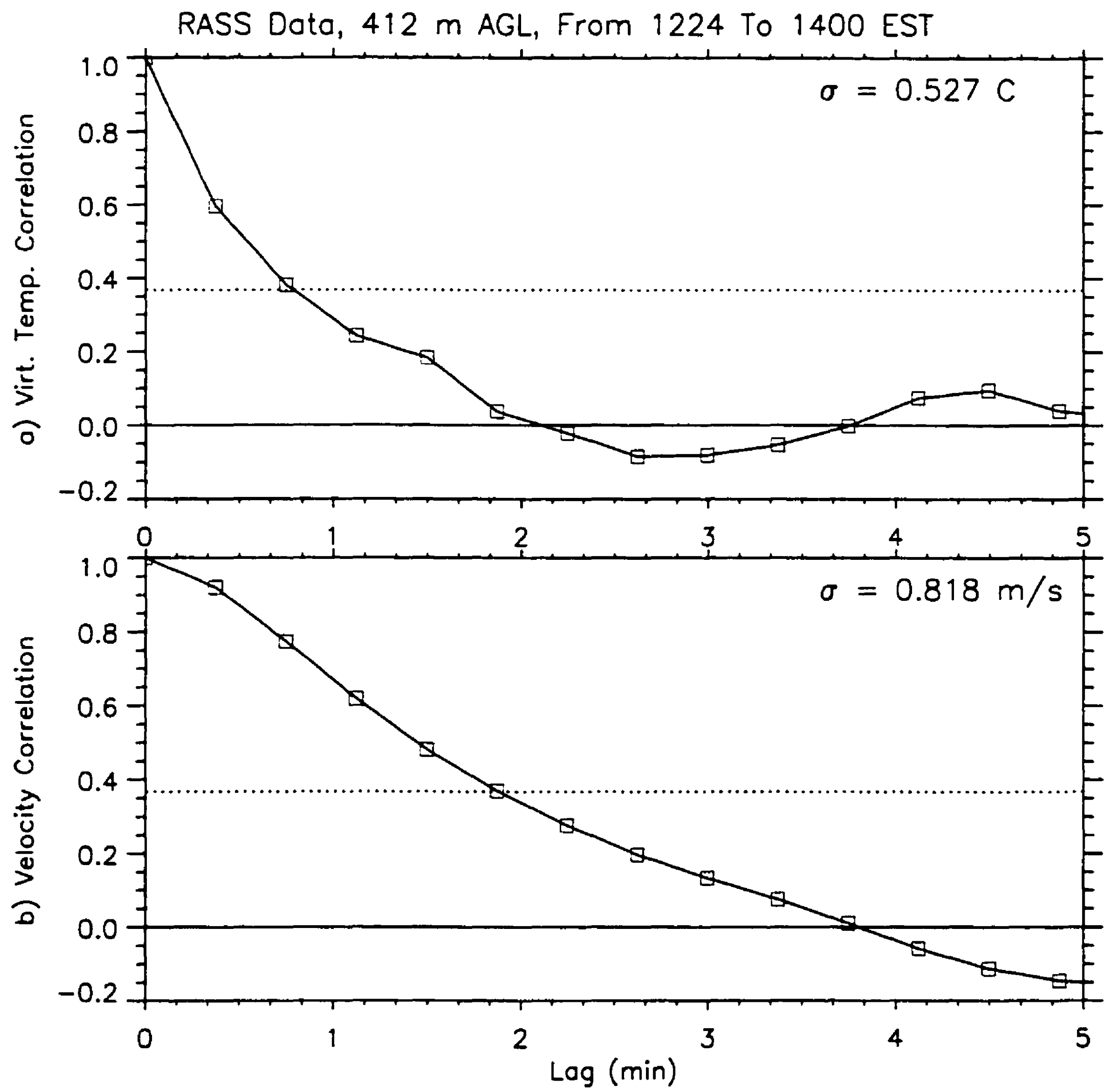

Figure 5.19: Same as Fig. 5.19, but for RASS data at 412 m AGL from 1224 to 1400 EST.

second-order moment of a power spectrum and is equal to half the spectral width squared ($\sigma_D^2 = (\mu_D/2)^2$, see Eq. 2.22 in section 2.1). Adding the spectral variance helps somewhat, but it should be noted that this quantity is not necessarily equal, or even proportional, to the vertical velocity variance of the small eddies. See section 2.1 for an analysis of the physical meaning of clear-air spectral moments. The dashed line should only be seen as a rough estimate of the total variance.

The RASS vertical air velocity variance profiles in Figs 5.20 and 5.21 are roughly what we would expect from Fig. 4.6, namely a smooth curve with a maximum at about $0.4z_i$. In Fig. 5.20, we estimate the CBL to be approximately 0.6 km deep, and we have a maximum velocity variance at about 0.25 km. In Fig. 5.21, the CBL grows from 0.6 to about 1 km over the averaging period, so z_i is not easy to evaluate. But if we take the average over the period, $z_i \approx 0.8$ km, then the maximum variance should be at about 0.3 km, which given the error bars, is approximately correct. Both variance profiles do not decrease as fast with height near the top of the CBL as the idealized profile in Fig 4.6, however. This may be due to weak returned signals at those altitudes, giving unreliable vertical air velocity measurements with an error component which increases the total variance. However, the lag 1 value of the autocovariance function is plotted specifically to avoid this effect. We can only conclude that if unreliable measurements are responsible, then the errors must be correlated to some degree, over one time lag or more. The aircraft variance profiles do not seem to follow the form of the RASS profiles. Indeed, the profile in Fig. 5.20 appears constant with height. Possible reasons for this difference will be discussed later, in chapter 6.

According to Stull (1988), vertical motions dominate the turbulent kinetic energy (TKE) in the mixed layer, which means that the vertical air velocity variance approximates the TKE, and the vertical velocity variance flux approximates the TKE flux. We expect the profiles in Figs. 5.22 and 5.23 to be positive everywhere within

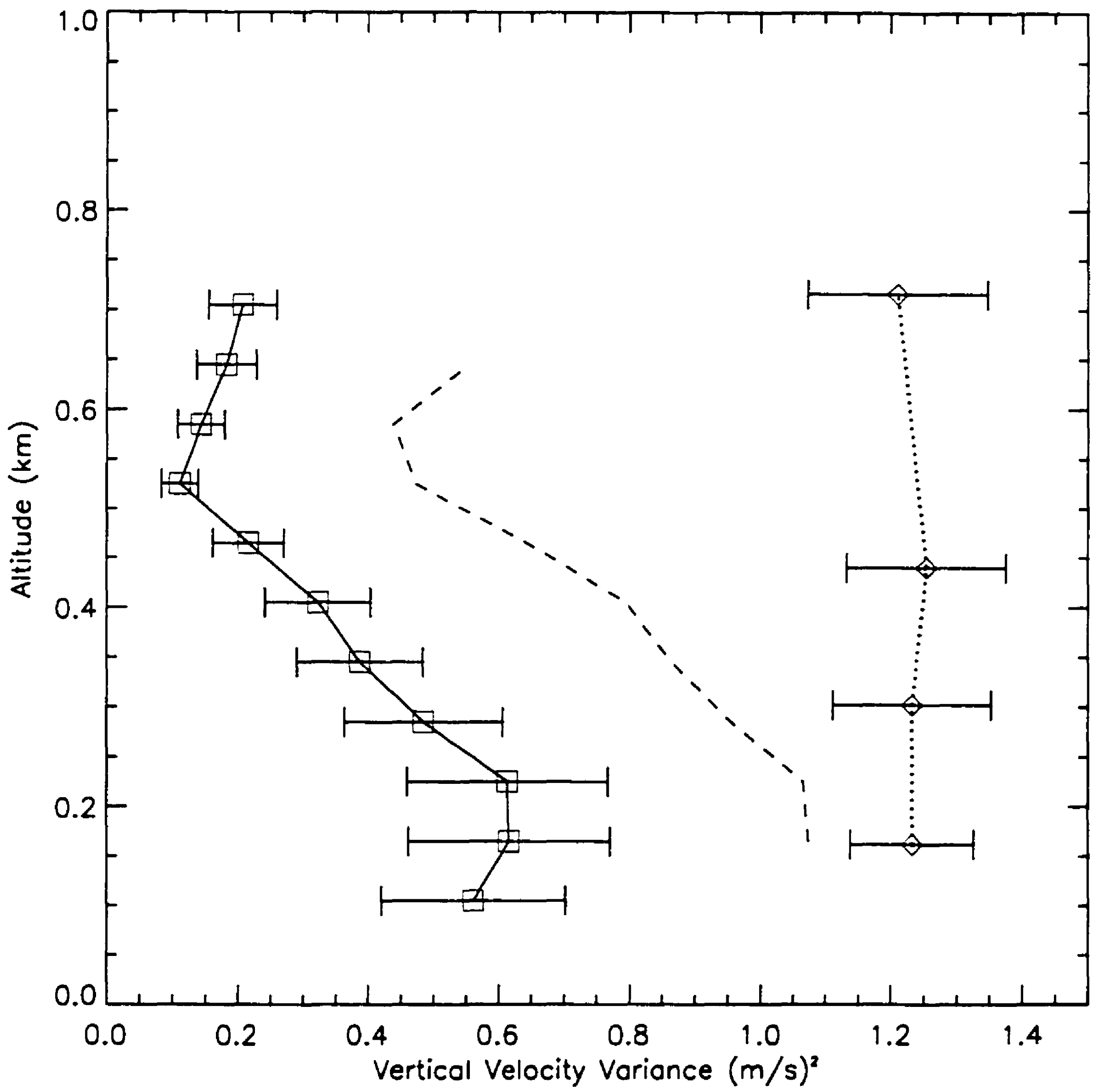

Figure 5.20: RASS (solid line with squares) and aircraft (dotted lines with diamonds) profiles of vertical air velocity variance, with error bars. The time period represented here is 1048 to 1224 EST for RASS, 1155 to 1235 EST for aircraft. The dashed line is the RASS vertical air velocity variance plus the average Doppler velocity variance of the clear-air spectra.

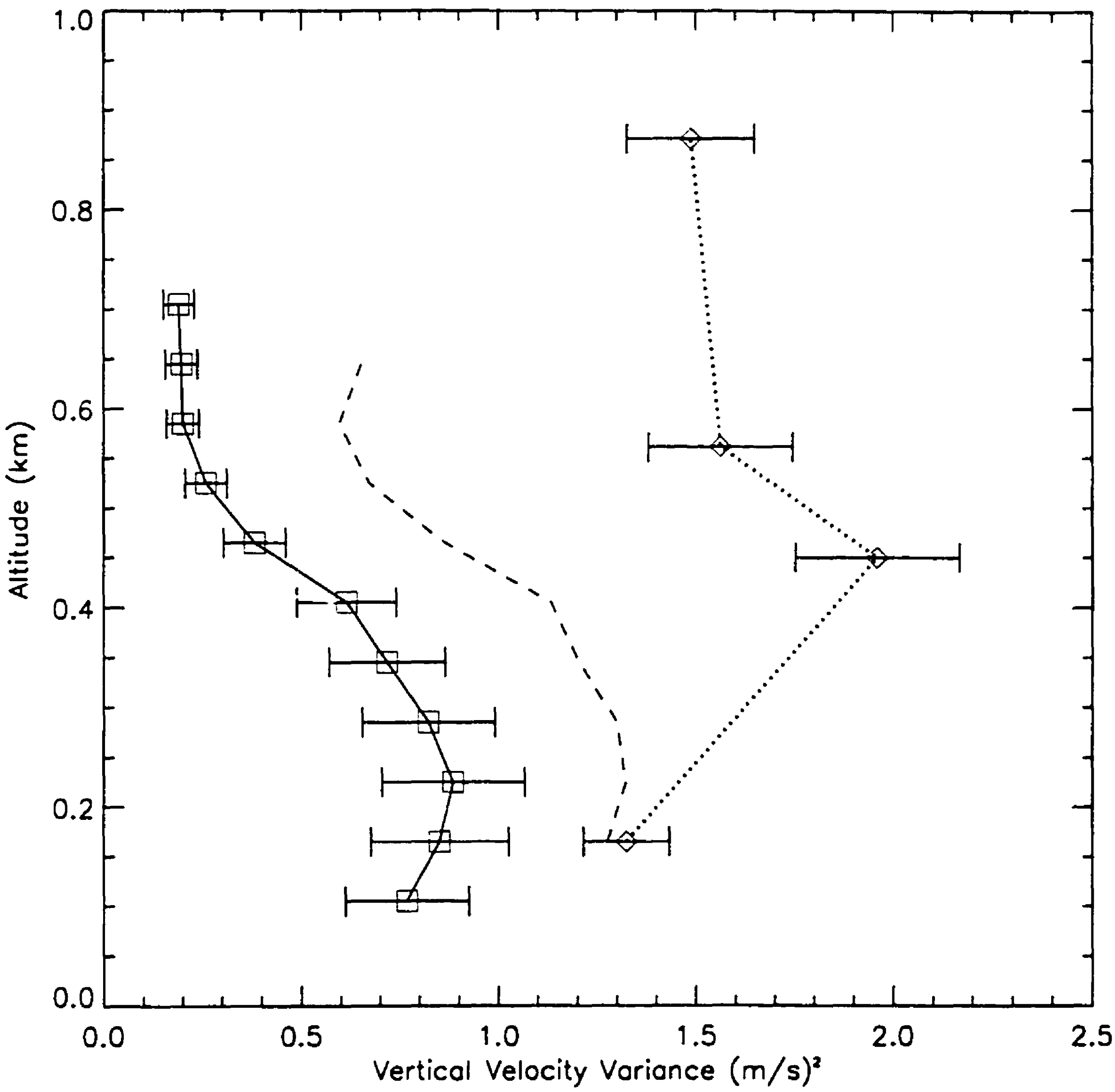

Figure 5.21: Same as in Fig. 5.20, but for the period 1224 to 1400 EST for RASS and 1247 to 1335 EST for aircraft.

the CBL and to reach a maximum around its middle, because we expect a growing CBL to transport TKE upwards. We also expect that the maximum of the vertical velocity variance profile corresponds to a convergence zone of the TKE flux. This is approximately what we observe for the RASS data, though while the aircraft profiles are positive, only the second profile has a convergence zone that corresponds to the variance maximum (compare Fig. 5.21 with Fig. 5.23).

Figures 5.24 and 5.25 show profiles of virtual heat flux from RASS and aircraft data. The RASS profile was obtained from time averages of traces as in Fig. 5.12(d) at different altitudes and times. For the aircraft data, the virtual heat flux was obtained from time averages of traces, as in Fig. 5.6(c), along flight tracks at different altitudes and times. Two RASS and aircraft profiles are plotted: Fig. 5.24 for aircraft runs between 1155 and 1235 EST and a RASS period from 1048 to 1224 EST; Fig. 5.25 for runs between 1247 and 1335 EST and RASS period from 1224 to 1400 EST. The evolution of the CBL is evident by marked difference between the RASS profiles. There is reasonable agreement between the later RASS profile and the aircraft profile between 0.15 and 0.5 km. Similarly, there is reasonable agreement between the early RASS profile and the aircraft profile between 0.25 and 0.5 km. Below 0.25 km, the early RASS heat flux values are less than 10 W/m^2, much less than the aircraft values of approximately 135 W/m^2. This may be due to the static stability of that layer at the start of the observation period, which inhibits convection and favors a negative heat flux if only small eddies are present (Garratt, 1992). Above 0.5 km, both RASS flux profiles decrease with height and become negative, as expected at the top of a CBL (Garratt, 1992). The aircraft flux values decrease only weakly above 0.5 km. From the RASS profiles, however, it would appear that the top of the CBL increases from about 0.55 (early profile) to 0.7 km (late profile). But in Fig. 5.9, we see that the CBL top increases from 0.6 to 1 km, mainly in the second half of the observation period. It should be noted that these profiles really represent the average heat flux profile over the averaging period. Therefore, the later RASS profile should show a

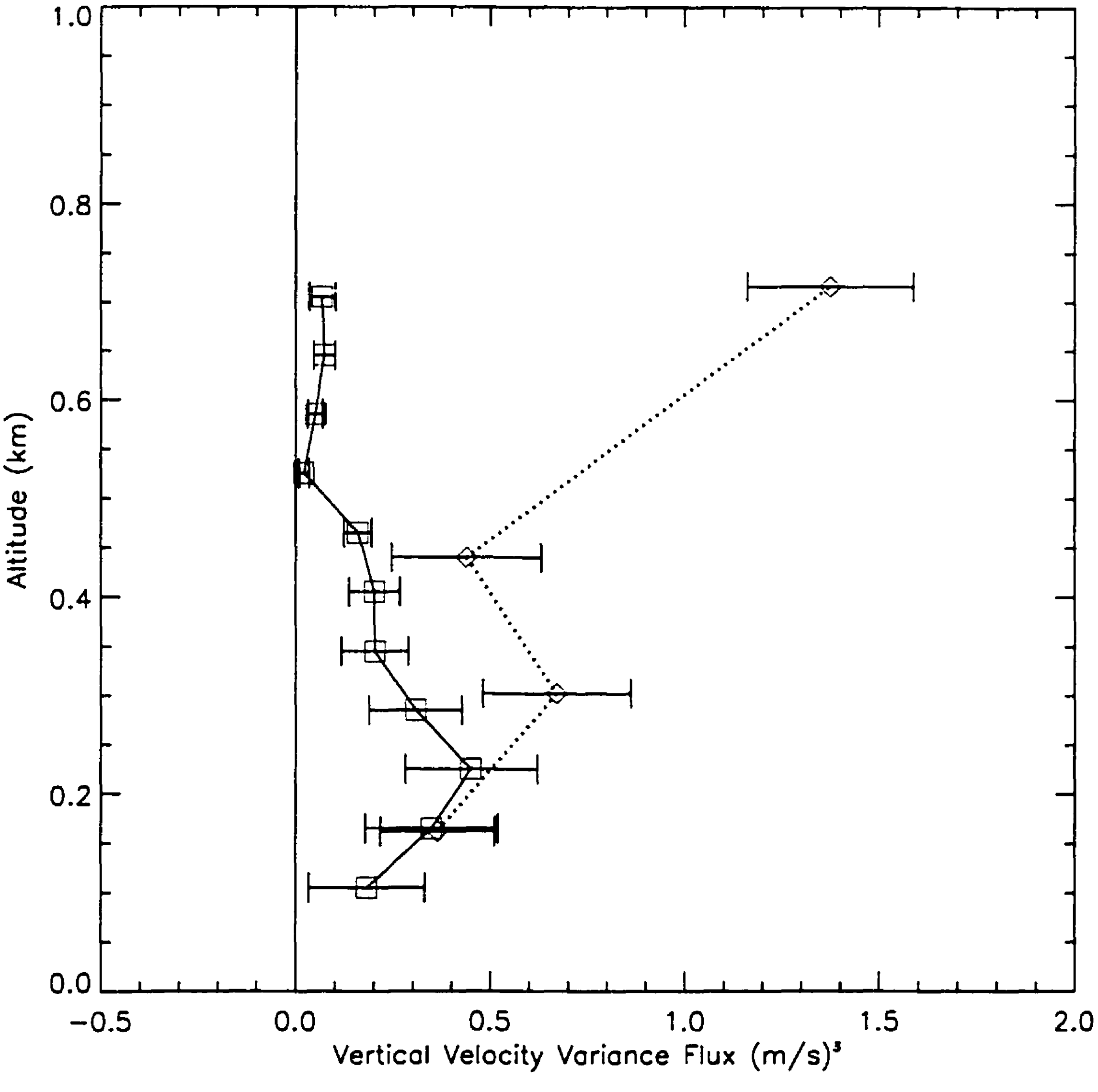

Figure 5.22: RASS (solid line with squares) and aircraft (dotted lines with diamonds) profiles of vertical air velocity variance flux, with error bars. The time period represented here is 1048 to 1224 EST for RASS, 1155 to 1235 EST for aircraft.

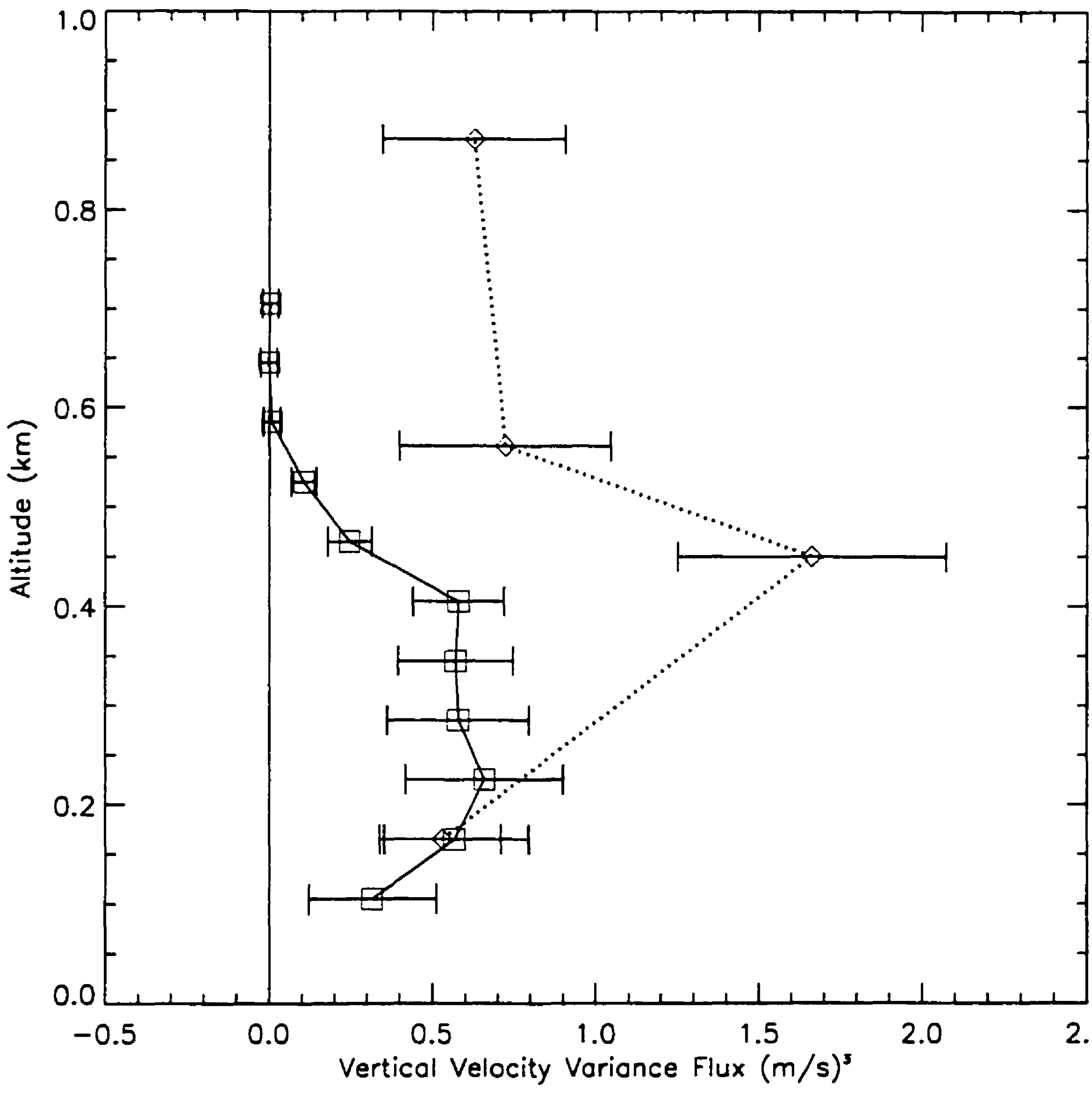

Figure 5.23: Same as in Fig. 5.22, but for the period 1224 to 1400 EST for RASS and 1247 to 1335 EST for aircraft.

CBL top halfway between 0.6 and 1 km – about 0.8 km. A CBL top at 0.7 km in the later profile is therefore acceptable considering the errors in the heat flux estimates due to their intermittency.

Temperature Correction for Turbulence

Figure 5.26 shows an example of clear-air and RASS Doppler power spectra for several heights. On the left-hand-side of the figure, we see an updraft extending from 172 to 532 m AGL, and a downward motion at 592 m AGL and higher. The change in vertical velocity creates a region of strong convergence from 472 to 592 m AGL. It is reasonable to assume that the shear produces small-scale turbulence, which manifests itself in the wide clear-air spectral widths, particularly at 532 m. The corresponding RASS spectrum at 532 m AGL is also wide, presumably caused by the turbulent eddies perturbing the acoustic wavefront. According to Peters and Angevine (1996), among others, the perturbation of the acoustic wavefront can only increase the measured RASS temperature. Therefore, rather than widening in both directions equally, as for the clear-air spectrum, the RASS spectrum widens towards higher acoustic velocities only. In addition, because the acoustic wave continues to propagate upwards after being perturbed, the temperature error also propagates upwards. We can see this effect in the RASS spectrum at 592 m. It is broader than the corresponding clear-air spectrum at the same altitude, suggesting that it is the turbulence at 532 m which caused its wide bimodal form. As far as heat flux is concerned, the exceedingly warm temperature at 592 m leads to a falsely positive temperature fluctuation where the vertical air velocity is negative, resulting in an erroneous negative heat flux. Other factors influence the width of the RASS spectra (temperature gradients, length of the Bragg-match region within the pulse volume, etc.), but we will assume, in this subsection, that only the turbulent eddies cause the asymmetrical spreading of the RASS spectra.

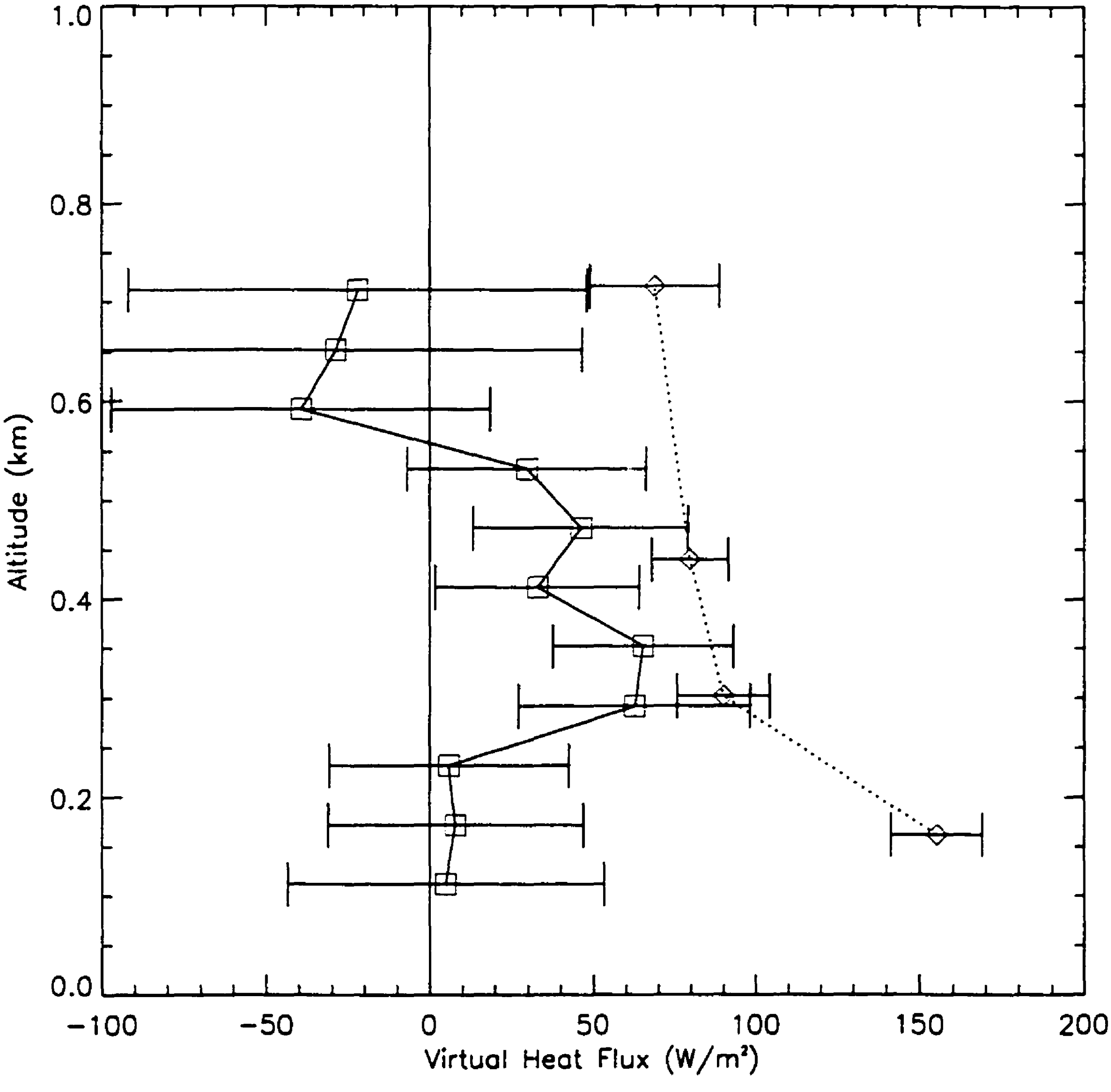

Figure 5.24: RASS (solid line with squares) and aircraft (dotted lines with diamonds) profiles of virtual heat flux ($\rho c_p (p_0/\overline{p})^{\kappa} \overline{w'T'_v}$, where ρ is the density of air, c_p is the specific heat capacity at constant pressure, and $\kappa \doteq 0.286$), with error bars. The time period represented here is 1048 to 1224 EST for RASS, 1155 to 1235 EST for aircraft.

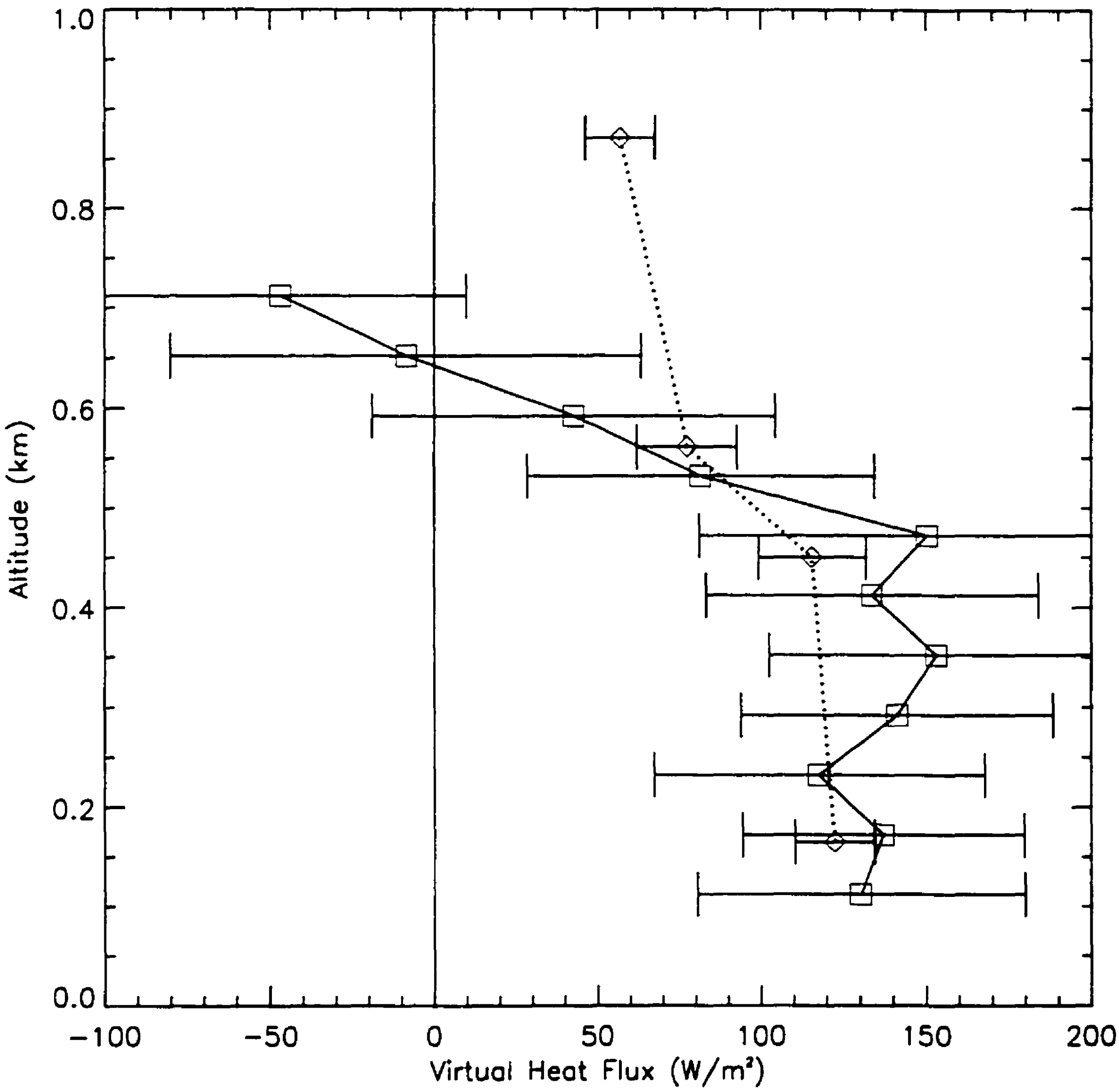

Figure 5.25: Same as in Fig. 5.24, but for the period 1224 to 1400 EST for RASS and 1247 to 1335 EST for aircraft.

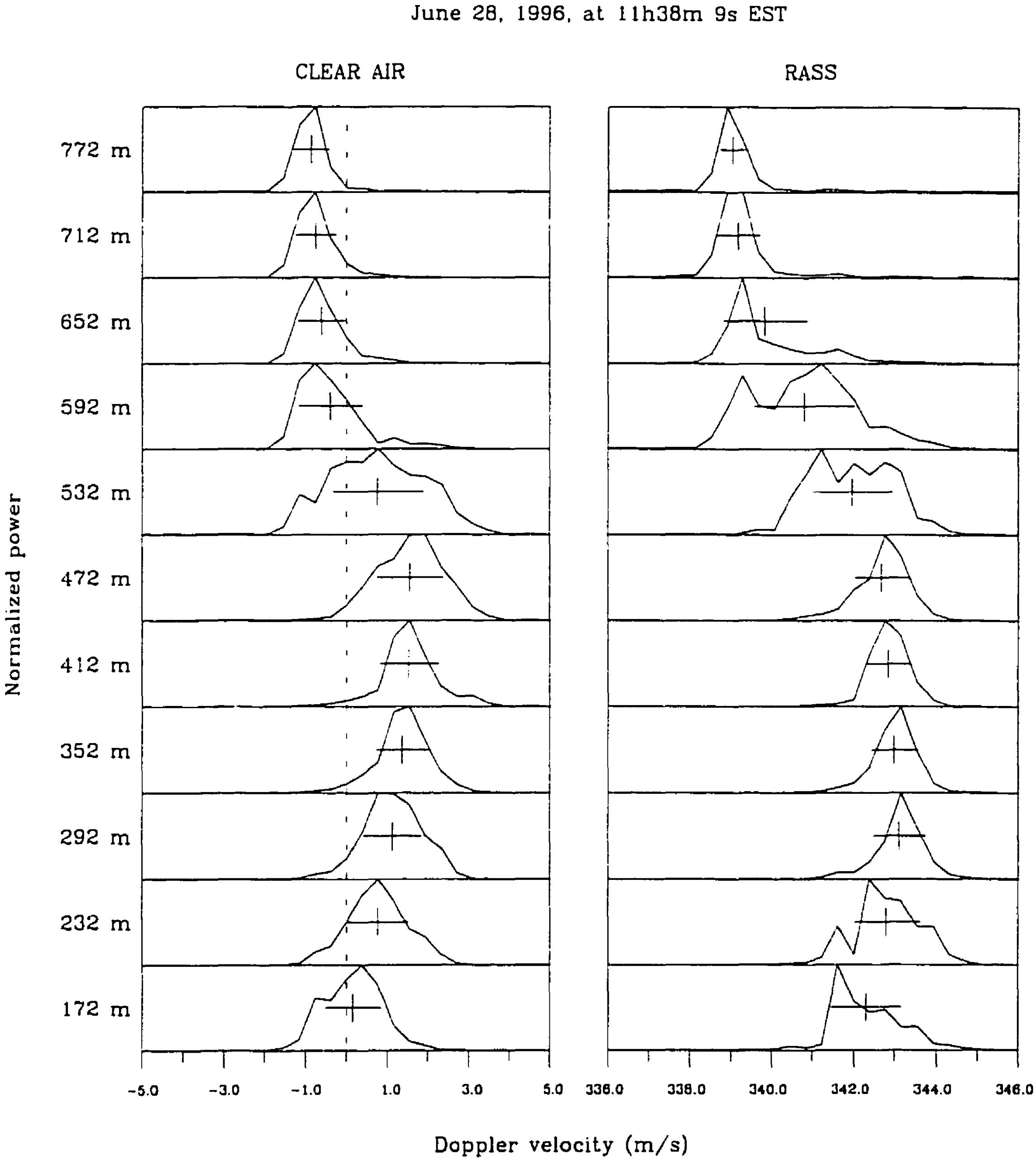

Figure 5.26: Clear-air (left) and RASS (right) spectra over St-Anicet, at 1138 EST. Note that the spectra are stacked as a function of altitude (in meters AGL). Also, the spectra are normalized so that the maximum of each spectrum reaches the top of its display rectangle. The vertical line in each spectrum denotes the mean Doppler velocity ($\overline{v}$), the horizontal line the spectral width ($2\sigma_v$).

Peters and Angevine (1996) propose a method for correcting the RASS temperature for errors due to turbulence. This method only applies to the first-order moments of the RASS spectra, not to the spectra themselves. The proposed turbulence temperature correction can be formulated as

$$\frac{\delta T}{T} = 0.483\ z^{6/5}\ k_a^{2/5} (C_a^{\prime 2})^{6/5} \tag{5.9}$$

where $\delta T/T$ is the relative temperature correction, z is the altitude in meters, k_a is the acoustic wavenumber (m^{-1}), and $C_a^{\prime 2}$ ($\mathrm{m}^{-2/3}$) is a weighted path average of the acoustic refractive index structure parameter

$$C_a^{\prime 2} = \frac{\int_0^z C_a^2(\zeta)(\zeta^{5/3})d\zeta}{\int_0^z (\zeta^{5/3})d\zeta} \tag{5.10}$$

where $C_a^2(z)$ is the local acoustic refractive index structure parameter, which is expressed as

$$C_a^2(z) = \frac{C_T^2(z)}{4T^2(z)} + \frac{C_v^2(z)}{c_a^2(z)} \tag{5.11}$$

where $C_T^2(z)$ and $C_v^2(z)$ are, respectively, the temperature and velocity structure parameters, $T(z)$ is the absolute temperature and $c_a(z)$ is the speed of sound. The velocity structure parameter, C_v^2, is taken to be proportional to the square of the clear-air spectral width, and C_T^2 is assumed to be negligible.

In other words, the turbulence temperature correction depends mainly on the altitude and a weighted integral of the square of the clear-air spectral width. The integration in Eq. 5.10 can be problematic since we only have a limited number of altitudes to work with, and the spectral width values may not be accurate. Figure 5.27 shows a comparison between the virtual temperature fluctuations at 532 m AGL, and the temperature correction, δT, due to turbulence, calculated from Eqs. 5.9 and 5.10. There is a definite correlation between the two quantities. In particular, we suspect that the large positive temperature fluctuations at 1230 and 1345 EST may be due to turbulence. Correspondingly, we see large spikes in the turbulence temperature correction time series at the same times. However, we also see that the temperature correction is about one order of magnitude too small to adequately correct the temperature fluctuations. A possible explanation would be that the method used is based on the assumption of homogeneous turbulence with no coherent large-scale structures. But in a CBL, the turbulence is not homogeneous but rather depends on large-scale coherent structures, such as thermal plumes. The assumption may therefore cause an underestimation of the temperature correction. Another source of error may be our method of estimating the spectral widths (integration over the useable portion of the clear-air spectrum). Perhaps other methods (such as the log-fitting of a Gaussian function to the clear-air spectrum (Gossard *et al.*, 1998)) might yield better results.

Figure 5.28 shows the effect of the temperature correction for turbulence on the virtual heat flux profile in Fig. 5.25. Overall, there is a slight reduction in the magnitude of the heat flux at all altitudes. This is consistent with the picture mentioned above, where the turbulence causes a warming of the temperature fluctuations. Correcting for turbulence would reduce the magnitude of the temperature fluctuations, and consequently the heat flux. However, when we compare with Fig. 5.25, we see that the effect of the correction falls well within the error bars of the heat flux estimates. This does not necessarily mean that the effect of turbulence itself on the heat flux estimate is negligible, but only that our method to correct for it is inadequate. However, the method by Peters and Angevine is concerned with correcting for the systematic error on the mean temperature measurements due to turbulence, not with the cross-correlation of temperature with the vertical air velocity.

5.3.2 McGill Data

In this subsection, we perform the same analysis on the McGill data as on the St-Anicet data. However, given the necessity to treat the McGill data, we must first calibrate ROSPA so as to obtain the best possible performance.

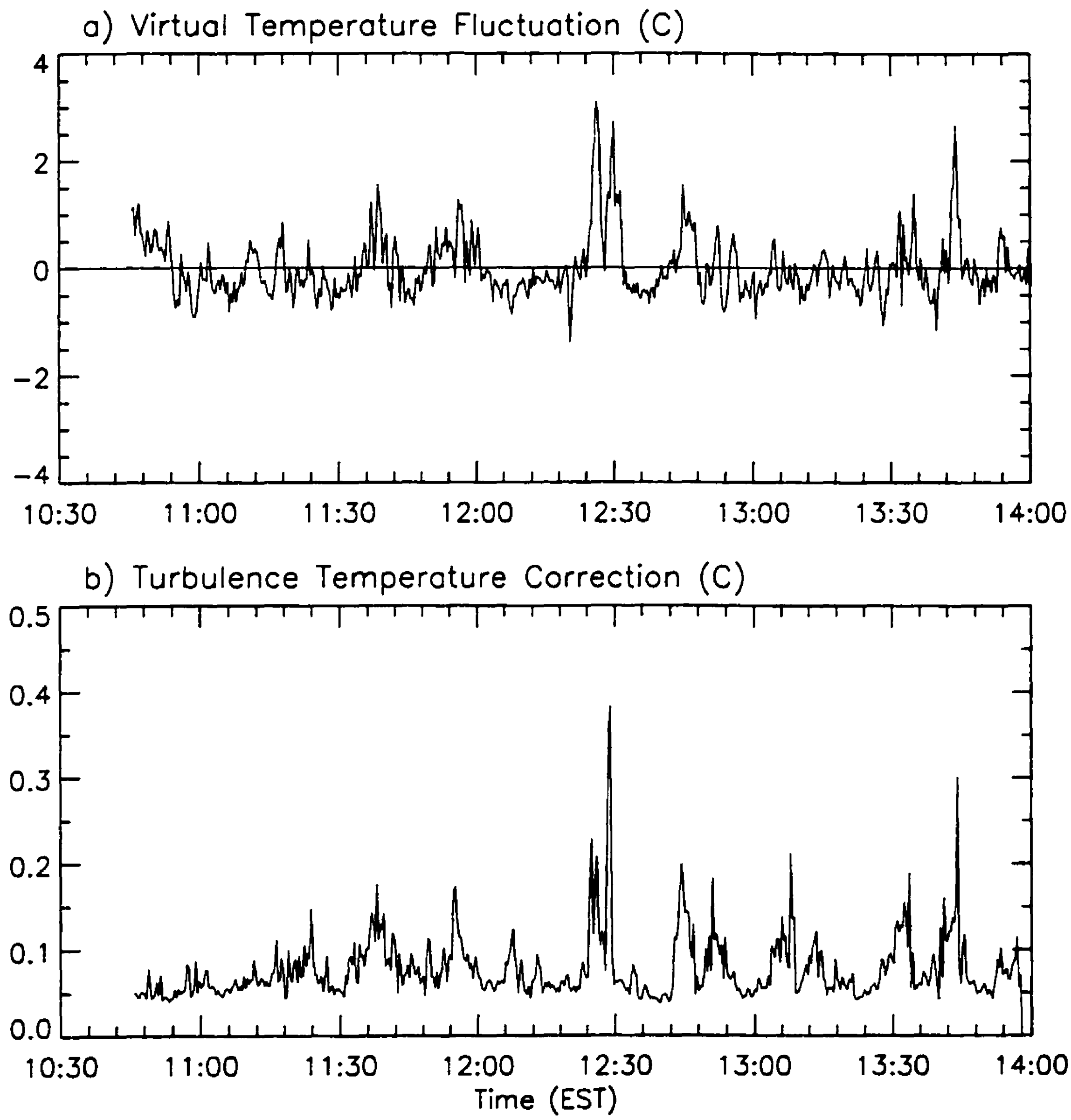

Figure 5.27: The virtual temperature fluctuation (a) and the turbulence temperature correction (b) time series for St-Anicet, at 532 m AGL.

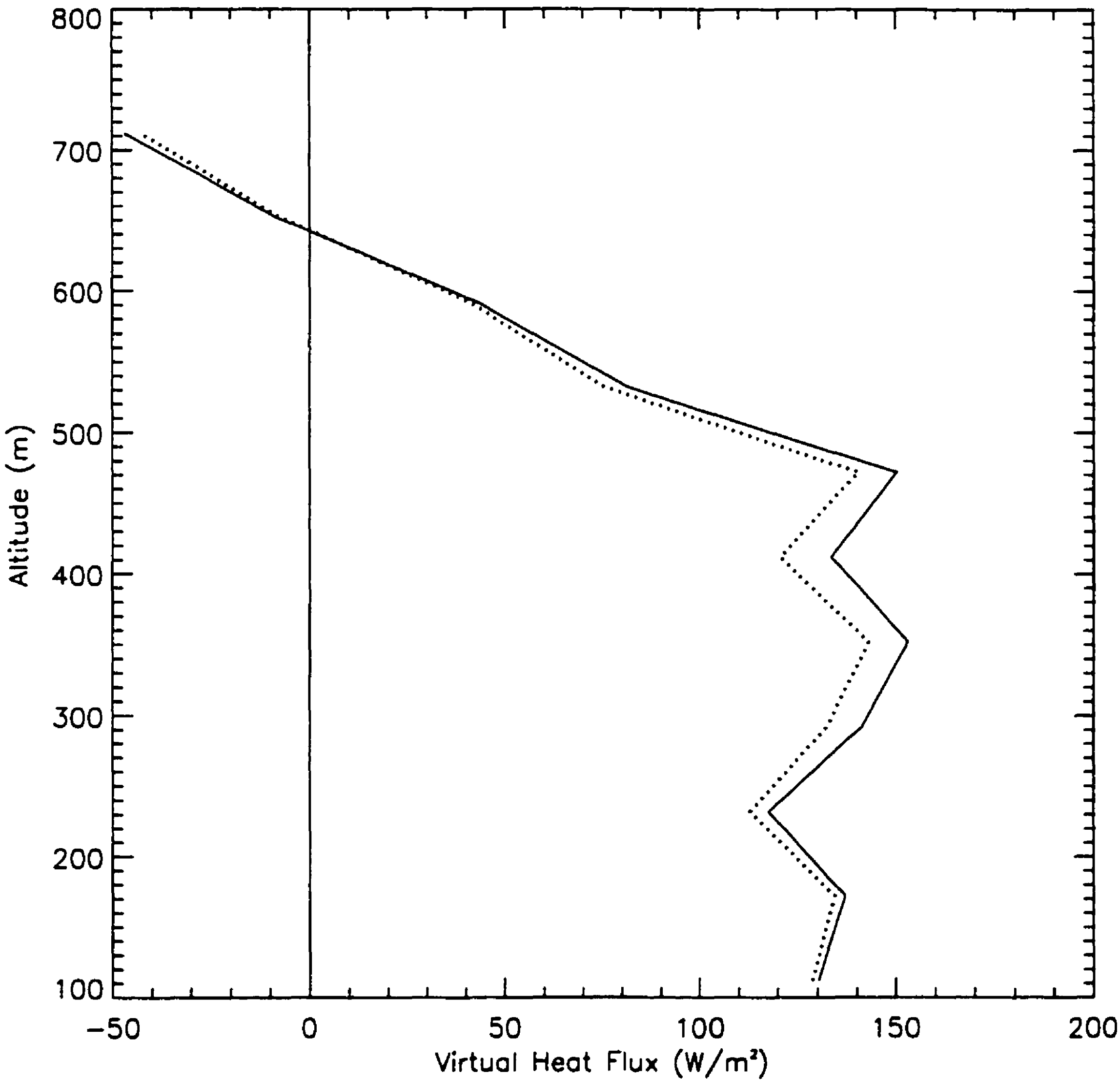

Figure 5.28: The RASS virtual heat flux profiles from 1224 to 1400 EST (as in Fig. 5.25), with (dotted line) and without (solid line) turbulence temperature corrections.

Calibration of ROSPA

Before we can examine the McGill data, we must first determine the most appropriate choice of the thresholds required by ROSPA. The threshold values will be chosen according to two criteria. The first, called the RASS correlation criterion, is based on the correlation between the treated vertical air velocity time series and the raw RASS velocity time series. A high correlation is expected if the treated velocities are accurate. The second criterion is the degree to which the algorithm leaves good vertical air velocity data, like the St-Anicet data, unchanged. This will be measured by the correlation between the treated and untreated time series of the good data, a correlation of 1 indicating no change. It should be stressed, however, that the first criterion is more important, particularly for measurements taken in the mixed layer of a CBL. This is because the RASS velocity fluctuations due to temperature fluctuations are small compared to those due to vertical air velocity fluctuations. Therefore, if the RASS data is good (no power drop-outs, no RFI, etc...), we would expect the accurate vertical air velocity time series to closely resemble the RASS velocity time series, and we would expect a good correlation between them. We assume, then, that any improvement in the RASS correlation criterion implies better vertical air velocity estimation, and is not fortuitous. Also, we can avoid fixing the threshold values once and for all, but rather adjust them for every new dataset. Thus, in the event of clean data, the RASS correlation criterion would allow threshold values high enough to allow the good data through ROSPA unaltered, thereby satisfying the second criterion automatically.

In order to explore the RASS correlation criterion, we examine it mathematically to find an expression for the best possible correlation. We begin by describing the main features of the RASS signal (at a fixed altitude):

$$R[i] = c[i] + w[i] + \epsilon[i] \tag{5.12}$$

where $R[i]$ is the RASS velocity time series, $c[i]$ the speed of sound in still air as a function of the time index i, $w[i]$ the vertical air velocity, and $\epsilon[i]$ the error on the RASS measurement, which we assume has the characteristics of white noise. It is useful to partition the speed of sound into two components:

$$c[i] = m[i] + f[i] \tag{5.13}$$

where $m[i]$ is an average speed of sound which may change over the observing time because of the overall warming or cooling of the boundary layer, over time scales of at least an hour, and $f[i]$ is the short-term fluctuations due to temperature fluctuations associated mainly with thermals. Over a period of three hours, we assume that the trend can be adequately expressed as a quadratic, $m[i] = a + bi + c(i)^2$. In addition, we have a profiler-measured time series of the air velocity which we assume is clutter free:

$$P[i] = w[i] + \eta[i] \tag{5.14}$$

where $w[i]$ is the vertical air velocity, and $\eta[i]$ is the error on the profiler measurement, assumed to be white noise. All the statistics needed for the correlation will be estimated using a time average over the N points of the time series, denoted by an overbar. The average RASS measurement is then $\overline{R} = \overline{m}$, where we have assumed, without loss of generality, that $\overline{f} = \overline{w} = \overline{\epsilon} = 0$. Similarly, the average profiler air measurement is $\overline{P} = 0$, assuming $\overline{\eta} = 0$. The variance of the RASS time series can be decomposed as

$$\sigma_R^2 = \sigma_m^2 + \sigma_f^2 + \sigma_w^2 + \sigma_\epsilon^2 + 2\overline{mf} + 2\overline{wf} + 2\overline{mw} \tag{5.15}$$

where we have assumed that ϵ is independent of m, f, and w. However, we will neglect the terms $2\overline{mf}$ and $2\overline{mw}$, assuming that the average speed of sound, $m[i]$, is approximately constant over the decorrelation times of f and w, so that

$$\sigma_R^2 = \sigma_m^2 + \sigma_f^2 + \sigma_w^2 + \sigma_\epsilon^2 + 2\overline{wf}. \tag{5.16}$$

Similarly, for the air signal, we can state

$$\sigma_P^2 = \sigma_w^2 + \sigma_\eta^2 \tag{5.17}$$

where we have assumed that η is independent of w. And using Eqs. 5.12 and 5.14, we can find the joint moment

$$\overline{PR} = \overline{wf} + \sigma_w^2 \tag{5.18}$$

where we have assumed that $\overline{\epsilon\eta} = \overline{m\eta} = \overline{f\eta} = 0$. It is now convenient to introduce the time series $\gamma[i] = f[i] + w[i]$, and the corresponding variance σ_γ^2. Also, we will need to introduce the correlation between f and w: $r_H = \overline{wf}/(\sigma_w \sigma_f)$, where the subscript H denotes its relationship to the heat flux. Finally, let $\beta_{x|y} = \sigma_x/\sigma_y$ denote the ratio of the standard deviations of the quantities x and y. Using these conventions and a bit of algebra, we can write an expression for the correlation $r = \overline{PR}/(\sigma_P \sigma_R)$:

$$r = \left[\frac{1}{\sqrt{(1+\beta_{\eta|w}^2)}}\right]\left[\frac{1}{\sqrt{(1+\beta_{m|\gamma}^2+\beta_{\epsilon|\gamma}^2)}}\right]\left[\frac{1+r_H\beta_{f|w}}{\sqrt{(1+2r_H\beta_{f|w}+\beta_{f|w}^2)}}\right] \tag{5.19}$$

$$= H(\beta_{\eta|w})G(\beta_{m|\gamma}, \beta_{\epsilon|\gamma})F(\beta_{f|w}, r_H) \tag{5.20}$$

where $0 < H(\beta_{\eta|w}) \leq 1$ represents the loss of correlation due to the error in the profiler measurements, $0 < G(\beta_{m|\gamma}, \beta_{\epsilon|\gamma}) \leq 1$ represents the loss of correlation due to the trend in the RASS time series and the error on the RASS measurements, and $-1 \leq F(\beta_{f|w}, r_H) \leq 1$ is the correlation between $\gamma = f + w$ and w. In the mixed layer, we have $0 < \beta_{f|w} < 1$, and if $r_H = 1$, then $F = 1$; if $r_H = -1$, $F = 1$; and F reaches its minimum at $r_H = -\frac{1}{2}\beta_{f|w}$, where $F = 1 - \frac{1}{2}\beta_{f|w}^2$. Therefore, if $\beta_{f|w} = 0.35$, a reasonable value for the mixed layer, then $0.938 < F \leq 1$, depending on the value of r_H. Taking into account H and G then, a correlation of $r \approx 0.9$ is probably the most we can reasonably expect in the mixed layer of a CBL.

Figure 5.29 demonstrates how well the RASS correlation criterion serves as an indicator of the accuracy of the vertical air velocity retrieval. The solid lines are the correlation values between the untreated and treated vertical air velocities for the St-Anicet data. They indicate how well the TMIN7 filter recovers the original vertical air velocities, as a function of the spectral threshold. The correlation is very nearly unity for spectral threshold values greater than 30 dB, which means that at this level the TMIN7 filter does not substantially modify the spectral data. The slight initial drop in correlation is due to the fact that as the spectral threshold value increases beyond 0 dB, the resulting vertical air velocity time series does not change its overall shape, but rather becomes noisier. This means that the joint moment $\overline{PR}$ does not change, while σ_η^2 increases, which causes a slight reduction in correlation. The dashed lines in Fig 5.29 are the correlation values between the untreated RASS signal and the treated air signal. We see a reasonably good correspondence between the solid and dashed lines, particularly for the lowest altitude. This may be due to the action of turbulence and winds on the RASS measurements, which affect the higher range gate more (see, for instance, Angevine and Ecklund (1994)). Another factor could be the decrease of the signal-to-noise ratio with height of the air signal. Together, these factors can help explain why at 532 m AGL, the RASS correlation criterion (dashed line) starts at approximately 50% and attains a plateau at about 10 dB, while at 172 m AGL, it starts at 75% and attains a plateau at about the same level as the solid line (30 dB). Therefore, it seems that when choosing an appropriate spectral threshold level, we should favor the RASS correlation criterion at the lower range gates.

Figure 5.30 shows the RASS-profiler correlation for various values of the spectral threshold of a TMIN7 filter, with (solid line) or without (dashed line) an XMED5 filter afterwards, for the McGill data. Without the XMED5 filter, the correlations fall rapidly after reaching their maxima which occur at 10 dB for 225 m and at 5 dB for 405 m and 585 m. With the XMED5 filter, the correlation seems much less sensitive to the choice of threshold, though peaking at about the same threshold values as before. The initial increase in correlation is because at the low threshold values, we allow more and more good spectral power values while still exluding bad values. The subsequent decrease in correlation arises because at those threshold values we have already allowed most or all of the good spectral power values, and are beginning to include bad values of ever increasing severity, as we saw in subsection 3.2.2 on the

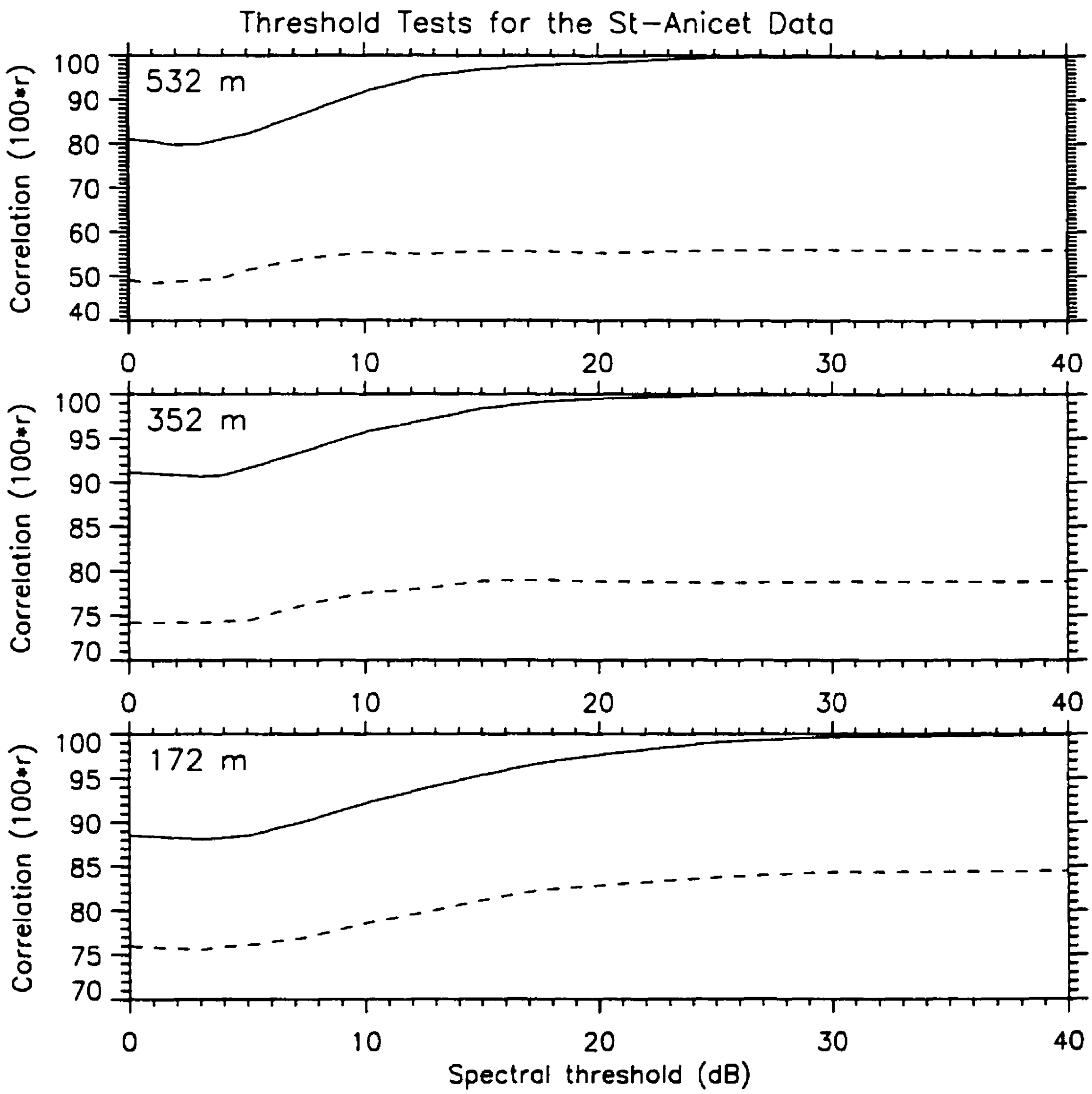

Figure 5.29: The correlation ($\times 100$) between the untreated RASS data and the profiler data treated by a TMIN7 filter (dashed line) and between the untreated and treated profiler data (solid line) for the St-Anicet dataset, as a function of the spectral threshold and for three altitudes (bottom graph: 172 m AGL; center: 352 m AGL; top: 532 m AGL).

threshold minimum filter. The consistently better result of the combined TMIN7-XMED5 filter shows the ability of the median filter to select good Doppler velocity values. Indeed, at the 225 and 405 m levels, the TMIN7-XMED5 filter almost reaches 90% correlation, the highest we can reasonably expect. Figure 5.30 suggests that the best spectral threshold values would be between 5 and 10 dB.

The performance of the threshold median on the St-Anicet data is shown in Fig. 5.31. As expected from the definition of the threshold median (subsection 3.2.7), we have a subset of points ($\approx 65\%$) that are always accepted as the normalized threshold (ν) tends towards zero. Most of the missing points are recovered at $\nu = 1$, and essentially all are recovered at $\nu = 2$. We will therefore set $\nu = 2$ in what follows to insure that good Doppler velocity values are accepted, thereby satisfying the second criterion mentioned previously. As we will see, the McGill data have a greater time scale than the St-Anicet data, which implies that the normalized variability within a 5-point window should be less and that the TMED5 filter should be able to accept more good points.

Structure and Evolution of the CBL

Figures 5.32 and 5.33 show, respectively, the range normalized clear-air reflectivity over McGill before and after the continuous RASS period. Figure 5.32 shows strong growth of the CBL beginning as early as 0900 EST, and continuing until the end of the plot, when it reaches a height of approximately 1.5 km. This is in sharp contrast with the CBL over St-Anicet (Fig. 5.9), which only begins to grow significantly after 1230 EST. Figure 5.33 shows a CBL approximately 1.8 km high at 1530 EST, remaining relatively constant until 1700 EST, when it begins to descend. Figure 5.34 indicates a more or less uniform warming of the virtual potential temperature of the CBL during the RASS observing period, with a mildly stable layer extending from the ground up to about 0.3 km AGL, and a broad maximum of potential temperature between 0.5 and 0.7 km AGL. The temperatures were corrected using the vertical air

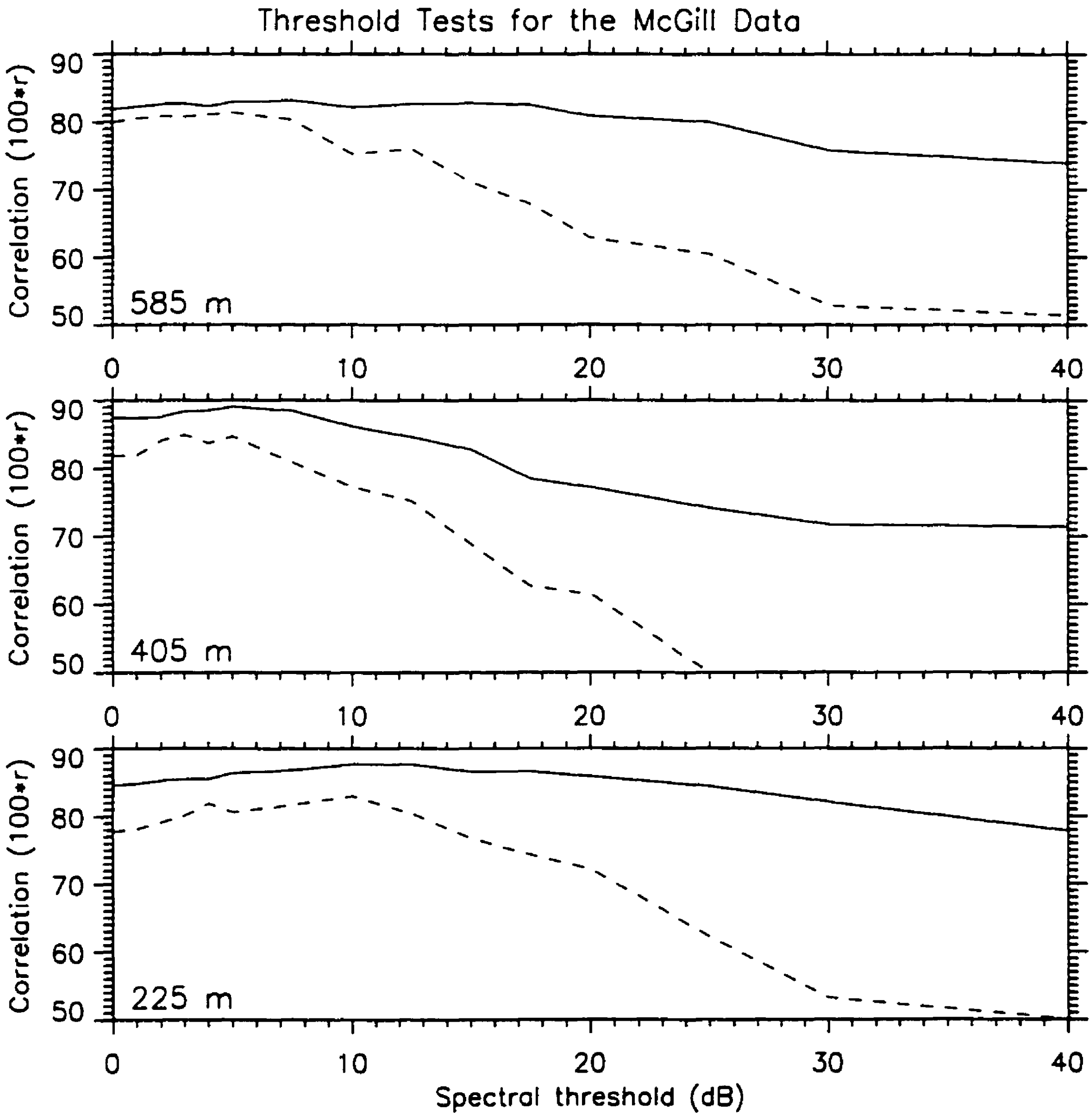

Figure 5.30: The correlation ($\times 100$) between the untreated RASS data and the profiler data treated by a TMIN7 filter only (dashed line) and by a TMIN7 filter followed by a XMED5 filter (solid line), as a function of the spectral threshold and for three altitudes (bottom graph: 225 m AGL; center: 405 m AGL; top: 585 m AGL), for the McGill data.

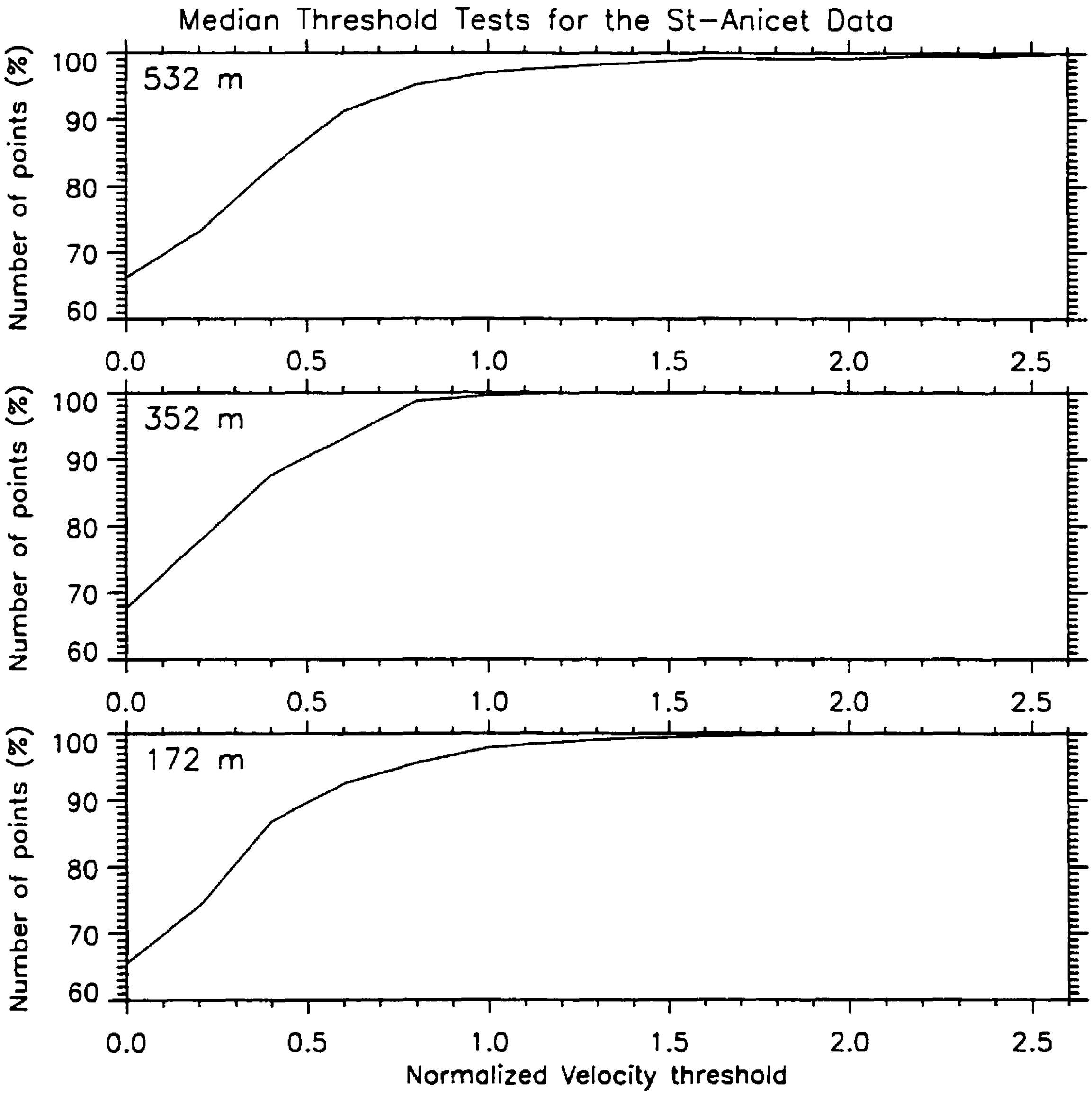

Figure 5.31: The number of points (in percentage) of the vertical velocity data for St-Anicet, that are accepted by the threshold median TMED5 as a function of the normalized velocity threshold (bottom: 172 m AGL; middle: 352 m; and top: 532 m).

velocity fluctuations shown in Fig. 5.35 prior to the half-hour running average and median filter. The vertical velocity fluctuations in Fig. 5.35, obtained using a TMIN7-XMED5 filter with a spectral threshold of 5 dB and a TMED5 filter with $\nu = 2$. They demonstrate the same sort of vertical structure as for the St-Anicet data, except that the plumes are taller, more intense and longer lasting. The convection appears well developed over the entire observing period. From all these observations, we conclude that the CBL grew more or less constantly from 1.5 to 1.8 km, and possessed more or less stationary statistics, over the continuous RASS observation period. Turbulent statistics will therefore be compiled over the entire period. Contrary to the St-Anicet data, no segmentation is necessary.

Data and Heat Flux Analysis

Here, we will use the same data analysis methods used for the St-Anicet data, while bearing in mind the possible effects of ROSPA on the results. The appearance of the vertical air velocity retrieval is evident in Fig. 5.36. There is an obvious correlation between the uncorrected virtual temperature (curve a) and the treated vertical air velocity (curve b), 89% in fact, particularly with respect to the major features. It is interesting to compare the strength of the convection over McGill with the rather weak convection at St-Anicet. The corrected virtual temperature in curve (c), along with the least-squares quadratic fit (smooth line in (c)), show a long-term warming of about 2° C over the $3\frac{1}{2}$ hour period. The fluctuations in the uncorrected temperature time series, as much as 7° C in magnitude, are reduced to about 1° C on average in the corrected virtual temperature time series. However, curve (c) still shows important temperature fluctuations, as much as 3-4° C in magnitude, much stronger than in the St-Anicet data. The urban CBL is usually driven by a greater surface heat flux than the rural CBL, which is expected to create greater temperature fluctuations in the urban CBL. Nevertheless, we suspect that imperfect retrievals of the vertical air velocities, along with errors on the RASS measurements caused by turbulence and

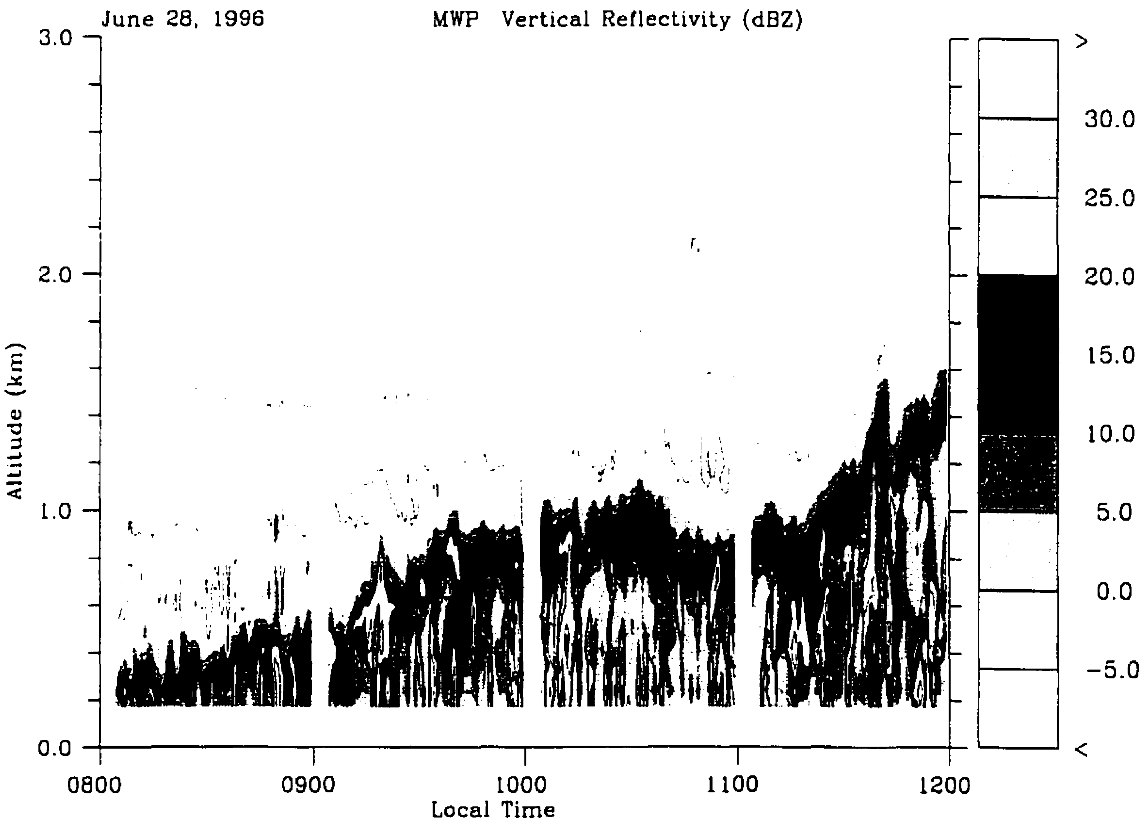

Figure 5.32: Time-height plot of the range normalized clear-air reflectivity over McGill on June 28, 1996, for the four hour period preceding the continuous RASS measurements.

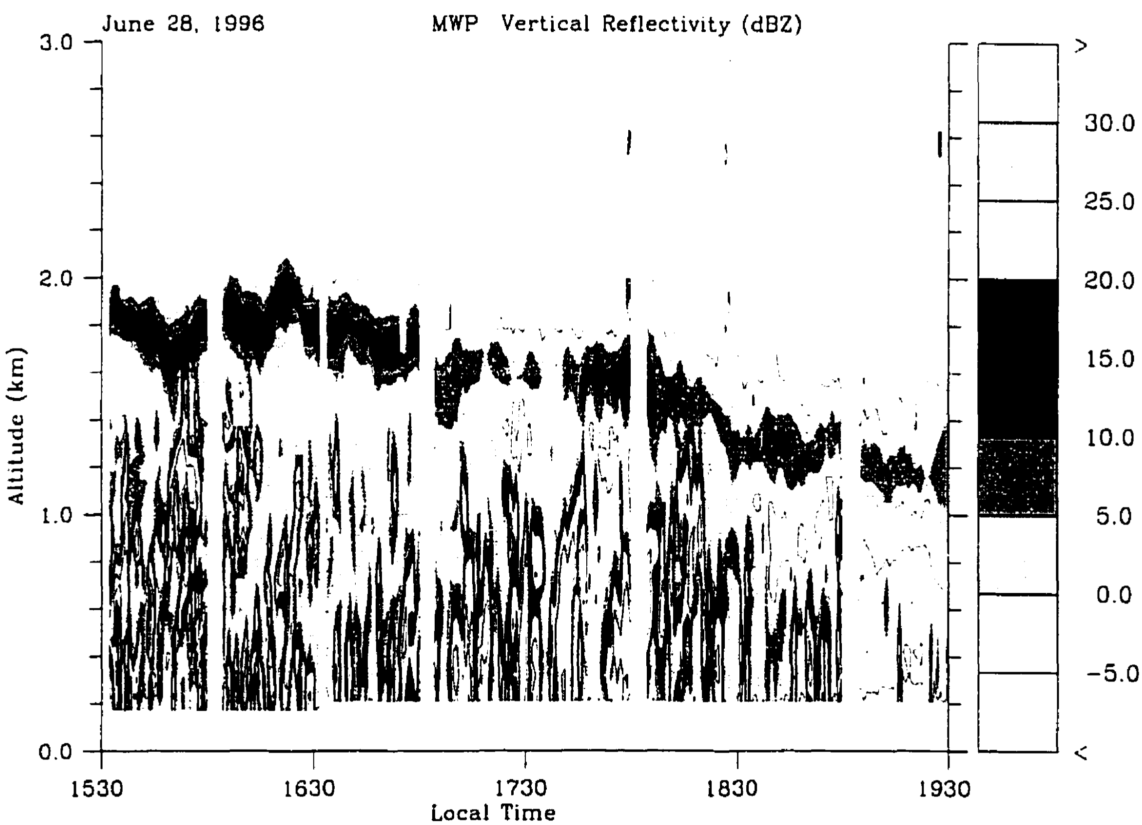

Figure 5.33: Time-height plot of the range normalized clear-air reflectivity over McGill on June 28, 1996, for the four hour period following the continuous RASS measurements.

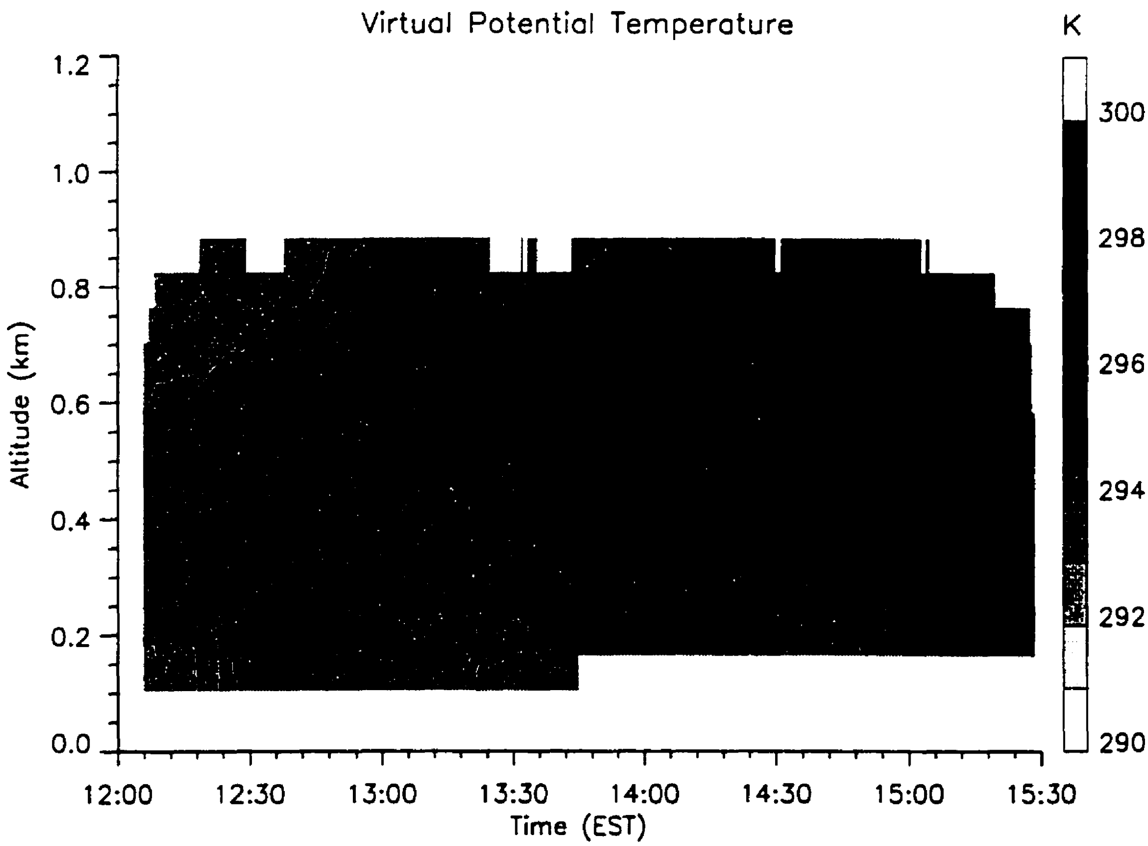

Figure 5.34: Time-height plot of the virtual potential temperature over McGill on June 28, 1996.

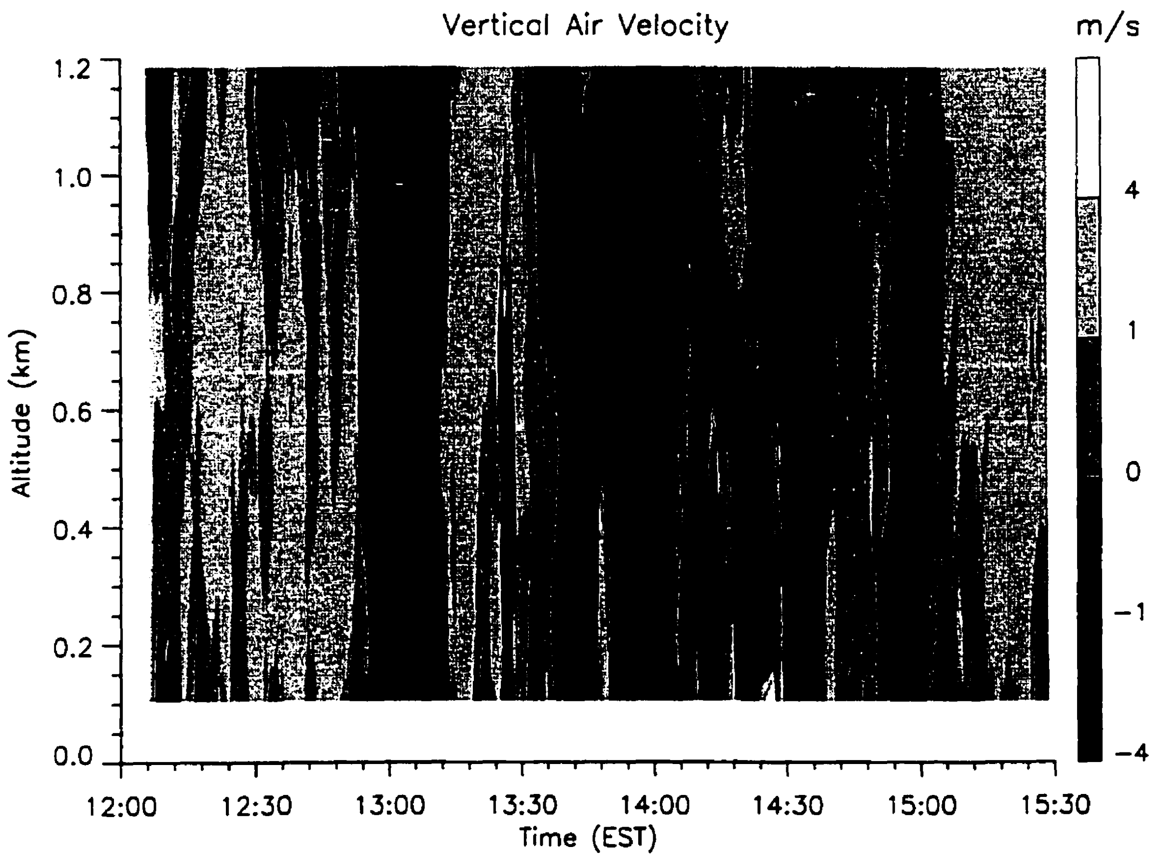

Figure 5.35: Same as in Fig. 5.34, but for vertical air velocity. Note that the solid line is the zero velocity contour.

winds, are also partly responsible for the noisy appearance of the corrected temperature time series. We presume that this noise is also responsible for the appearance of the virtual heat flux trace (curve d). Instead of the intermittent bursts of positive heat flux observed in the St-Anicet data, we have almost continual bursts of heat flux in either direction. While the heat flux trace might actually be more turbulent over the McGill site, we suspect this is due mainly to the errors in the vertical air velocity and corrected temperature time series.

Figure 5.37 is a time-height contour plot of the virtual temperature fluctuations, like the ones shown in Fig. 5.36(c), while Fig. 5.38 is a contour plot of the virtual heat flux, the same quantity in the trace in Fig. 5.36(d). In these figures, we see an overall vertical structure of the temperature fluctuations and heat flux that is consistent with strong convection. Note, however, that there is a slight predominance of negative heat flux between 0.4 and 0.6 km AGL over the observing period. Figure 5.39 is a time-height plot of the virtual heat flux quadrants. The structure of descending cool air separated by thin walls of rising warm air, visible in the St-Anicet data, is not evident here. The updrafts to not appear to be predominately warm, just as the downdrafts do not seem predominately cool. This could be due to the noise in the temperature fluctuations mentioned earlier, which would overwhelm the real temperature fluctuations responsible for the heat flux. There could also be a question of scale involved, namely that the CBL height is about 1.65 km AGL and that the timescale is longer than at St-Anicet. Therefore, we do not see the entire vertical extent of the CBL as we did in the St-Anicet data, and the observing time period is proportionally shorter if we take into account the longer timescale. More important, however, is the possibility that the city induced a slowly changing circulation pattern over the McGill RASS, like the kind described in section 4.2. Physically, this means that rather than having a spatial pattern of cool descending air and warm ascending air moving over us, we instead have a local circulation pattern caused by the city that is not being advected over us. Therefore, Figs 5.37 to 5.39 may not represent

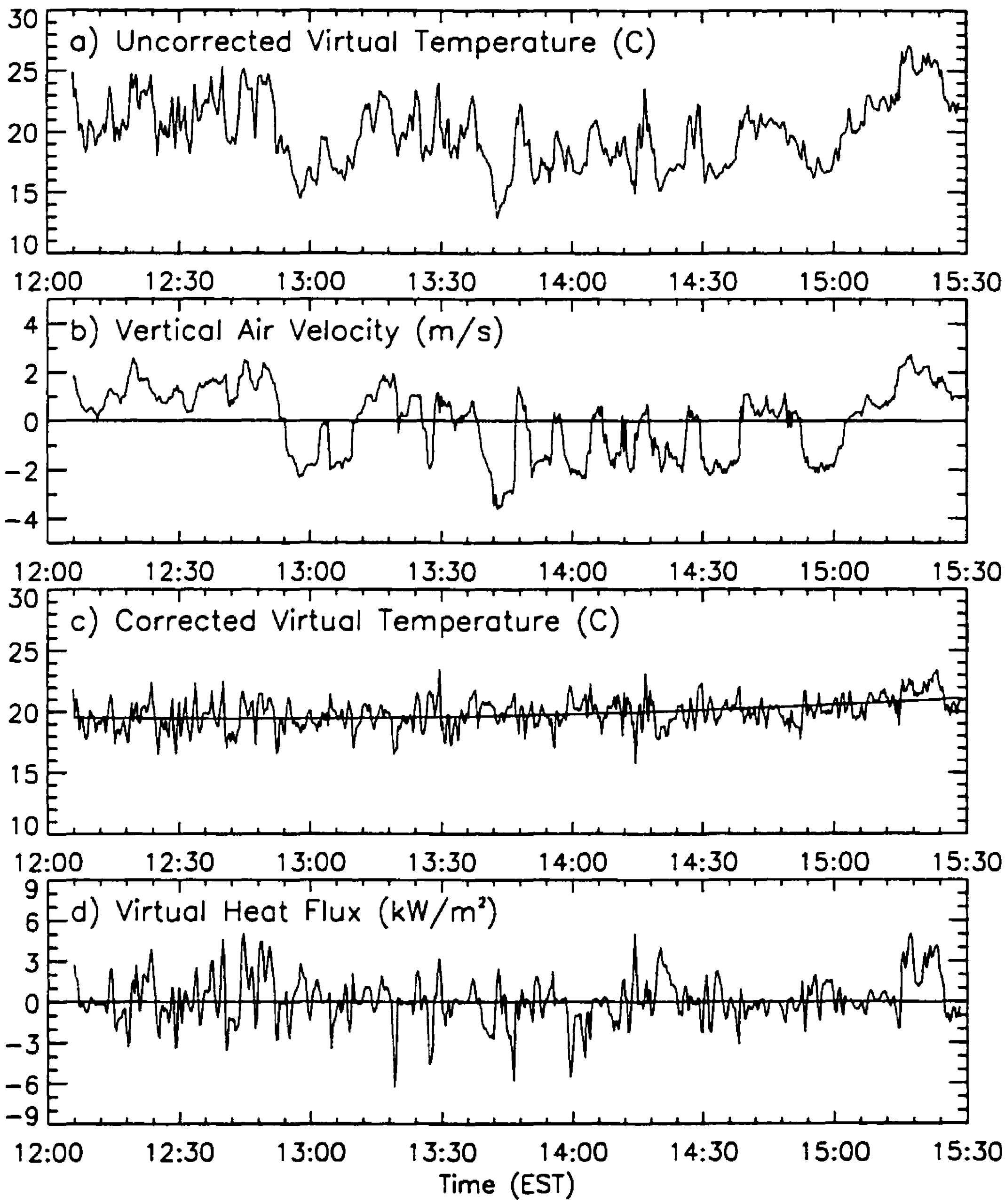

Figure 5.36: Time series of (a) uncorrected RASS temperature, (b) vertical air velocity, (c) corrected temperature, (d) virtual heat flux, at 405 m AGL over McGill on June 28, 1996. Note that the vertical air velocity was treated with a TMIN7 filter with a 5 dB threshold, followed by a XMED5 filter.

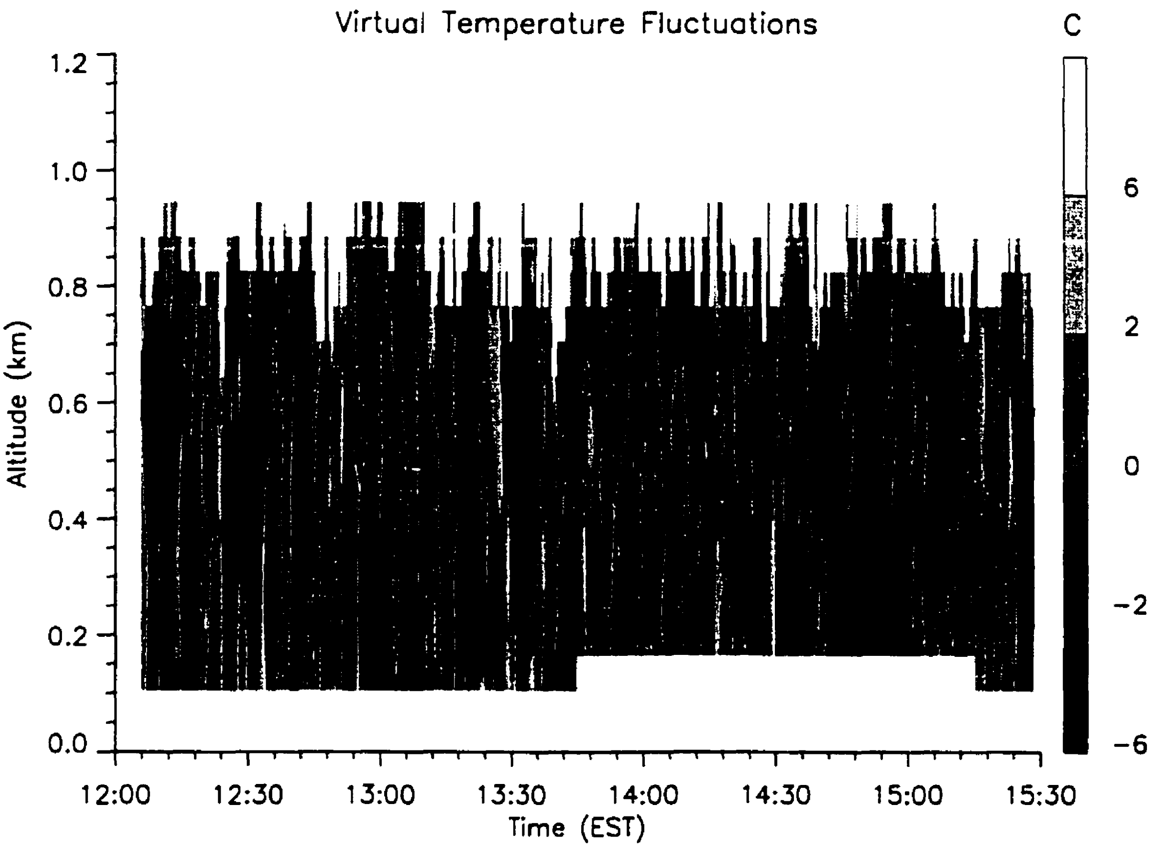

Figure 5.37: Time-height plot of virtual temperature fluctuations over McGill, on June 28, 1996. Note that the solid line represents the zero value contour.

a horizontal cross section given some advection velocity, but rather a changing local circulation pattern over the McGill site.

Figures 5.40 and 5.41 demonstrate the spectral and correlation structure of the McGill RASS data. The windowing and smoothing performed on the power spectra and cospectrum in Fig. 5.40 are identical to that done on the St-Anicet data. The velocity spectrum has a broad maximum extending from 6×10^{-4} to 3×10^{-3} Hz (6 to 28 min periods) with a maximum at about 8 min. The slope at high frequencies is steeper than 2/3, maybe due to a low-pass filter effect caused by the averaging

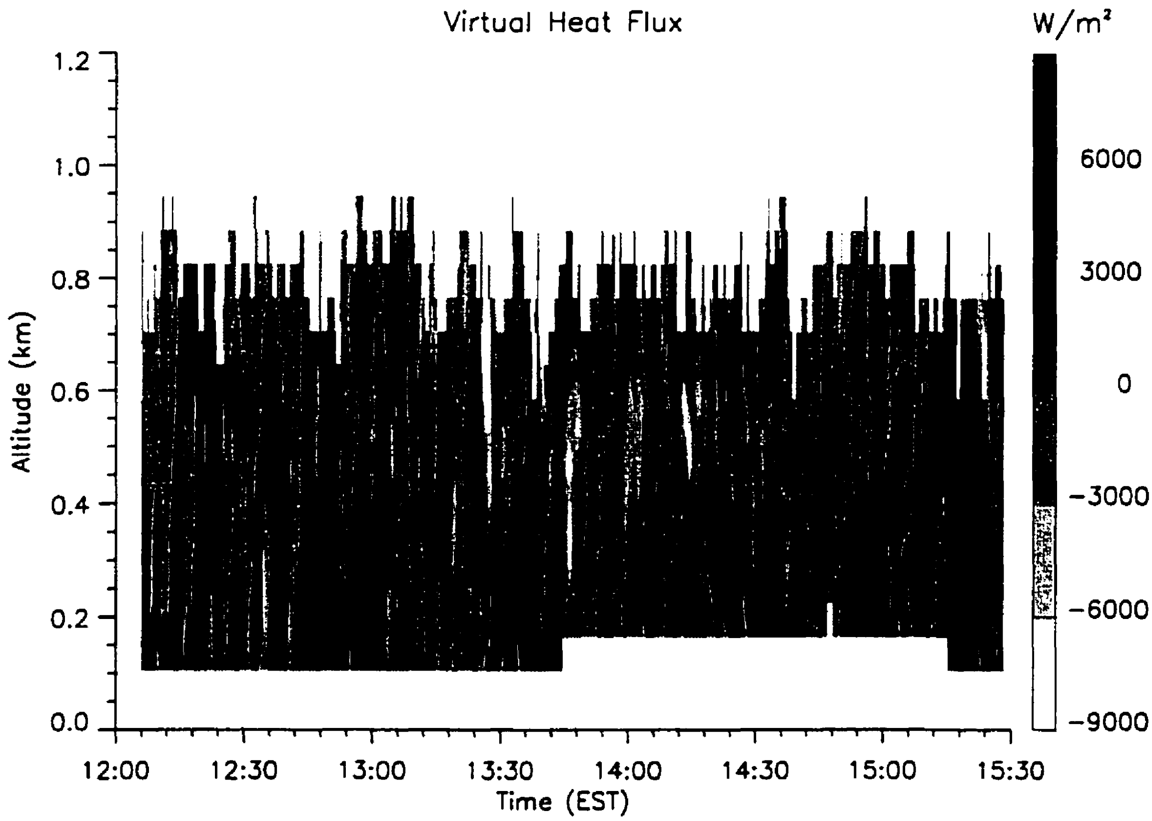

Figure 5.38: Same as in Fig. 5.37, but for the virtual heat flux. Note that the solid line represents the zero value contour.

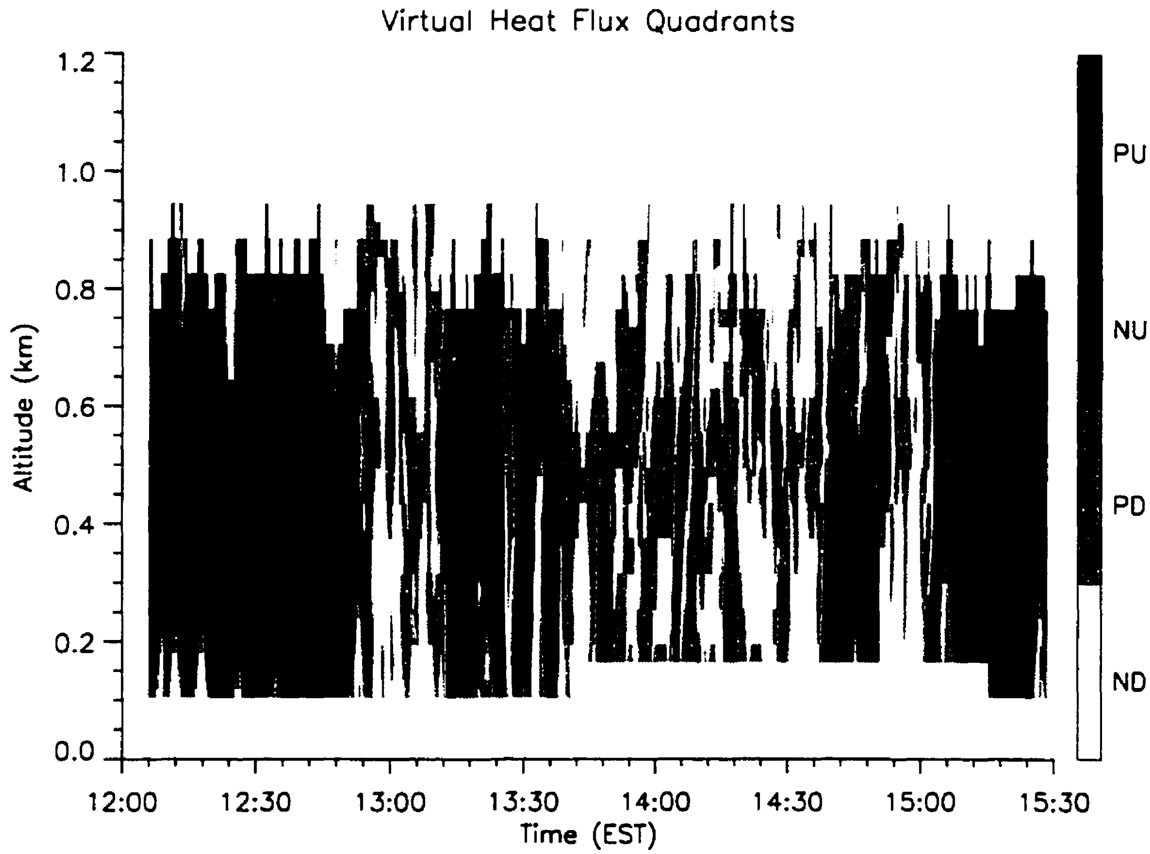

Figure 5.39: Same as in Fig. 5.37, but for the virtual heat flux quadrants. Note that, PU = positive virtual temperature fluctuation and upward vertical velocity fluctuation, NU = negative-upward, PD = positive-downward, and ND = negative-downward.

of the pulse volume, as was explained in the section on the St-Anicet data. Note that beyond about 10^{-2} Hz, the velocity spectrum displays a positive slope of about 1. This may mean that at those frequencies the spectral power is dominated by the vertical velocity measurement errors (white noise spectrum). Also, in Fig. 5.41(a) we see that the vertical air velocity has a timescale of about 6 min and a standard deviation of 1.5 m/s, which are significantly greater than the corresponding values for the St-Anicet data (2-3 min and 0.6-0.8 m/s, see Figs. 5.18(a) and 5.19(a)). The temperature spectrum in Fig. 5.40(a) appears to be strongly contaminated by measurement errors (white noise), as we would expect from our previous analysis, which makes the identification of a peak unreliable and increases the uncertainty of the heat flux estimates. Further evidence of white noise in the temperature time series is seen in the rapidly decreasing autocorrelation function in Fig. 5.41(a). The heat flux cospectrum in Fig. 5.40(b) shows a sizeable peak, almost 250 W/m^2 at its maximum, between 10^{-3} and 2×10^{-3} Hz (8 to 17 min). Just as for the St-Anicet data, the peak is much greater than for the aircraft copsectrum (85 W/m^2), but with important negative components. Note that the cospectrum in Fig. 5.40(b) was not subject to a Hamming window since this procedure made the integral of the cospectrum (total heat flux) artificially negative.

Figure 5.42 shows profiles of vertical air velocity variance, and Fig. 5.43 shows profiles of vertical air velocity variance flux, for both McGill RASS and aircraft measurements. Figure 5.42 shows that there is good agreement between the later aircraft profile (diamonds with dotted lines) and the RASS profile (squares with solid lines) up to about 0.5 km. This good agreement may be deceptive, however, given that the aircraft detects eddies which are averaged out over the resolution volume of the profiler. The dashed line represents the sum of the variance and the average of the clear-air spectral variance, same as the dashed line in Figs. 5.20 and 5.21 for the St-Anicet data. However, given the clutter contamination of the clear-air measurements, the spectral variance is quite unreliable, which explains the erratic shape of

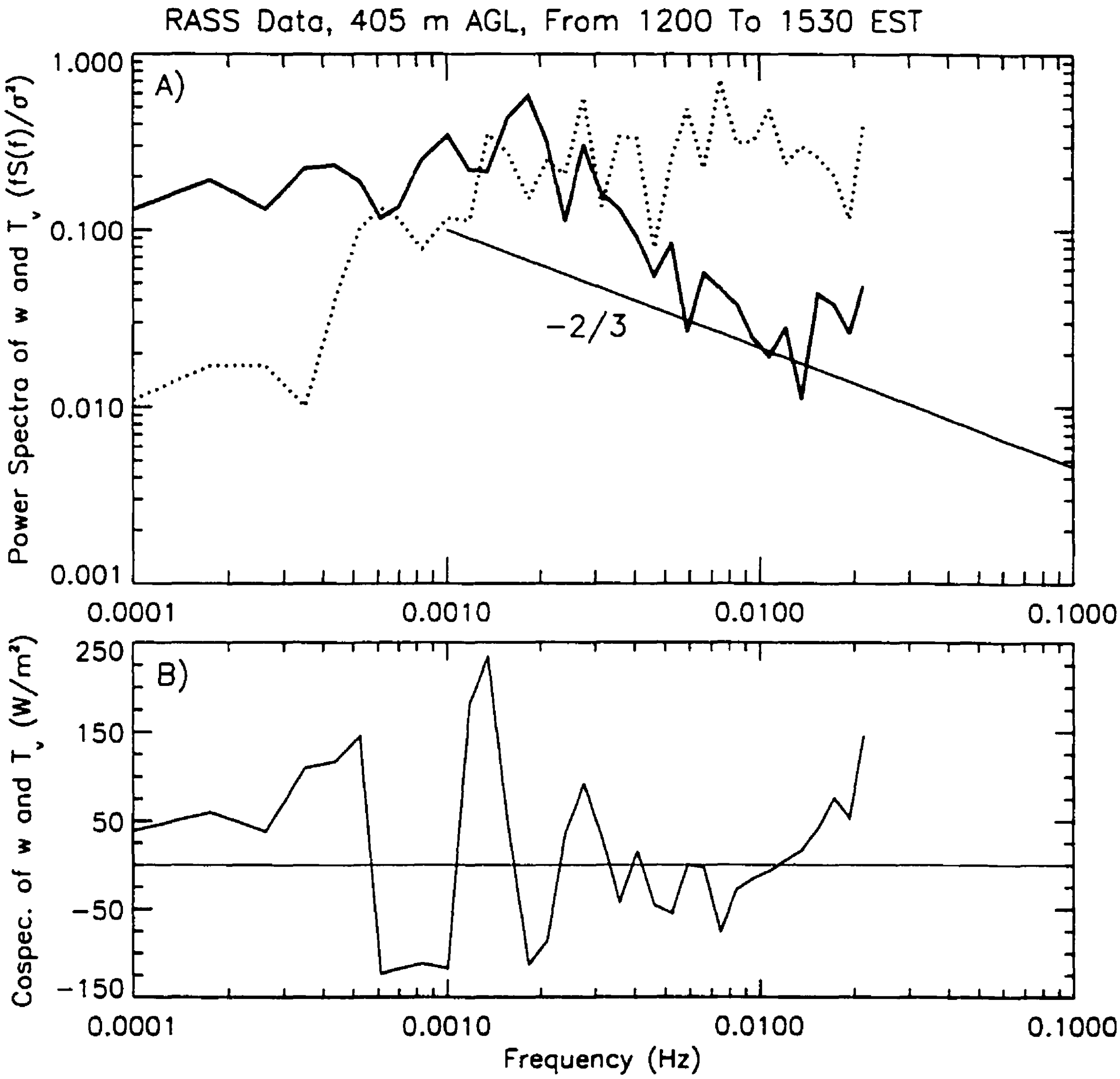

Figure 5.40: Power spectra and cospectrum of the RASS data at 405 m AGL from 1200 to 1530 EST. Graph (a) shows the power spectra of the vertical velocity (solid line), and the virtual temperature (dashed line), multiplied by the frequency and divided by the variance, that is, $fS(f)/\sigma^2$. Graph (b) shows the cospectrum of the vertical velocity and the virtual temperature, multiplied by the density, specific heat, and frequency, that is, $\rho c_p f S_{wT}(f)$.

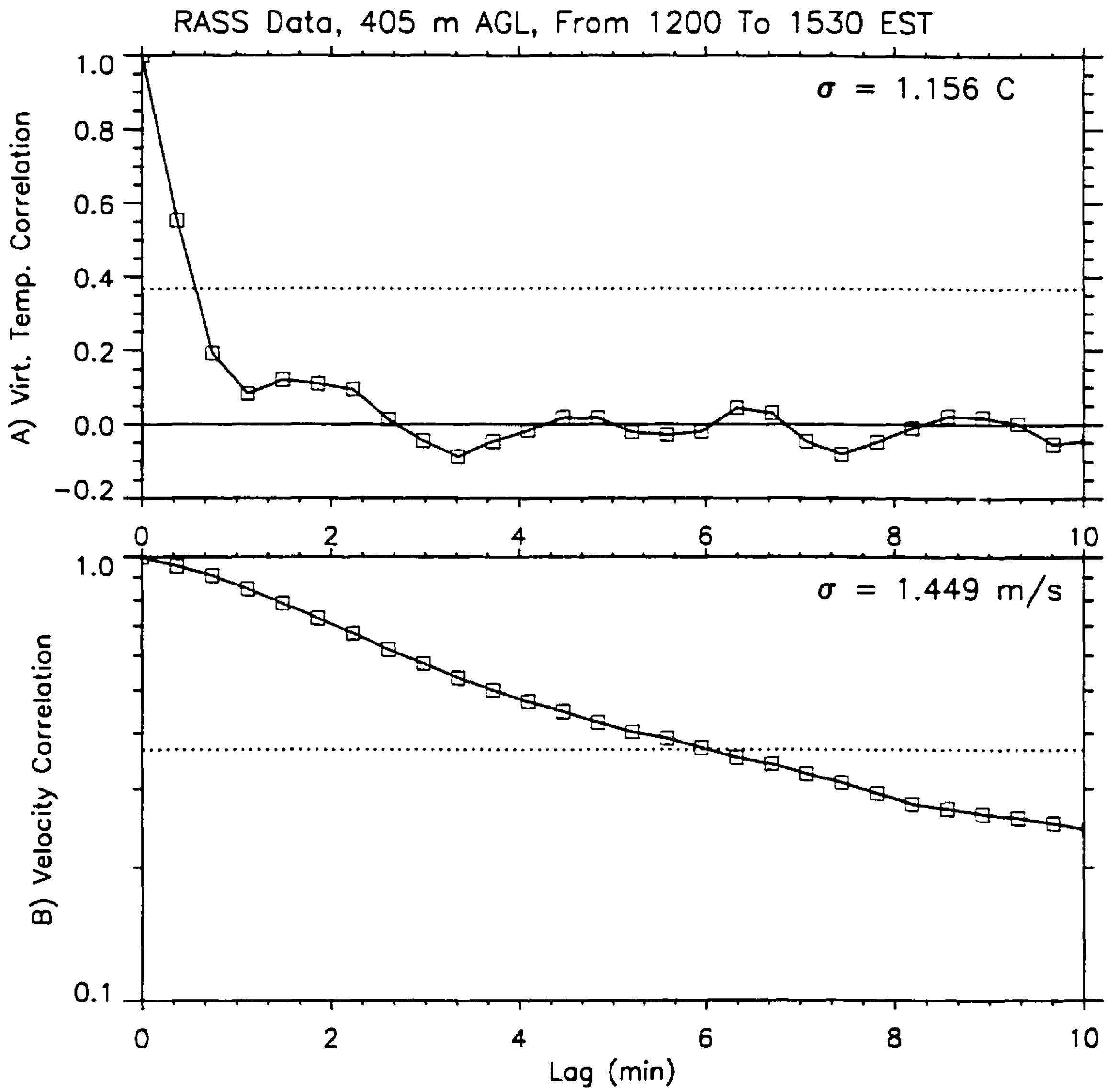

Figure 5.41: Virtual temperature (a) and vertical velocity (b) autocorrelation function for RASS data at 405 m AGL from 1200 to 1530 EST. Note the corresponding stantard deviations, σ, in the upper righthand corners. The squares represent the discrete lags, 22 s apart, and the dotted line represents the $1/e$ value (0.3679) of the correlation.

the dashed line. ROSPA was designed to find only the mean Doppler velocities of clear air; it cannot estimate the second-order moments of the clear air spectra with any accuracy. We therefore cannot use the dashed line as a rough estimate of the total variance. Be that as it may, the RASS variance profile (squares with solid lines) is roughly what we expect from the idealized profiles in Fig. 4.6, which is a smooth curve with a maximum at about 0.4 z_i. Given $z_i \approx 1.65$ km, we expect a maximum at about 0.65 km, which is consistent with the observed profile, taking into account the error bars.

The fluxes of vertical air velocity variance in Fig. 5.43, and heat in Fig. 5.44 are unexpected. The RASS vertical air velocity variance flux is not positive at all altitudes, which is the case for the aircraft variance flux profiles, but instead is negative below 0.7 km with a minimum between 0.4 and 0.6 km. There is therefore a flux convergence of vertical air velocity variance below 0.5 km, and a divergence above that level. Similarly, the RASS virtual heat flux in Fig. 5.44 shows a sudden decrease in heat flux between 0.4 and 0.6 km. One suspects that the heat flux decrease may be due in part to the effect of turbulence on the RASS temperature measurements. We will attempt to correct for turbulence later. However, the errors on the RASS temperature measurements do not explain the shape of the variance flux profile in Fig. 5.42. It is possible that these flux profiles may be due to an imperfect retrieval by ROSPA. As Fig. 5.45 shows, though, varying the spectral threshold for the TMIN7 filter from 5 to 10 dB, the range where TMIN7-XMED5 is optimal, does not significantly alter the heat flux values, considering the error on these estimates. The same can be said about the variance flux profile, though this is not shown in a figure. Another explanation for the unexpected profiles in Figs. 5.43 and 5.44, would be the horizontal advection of virtual temperature and TKE caused by changes in surface temperature, roughness and moisture. Indeed, the urban area immediately around the McGill site is a patchwork of high-rise and low-rise buildings, parks, a wooded hill, not to mention a river less than 2 km upwind. We must also consider the possible

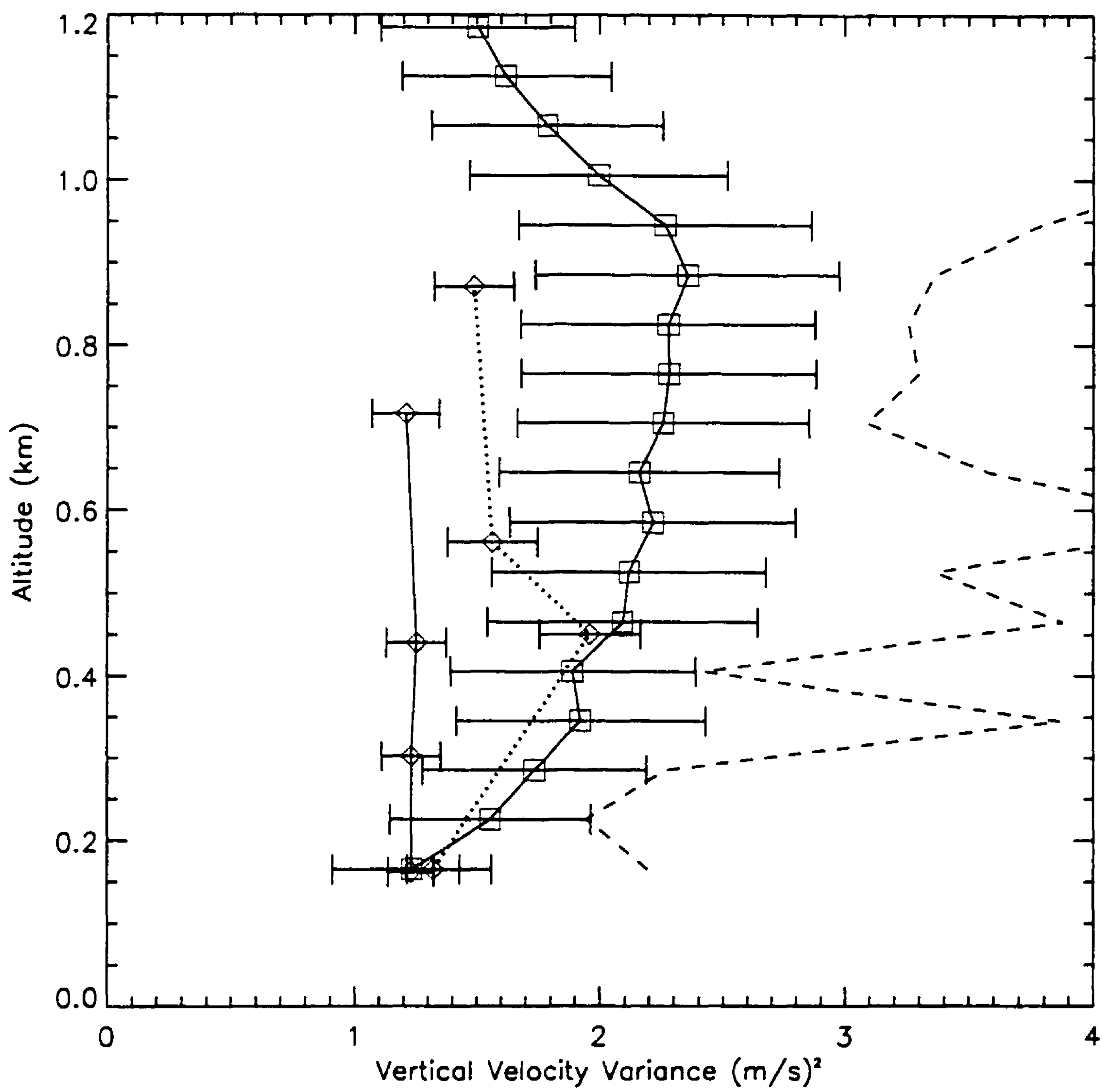

Figure 5.42: Profile of vertical air velocity variance, with error bars, for McGill RASS data (squares). The dashed line is the RASS vertical air velocity variance plus the average Doppler velocity variance of the clear-air spectra. Also shown are the vertical air velocity variance profiles for aircraft data (diamonds), from 1155 to 1235 EST (solid line) and from 1247 to 1335 EST (dotted line).

local circulation induced by the urban heat island, which may cause temperature and TKE advections of its own. All these factors may cause virtual temperature advections much greater than those measured along the aircraft runs over essentially rural terrain ($\approx 10^{-2}$ K/hr (Potvin *et al.*, 1997)). See Kaimal and Finnigan (1994) for a review of the effects of complex terrain on boundary layers.

Two important features of the heat flux profiles in Fig. 5.44 are the surface virtual heat flux, obtained by the intercept at the ground of the linear least-squares fit to the profiles, and the rate of warming of the CBL implied by the slope of the linear fit. Note that only the first five heat flux estimates of the RASS profile are used for the linear fit, since we assume that the RASS temperature measurements are reliable at those altitudes. We also assume that the heat flux profile should have an approximately linear form from about $0.1z_i$ to about $0.8z_i$, as shown in Fig. 4.6. Since we estimate $z_i \approx 1.65$ km over the McGill site, the first five RASS heat flux estimates fall within this range. By inspection of Fig. 5.44, the linear profile hypothesis seems to be appropriate for the aircraft heat flux profile as well. The RASS surface heat flux is 523 ± 239 W/m^2, and 146 ± 0.77 W/m^2 for the aircraft. The RASS surface heat flux value is approximately 3.5 times greater than the aircraft value. This is consistent with the finding by Hildebrand and Ackerman (1984), that the urban surface heat flux is 2-4 times greater than the rural surface heat flux. Also noteworthy is the large error on the RASS surface heat flux value, $\pm$ 239 W/m^2, compared with the aircraft error, $\pm$ 0.77 W/m^2. Possible reasons for this difference with be discussed in greater detail in chapter 6. The negative slopes of the linear fits implies a convergence of heat flux for both profiles. If we assume no horizontal virtual temperature advection, then the heat flux convergence may be transformed into a warming rate by the formula

$$\frac{\partial \theta_v}{\partial t} = \frac{-1}{\rho c_p} \frac{\partial H_v}{\partial z} + S \tag{5.21}$$

where θ_v is the virtual potential temperature, H_v is the virtual heat flux, ρ is the density of air, c_p is the specific heat of dry air at constant pressure, and S is the sum of latent heating, net radiation and potential temperature advection, which we

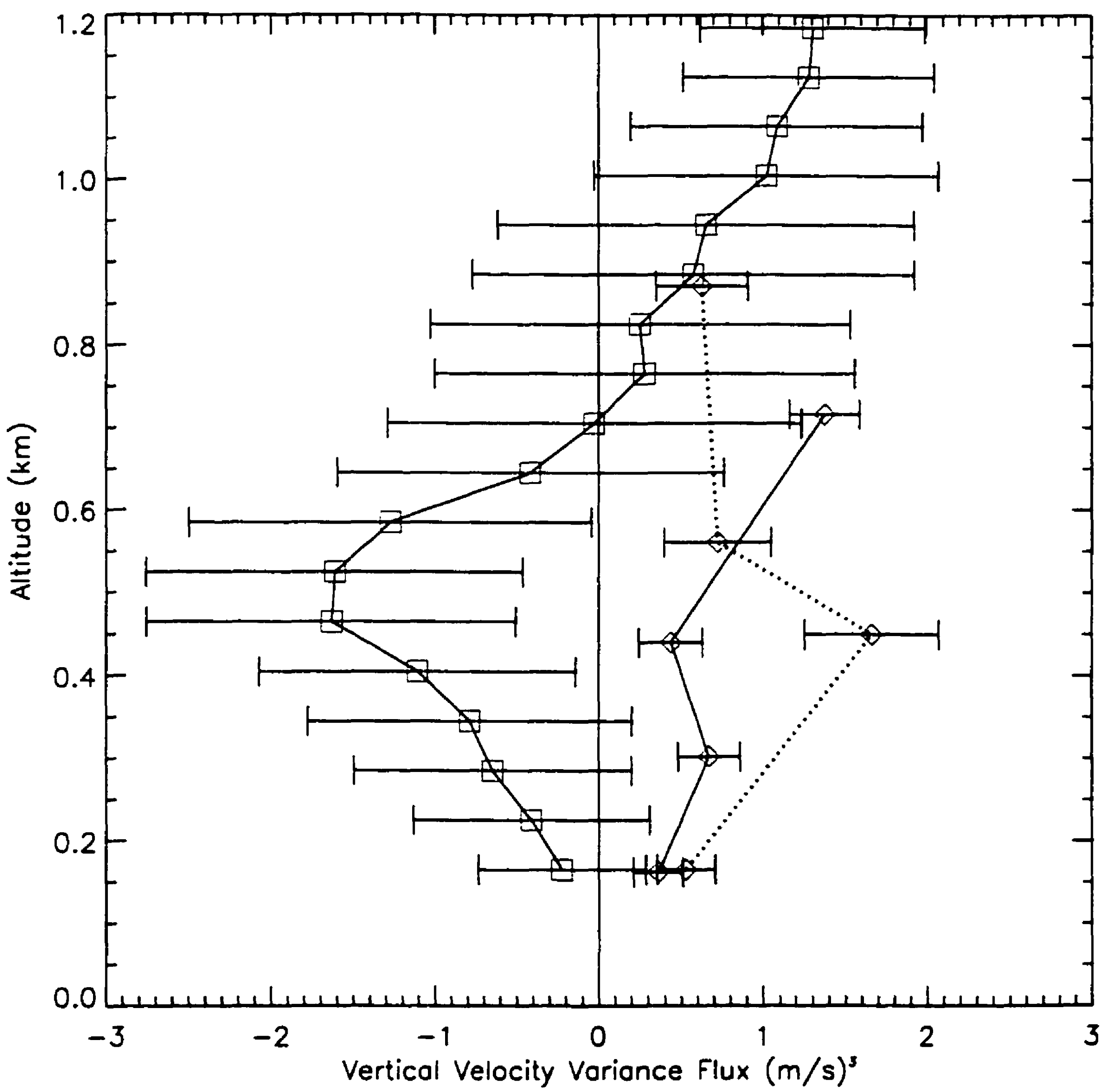

Figure 5.43: Same as in Fig. 5.42, but for the vertical air velocity variance flux.

assume $S = 0$. The RASS heat flux profile yields a warming of 2.36 ± 2.53 K/hr, while the aircraft gives 0.329 ± 0.004 K/hr. Obviously, the virtual temperature time series shown in Fig. 5.36(c) does not demonstrate a warming of 2.36 K/hr, nor does the virtual potential temperature contour plot in Fig. 5.34. A warming of about 0.5 K/hr over the McGill site is more realistic. The discrepancy may be explained by the uncertainty on the RASS warming rate, but also there is the possibility of significant temperature advection over the urban site.

Temperature Correction for Turbulence

We will now apply the temperature correction for turbulence to the McGill data mainly for the sake of consistency with respect to our treatment of the St-Anicet data. As we will see, the clear-air spectral width estimates for the McGill data are very uncertain, making the temperature correction not entirely appropriate for this dataset. The normalized clear-air spectra over McGill, shown in Fig. 5.46, were treated with a TMIN7 filter with a 7.5 dB threshold, follwed by the spectral noise suppression, ground clutter removal and peak identification algorithms. The XMED5 and the TMED5 filters were not used here as they deal only with the mean Doppler velocities, not the spectra themselves. The clear-air spectra show an updraft from 225 to 345 m AGL, and a downdraft at 405 m AGL. At 465 m AGL, however, we see a bimodal spectrum with one peak aligned with the peak at 405 m, and the other centered at about +3.5 m/s. We suspect that the second peak at 465 m is intermittent clutter that survived the filtering algorithms. The resulting bimodal spectrum has an artificially wide spectral width, which will adversely affect the turbulence temperature correction. The clutter also affects the clear-air spectra at 525 and 585 m AGL. Only at 645 m AGL do we recover the downdraft. The RASS spectra seem to confirm the hypothesis of an updraft at low levels and a downdraft above, given the decrease of the RASS velocities between 345 m to 525 m AGL.

The clutter, therefore, has two effects on the spectral profiles in Fig. 5.46. First,

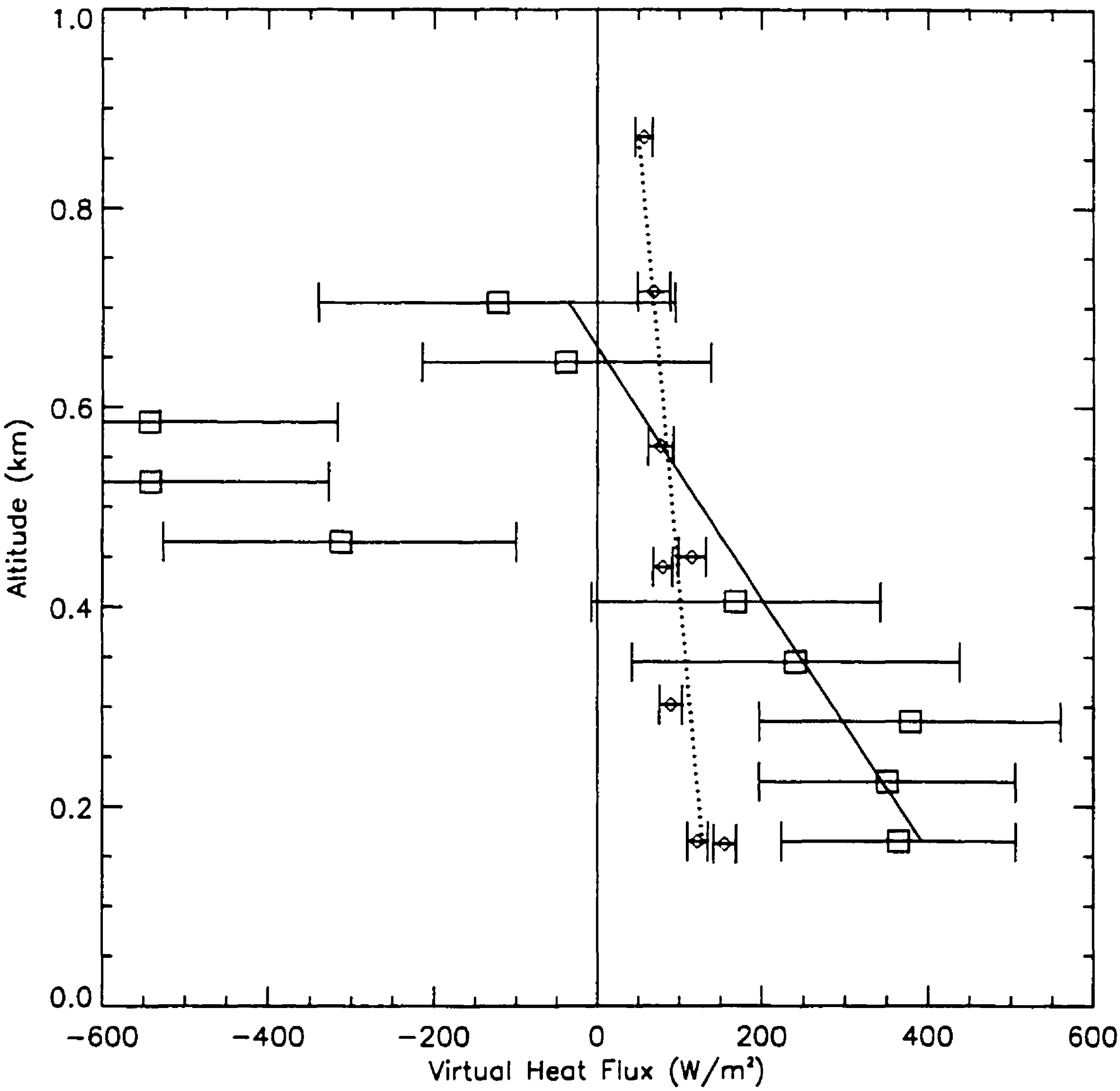

Figure 5.44: RASS (squares) and aircraft (diamonds) profiles of virtual heat flux $(\rho c_p(p_0/\overline{p})^\kappa \overline{w'T_v'})$, with error bars. The dotted line is the least squares fit of the aircraft heat flux values, which yields a surface heat flux (zero intercept) of 146 $\pm$ 0.77 W/m^2. The slope of the line implies a warming of 0.329 $\pm$ 0.004 K/hr. The goodness-of-fit of the dashed line is 91%. The solid line is the least squares fit of the first five RASS virtual heat flux values. The surface virtual heat flux is 523 $\pm$ 239 W/m^2, and the warming is 2.36 $\pm$ 2.53 K/hr. The goodness-of-fit is 3.7%.

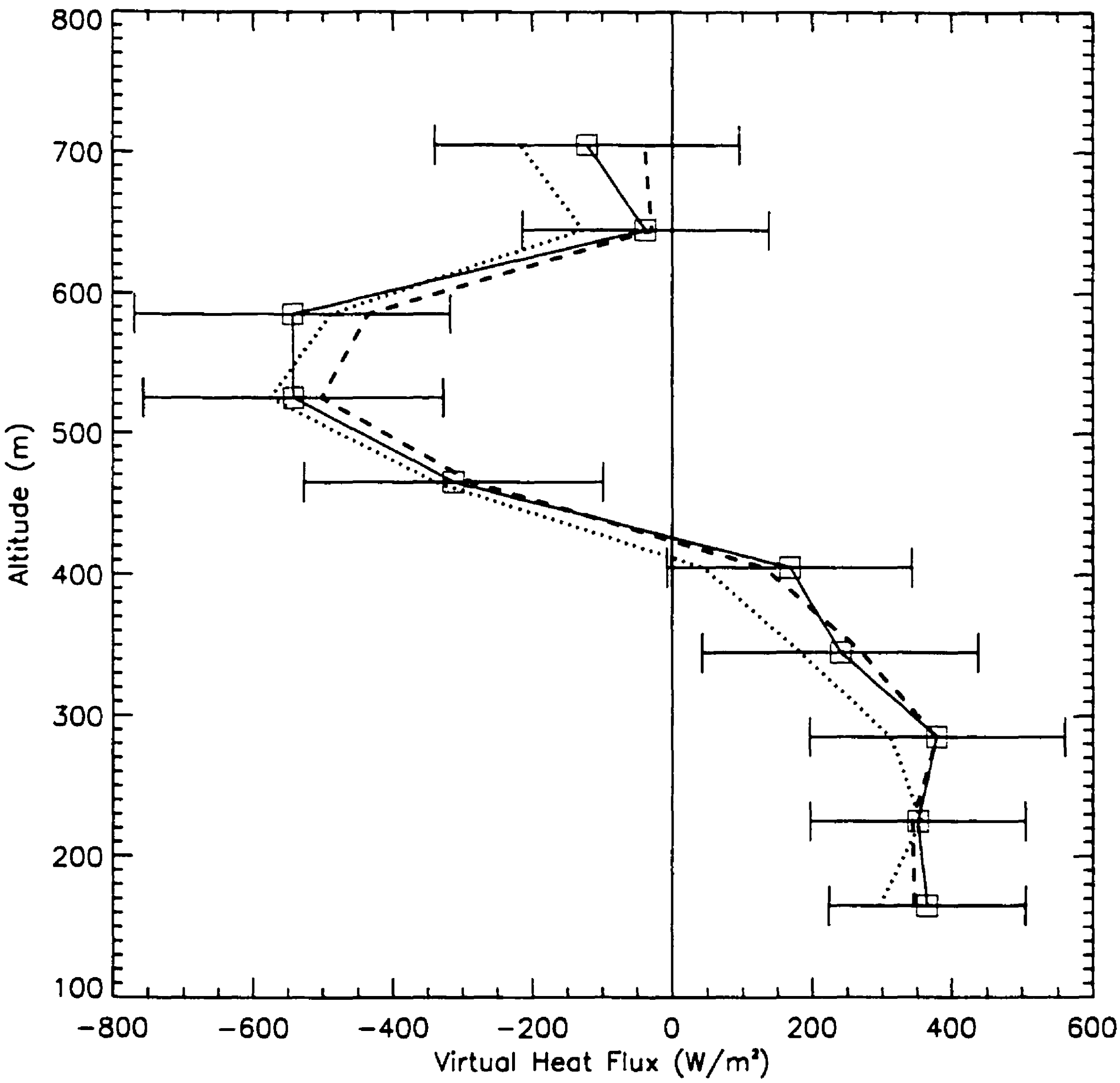

Figure 5.45: RASS virtual heat flux profiles where the clear-air spectral data is treated with TMIN7 and XMED5 filters, with different values of the spectral threshold for the TMIN7 filter. The TMIN7 threshold is 5 dB (dashed line), 7.5 dB (solid line) and 10 dB (dotted line). Note the errors bars on the 7.5 dB line.

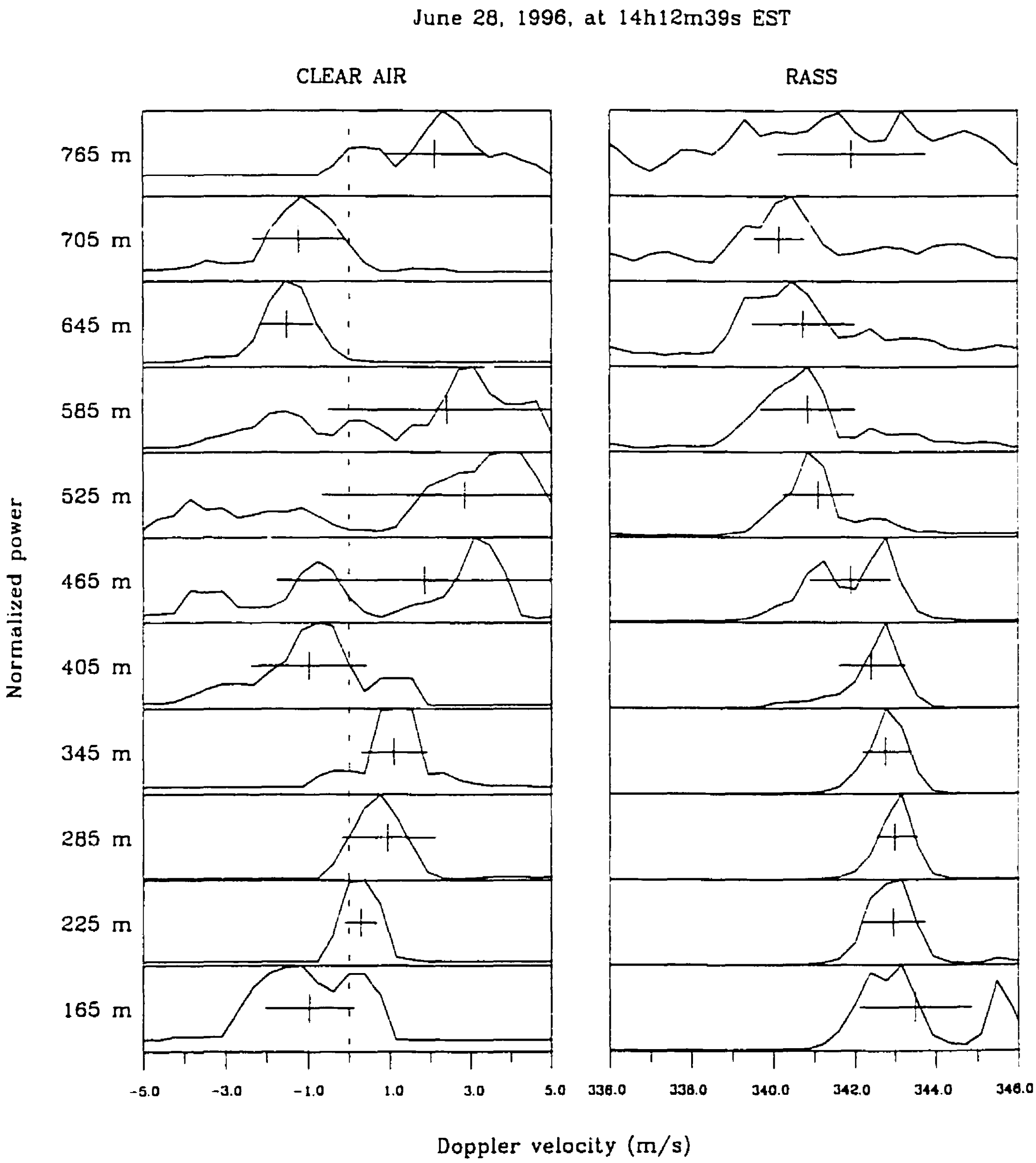

Figure 5.46: Clear-air (left) and RASS (right) spectra over McGill, at 1413 EST. Note that the spectra are stacked as a function of altitude (in meters AGL). Also, the spectra are normalized so that the maximum of each spectrum reaches the top of its display rectangle. The clear-air spectra were treated with a TMIN7 filter with a 7.5 dB threshold and ground clutter removal. The vertical line in each spectrum denotes the mean Doppler velocity ($\overline{v}$), the horizontal line the spectral width ($2\sigma_v$).

by creating an erroneous positive vertical air velocity between 465 and 585 m, it also creates a falsely negative temperature fluctuation when we correct the RASS temperature for vertical velocities. The result is an erroneously negative heat flux fluctuation. Second, the clutter creates artificially wide clear-air spectra at those heights, which causes an artificially high turbulence temperature correction value at that time. These effects can be seen in Fig. 5.47. The clutter in the profiles in Fig. 5.46, corresponds to the large negative temperature fluctuation at 1413 EST, in Fig. 5.47(a), and the large turbulence temperature correction value at the same time, in Fig. 5.47(b). The same thing happens, to a lesser extent, at 1243 EST. So in cases like these, the turbulence temperature correction makes the temperature fluctuations more inaccurate. Nevertheless, the positive temperature fluctuations at 1325 and 1515 EST do have corresponding turbulence temperature correction fluctuations at the same times and with roughly comparable magnitudes. This indicates a certain degree of effectiveness of the method by Peters and Angevine (1996) under these conditions. Also note that if the clutter created an artificially negative velocity fluctuation, it would lead to an artificially positive temperature fluctuation, which would lead to a falsely negative heat flux fluctuation. It is not certain if the turbulence temperature correction would adequately compensate in this case.

We see the effect of the turbulence temperature correction on the virtual heat flux profile in Fig. 5.48. Just as for the St-Anicet heat flux profiles, the turbulence correction has little effect, with respect to the error bars in Fig. 5.44, on the virtual heat flux profile. Note, moreover, that the heat flux values between 450 and 600 m AGL are noticeably more negative with the turbulence correction, although still within the error range. This may mean that the remaining clutter and inaccurate clear-air spectral widths combine to make matters worse in that height range when the correction is applied.

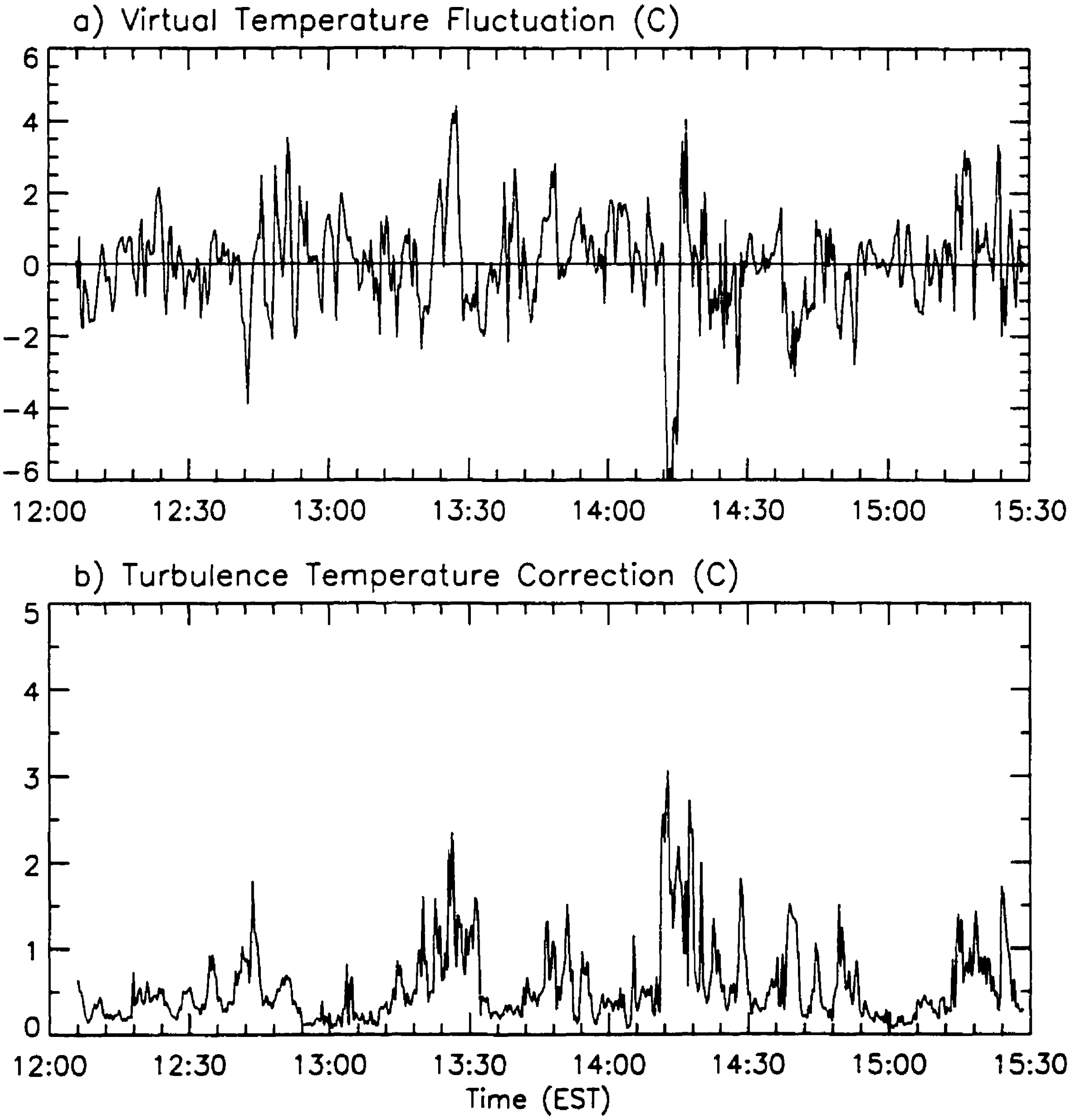

Figure 5.47: The virtual temperature fluctuation (a) and the turbulence temperature correction (b) time series for McGill, at 585 m AGL.

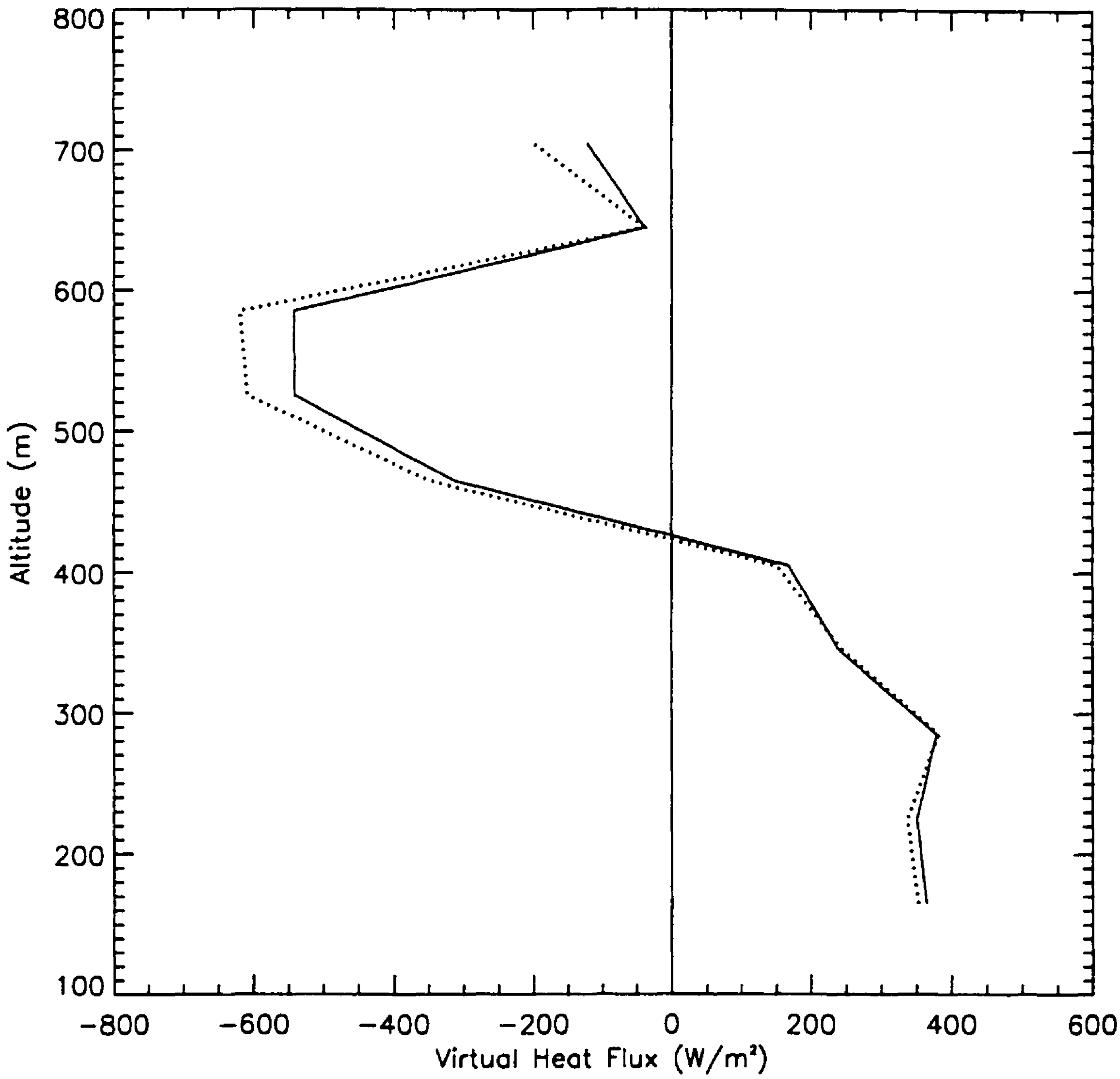

Figure 5.48: A comparison of the virtual heat profile for McGill with (dotted line) and without (solid line) the turbulence temperature correction

5.4 Synthesis

This chapter began with an overview of the type, characteristics, and location of the instruments used on the afternoon of June 28, 1996, during the MERMOZ project. The clear, calm and convective conditions on that afternoon were examined using radiosonde, surface station, and wind profiler data. The spectral, cospectral, and correlation structure of the aircraft data were also examined. The clean, clutter free data collected by the profiler/RASS located at St-Anicet were then analyzed. Specifically, we examined the time-height structure of the clear-air reflectivity, virtual potential temperature and vertical air velocity. This revealed a nonstationary CBL within the observing period. The spectral, cospectral and correlation structure of the St-Anicet data were analyzed, along with profiles of virtual heat flux, vertical air velocity variance and variance flux, which were compared with the corresponding aircraft profiles. A method for correcting the errors due to turbulence on the RASS temperature measurements was tested on the St-Anicet data. For the McGill data, the clutter removal algorithm, ROSPA, was first calibrated to give the optimal performance on this dataset. Subsequently, the McGill data were analyzed in the same way as the St-Anicet data.

During the course of these analyses, many issues were brought up which deserve an in-depth discussion. Among these is the comparability of profiler/RASS measurements with aircraft measurements. More important is the relationship between timescales measured by the profiler/RASS and the spatial scales measured by the aircraft: namely, the validity of Taylor's hypothesis in a CBL. Also, issues such as the effects of detrending, space and/or time averaging, and nonstationarity on the estimates of turbulent and mean properties deserve to be discussed. Finally, issues relating specifically to the RASS data from the McGill site should be analyzed. Foremost among these are the possible effects of the urban environment on the estimates of turbulence statistics. These topics, and suggestions for future work, will be discussed in chapter 6.

Chapter 6

Discussion

In order to obtain a more comprehensive view of the results presented in chapter 5, we should now examine some of the issues relating to them. First, we will discuss the problems associated with RASS-aircraft turbulent flux comparisons, and how they relate specifically to the RASS profiles over St-Anicet and McGill. Second, the possible effects of the various data processing operations on the profiles will be investigated. Lastly, we will suggest various topics for future work.

6.1 RASS-Aircraft Comparison

In the previous chapter, aircraft profiles were used as the standard by which we would judge the corresponding RASS profiles. However, estimates of turbulent quantities from aircraft data also suffer from errors and uncertainties. As Angevine *et al.* (1993b) argued, some of the differences between RASS and aircraft profiles are due to their different kind of samplings of the CBL. In fact, RASS-aircraft comparisons have many points in common with tower-aircraft comparisons, the characteristics of which are described by Desjardins *et al.* (1995) and Mahrt (1998), among others. In this section, we will review the various sources of error for aircraft and RASS, and discuss how they relate to our results.

6.1.1 The Aircraft Data

The Twin Otter research aircraft flux measurement system is a mature platform, which has been compared favourably with other aircraft on numerous occasions, and was acknowledged as the comparison standard for aircraft measurements in the BOREAS experiment (Dobosy *et al.*, 1997). Nevetheless, given that aircraft measurements are usually taken over long distances at constant altitude, and over relatively short time periods, the aircraft statistics are basically spatial statistics. Since virtually all land surfaces are heterogeneous to one extent or another, this means that the aircraft flies over different types of terrain. Aircraft statistics are therefore composites over various terrain types. This effect is strongly dependent on the altitude of the aircraft run. The higher the aircraft, the farther upwind the terrain may be which contributes to the measurements. For example, even at 30 m above ground, significant horizontal transport may occur on scales larger than 5 or 10 km (Mahrt, 1998).

Aircraft flights may not be completely level due to vertical displacements of the aircraft by turbulent motion and the difficulty of maintaining a constant altitude over changing terrain. If the quantity being measured has a mean vertical gradient, then variations in altitude will lead to artificial fluctuations in the aircraft time series. Some of the long (about 5 km) virtual temperature fluctuations in Fig. 5.6(b) may be due to altitude variations of the aircraft. This effect is compensated for in the heat flux calculations by using the virtual potential temperature (MacPherson, 1990), because that quantity is not expected to have a mean vertical gradient in the mixed layer of a CBL. Also, nonstationarity may appear in the aircraft data because of large scale horizontal gradients, or possible drifts in the aircraft navigational systems used to compensate for the aircraft motion in wind measurements. These drifts are compensated for during post-processing, as mentioned in section 5.1, but that still leaves the question of large scale vertical motion and temperature gradients. We will discuss different ways of eliminating nonstationarity in subsection 6.2.1.

We end this subsection by mentioning certain features of aircraft measurements. The first is the scale of the individual measurements. With respect to the profiler resolution volume and integration times, the individual aircraft measurements are essentially instantaneous averages along a thin line about 5 meters long. Also, since a given aircraft run is 30-35 km long, each run most likely samples a large number of coherent structures, namely thermal plumes in the case of a CBL. Since it is the thermal plumes that are considered to be largely responsible for the fluxes in the CBL, the aircraft should obtain reliable flux estimates provided that the flux statistics are relatively homogeneous over the length of the run.

6.1.2 The St-Anicet RASS Data

The agreement between the St-Anicet RASS and aircraft profiles of virtual heat flux is good, but only within a limited altitude range and for the second half of the RASS data. In general, comparisons between aircraft and tower fluxes reveal that aircraft sensible heat flux values are usually less than tower values (Desjardins *et al.*, 1995; Mahrt, 1998), but this is perhaps attributable to the differing footprints of the measurements. Just as an aircraft may fly over many different terrain types, a RASS or tower may be subject to those types of terrain that predominate locally. Of course, the 'field of view' of the RASS, that is the surface area that contributes to the flux, may increase with altitude. However, the field of view of the RASS also depends on the characteristics of the convection carrying the flux. With weak winds and significant local surface heating, stationary convective eddies might develop close to the RASS and create a more or less local, nonadvecting and stationary circulation over the RASS. This is not expected to be a problem for the St-Anicet RASS site, but as we will see, may pose a significant problem for the McGill RASS site.

The discrepancies observed in Figs. 5.24 and 5.25 between the heat flux profiles measured by RASS and aircraft, could also be explained by spatial differences between the observations. The aircraft runs were 35 km long, and no closer than 30 km to the St-Anicet RASS site. A greater boundary layer thickness at the location of the aircraft runs could explain why the aircraft virtual heat flux profiles never become negative. For example, the highest aircraft flux run shown in Figure 5.25, at an altitude of 870 m, occurred approximately 300 m below the CBL height estimated from the aircraft data, where one could reasonably expect either positive or negative fluxes. Indeed, as Barnes *et. al.* (1980) showed, the variability of the boundary layer may cause different results from different instruments even when conditions are more favorable than for this case. A difference in CBL height may also help to explain the different shape of the aircraft vertical air velocity variance profiles in Figs. 5.20 and 5.21, with respect to the St-Anicet RASS profiles.

Furthermore, the horizontal wind speed during the observing period was very weak at all levels, making it questionable to assume the equivalence of temporal and spatial statistics (Taylor's Hypothesis). If we define the integral scale as the lag where the autocorrelation function falls to $1/e$, (see Teunissen (1980), for the relative merits of different integral scale retrieval methods), then Fig. 5.8(b) gives an integral spatial scale of the vertical velocity of about 190 m, and Fig. 5.19(b) gives a temporal time scale of about 110 s. The ratio of these scales yields 1.73 m/s as an advection velocity, which is comparable to the horizontal wind at that altitude. Nevertheless, there is every reason to expect that the eddies evolve considerably as they are advected over the RASS. The 'frozen turbulence' assumption is thus undermined. Under such conditions, Antonia *et. al.* (1980) demonstrated that the temporal spectra of a given quantity are related to the spatial spectra by a complex convolution involving the horizontal velocity spectrum. This may help to explain the different forms of the aircraft and RASS cospectra.

Furthermore, under weak wind conditions, relatively few convective eddies will pass over the RASS during a given observation period. Therefore, over an averaging time of $1\frac{1}{2}$ hours, RASS probably does not sample as many thermal plumes as a 30 km long aircraft run. Insufficient sampling explains why the RASS error bars are consistently larger than the aircraft error bars. Reliable estimates of the flux require long averaging times, but these are not feasible because of the nonstationarity of the data (Lippmann *et al.*, 1996). Despite all the problems, the agreement between aircraft and RASS below 500 m, and in the second half of the observation period, is good. This suggests that the regime of large eddies and plumes in the mixed layer was sufficiently strong, persistent and widespread to allow a meaningful comparison between the aircraft and the St-Anicet RASS. Therefore, the low cost, high reach and easy application of the RASS make it an invaluable tool for boundary layer research.

As mentioned previously, the profiler/RASS measurements are weighted averages over the resolution volume and the integration time. It is therefore not obvious how the aircraft data may be processed in order to resemble profiler data. Simply averaging the aircraft data over the width of the resolution volume seems unlikely to reduce the variability of the aircraft data to match that of the profiler data. An instantaneous line average the size of the width of the resolution volume is still not equivalent to the profiler space-time average. The instantaneous line average therefore has a greater variability than the profiler measurements, and the aircraft vertical velocity data would still possess a greater variance, as in Figs. 5.20 and 5.21.

6.1.3 The McGill RASS Data

The McGill RASS site is located towards the southeast of the center of an urban agglomeration. The Montreal urban heat island is precisely the kind of local surface heating, mentioned previously, that can cause a stationary convective eddy. Indeed, the mesoscale circulation around a city, described in chapter 4, is an example of a stationary eddy. A stationary eddy can cause problems: it obviously transports heat and TKE, but the eddy-correlation method requires that we remove the average of

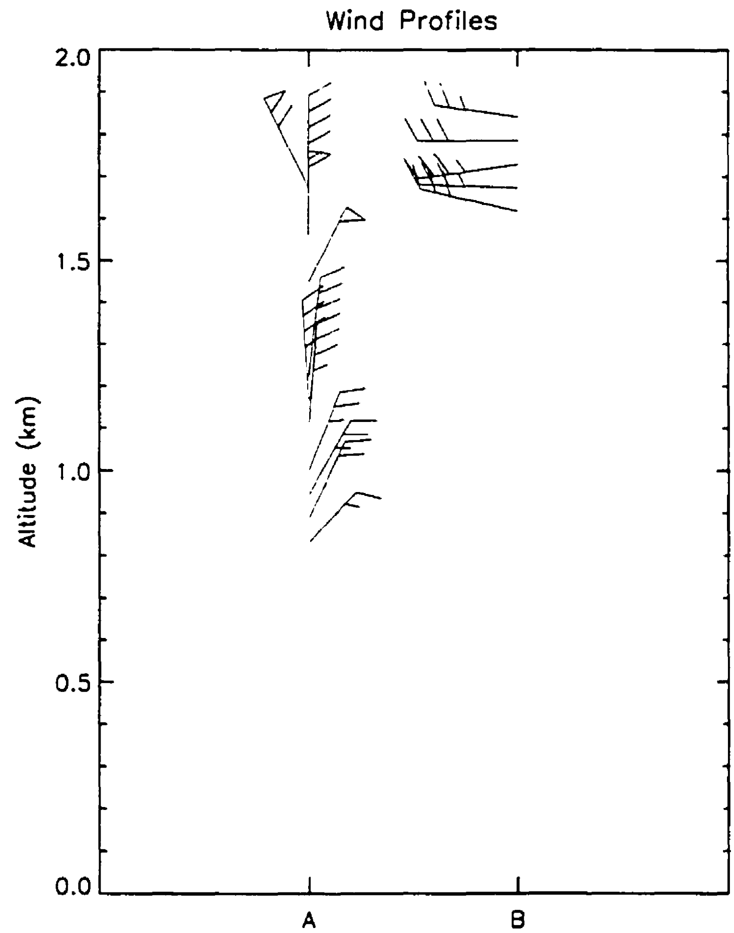

Figure 6.1: Wind profiles over McGill taken by the profiler, on June 28, 1996. Profile A is a consensus average the one-hour period preceding the continuous RASS measurements (1100 to 1200 EST), while B is for the half-hour following the RASS measurements (1530 to 1630 EST). A half barb represents 0.5 m/s, a full barb 1 m/s, and a triangle 5 m/s.

the time series prior to computing the flux. For RASS data, removing the average of the time series is the same as removing the flux due to the stationary eddy. Following Mahrt (1998), we will use the example of heat flux, $H = \overline{w\theta} = \overline{w'\theta'} + \overline{w}\,\overline{\theta}$, where the overbar denotes here an average over a wide area, and the primes denote the deviation with respect to that average, $w' = w - \overline{w}$, $\theta' = \theta - \overline{\theta}$. If we assume $\overline{w} = 0$, then

$$H = \overline{w'\theta'}. \tag{6.1}$$

The RASS measurements are taken at one location over time. If the RASS is located in the vicinity of a stationary convective eddy, then the time averaged vertical velocity $< w' > \neq 0$ over the RASS. The time averaged vertical velocity, $< w' >$, can therefore be a function of position. Defining $\Delta w' = w' - < w' >$, and likewise for θ', then we can state

$$H = H_R + < w' >< \theta' > . \tag{6.2}$$

where $H_R =< \Delta w' \Delta\theta' >$ is the heat flux measured by the RASS. This flux, therefore, does not necessarily correspond to the area averaged heat flux, $H_R = H - < w' >< \theta' >$, which we take to be the true heat flux. These considerations also apply to the vertical velocity variance flux.

The wind profiles over McGill, shown in Fig. 6.1, suggest the presence of the kind of mesoscale circulation around a city, shown in Fig. 4.3. Wind profile B, in particular, is in sharp contrast with the St-Anicet wind profiles, in Fig. 5.2. The later St-Anicet winds (profile B) are generally from the east, while the later McGill winds (B), between 1.5 and 2 km, come from the west. This might be a manifestation of the divergence of the mesoscale circulation near the top of the CBL, assuming that the center of the circulation is to the west of the McGill site. The height of the CBL over McGill after the RASS observation period was 1.8 km, which is approximately the altitude of the winds barbs in profile B. Profile A in Fig. 6.1 is harder to explain. The wind profiles in Fig. 6.1 must be interpreted with caution, however, given the contamination of the profiler data at the McGill site. Only the consensus averaging

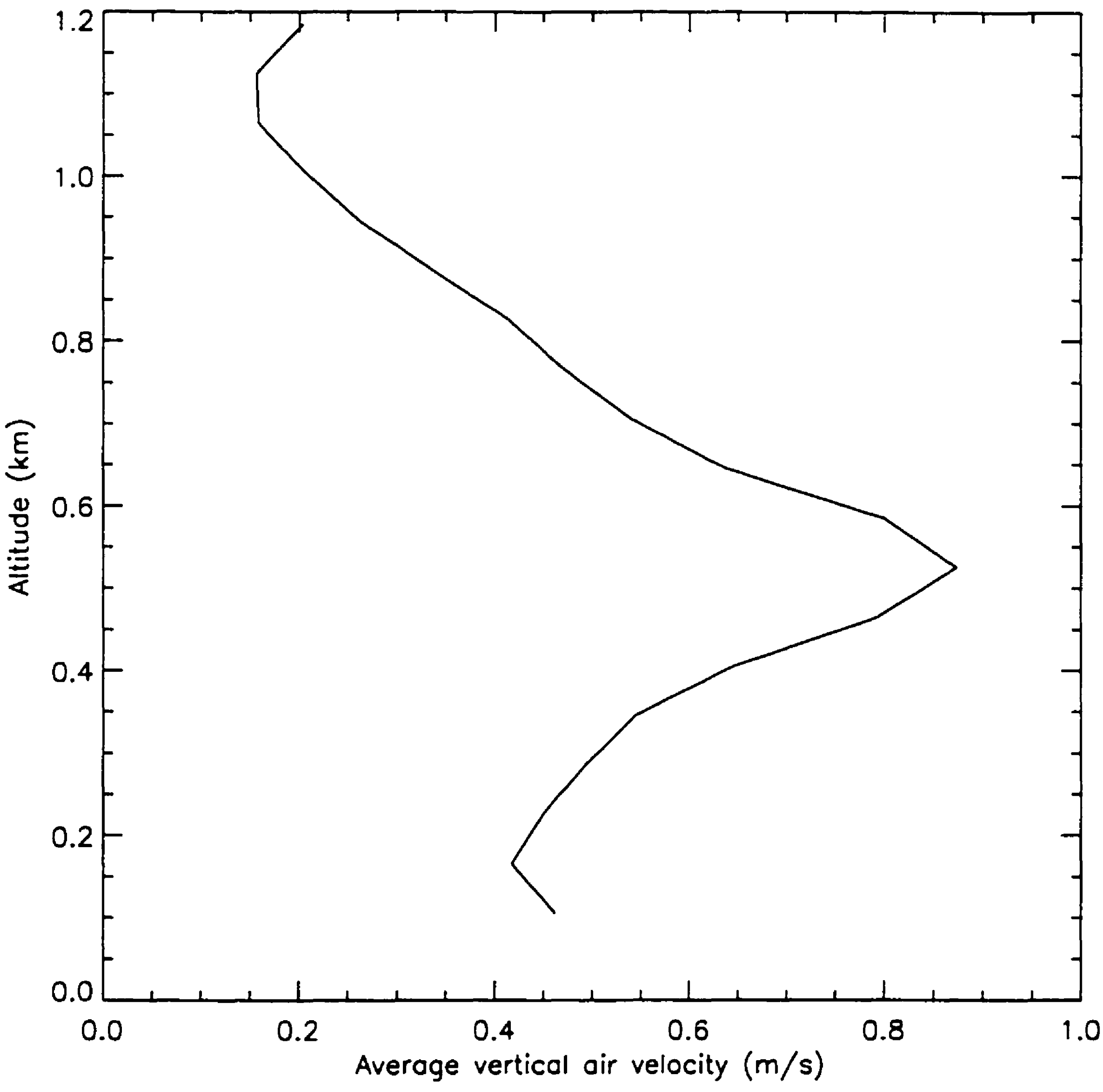

Figure 6.2: The profile of the average vertical air velocity over McGill, on June 28, 1996. The average was performed over the continuous RASS observation period, from 1200 to 1530 EST.

algorithm was used to eliminate outliers from the wind profiles (ROSPA was designed for profiler data operating in continuous RASS mode). The intermittent clutter can reach as high as 1.5 km (the white patches in Figs. 5.32 and 5.33), and the wind barbs can change appreciably as we change the consensus averaging parameters or the averaging period. Nevertheless, the winds in profile B between 1.5 and 2 km should be relatively reliable.

Figure 6.2 shows the profile of the vertical air velocity averaged over the RASS observation period (1200 to 1530 EST) over the McGill site. This therefore corresponds to a profile of $< w' >$. We see that the vertical velocity is everywhere positive and has a broad maximum between 0.4 and 0.6 km, almost reaching 0.9 m/s at its peak. The altitude of the maximum corresponds roughly to the region of the very negative virtual heat flux in Fig. 5.44, and the negative vertical air velocity variance flux in Fig. 5.43. It therefore seems possible that the unexpected flux profiles in Figs. 5.44 and 5.43 are a result the fluxes due to a stationary convective circulation which are not taken into account by the eddy-correlation method. We could, in theory, correct the virtual heat flux profile in Fig. 5.44 by adding to it the product of the profile in Fig. 6.2 with the profile of $< \theta' >$, as in Eq. 6.2. The profile of $< \theta' >$ is the time average of a potential temperature spatial anomaly, presumably the urban heat island intensity profile, similar to the one in Fig. 4.4(d). The correction can be very sensitive to the choice of $< \theta' >$, however, which we do not know very precisely. In addition, we must also use the profile in Fig. 6.2 with caution. According to Angevine (1997), the vertical air velocities measured by a profiler may contain significant systematic errors. The systematic errors are always negative, between approximately -0.25 to 0 m/s, and vary with respect to altitude, time of day, and day of the year. Angevine suggests that the error may be due to falling particulate scatterers in a CBL.

With respect to any comparison between the aircraft data and the McGill RASS, it seems obvious that Taylor's hypothesis does not hold if there is in fact a stationary circulation above the McGill site. The stationary circulation can also adversely affect the McGill RASS's sampling of the thermals in the CBL. It may also help to explain why the vertical velocity timescale over McGill (6 min) is greater than the St-Anicet timescale (2-3 min). This inadequate sampling of the CBL over McGill, along with imperfect vertical air velocity retrievals by ROSPA, and the effect of winds and turbulence on the RASS temperature measurements, may explain the large errors in the RASS heat flux estimates compared with the errors on the aircraft estimates in Fig. 5.44.

6.2 Data Processing

6.2.1 Removing Nonstationarity

Both the RASS and aircraft data may contain nonstationarities in the mean. The aircraft might fly through a large scale horizontal gradient, while the warming of the boundary layer may cause a nonstationary RASS temperature time series. How we remove the trend can affect the shape of the power spectra, cospectra, and covariance functions of the time series (Kaimal and Finnigan, 1994). This, in turn, can affect estimates of integral scale, variance and heat flux. A quadratic least-squares fit was used to remove the nonstationarity from the St-Anicet and McGill corrected virtual temperature time series. The fit for the St-Anicet data in Fig. 5.12(c) is convincing, but the fit for the McGill data, in Fig. 5.36(c), is less so. Indeed, a linear least-squares fit in Fig. 5.36 might seem just as appropriate, but would yield a different heat flux value.

Nonstationarity in the aircraft data was removed using a high-pass filter that strongly attenuated any signal component with a wavelength of 12 km or greater. High-pass filters have the advantage of being simpler and their effects on spectra are well understood. However, there still remains the choice of the wavelengths to attenuate. Using only signal components with a wavelength 12 km or less assumes that mesoscale motions make no significant contributions to the flux, which may or may not be true. All we can say with certainty is that removing nonstationarities is somewhat arbitrary and may lead to bias (Mahrt, 1998).

6.2.2 Ground Clutter Removal

As we explained in subsection 3.2.4 on ground clutter removal, all ground clutter removal algorithms perform poorly when the vertical air velocity is equal or very close to zero. Figure 6.3 shows an example of the effects of the ground removal algorithm on the clear-air data over St-Anicet. The untreated data (curve a) is already free of ground clutter. When we apply the ground clutter removal, we see that the points that were originally equal or close to zero in curve (a) get 'pushed' away from the zero velocity line, in both directions. The reason is that if we have a clear-air power spectrum with no ground clutter and a peak near zero, +0.5 m/s say, but that also 'spreads' over the zero Doppler velocity bin and into the negative velocities, then the ground clutter removal algorithm used here will eliminate the spectral components on the negative Doppler velocity side, as well as remove some spectral power from the positive Doppler velocity side. The end result is a power spectrum with spectral power on the positive side only. The mean of the treated power spectrum will be further from the zero Doppler velocity bin than the untreated mean. The same reasoning applies to negative mean Doppler velocities. It also follows that a power spectrum with a peak far enough from zero so that it does not cross over to the other side, is unaffected by ground clutter removal.

As Fig. 6.3 shows, the ground clutter removal algorithm induces distortions in the vertical air velocities. Of course, if ground clutter is present, and the ground clutter removal algorithm is not applied, then the vertical air velocities will be to close to the zero velocity line, which is another kind of distortion. Since we determine the temperature fluctuations by subtracting the vertical air velocities from the acoustic velocities, these distortions can influence the temperature fluctuations and, in turn,

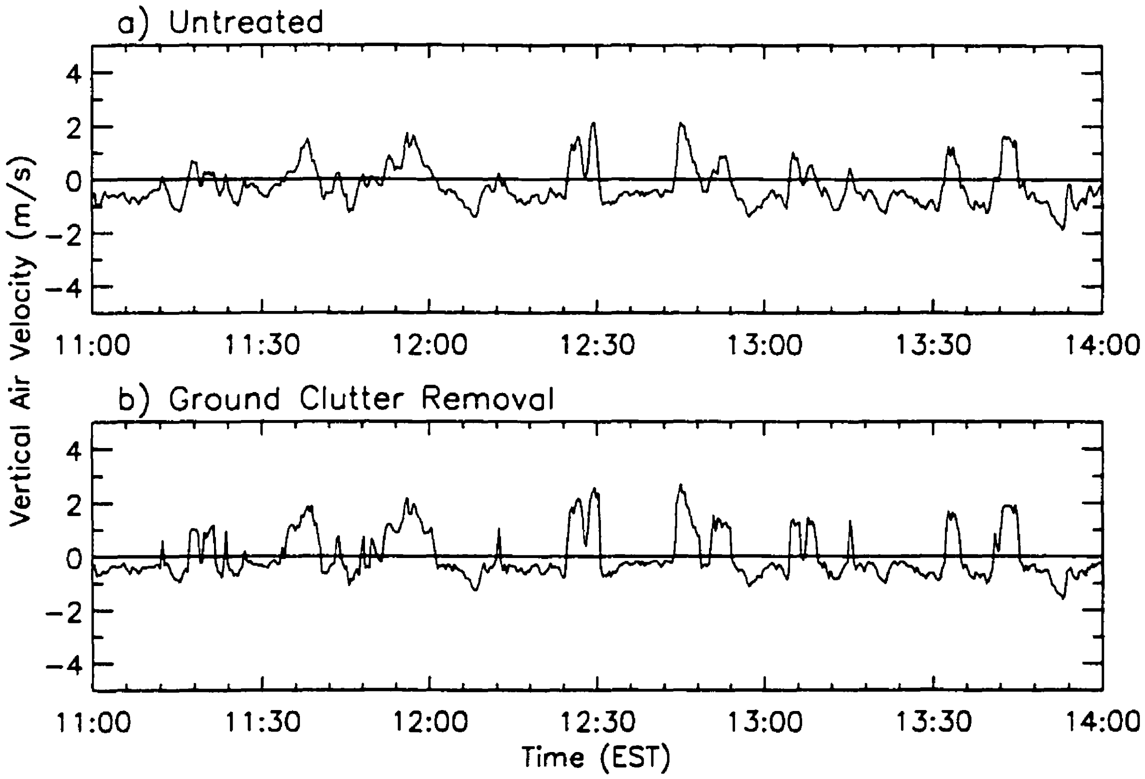

Figure 6.3: An example of the effect of ground clutter removal on the vertical air velocity at 412 m AGL over St-Anicet, on June 28, 1996. Curve (a) is the untreated data, while curve (b) has been treated with the ground clutter removal algorithm.

the heat flux values. For the McGill data, we chose to remove the ground clutter because we estimated that the distortions caused by removing ground clutter were less detrimental than those caused by the ground clutter itself. The reason is that the distortions caused by the ground clutter removal algorithm decrease with increasing magnitude of the velocity. Therefore, not all of the vertical air velocities are seriously affected. If we do not remove the ground clutter, more vertical velocity values would be affected, even taking into account the peak identification algorithm (subsection 3.2.5). That is because almost any overlap between the ground clutter and clear-air power spectra will cause the peak identification algorithm to include both, and even if the power spectra are well separated, the peak identification algorithm may still isolate the ground clutter spectrum if its peak power value is greater than that of the clear-air spectrum. We conclude, therefore, that ground clutter removal is a compromise between two types of distortions. Whether it is worthwhile depends on the presence and the strength of the ground clutter.

6.3 Future Work

The following are suggestions for future work. These suggestions are meant to draw attention to certain problems encountered in this thesis, and to possible solutions. Also, we wish to suggest ways to expand on, and go beyond, the work already done.

6.3.1 Improving ROSPA

ROSPA is, by necessity, an exclusively post-processing signal processing algorithm. This is because, for the McGill profiler/RASS, none of the on-line signal processing steps (coherent integration, windowing, FFT, spectral averaging), do anything to reduce or eliminate clutter, with the possible exception of the DC filtering. Therefore, ROSPA could only use power spectra obtained after the on-line signal processing. As we have seen, however, the St-Anicet profiler/RASS on-line signal processing program uses the SAM algorithm to eliminate intermittent clutter. This opens the possibility that ROSPA could improve if used in conjunction with an on-line clutter suppression algorithm, such as SAM, and/or the various kinds of time series processing done prior to, or in place of, the FFT (wavelets, digital filters, polynomial fits, see subsection 3.1.2).

But even without on-line algorithms, there is certainly room for improvement. A better ground clutter removal algorithm might be devised, for instance, without the distortions mentioned previously. Many different kinds of non-linear digital filters, not necessarily based on order statistics, are available to us (Pitas and Venetsanopoulos, 1990; Astola and Kuosmanen, 1997). All we require is that, based on order statistics or not, the outputs of these filters must be robust with respect to outliers (see Rousseeuw and Leroy (1987) for an simple and intuitive introduction to the use of robust statistics for real data).

ROSPA uses two threshold parameters: a multiplicative threshold on the spectral data, used for the TMIN filter, and an additive threshold on the mean Doppler velocities, used for the TMED filter, both of which must be calibrated for each dataset with the help of good RASS velocity data. More sophisticated threshold schemes can therefore be used, though one must try to keep things as simple as possible. All of the improvements just mentioned might benefit from the use of fuzzy logic methods (one application of which was described in subsection 3.1.2). For example, one may use membership functions instead of the thresholds just mentioned.

6.3.2 Improving the Turbulence Temperature Correction

The temperature correction for turbulence, proposed by Peters and Angevine (1996), gives less than satisfactory results, at least with respect to short term temperature fluctuations. We saw this in the St-Anicet data, for which the temperature correction appeared to be an order of magnitude too small. Applying the temperature correction to the McGill data only made matters worse, although this was mainly due to poor spectral width retrievals by ROSPA. However, an adequate correction for turbulence may help in heat flux estimates and the calibration of ROSPA.

The turbulence temperature correction method employed in this thesis used exclusively the spectral width of the clear-air spectra. In fact, Peters and Angevine also took into account the effect of the horizontal wind on the temperature correction. For both the St-Anicet and McGill data, however, the horizontal winds were light, and not known very precisely, during the RASS observation periods. The horizontal winds were therefore neglected.

Peters and Angevine assumed that the turbulence above the RASS was both homogeneous and stationary, and that it was evident mainly in the spectral broadening of the clear-air Doppler spectra. This did not take into account the inhomogeneities and nonstationarities caused by the coherent structures in a CBL. It is entirely plausible that the shearing and shifting of the wind field brought on by a thermal can have important effects on the measured RASS temperature. Therefore, it seems that a more complete account of the effect of turbulence on RASS temperature measurements should include the changes of vertical air velocity in height and time.

6.3.3 Supporting Observations of the Urban Boundary Layer

The only urban boundary layer data used in this thesis were taken by the McGill profiler/RASS. But the data had to be treated by ROSPA to be useful. Therefore, other measurements of the urban boundary layer, preferably close to the McGill site, would also have been useful. Doppler sodar measurements of vertical velocity, for instance, would have permitted us to check on the effectiveness of ROSPA. Doppler sodar measurements of winds would also give us a better idea of the circulation pattern over and around the city, and whether there is any bias in the average vertical velocity profile in Fig. 6.2. Instrumented aircraft measurements over the city would have given us another set of profiles with which to verify the McGill profiler/RASS profiles. Obviously, other instruments may also contribute, directly or indirectly, to our understanding: tetroons, lidars, towers, and so on. The important thing is that such observations can be used to validate the treated profiler/RASS measurements, or enhance our knowledge of the urban boundary layer, or both.

Chapter 5 presented the results from the aircraft and the profiler/RASS data on the convective boundary layer, rural and urban, on June 28, 1996. In Chapter 6, we have dealt with some of the broader issues made relevant by the previous chapter. The following chapter will summarize the results of this thesis and state the conclusions.

Chapter 7

Conclusions

The work in this thesis sought, first, to develop a signal processing algorithm, named ROSPA, for heavily contaminated clear-air profiler/RASS measurements: second, to use ROSPA on urban RASS measurements and to compare them with rural RASS and aircraft measurements. ROSPA is based on order statistics and operates in two principal stages. The first stage treats the Doppler velocity power spectra of the clear-air measurements. It applies what is called a threshold minimum filter, which is a variant of the minimum filter, to successive spectral power values at a given fixed height and Doppler velocity bin. Various theoretical aspects of the minimum filter, and the threshold minimum filter, are explored using a model of the input time series. It is demonstrated that the minimum filter is highly insensitive to rare, brief, but very strong intermittent clutter power values. The threshold minimum filter is less restrictive than the minimum filter, as it allows for a more flexible, less rigid, output. As the name suggests, the threshold minimum filter requires that the value of a multiplicative spectral threshold be specified. It is shown, using the same model input, that an optimal spectral threshold value exists that accepts the most uncontaminated power values while rejecting the most intermittent clutter power values.

The second stage of ROSPA operates on the clear-air mean Doppler vertical velocity values. It imposes a moving X-shaped window on the time-height vertical air velocity data, which it uses in a median filter, called an X-median filter. Again, on the basis of model input data, it is shown that median filters are effective in exluding intermittent clutter from their outputs. In between the first and second stages, ROSPA uses intermediate steps to eliminate spectral white noise, ground clutter and to isolate the strongest peak in the spectrum. After the second stage, ROSPA eliminates the few remaining vertical air velocity outliers by using what is called a threshold median filter. It should be noted that the first and second stages form the core of ROSPA, while the intermediate steps and the outlier rejection procedure are not essential to ROSPA. They can be altered, improved or replaced without fundamentally changing ROSPA.

The aircraft and profiler/RASS data were taken on June 28, 1996, during the early afternoon which was clear and convective with weak winds. The aircraft data were taken between 1155 and 1335 EST, over mainly rural terrain where the height of the CBL was estimated from the aircraft data at about 1.2 km. The vertical air velocity power spectrum shows a peak between wavelenghts of 1 and 3.3 km and an inertial subrange extending from 330 m down to about 10 m. The aircraft virtual temperature power spectrum has its peak over slightly longer wavelengths, between 1.7 and 3.3 km. The aircraft heat flux cospectrum shows a sharp peak at the 2.5 km wavelength, and vanishes over the inertial subrange.

The profiler/RASS data taken at the rural St-Anicet site extend from 1045 to 1400 EST. The time-height SNR, virtual potential temperature, and vertical air velocity datasets over St-Anicet show an initially stable boundary layer, 0.6 km deep, from 1045 to 1230 EST. After that time there was a sudden growth of the boundary layer, which became convective and reached up to 1 km at the end of the observation period (1400 EST). Because of this evolution, the observation period was partitioned into an early period (1045 to 1230 EST) with a basically stable boundary layer, and a later period (1230 to 1400 EST) with a growing convective boundary layer. The structure of the convection over St-Anicet was consistent with the expected pattern of thin walls of warm rising air separating regions of cool descending air. The early vertical air velocity power spectrum has a broad maximum extending from 14 to 28 min periods with a maximum power value at 17 min, while the later vertical air velocity power spectrum has a maximum power value at a period of 9 min. Both the early and later virtual temperature power spectra are too contaminated by white noise to possess clearly distinguishable maxima. Also, the early and later heat flux cospectra possess peak values that are much greater than the aircraft cospectrum peak value, along with substantial negative components.

The profiler/RASS data taken at the urban McGill site extend from 1200 to 1530 EST. They show a very convective boundary layer initially 1.5 km deep, rising to 1.8 km deep at the end of the observation period. The McGill clear-air measurements are very contaminated by clutter, and so must be treated with ROSPA. The correlation between the RASS measurements and the treated vertical air velocity measurements is used as a guide to choose the threshold values. The theoretical aspects of the correlation between reliable RASS measurements and uncontaminated vertical air velocity measurements are explained. It is shown that a correlation value of about +90% is the most that can be reasonably expected in a CBL. For the optimal range of values of the spectral threshold, from 5 to 10 dB, a RASS-profiler correlation value as high as +89% is achieved. It is also demonstrated that the heat flux estimates are insensitive to the exact choice of the spectral threshold within the optimal range. The treated vertical air velocity data show a broad spectral maximum between 6 and 28 min periods, with a maximum at about 8 min. The heat flux cospectrum has a significant peak between about 8 to 17 min. The convective thermals over McGill appear more intense and longer lasting than the convection over St-Anicet. The covariance function of the treated vertical air velocity over McGill shows an integral timescale of 6 min (as compared to timescales of 2-3 min over St-Anicet) and a standard deviation of about 1.5 m/s (0.6-0.8 m/s over St-Anicet).

RASS-aircraft comparisons were done for profiles of vertical air velocity variance, vertical air velocity variance flux, and virtual heat flux. The St-Anicet vertical air velocity variance profiles, and the corresponding flux profiles, conform relatively well to the form expected in a CBL. The corresponding aircraft profiles have values that are consistently larger than the St-Anicet RASS values, and the profiles have a different form. This is attributed to the differences in the CBL between St-Anicet and the aircraft location. Also, the greater spatial resolution of the aircraft measurements allow it distinguish smaller eddies than a profiler, which contribute to the variance. The early heat flux profile does not agree very well with the aircraft profile, while the later heat flux profile agrees well with the aircraft measurements up to about 0.6 km AGL. Again, the difference is attributed to the different characteristics of the boundary layers at the aircraft location and at the St-Anicet site for the early and later periods.

The profile of vertical air velocity variance over McGill conforms reasonably well to the expected CBL profile, but the profiles of heat and vertical air velocity variance flux show unexpected negative values, particularly between 0.4 and 0.6 km AGL. It is suggested that a stationary convective eddy may reside over the McGill RASS. In support of this hypothesis, a profile of time-averaged vertical air velocity over the observation period, is presented. It shows a velocity profile that is everywhere positive and possesses a maximum between 0.4 and 0.6 km. The portion of the fluxes carried by the stationary eddy would be unaccounted for by the eddy-correlation method used on the profiler/RASS data. A close relationship is not expected between the McGill RASS and the aircraft profiles since the McGill profiles are urban in character while the aircraft profiles are rural. However, a least-squares fit of the lowest five McGill virtual heat flux estimates give a surface virtual heat flux value of $+523 \pm 239$ W/m^2, while a similar analysis on the aircraft virtual heat flux estimates gives a surface value of $+146 \pm 0.77$ W/m^2. The McGill surface virtual heat flux is thus about 3.5 times greater than the aircraft value (and also the later St-Anicet value), which is consistent with previous findings on urban and rural surface virtual heat flux values. Also, it is suggested that the aircraft samples many more flux-carrying coherent structures than the profiler/RASS, which might help explain the much greater errors on the McGill heat flux estimates relative to the aircraft error values.

The possibility that turbulence induced errors on the RASS temperature measurements adversely affects heat flux estimates is investigated using the temperature correction method proposed by Peters and Angevine (1996). The method uses mainly the clear-air spectral width to estimate the effect of turbulence on the RASS temperature. It is shown that, for the St-Anicet data, the temperature correction is approximately one order of magnitude too small to adequately account for the apparent temperature fluctuations due to turbulence, while for the McGill data, errors in clear-air spectral width estimates render the temperature correction unreliable. The effect of the temperature correction on both datasets is negligible.

Finally, we conclude that with the proper signal processing algorithm, the profiler/RASS can be a valuable tool for urban boundary layer studies. We believe that the algorithm proposed, ROSPA, was able to retrieve vertical air velocities accurate enough to produce acceptable second-order turbulent statistics. The expected flux profiles over McGill may have been caused by difficulties inherent in RASS measurements and independent of ROSPA, namely, RASS temperature errors and stationary convective eddies caused by the turbulence and mesoscale circulation characteristic of an urban boundary layer. As we have seen, profiler/RASS data treated with ROSPA allow us to determine a great deal about the urban boundary, including the evolution of the virtual potential temperature profile, the time-height structure of updrafts and downdrafts, and vertical fluxes of heat and vertical velocity variance. Even more can be learned if one has access to simultaneous urban measurements from other instruments at different location, and/or nearby rural measurements. We can predict that in the future, the profiler/RASS will play an important part in any urban boundary layer measurement project.

Appendix A

The Profiler Equation

The profiler is essentially a vertically pointing radar capable of detecting refractive index fluctuations in clear air, along with rain and snow. The refractive index fluctuations in air are caused principally by turbulence acting on an existing background gradient of refractivity, but can also, in the case of RASS, be created artificially by generating an appropriate acoustic wave. In the following, we shall use the work of Tatarski (1961) and Doviak and Zrnić (1993) to, first, explore the interaction between an electromagnetic wave and the refractive index field, and then derive the equation describing measurements by a profiler.

A.1 Fundamental Electrodynamics in Air

The Maxwell equations are

$$\vec{\nabla} \cdot \vec{D} = 4\pi\rho \tag{A.1}$$

$$\vec{\nabla} \cdot \vec{B} = 0 \tag{A.2}$$

$$\vec{\nabla} \times \vec{H} - \frac{1}{c}\frac{\partial \vec{D}}{\partial t} = \frac{4\pi}{c}\vec{J} \tag{A.3}$$

$$\vec{\nabla} \times \vec{E} + \frac{1}{c}\frac{\partial \vec{B}}{\partial t} = 0 \tag{A.4}$$

where $\vec{D}$ is the electric displacement field, ρ is the charge density field, $\vec{B}$ is the magnetic induction field, $\vec{H}$ is the magnetic field, $\vec{J}$ is the current density field, $\vec{E}$ is the electric field, and c is the speed of light. We assume that air is electrically neutral and nonconducting (i.e. $\rho = 0$ and $\vec{J} = 0$). Also, we assume that air is a simple isotropic medium (Jackson, 1975), which implies

$$\vec{D} = \epsilon \vec{E} \tag{A.5}$$

$$\vec{B} = \mu \vec{H} \tag{A.6}$$

where $\epsilon = \epsilon(\vec{x}, t)$ is the dielectric constant field, $\mu = \mu(\vec{x}, t)$ is the magnetic permeability field. Moreover, following Tatarski, we shall assume that $\mu = 1$ everywhere and for all time. The Maxwell equations now become,

$$\vec{\nabla} \cdot (\epsilon \vec{E}) = 0 \tag{A.7}$$

$$\vec{\nabla} \cdot \vec{H} = 0 \tag{A.8}$$

$$\vec{\nabla} \times \vec{H} - \frac{1}{c}\frac{\partial(\epsilon \vec{E})}{\partial t} = 0 \tag{A.9}$$

$$\vec{\nabla} \times \vec{E} + \frac{1}{c}\frac{\partial \vec{H}}{\partial t} = 0. \tag{A.10}$$

An equation involving only the electric field follows by taking the curl of Eq. A.10 and using the vector formula, $\vec{\nabla} \times (\vec{\nabla} \times \vec{E}) = \vec{\nabla}(\vec{\nabla} \cdot \vec{E}) - \nabla^2 \vec{E}$,

$$\vec{\nabla}(\vec{\nabla} \cdot \vec{E}) - \nabla^2 \vec{E} + \frac{1}{c}\frac{\partial}{\partial t}(\vec{\nabla} \times \vec{H}) = 0 \tag{A.11}$$

and using Eq. A.9 to eliminate the curl of the magnetic field,

$$\vec{\nabla}(\vec{\nabla} \cdot \vec{E}) - \nabla^2 \vec{E} + \frac{1}{c^2}\frac{\partial^2}{\partial t^2}(\epsilon \vec{E}) = 0. \tag{A.12}$$

Equation A.7 can be rewritten as $\vec{E}\cdot\vec{\nabla}\epsilon+\epsilon\vec{\nabla}\cdot\vec{E} = 0$, which yields $\vec{\nabla}\cdot\vec{E} = -\vec{E}\cdot\vec{\nabla}(\ln\epsilon)$. Using this in Eq. A.12, and writing the second-order time derivative explicitly, we obtain

$$-\vec{\nabla}(\vec{E}\cdot\vec{\nabla}(\ln\epsilon)) - \nabla^2\vec{E} + \frac{1}{c^2}\left[\vec{E}\frac{\partial^2\epsilon}{\partial t^2} + 2\frac{\partial\epsilon}{\partial t}\frac{\partial\vec{E}}{\partial t} + \epsilon\frac{\partial^2\vec{E}}{\partial t^2}\right] = 0. \tag{A.13}$$

The index of refraction satisfies the formula $n^2 = \epsilon\mu$, or in this case, $n^2 = \epsilon$. However, it is convenient to write $n = \overline{n}+\eta$, where $\overline{n}$ represents the ensemble average refractive index and η is the fluctuation with respect to the average. Also, $\overline{n}$ is usually very close to unity, so in what follows we will set $\overline{n} = 1$, and consequently $\epsilon \approx 1 + 2\eta$ and $\ln(\epsilon) \approx 2\eta$, to a first-order approximation. Equation A.13 then becomes

$$\nabla^2\vec{E} - \frac{1}{c^2}\frac{\partial^2\vec{E}}{\partial t^2} = -2\vec{\nabla}(\vec{E}\cdot\vec{\nabla}\eta) + \frac{2}{c^2}\left[\vec{E}\frac{\partial^2\eta}{\partial t^2} + 2\frac{\partial\eta}{\partial t}\frac{\partial\vec{E}}{\partial t} + \eta\frac{\partial^2\vec{E}}{\partial t^2}\right]. \tag{A.14}$$

Note that we need not formulate an equation for the magnetic field since for electromagnetic waves, the electric and magnetic fields are directly related to one another. It is sufficient, therefore, to determine only one of them.

A.2 Profiler Measurements

In order to proceed, we must make certain assumptions about the electric and refractive index fields. Since the source of the electromagnetic field is a profiler, we assume the field has a frequency very close to the profiler frequency (about 915 MHz in our case). We assume that the time dependence of the electric field has the form

$$\vec{E}(\vec{x},t) = \vec{E}(\vec{x})e^{-i\omega t} \tag{A.15}$$

where ω is the frequency of the radar wave, close to the profiler frequency ω_0. The difference is due to the interaction between the emitted radar wave and the evolving refractive index field. We assume the same form for the magnetic field. Equation

A.14 can be written as

$$\nabla^2\vec{E} + k^2\vec{E} = -2\vec{\nabla}(\vec{E}\cdot\vec{\nabla}\eta) + \frac{2\vec{E}}{c^2}\left[\frac{\partial^2\eta}{\partial t^2} - 2i\omega\frac{\partial\eta}{\partial t} - \omega^2\eta\right] \tag{A.16}$$

where $k^2 = (\omega/c)^2$ is the wavenumber squared of the radar wave. Note that if $\overline{n} \neq 1$, then we would have $k^2 = (\overline{n}\omega/c)^2$. If we postulate the existence of a characteristic scale η_* and a characteristic frequency Ω for the refractive index fluctuations, then we can say that $|\partial_t^2\eta| \approx \eta_*\Omega^2$ and $|\partial_t\eta| \approx \eta_*\Omega$. Note that η_* and Ω may either refer to the intensity and eddy turnover time of the energy-containing eddies of turbulence, or to the amplitude and frequency of an acoustic wave. Since it is reasonable to assume that $\eta_* \ll 1$ and $\Omega \ll \omega$, we can neglect the first two terms in the square brackets in Eq. A.16,

$$\nabla^2\vec{E} + k^2\vec{E} = -2\vec{\nabla}(\vec{E}\cdot\vec{\nabla}\eta) - 2k^2\eta\vec{E}. \tag{A.17}$$

Solving Eq. A.17 is simplified if we adopt the method of small perturbations, which entails using the expansion method to express to solution in the form (Hinch, 1991),

$$\vec{E} = \vec{E}_0 + \eta_*\vec{E}_1' + \eta_*^2\vec{E}_2' + \ldots \tag{A.18}$$

where $\vec{E}_j'$ represents the perturbation electric field associated with the j-th power of the refractive index fluctuations. Physically, $\vec{E}_0$ represents the emitted radar wave from the profiler. If there are no refractive index fluctuations ($\eta_* = 0$), then the emitted wave is the solution. Substituting the expansion in Eq. A.18 into Eq. A.17 and equating like coefficients, we obtain

$$\nabla^2\vec{E}_0 + k^2\vec{E}_0 = 0 \tag{A.19}$$

$$\nabla^2\vec{E}_1 + k^2\vec{E}_1 = -2\vec{\nabla}(\vec{E}_0\cdot\vec{\nabla}\eta) - 2k^2\eta\vec{E}_0 \tag{A.20}$$

where $\vec{E}_1 = \eta_* \vec{E}_1'$. We ignore the second-order and higher perturbation fields because $\eta_* \ll 1$. We therefore take the first-order perturbation field to constitute the entire product of the interaction between the emitted wave and the refractive index fluctuation field. Equation A.19 is a source-free wave equation for $\vec{E}_0$, while Eq. A.20 is a wave equation for $\vec{E}_1$ on the left-hand side, with the terms on the right-hand side acting as a source distribution for these waves. The field $\vec{E}_1$ can be seen as a superposition of spherical waves originating from the source distribution:

$$\vec{E}_1(\vec{x}, t) = -\frac{1}{4\pi}\int_{t'}\int_{V'} \vec{f}(\vec{x}', t')\frac{\delta(t - t' - |\vec{x} - \vec{x}'|/c)}{|\vec{x} - \vec{x}'|}\mathrm{d}V'\mathrm{d}t' \qquad \text{(A.21)}$$

where $\vec{f} = -2\vec{\nabla}(\vec{E}_0 \cdot \vec{\nabla}\eta) - 2k^2\eta\vec{E}_0$ is the source distribution, which we assume is completely contained in the volume V'. We can integrate Eq. A.21 with respect to t',

$$\vec{E}_1(\vec{x}, t) = -\frac{1}{4\pi}\int_{V'} \frac{\vec{f}(\vec{x}', t - |\vec{x} - \vec{x}'|/c)}{|\vec{x} - \vec{x}'|}\mathrm{d}V'. \qquad \text{(A.22)}$$

It is convenient to decompose the source distribution into two functions, $\vec{f}_1 = k^2\eta\vec{E}_0$ and $\vec{f}_2 = \vec{\nabla}(\vec{E}_0 \cdot \vec{\nabla}\eta)$, so that Eq. A.22 becomes

$$\vec{E}_1(\vec{x}, t) = \frac{1}{2\pi}\int_{V'} \frac{\vec{f}_1(\vec{x}', t - |\vec{x} - \vec{x}'|/c)}{|\vec{x} - \vec{x}'|}\mathrm{d}V' + \frac{1}{2\pi}\int_{V'} \frac{\vec{f}_2(\vec{x}', t - |\vec{x} - \vec{x}'|/c)}{|\vec{x} - \vec{x}'|}\mathrm{d}V'. \qquad \text{(A.23)}$$

We must now specify the emitted radar wave $\vec{E}_0$. Following Doviak and Zrnić (1993), we state

$$\vec{E}_0(r, \theta, \phi, t) = \frac{\vec{A}(\theta, \phi)}{r}U(t - r/c)\exp[-i\omega_0(t - r/c)] \qquad \text{(A.24)}$$

where r is the range from the profiler, θ is the angular deviation from the axis of the main lobe of the profiler beam, ϕ is the azimuthal angle about the axis of the main lobe, $\vec{A}(\theta, \phi)$ describes the angular distribution of emitted power within the beam,

ω_0 is the angular frequency of the profiler, and $U(t - r/c)$ describes the radial power distribution over the length of one pulse. Also, we assume

$$U(t^*) = 1, \qquad 0 \leq t^* \leq \tau$$
$$= 0, \qquad \text{otherwise} \tag{A.25}$$

where $t^* = t - r/c$ is the retardation time and describes a pulse traveling in the positive r direction at the speed of light. Equation A.24 basically describes a spherical wave emitted over a finite time, τ, and where the power is not evenly distributed over all directions, but rather is focused mainly in one direction. It is the spherical form of the wave that justifies the use of spherical coordinates. Equation A.24 is valid far from the profiler (see Jackson (1975) for the distinction between the near-field and far-field of an antenna system). Since by definition the line $\theta = 0$ is the axis of the main lobe of the profiler, which we assume is vertically pointing, it also corresponds to a vertical line.

Equation A.23 can be rewritten in spherical coordinates. Moreover, since the point $r = 0$ is the location of the profiler, and since the transmission and reception of the radar waves are done at the same place (a monostatic profiler; see Doviak and Zrnić (1993) and Doviak *et al.* (1994) for the bistatic case), and assuming we can neglect the finite aperture size of the profiler antenna, we are only interested in the returned electric field at $\vec{x} = 0$. We obtain

$$\vec{E}_1(0, t) = \frac{1}{2\pi}\int_{V'} \frac{\vec{f}_1(r', \theta', \phi', t - r'/c)}{r'} \mathrm{d}V' + \frac{1}{2\pi}\int_{V'} \frac{\vec{f}_2(r', \theta', \phi', t - r'/c)}{r'} \mathrm{d}V'. \tag{A.26}$$

Since the integrands in Eq. A.26 contain the emitted radar wave $\vec{E}_0$, they also contain the pulse function, where $U(t' - r'/c) \rightarrow U([t - r'/c] - r'/c) = U(t - 2r'/c)$ due to the integration with respect to t' in Eq. A.21. This means that we only need integrate with respect to r' over an interval $\Delta r' = c\tau/2$. We take $L = c\tau/2$ to be the *resolution length* of the profiler, which is only half as long as the length of the emitted pulse, $c\tau$. If we assume that the integration with respect to r' is centered about the value

r_0, and that $r_0 \gg \Delta r'$, then we can say that $(r')^{-1} \approx (r_0)^{-1}$ and remove it from the integrand,

$$\vec{E}_1(0,t) = \frac{1}{2\pi r_0}\int_{\phi=0}^{2\pi}\int_{\theta=0}^{\pi/2}\int_{r=r_0-L/2}^{r_0+L/2}[\vec{f}_1(r,\theta,\phi,t-r/c) + \vec{f}_2(r,\theta,\phi,t-r/c)]r^2\sin\theta \mathrm{d}r\mathrm{d}\theta\mathrm{d}\phi \tag{A.27}$$

where θ only extends to $\pi/2$ radians because the plane $\theta = \pi/2$ is parallel and close to the ground. Note that we dropped the primes for convenience. Given a function $g(\vec{x},t^*) = g(\vec{x},t-r/c)$, and that t is held constant, we can define a total gradient operator:

$$\vec{\nabla}_T g(\vec{x},t^*) = \vec{\nabla} g(\vec{x},t^*) + \vec{\nabla} t^* \frac{\partial}{\partial t^*} g(\vec{x},t^*) \tag{A.28}$$

where $\vec{\nabla}_T$ is the total gradient operator, one that takes into account the fact $t^* = t - r/c$, and $\vec{\nabla}$ is the gradient operator for fixed t^*. In other words, the function $g'(\vec{x},t) = g(\vec{x},t-r/c)$ does not have the same spatial dependence as $g(\vec{x},t)$, which must be taken into account when finding the gradient of $g'(\vec{x},t)$. This means that $\vec{\nabla}_T g(\vec{x},t^*) = \vec{\nabla} g'(\vec{x},t)$. As it turns out, $\vec{f}_2 = \vec{\nabla} g$, where $g = \vec{E}_0 \cdot \vec{\nabla}\eta$, and $\vec{\nabla} t^* = -c^{-1}\vec{\nabla} r = -c^{-1}\hat{r}$, where $\hat{r}$ is the unit radial vector. Equation A.28 now gives

$$\vec{f}_2 = \vec{\nabla}_T(\vec{E}_0 \cdot \vec{\nabla}\eta) + \frac{\hat{r}}{c}\frac{\partial}{\partial t^*}(\vec{E}_0 \cdot \vec{\nabla}\eta). \tag{A.29}$$

The second term in Eq. A.29 can be approximated as $c^{-1}\hat{r}\partial_{t^*}(\vec{E}_0 \cdot \vec{\nabla}\eta) \approx -ik\hat{r}(\vec{E}_0 \cdot \vec{\nabla}\eta)$ where $k = \omega/c \approx (\omega_0 + \Omega)/c$. Here, we take the angular frequency of the returned wave, ω, to be about equal to the sum of the incident wave angular frequency, ω_0, and the characteristic angular frequency of the refractive index fluctuations, Ω. When we place Eq. A.29 into Eq. A.27, we see that Gauss' theorem applies to the volume integral of the first term of Eq. A.29, thereby turning it into a surface integral. But since the boundary of the integration volume is arbitrary, and since the electric field vanishes outside the pulse volume of the profiler, the boundary can always be pushed out where the surface integral vanishes. Therefore, only the second term contributes to the integral. We can apply the same reasoning to obtain

$$\vec{E}_0 \cdot \vec{\nabla}\eta = \vec{\nabla}_T(\eta\vec{E}_0) - \eta\vec{\nabla}_T \cdot \vec{E}_0 + \frac{\vec{E}_0 \cdot \hat{r}}{c}\frac{\partial\eta}{\partial t^*} \tag{A.30}$$

where the first term can be neglected as before, the gradient of the incident electric field in the second term is proportional to $1/r_0^2$, which we neglect, and the third term is zero since $\vec{E}_0$ is a transverse wave propagating in the $\hat{r}$ direction ($\vec{E}_0 \cdot \hat{r} = 0$). We conclude that $\vec{f}_2$ does not contribute significantly to Eq. A.27. Note that $\vec{f}_2$ vanishes only because the profiler is monostatic; for the bistatic case, $\vec{f}_2$ would ensure that the received waves are transverse (Tatarski, 1961; Doviak and Zrnić, 1993). This leaves us with

$$\vec{E}_R(t) = \frac{k^2}{2\pi r_0} \int_{V_p} \vec{E}_0(r, \theta, \phi, t - r/c)\eta(r, \theta, \phi, t - r/c)\mathrm{d}V_p, \tag{A.31}$$

where $\vec{E}_R(t) = \vec{E}_1(0, t)$ is the returned electric field; V_p is the pulse volume whose boundaries propagate in the positive r direction at half the speed of light. If we insert Eq. A.24 into Eq. A.31, and we approximate $r^{-1} \approx r_0^{-1}$:

$$\vec{E}_R(t) = \frac{k^2}{2\pi r_0^2} \int_{\phi=0}^{2\pi} \int_{\theta=0}^{\pi/2} \int_{r=r_0-L/2}^{r_0+L/2} \vec{A}(\theta, \phi) e^{i(2k_0 r - \omega_0 t)} \eta(r, \theta, \phi, t - r/c)\mathrm{d}V_p \tag{A.32}$$

where $k_0 = \omega_0/c$ and $r_0 = ct/2$ is also a function of time. Equation A.32 describes the returned electric field of one pulse emitted at $t = 0$. Of greater relevance to us, however, is the *detected* electric field, which is the electric field after its reception by the profiler antenna. It is given as

$$E_D(t) = \frac{k^2}{2\pi r_0^2} \int_{\phi=0}^{2\pi} \int_{\theta=0}^{\pi/2} \int_{r=r_0-L/2}^{r_0+L/2} |\vec{A}(\theta, \phi)|^2 e^{i(2k_0 r - \omega_0 t)} \eta(r, \theta, \phi, t - r/c)\mathrm{d}V_p \tag{A.33}$$

where $|\vec{A}(\theta, \phi)|^2$ expresses both the transmission and reception of the electric field for a monostatic profiler, and where we can ignore the vector nature of the detected electric field (Doviak and Zrnić, 1993).

Of interest is the detected electric field from a fixed height. To accomplish this, the profiler emits pulses at regular intervals, T_{ipp}, called the inter-pulse period (IPP). A specific altitude, r_0, is isolated when the profiler measures the detected field at a time $T_0 = 2r_0/c$ after the emission of the latest pulse. If the pulses are emitted at the times $t_n = nT_{\text{ipp}}$, where $n = ..., -2, -1, 0, 1, 2, ...$, then the detected field is measured at the times $t_n + T_0$. We can now construct a time-height data field,

$$E_p(n, r_0) = E_D(nT_{\text{ipp}} + 2r_0/c) \tag{A.34}$$

where $E_p(n, r_0)$ is the form of the data recorded by the profiler. The height can only be unambiguously determined if the detected electric field from one pulse vanishes before the emission of the next pulse. The maximum unambiguous height is given as $r_a = cT_{\text{ipp}}/2$. Otherwise, there will be confusion whether a given detected field is due to a highly reflective object at high altitudes, $r > r_a$, reflecting energy from the pulse previous to the latest, or a weakly reflective object at low altitudes, $r < r_a$, reflecting energy from the latest pulse. This phenomenon is known as *range folding*.

We can now formulate the equation describing the detected electric field of a pulsed Doppler radar. We simply place Eq. A.34 in Eq. A.33 to obtain

$$E_p(n, r_0) = \frac{k^2}{2\pi r_0^2} \int_{\phi=0}^{2\pi} \int_{\theta=0}^{\pi/2} \int_{r=r_0-L/2}^{r_0+L/2} |\vec{A}(\theta, \phi)|^2 e^{i(2k_0 r_p - \omega_0 T_{\text{ipp}} n)}$$
$$\eta(r, \theta, \phi, nT_{\text{ipp}} + r_0/c - r_p/c) \mathrm{d}V_p \tag{A.35}$$

where, for convenience, we have defined $r_p = r - r_0$.

Appendix B

Discrete-Time Signal Processing

The profilers used here are pulsed radars. Morever, the discrete-time data given by the profiler can be regarded as the sampling by instantaneous measurements equally spaced in time of a hypothetical continuous atmospheric signal. It is then important to review the special characteristics of discrete-time signal processing. We will explore the theory behind the discrete Fourier transform (DFT), which is based mainly on the work of Oppenheim and Schafer (1989).

B.1 Discrete Time Sampling

Given a continuous-time signal, $x_c(t)$, where $-\infty < t < \infty$ is a real time parameter, we can create a discrete-time time series, $x[n]$, as follows,

$$x[n] = x_c(nT) \qquad n = ..., -2, -1, 0, 1, 2, ... \tag{B.1}$$

where n is an integer time parameter and T is the sampling interval. Note that square brackets are used to indicate a discrete argument. Also note that x and x_c may be complex. We define the Fourier transform

$$X(\omega) = \sum_{n=-\infty}^{\infty} x[n]e^{-i\omega n} \tag{B.2}$$

where X is a continuous function of the real angular frequency ω. The Fourier transform is periodic in ω with a period of 2π,

$$X(\omega + 2\pi k) = \sum_{n=-\infty}^{\infty} x[n]e^{-i\omega n - i2\pi kn} \tag{B.3}$$

$$= \sum_{n=-\infty}^{\infty} x[n]e^{-i\omega n}(e^{-i2\pi})^{kn} \tag{B.4}$$

$$= X(\omega) \tag{B.5}$$

since $e^{-i2\pi} = 1$ and where k is any integer.

The inverse Fourier transform is

$$x[n] = \frac{1}{2\pi}\int_{-\pi}^{\pi} X(\omega)e^{i\omega n}\mathrm{d}\omega \tag{B.6}$$

where the periodicity of $X(\omega)$ means we need only integrate from $-\pi$ to π because that interval contains all the information necessary to retrieve the time series.

The Fourier transform of the continuous-time signal is

$$X_c(\Omega) = \int_{-\infty}^{\infty} x_c(t)e^{-i\Omega t}\mathrm{d}t \tag{B.7}$$

which we will call the *continuous Fourier transform*. Just as we went from a continuous to a discrete time, $t \to nT$, the angular frequencies transform as $\Omega \to \omega/T$. The inverse continuous Fourier transform is

$$x_c(t) = \frac{1}{2\pi}\int_{-\infty}^{\infty} X_c(\Omega)e^{i\Omega t}\mathrm{d}\Omega. \tag{B.8}$$

We can place Eq. B.8 into Eq. B.1 to obtain

$$x[n] = \frac{1}{2\pi}\int_{-\infty}^{\infty} X_c(\Omega)e^{i\Omega Tn}\mathrm{d}\Omega \tag{B.9}$$

which we then place in Eq. B.2,

$$X(\omega) = \frac{1}{2\pi}\int_{-\infty}^{\infty} X_c(\Omega)\left[\sum_{n=-\infty}^{\infty} e^{i(\Omega T - \omega)n}\right]\mathrm{d}\Omega. \tag{B.10}$$

Furthermore, we know that (Oppenheim and Schafer, 1989)

$$\frac{1}{2\pi}\sum_{n=-\infty}^{\infty} e^{i(\Omega T-\omega)n} = \sum_{k=-\infty}^{\infty} \delta(\omega-\Omega T+2\pi k) \tag{B.11}$$

which, if we place in Eq. B.10 we get

$$X(\omega)=\frac{1}{T}\sum_{k=-\infty}^{\infty} X_c\left(\frac{\omega}{T}+\frac{2\pi k}{T}\right) \qquad -\pi\le\omega<\pi. \tag{B.12}$$

As Eq. B.6 showed, the angular frequency bandwidth $-\omega_N \le \omega < \omega_N$, where $\omega_N = \pi$ is the limit frequency, includes all meaningful angular frequencies of the Fourier transform. The corresponding physical frequency, $2\pi f_N = \omega_N/T \rightarrow f_N = 1/(2T)$ is called the *Nyquist frequency.* The Nyquist frequency represents the range of frequencies that can be unambiguously recorded by the sampling operation, Eq. B.1. That is, if the continuous Fourier transform, $X_c(\Omega)$, vanished outside the angular frequency interval $-2\pi f_S \le \Omega < 2\pi f_S$ and if $f_S < f_N$, then all the frequencies of the continuous signal have been adequately recorded. In that case, only the $k=0$ term in Eq. B.12 contributes to the sum and we have

$$X(\omega)=\frac{1}{T}X_c\left(\frac{\omega}{T}\right) \qquad -\pi\le\omega<\pi \tag{B.13}$$

which is an unambiguous relationship between $X(\omega)$ and $X_c(\Omega)$. If, on the other hand, $f_S > f_N$ but $f_S < 2f_N$, then Eq. B.12 becomes

$$\begin{aligned} X(\omega) &= \frac{1}{T}X_c\left(\frac{\omega}{T}\right)+\frac{1}{T}X_c\left(\frac{\omega}{T}+\frac{2\pi}{T}\right) \qquad && -\pi\le\omega<0 \\ &= \frac{1}{T}X_c\left(\frac{\omega}{T}\right)+\frac{1}{T}X_c\left(\frac{\omega}{T}-\frac{2\pi}{T}\right) && 0\le\omega<\pi \end{aligned} \tag{B.14}$$

and so on for even greater values of f_S. This phenomenon is called *aliasing* and represents the spectral energy outside the Nyquist bandwidth being folded back into it. Aliasing is a major preoccupation when selecting parameters, such as the IPP, for instance, of radar systems.

B.2 Periodic Time Series

We introduce a periodic time series $x_p[n]$, which is defined as

$$x_p[n] = x_p[n + lN] \tag{B.15}$$

where $l = ..., -2, -1, 0, 1, 2, ...$ is an arbitrary integer, and N is the period of the time series. It can be shown that for a periodic time series, we do not need a Fourier transform continuous in frequency, like the one defined in Eq. B.7 (Oppenheim and Schafer, 1989). Rather, a Discrete Fourier Transform (DFT), $X_p[k]$, ($k = 0, ..., N-1$ is a discrete frequency index) is enough to completely specify the periodic time series, $x_p[n]$. The DFT and inverse DFT are, respectively:

$$X_p[k] = \sum_{n=0}^{N-1} x_p[n] W_N^{kn} \tag{B.16}$$

and

$$x_p[n] = \frac{1}{N} \sum_{k=0}^{N-1} X_p[k] W_N^{-kn} \tag{B.17}$$

where $W_N = e^{-i(2\pi/N)}$. The discrete frequency in Eq. B.17 is summed over positive values only (from 0 to $N-1$). This is solely a matter of convention. The periodicity of the Fourier transform ensures that $X_p[k] = X_p[k-N]$. From that, it is easy to show that k in Eq. B.17 can also be summed from $-N/2$ to $N/2-1$. In that case, the sum over the discrete frequency k in Eq. B.17 is analogous to the integral over the continuous frequency ω in Eq. B.6.

B.3 Windowing

In practice, we never have access to an infinitely long time series. Instead, we only have a finite number of points to estimate the Fourier transform of the infinite time series, $X(\omega)$. The sampled time series can be expressed as

$$x_w[n] = w[n]x[n] \tag{B.18}$$

where $x[n]$ is the infinitely long time series, and $w[n]$ is the *window* which determines both the size of the sample and the weight of every point in the sample. For example, if we sample N points only ($n = 0...N-1$) with equal weight, we have a *rectangular* window

$$\begin{aligned} w[n] &= 1 \qquad 0 \leq n \leq N-1 \\ &= 0 \qquad \text{otherwise.} \end{aligned} \tag{B.19}$$

The Fourier transform of the rectangular window is

$$W(\omega) = e^{-i\omega(N-1)/2} \frac{\sin(\omega N/2)}{\sin(\omega/2)}. \tag{B.20}$$

The windowed Fourier transform, $X_w(\omega)$, is

$$\begin{aligned} X_w(\omega) &= \sum_{n=-\infty}^{\infty} x_w[n]e^{-i\omega n} \\ &= \sum_{n=-\infty}^{\infty} w[n]x[n]e^{-i\omega n} \\ &= \sum_{n=-\infty}^{\infty} \left(\frac{1}{2\pi}\int_{-\pi}^{\pi} W(\alpha)e^{i\alpha n}\mathrm{d}\alpha\right)\left(\frac{1}{2\pi}\int_{-\pi}^{\pi} X(\beta)e^{i\beta n}\mathrm{d}\beta\right)e^{-i\omega n}. \end{aligned} \tag{B.21}$$

Rearranging the order of integration and summation, and using Eq. B.11, we obtain

$$\begin{aligned} X_w(\omega) &= \frac{1}{2\pi}\int_{-\pi}^{\pi}\int_{-\pi}^{\pi} W(\alpha)X(\beta)\left(\frac{1}{2\pi}\sum_{n=-\infty}^{\infty} e^{i(\alpha+\beta-\omega)n}\right)\mathrm{d}\beta\mathrm{d}\alpha \\ &= \frac{1}{2\pi}\int_{-\pi}^{\pi}\int_{-\pi}^{\pi} W(\alpha)X(\beta)\left(\sum_{k=-\infty}^{\infty}\delta(\omega-\alpha-\beta+2\pi k)\right)\mathrm{d}\beta\mathrm{d}\alpha. \end{aligned} \tag{B.22}$$

We integrate with respect to β and exploit the periodicity of $X(\omega)$ to obtain

$$\begin{aligned} X_w(\omega) &= \frac{1}{2\pi}\int_{-\pi}^{\pi} W(\alpha)X(\omega-\alpha)\mathrm{d}\alpha \\ X_w &= W * X \end{aligned} \tag{B.23}$$

where the asterisk denotes the preceding operation, namely a *convolution*. Most windows in use have a Fourier transform with same basic shape. The magnitude, $|W(\alpha)|$, is symmetric about $\alpha = 0$, with a main lobe at zero frequency and side lobes on either side. Therefore, Eq. B.23 means that those values of $X(\omega - \alpha)$ in the neighbourhood of $\alpha = 0$ contribute the most to $X_w(\omega)$. The existence of side lobes means that there is also a contribution from frequencies far from ω. The contribution to $X_w(\omega)$ from frequencies other than ω is called *leakage* due to windowing.

Two other relevant windows are the *Hanning* and *Hamming* windows. The Hanning window has the form

$$\begin{aligned} w[n] &= 0.5 - 0.5\cos(2\pi n/(N-1)) \qquad && 0 \leq n \leq N-1 \\ &= 0 && \text{otherwise} \end{aligned} \tag{B.24}$$

and the Hamming window

$$\begin{aligned} w[n] &= 0.54 - 0.46\cos(2\pi n/(N-1)) \qquad && 0 \leq n \leq N-1 \\ &= 0 && \text{otherwise.} \end{aligned} \tag{B.25}$$

Of the three windows seen here, the rectangular window has the narrowest main lobe with a width of $4\pi/N$, as compared with the Hanning and Hamming windows, with $8\pi/(N-1)$ each. However, the peak side lobe power of the rectangular window is 13 dB less than the peak power of the main lobe. This is much more than the Hanning window, at 31 dB less, as well as the Hamming window, at 41 dB less (Oppenheim and Schafer, 1989).

Appendix C

Hypothesis Tests

A *hypothesis test* is a test performed on a random variable used for deciding whether or not that variable belongs to a specified probability distribution (see, for instance, Bendat and Piersol (1966) for an demonstration of such a test on data). We begin by defining a *null hypothesis*, H_0, which is the statement that the random variable, x, belongs to the probability density function $f(x)$, with distribution $F(x) = \int_x^\infty f(x')\mathrm{d}x'$. Conversly, we define the *alternative hypothesis*, H_1, which is simply the statement that the random variable does not belong to the distribution $F(x)$. Consequently, if H_1 is true, then we postulate the distribution $G(x)$. However, in most cases only $F(x)$ is known precisely. Note that H_1 is simply the opposite of H_0. Therefore, in what follows, when we say that H_0 is true (accepted), we also mean that H_1 is false (rejected), and vice-versa.

We must now define a *region of rejection* or a *critical region* C, which is the set of values of x where H_0 is rejected (and H_1 accepted). Conversely, we define a *region of acceptance* where H_0 is accepted (and H_1 rejected). To this end, we introduce an interval with bounds $a < b$, where the critical region C is $-\infty < x < a$ and $b \leq x < \infty$, and the region of acceptance is $a \leq x < b$.

As Table C.1 indicates, there are four possibilities to consider. The first is where we accept H_0 when it is true. The second is where we reject H_0 when it is true, which

Table C.1: The possible conclusions regarding the truth of H_0 (left to right) and the decision to accept or reject H_0 (top to bottom). The probability of making a type *I* error is α, and β for a type *II* error.

	H_0 is true	H_0 is false
H_0 is accepted	Correct decision	Type *II* error (β)
H_0 is rejected	Type *I* error (α)	Correct decision

is called a type *I* error and has a probability α. If H_0 is true, then x has the distribution $F(x)$. So the probability of accepting H_0 is $F(a) - F(b)$ and $\alpha = 1 - F(a) + F(b)$. The probability of making a type *I* error is also called the *significance level* of the test. The third possibility is where H_0 is rejected when it is false. Finally, the forth is where H_0 is accepted when it is false, which is called a type *II* error and has a probability $\beta = G(b) - G(a)$.

Since rejecting the null hypothesis when it is in fact true is often considered serious, α is usually made small, typically $\alpha \leq 0.1$. If we do not know the form of $G(x)$, then β is also unknown. In general, though, when we decrease α, we also increase β.

References

ANGELL, J. K., HOECKER, W. H., DICKSON, C. R., AND PACK, D. H. (1973). Urban influence on a strong daytime air flow as determined from tetroon flights. *J. Appl. Meteor.*, 12:924–936.

ANGEVINE, W. M. (1994). Heat and momentum flux measurements in the planetary boundary layer with a wind profiling radar/radio acoustic sounding system. Report NOAA Tech. Mem. ERL AL-12, NOAA/ERL Aeronomy Lab.

ANGEVINE, W. M. (1997). Errors in mean vertical velocities measured by boundary layer wind profilers. *J. Atmos. Ocean. Tech.*, 14(3):565–569.

ANGEVINE, W. M., AVERY, S. K., ECKLUND, W. L., AND CARTER, D. A. (1993a). Fluxes of heat and momentum measured with a boundary-layer wind profiler radar-radio acoustic sounding system. *J. Appl. Meteor.*, 32:73–80.

ANGEVINE, W. M., AVERY, S. K., AND KOK, G. L. (1993b). Virtual heat flux measurements from a boundary-layer profiler-RASS compared to aircraft measurements. *J. Appl. Meteor.*, 32:1901–1907.

ANGEVINE, W. M., BAKWIN, P. S., AND DAVIS, K. J. (1998). Wind profiler and RASS measurements compared with measurements from a 450-m-tall tower. *J. Atmos. Ocean. Tech.*, 15:818–825.

ANGEVINE, W. M., DOVIAK, R. J., AND SORBJAN, Z. (1994a). Remote sensing of vertical velocity variance and surface heat flux in a convective boundary layer. *J. Appl. Meteor.*, 33:977–983.

ANGEVINE, W. M. AND ECKLUND, W. L. (1994). Errors in radio-acoustic sounding of temperature. *J. Atmos. Ocean. Tech.*, 11:837–842.

ANGEVINE, W. M., ECKLUND, W. L., CARTER, D. A., GAGE, K. S., AND MORAN, K. P. (1994b). Improved radio acoustic sounding techniques. *J. Atmos. Ocean. Tech.*, 11:42–49.

ANGEVINE, W. M., WHITE, A. B., AND AVERY, S. K. (1994c). Boundary-layer depth and entrainment zone characterization with a boundary-layer profiler. *Boundary-Layer Meteorol.*, 68:375–385.

ANTONIA, R. A., CHAMBERS, A. J., AND PHAN-THIEN, N. (1980). Taylor's hypothesis and spectra of velocity and temperature derivatives in a turbulent shear flow. *Boundary-Layer Meteorol.*, 19:19–29.

ARCE, G. R., GALLAGHER, N. C., AND NODES, T. A. (1986). Median filters: theory for one- and two- dimensional filters. In HUANG, T. S., editor, *Advances in computer vision and image processing*, volume 2, pages 89–166. Greenwich, Connecticut / London, England. JAI Press Inc.

ARFKEN, G. (1985). *Mathematical Methods for Physicists.* Academic Press, Inc., Orlando/San Diego, 3rd edition. 985 pp.

ASTOLA, J. AND KUOSMANEN, P. (1997). *Fundamentals of Nonlinear Digital Filtering.* CRC Press, Boca Raton/New York. 276 pp.

ATAMAN, E., AATRE, V. K., AND WONG, K. M. (1981). Some statistical properties of median filters. *IEEE Trans. Acoustics, Speech, Signal Processing*, ASSP-29(5):1073–1075.

ATLAS, D. (1962). Indirect probing techniques. *Bull. Amer. Meteor. Soc.*, 43(9):457–466.

BARNES, G., EMMITT, G. D., BRUMMER, B., LEMONE, M. A., AND NICHOLLS, S. (1980). The structure of a fair weather boundary layer based on the results of several measurement strategies. *Mon. Wea. Rev.*, 108:349–364.

BARNETT, V. AND LEWIS, T. (1978). *Outliers in Statistical Data.* Wiley, Chichester. 365 pp.

BATEMAN, H. (1918). Mathematical theory of sound ranging. *Mon. Wea. Rev.*, 46:4–11.

BAUER, M. AND PETERS, G. (1993). On the altitude coverage of temperature profiling by RASS. In *Preprints, 26th International Conference on Radar Meteorology*, pages 487–489, Norman, Oklahoma. Amer. Meteor. Soc.

BENDAT, J. S. AND PIERSOL, A. G. (1966). *Measurement and Analysis of Random Data*. Wiley, New York. 390 pp.

BERGSTROM, R. W. AND VISKANTA, R. (1973a). Modeling of the effects of gaseous and particulate pollutants in the urban atmosphere. part I: Thermal structure. *J. Appl. Meteor.*, 12(6):901–912.

BERGSTROM, R. W. AND VISKANTA, R. (1973b). Modeling of the effects of gaseous and particulate pollutants in the urban atmosphere. part II: Pollutant dispersion. *J. Appl. Meteor.*, 12(6).

BONINO, G., LOMBARDINI, P. P., LONGHETTO, A., AND TRIVERO, P. (1981). Radio acoustic measurement of fog-capping thermal inversions. *Nature*, 290:121–123.

BORNSTEIN, R. D. (1968). Observations of the urban heat island effect in New York City. *J. Appl. Meteor.*, 7:575–582.

BROWN, E. H. AND CLIFFORD, S. F. (1976). On the attenuation of sound by turbulence. *J. Acoust. Soc. Am.*, 60(4):788–794.

CARSON, J. D. (1973). The development of a dry inversion-capped convectively unstable boundary layer. *Quart. J. R. Met. Soc.*, 99:450–467.

CASADIO, S., DI SARRA, A., FIOCCO, G., FUÀ, D., LENA, F., AND RAO, M. (1996). Convective characteristics of the nocturnal urban boundary layer as observed with Doppler sodar and Raman lidar. *Boundary-Layer Meteorol.*, 79:375–391.

CAUGHEY, S. J. (1984). Observed characteristics of the atmospheric boundary layer. In NIEUWSTADT, F. T. M. AND VAN DOP, H., editors, *Atmospheric turbulence and air pollution modelling*, pages 107–158, Dordrecht/Boston/Lancaster. D. Reidel Publishing Company.

CHERNOV, L. A. (1960). *Wave Propagation in a Random Medium*. Dover, New York. 168 pp.

CHING, J. K. S., CLARKE, J. F., AND GODOWITCH, J. M. (1983). Modulation of heat flux by different scales of advection in an urban environment. *Boundary-Layer Meteorol.*, 25:171–191.

CLIFFORD, S. F. AND BROWN, E. H. (1970). Propagation of sound in a turbulent atmosphere. *J. Acoust. Soc. Am.*, 48(5):1123–1127.

CLIFFORD, S. F. AND WANG, T.-I. (1977). The range limitation on Radar-Acoustic Sounding Systems (RASS) due to atmospheric refractive turbulence. *IEEE Trans. Ant. Prop.*, AP-25(3):319–326.

CLOTHIAUX, E. E., PENC, R. S., THOMSON, D. W., ACKERMAN, T. P., AND WILLIAMS, S. R. (1994). A first-guess feature-based algorithm for estimating wind speed in clear-air Doppler radar spectra. *J. Atmos. Ocean. Tech.*, 11:888–908.

COHN, S. A., GYAKUM, J. R., ROGERS, R. R., ECKLUND, W. L., CARTER, D. A., AND WILSON, J. S. (1996). Wind profiler/RASS observations of two complex synoptic events. *Beitr. Phys. Atmosph.*, 69(1):37–48.

CORNMAN, L. B., GOODRICH, R. K., MORSE, C. S., AND ECKLUND, W. L. (1998). A fuzzy-logic method for improved moment estimation from Doppler spectra. *J. Atmos. Ocean. Tech.* in press.

CRAMER, O. (1993). The variation of the specific heat ratio and the speed of sound in air with temperature, pressure, humidity, and CO_2 concentration. *J. Acoust. Soc. Am.*, 93(5):2510–2516.

DAVID, H. A. (1970). *Order Statistics*. Wiley, New York. 272 pp.

DELAGE, Y. AND TAYLOR, P. A. (1970). Numerical studies of heat island circulations. *Boundary-Layer Meteorol.*, 1:201–226.

DEMARRAIS, G. A. (1961). Vertical temperature difference observed over an urban area. *Bull. Amer. Meteor. Soc.*, 42(8):548–554.

DESJARDINS, R. L., MACPHERSON, J. I., NEUMANN, H., DEN HARTOG, G., AND SCHUEPP, P. H. (1995). Flux estimation of latent and sensible heat, carbon dioxide, and ozone using an aircraft-tower combination. *Atmospheric Environment*, 29(21):3147–3158.

DOBOSY, R. J., CRAWFORD, T. L., MACPHERSON, J. I., DESJARDINS, R. L., KELLY, R. D., ONCLEY, S. P., AND LENSCHOW, D. H. (1997). Intercomparison among the four flux aircraft at boreas in 1994. *J. Geophys. Res.*, 102(D24):29,101–29,111.

DOVIAK, R. J., LATAITIS, R. J., HOLLOWAY, C. L., AND VAN BAELEN, J. (1994). A general theoretical analysis of cross-correlation and cross-spectra for spaced-antenna wind profilers. Report NCAR/TN-407+STR, Oct., National Center for Atmospheric Research. 105 pp.

DOVIAK, R. J. AND ZRNIĆ, D. S. (1993). *Doppler Radar and Weather Observations.* Academic Press, Inc., San Diego, 2nd edition. 562 pp.

DUCKWORTH, F. S. AND SANDBERG, J. S. (1954). The effect of cities upon horizontal and vertical temperature gradients. *Bull. Amer. Meteor. Soc.*, 35(5):198–207.

EMANUEL, K. A. (1994). *Atmospheric Convection.* Oxford University Press, New York/Oxford. 580 pp.

ENVIRONMENT CANADA (1987). The climate of Montreal. Climatological Studies 39, Atmospheric Environment Service, Downsview, Ontario. 62 pp.

FELLER, W. (1971). *An Introduction to Probability Theory and Its Applications*, volume II. Wiley, New York, 2nd edition. 669 pp.

GAGE, K. S. AND BALSLEY, B. B. (1978). Doppler radar probing of the clear atmosphere. *Bull. Amer. Meteor. Soc.*, 59(9):1074–1093.

GAGE, K. S., GREEN, J. L., AND VANZANDT, T. E. (1980). Use of Doppler radar measurement of atmospheric turbulence parameters from the intensity of clear-air echoes. *Radio Sci.*, 15(2):407–416.

GALLAGHER, N. C. AND WISE, G. L. (1981). A theoretical analysis of the properties of median filters. *IEEE Trans. Acoustics, Speech, Signal Processing*, ASSP-29(6):1136–1141.

GARRATT, J. R. (1990). The internal boundary layer - a review. *Boundary-Layer Meteorol.*, 50:171–203.

GARRATT, J. R. (1992). *The Atmospheric Boundary Layer.* Cambridge University Press, 1st edition. 316 pp.

GIOVANNONI, J.-M. (1987). A laboratory analysis of free convection enhanced by a heat island in a calm and stratified environment. *Boundary-Layer Meteorol.*, 41:9–26.

GODOWITCH, J. M. (1986). Characteristics of vertical turbulent velocities in the urban convective boundary layer. *Boundary-Layer Meteorol.*, 35:387–407.

GODOWITCH, J. M., CHING, J. K. S., AND CLARKE, J. F. (1987). Spatial variation of the evolution and structure of the urban boundary layer. *Boundary-Layer Meteorol.*, 38:249–272.

GOSSARD, E. E. AND STRAUCH, R. G. (1983). *Radar observation of clear air and clouds.* Elsevier, Amsterdam. 280 pp.

GOSSARD, E. E., WOLFE, D. E., MORAN, K. P., PAULUS, R. A., ANDERSON, K. D., AND ROGERS, L. T. (1998). Measurement of clear-air gradients and turbulence properties with radar wind profilers. *J. Atmos. Ocean. Tech.*, 15:321-341.

GRANT, R. H., BERTOLIN, G. E., AND HERRINGTON, L. P. (1986). The intermittent vertical heat flux over a spruce forest canopy. *Boundary-Layer Meteorol.*, 35:317-330.

HAMMON, W. H. AND DUENCHEL, F. W. (1902). Abstract of a comparison of the minimum temperatures recorded at the U.S. weather bureau and the forest park meteorological observatories, St. Louis, Missouri, for the year 1891. *Mon. Wea. Rev.*, 30(1):11-12.

HARRIS, C. M. (1966). Absorption of sound in air versus humidity and temperature. *J. Acoust. Soc. Am.*, 40(1):148-159.

HARRIS, C. M. (1971). Effects of humidity on the velocity of sound in air. *J. Acoust. Soc. Am.*, 49(3):890-893.

HEYGSTER, G. (1982). Rank filters in digital image processing. *Comp. Graph. Image Processing*, 19:148-164.

HILDEBRAND, P. H. AND ACKERMAN, B. (1984). Urban effects on the convective boundary layer. *J. Atmos. Sci.*, 41(1):76-91.

HILDEBRAND, P. H. AND SEKHON, R. S. (1974). Objective determination of the noise level in Doppler spectra. *J. Appl. Meteor.*, 13:808-811.

HINCH, E. J. (1991). *Perturbation Methods.* Cambridge University Press, Cambridge. 160 pp.

HOCKING, W. K. (1983). On the extraction of atmospheric turbulence parameters from radar backscatter Doppler spectra - I. Theory. *J. Atmos. Terr. Phys.*, 45(2/3):89–102.

HOCKING, W. K. (1997). System design, signal-processing procedures, and preliminary results for the Canadian (London, Ontario) VHF atmospheric radar. *Radio Sci.*, 32(2):687–706.

HOWARD, L. (1833). *The Climate of London*, volume I-III. Harvey and Darton, London.

HOWE, M. S. (1973). Multiple scattering of sound by turbulence and other inhomogeneities. *J. Sound Vib.*, 27(4):455–476.

INGARD, U. (1953). A review of the influence of meteorological conditions on sound propagation. *J. Acoust. Soc. Am.*, 25(3):405–411.

ISHIMARU, A. (1978). *Wave Propagation and Scattering in Random Media.* IEEE Press/Oxford University Press, New York/Oxford. 574 pp.

JACKSON, J. D. (1975). *Classical Electrodynamics.* Wiley, New York, 2nd edition. 848 pp.

JAYANT, N. S. (1976). Average- and median-based smoothing techniques for improving digital speech quality in the presence of transmission errors. *IEEE Trans. Commun.*, COM-24(9):1043–1045.

JORDAN, J. R., LATAITIS, R. J., AND CARTER, D. A. (1997). Removing ground and intermittent clutter contamination from wind profiler signals using wavelet transforms. *J. Atmos. Ocean. Tech.*, 14(6):1280–1297.

KAIMAL, J. C. (1973). Turbulence spectra, length scales and structure parameters in the stable surface layer. *Boundary-Layer Meteorol.*, 4:289–309.

KAIMAL, J. C. AND FINNIGAN, J. J. (1994). *Atmospheric Boundary Layer Flows.* Oxford University Press, 1st edition. 289 pp.

KAIMAL, J. C., WYNGAARD, J. C., HAUGEN, D. A., COTÉ, O. R., IZUMI, Y., CAUGHEY, S. J., AND READINGS, C. J. (1976). Turbulence structure in the convective boundary layer. *J. Atmos. Sci.*, 33:2152–2169.

KAIMAL, J. C., WYNGAARD, J. C., IZUMI, Y., AND COTÉ, O. R. (1972). Spectral characteristics of surface-layer turbulence. *Quart. J. R. Met. Soc.*, 98:563–589.

KATSOULIS, B. D. AND THEOHARATOS, G. A. (1985). Indications of the urban heat island in Athens, Greece. *J. Clim. Appl. Meteor.*, 24:1296–1302.

KEELER, R. J. AND PASSARELLI, R. E. (1990). Signal processing for atmospheric radars. In ATLAS, D., editor, *Radar in Meteorology*, chapter 20a, pages 199–229. American Meteorological Society, Boston.

KIM, V. AND YAROSLAVSKII, L. (1986). Rank algorithms for picture processing. *Comp. Vision Graph. Image Processing*, 35(2):234–258.

KON, A. I. AND TATARSKI, V. I. (1980). The scattering signal frequency spectrum for radioacoustical atmospheric soundings. *Bull. (Izv.), Acad. Sci. USSR, Atmos. and Oceanic Phys.*, 16(3):142–148.

KONRAD, T. G., HICKS, J. J., AND DOBSON, E. B. (1968). Radar characteristics of birds in flight. *Science*, 159:274–280.

KRAICHNAN, R. H. (1953). The scattering of sound in a turbulent medium. *J. Acoust. Soc. Am.*, 25(6):1096–1104.

KROON, L. J. M. AND BINK, N. J. (1996). Conditional statistics of vertical heat fluxes in local advection conditions. *Boundary-Layer Meteorol.*, 80:49–78.

KUHLMANN, F. AND WISE, G. L. (1981). On second moment properties of median filtered sequences of independant data. *IEEE Trans. Commun.*, COM-29(9):1374–1379.

KUNKEL, K. E., ELORANTA, E. W., AND SHIPLEY, S. T. (1977). Lidar observations of the convective boundary layer. *J. Appl. Meteor.*, 16:1306–1311.

LATAITIS, R. J. (1992). Signal power for radio acoustic sounding of temperature: The effects of horizontal winds, turbulence, and vertical temperature gradients. *Radio Sci.*, 27(3):369–385.

LATAITIS, R. J. (1993). Theory and application of a Radio-Acoustic Sounding System (RASS). Tech. Mem. ERL WPL-230, Nat. Oceanic and Atmos. Admin., Environ. Res. Lab., Boulder, CO. 207 pp.

LEACH, B. W. AND MACPHERSON, J. I. (1991). Application of Kalman filtering to airborne wind measurement. *J. Atmos. Ocean. Tech.*, 8:51–65.

LEBLANC, S. G. (1994). Studies of turbulence with a wind profiler. M.Sc. Thesis in Atmospheric Science, McGill University, Montreal. 63 pp.

LEE, D. O. (1984). Urban climates. *Progress Phys. Geog.*, 8(1):1–31.

LENSCHOW, D. H., MANN, J., AND KRISTENSEN, L. (1993). How long is long enough when measuring fluxes and other turbulence statistics? Tech. Note NCAR/TN-389+STR, Nat. Center for Atmos. Res., Boulder, CO. 53 pp.

LENSCHOW, D. H., MANN, J., AND KRISTENSEN, L. (1994). How long is long enough when measuring fluxes and other turbulence statistics? *J. Atmos. Ocean. Tech.*, 11:611–673.

LENSCHOW, D. H. AND STANKOV, B. B. (1986). Length scales in the convective boundary layer. *J. Atmos. Sci.*, 43(12):1198–1209.

LIGHTHILL, M. J. (1952). On sound generated aerodynamically: I. General theory. *Proc. Roy. Soc.*, A211:564–587.

LIGHTHILL, M. J. (1953). On the energy scattered from the interaction of turbulence with sound or shock waves. *Proc. Camb. Phil. Soc.*, 49:531–551.

LIGHTHILL, M. J. (1972). The fourth annual Fairley lecture: The propagation of sound through moving fluids. *J. Sound Vib.*, 24(4):471–492.

LIGHTHILL, M. J. (1978). *Waves in Fluids.* Cambridge University Press. Cambridge/New York. 504 pp.

LIPPMANN, J., BAUER, M., AND PETERS, G. (1996). Methods of virtual heat flux determination from boundary layer wind profiler/RASS measurements. *Beitr. Phys. Atmosph.*, 69(1):119–128.

LUDWIG, F. L. (1970). Urban temperature fields. WMO Tech. Note No. 108, WMO-No.254. TP.141. p. 80-107.

MACPHERSON, J. I. (1990). Wind and flux calculations on the NAE Twin Otter. Report Laboratory Technical Report LTR-FR-109. National Research Council of Canada.

MAHRT, L. (1998). Flux sampling errors for aircraft and towers. *J. Atmos. Ocean. Tech.*, 15:416–429.

MAILHOT, J., STRAPP, J. W., MACPHERSON, J. I., BENOIT, R., BÉLAIR, S., DONALDSON, N. R., FROUDE, F., BENJAMIN, M., ZAWADZKI, I., AND ROGERS, R. R. (1998). The Montreal-96 Experiment on Regional Mixing and Ozone (MERMOZ): An overview and some preliminary results. *Bull. Amer. Meteor. Soc.*, 79(3):433–442.

MAKAROVA, T. I. (1980). Nonlinear absorbtion of sound in problems of acoustic and radioacoustic sounding of the atmosphere. *Bull. (Izv.), Acad. Sci. USSR, Atmos. and Oceanic Phys.*, 16(2):123–125.

MARSHALL, J. S. AND HITSCHFELD, W. (1953). Interpretation of the fluctuating echo from randomly distributed scatterers. part I. *Can. J. Phys.*, 31:962–994.

MASUDA, Y. (1988). Influence of wind and temperature on the height limit of a radio acoustic sounding system. *Radio Sci.*, 23(4):647–654.

MATUURA, N., MASUDA, Y., INUKI, H., KATO, S., FUKAO, S., SATO, T., AND TSUDA, T. (1986). Radio acoustic measurement of temperature profile in the tropospheric and stratosphere. *Nature*, 323:426–428.

MAY, P. T., MORAN, K. P., AND STRAUCH, R. G. (1989). The accuracy of RASS temperature measurements. *J. Appl. Meteor.*, 28:1329–1335.

MAY, P. T. AND STRAUCH, R. G. (1989). An examination of some algorithms for spectral moment estimation. In *Preprints 24th Conference on Radar Meteor.*, pages 429–432, Boston. Amer. Meteor. Soc.

MAY, P. T. AND STRAUCH, R. G. (1998). Reducing the effect of ground clutter on wind profiler velocity measurements. *J. Atmos. Ocean. Tech.*, 15:579–586.

MAY, P. T., STRAUCH, R. G., AND MORAN, K. P. (1988). The altitude coverage of temperature measurements using RASS with wind profiler radars. *Geophys. Res. Letters*, 15(12):1381–1384.

MAY, P. T., STRAUCH, R. G., MORAN, K. P., AND ECKLUND, W. L. (1990). Temperature sounding by RASS with profiler radars: A preliminary study. *IEEE Trans. Geosci. Rem. Sensing*, 28(1):19–28.

MCBEAN, G. A. (1976). Scaling turbulence in the planetary boundary layer. *Atmosphere*, 14(4):254–267.

MELLING, H. AND LIST, R. (1980). Characteristics of vertical velocity fluctuations in a convective urban boundary layer. *J. Appl. Meteor.*, 19:1184–1195.

MERRITT, D. A. (1995). A statistical averaging method for wind profiler Doppler spectra. *J. Atmos. Ocean. Tech.*, 12(5):985–995.

MILNE, E. A. (1921). Sound waves in the atmosphere. *Phil. Mag. S. 6*, 42(247):96–114.

MONIN, A. S. (1962). Characteristics of the scattering of sound in a turbulent atmosphere. *Sov. Phys.-Acoust.*, 7(4):370–373.

MORAN, K. P. AND STRAUCH, R. G. (1994). The accuracy of RASS temperature measurements corrected for vertical air motion. *J. Atmos. Ocean. Tech.*, 11:995–1001.

MOSTELLER, F. AND TUKEY, J. W. (1977). *Data Analysis and Regression: A Second Course in Statistics.* Addison-Wesley, Reading, Mass. 588 pp.

MUSCHINSKI, A. (1998). The first moments of the variance- and cross-spectra of standard and interferometric clear-air-Doppler-radar signals. Report NCAR/TN-441+STR, May, National Center for Atmospheric Research. 102 pp.

NALBANDYAN, O. G. (1976a). Scattering of electromagnetic waves from a sound wave propagating in a turbulent atmosphere. *Bull. (Izv.), Acad. Sci. USSR, Atmos. and Oceanic Phys.*, 12(8):536–537.

NALBANDYAN, O. G. (1976b). The signal frequency spectrum in radioacoustic sounding of the atmosphere. *Bull. (Izv.), Acad. Sci. USSR, Atmos. and Oceanic Phys.*, 12(7):472–473.

NALBANDYAN, O. G. (1977). The theory of radioacoustic sensing of the atmosphere. *Bull. (Izv.), Acad. Sci. USSR, Atmos. and Oceanic Phys.*, 13(3):172–177.

NEIMAN, P. J., MAY, P. T., AND SHAPIRO, M. A. (1992). Radio Acoustic Sounding Sysytem (RASS) and wind profiler observations of lower- and midtropospheric weather systems. *Mon. Wea. Rev.*, 120:2298–2313.

NEIMAN, P. J., MAY, P. T., STANKOV, B. B., AND SHAPIRO, M. A. (1991). Radio acoustic sounding system observations of an arctic front. *J. Appl. Meteor.*, 30:881–892.

NODES, T. A. AND GALLAGHER, N. C. (1982). Median filters: some modifications and their properties. *IEEE Trans. Acoustics, Speech, Signal Processing*, ASSP-30(5):739–746.

NODES, T. A. AND GALLAGHER, N. C. (1984). The output distribution of median type filters. *IEEE Trans. Acoustics, Speech, Signal Processing*, COM-32(5):532–541.

NORTH, E. M., PETERSON, A. M., AND PARRY, H. D. (1973). RASS, a remote sensing system for measuring low-level temperature profiles. *Bull. Amer. Meteor. Soc.*, 54(9):912–919.

OHSAKI, Y. AND MASUDA, Y. (1996). Software-based cancellation of clutter in the Doppler spectrum measured by a wind profiler. *J. Meteor. Soc. Japan*, 74(5):941–945.

OKE, T. R. (1976). The distinction between canopy and boundary-layer urban heat islands. *Atmosphere*, 14(4):268–277.

OKE, T. R. (1982). The energetic basis of the urban heat island. *Quart. J. R. Met. Soc.*, 108(455):1–24.

OKE, T. R. (1988). The urban energy balance. *Progress Phys. Geog.*, 12(4):471–508.

OKE, T. R. (1990). Bibliography of urban climate, 1981-1988. Report WCAP - 15, World Meteological Organization. 64 pp.

OKE, T. R., CLEUGH, H. A., GRIMMOND, S., SCHMID, H. P., AND ROTH, M. (1989). Evaluation of spatially-averaged fluxes of heat, mass and momentum in the urban boundary layer. *Weather and Climate*, 9:14–21.

Oke, T. R. and East, C. (1971). The urban boundary layer in Montreal. *Boundary-Layer Meteorol.*, 1:411–437.

Oke, T. R. and Hannell, F. G. (1970). The form of the urban heat island in Hamilton, Canada. WMO Tech. Note No. 108, WMO-No.254. TP.141. p. 113-126.

Oke, T. R. and Maxwell, G. B. (1975). Urban heat island dynamics in Montreal and Vancouver. *Atmospheric Environment*, 9:191–200.

Oppenheim, A. V. and Schafer, R. W. (1989). *Discrete-Time Signal Processing*. Prentice Hall, Englewood Cliffs, New Jersey. 879 pp.

Ottersten, H. (1969). Radar backscattering from the turbulent clear atmosphere. *Radio Sci.*, 4(12):1251–1255.

Panchev, S. (1971). *Random Functions and Turbulence*. Pergamon Press, Oxford/New York. 444 pp.

Passarelli, R. E. (1981). Autocorrelation techniques for ground clutter rejection. In *Preprints 20th Conference on Radar Meteor.*, pages 308–313, Boston. Amer. Meteor. Soc.

Passarelli, R. E., Romanik, P., Geotis, S. G., and Siggia, A. D. (1981). Ground clutter rejection in the frequency domain. In *Preprints 20th Conference on Radar Meteor.*, pages 295–300, Boston. Amer. Meteor. Soc.

Peters, G. (1994a). Correction of turbulence induced errors of RASS temperature profiles. In *Ext. Abstracts, 3rd International Symp. on Tropospheric Profiling: Needs and Technologies*, pages 266–271, Hamburg, Germany. Amer. Meteor. Soc.

Peters, G. (1994b). Second-order Doppler shift of RASS echoes. *J. Atmos. Ocean. Tech.*, 11:593–598.

PETERS, G. AND ANGEVINE, W. M. (1996). On the correction of RASS-temperature errors due to turbulence. *Beitr. Phys. Atmosph.*, 69(1):81–96.

PETERS, G., HINZPETER, H., AND BAUMANN, G. (1985). Measurements of heat flux in the atmospheric boundary layer by sodar and RASS: A first attempt. *Radio Sci.*, 20(6):1555–1564.

PETERS, G. AND KIRTZEL, H. J. (1994). Measurements of momentum flux in the boundary layer by RASS. *J. Atmos. Ocean. Tech.*, 11:63–75.

PITAS, I. AND VENETSANOPOULOS, A. N. (1990). *Nonlinear Digital Filters: Principles and Applications.* Kluwer Academic Publishers, Boston/Dordrecht/London. 392 pp.

POTVIN, G. (1993). Space-time correlations and Taylor's hypothesis for rainfall. M.Sc. Thesis in Physics, McGill University, Montreal. 68 pp.

POTVIN, G., MACPHERSON, J. I., ROGERS, R. R., DONALDSON, N. R., AND STRAPP, J. W. (1997). An evaluation of a heat flux retrieval method using MERMOZ data. In *Preprints 12th Symp. on Boundary Layers and Turb.*, pages 441–442, Vancouver, Canada. Amer. Meteor. Soc.

PRIDMORE-BROWN, D. C. (1962). Sound propagation in a temperature- and wind-stratified medium. *J. Acoust. Soc. Am.*, 34(4):438–443.

RABINER, L. R., SAMBUR, M. R., AND SCHMIDT, C. E. (1975). Applications of a nonlinear smoothing algorithm to speech processing. *IEEE Trans. Acoustics, Speech, Signal Processing*, ASSP-23(6):552–557.

RAYLEIGH, J. W. S. (1896). *The Theory of Sound*, volume II. Dover, New-York, 2 edition. 504 pp.

REEVES, A. P. (1982). The local median and other window operations on SIMD computers. *Comp. Graph. Image Processing*, 19:165–178.

RENOU, E. (1862). Différences de température entre Paris et Choisyle-Roi. *Société Météorologique de France, Annuaire*, 10:105–109.

RIDDLE, A. C., ANGEVINE, W. M., ECKLUND, W. L., MILLER, E. R., PARSONS, D. B., CARTER, D. A., AND GAGE, K. S. (1996). In situ and remotely sensed horizontal winds and temperature intercomparisons obtained using integrated sounding systems during TOGA COARE. *Beitr. Phys. Atmosph.*, 69(1):49–61.

ROGERS, R. R., COHN, S. A., ECKLUND, W. L., WILSON, J. S., AND CARTER, D. A. (1994). Experience from one year of operating a boundary-layer profiler in the center of a large city. *Ann. Geophysicae*, 12:529–540.

ROGERS, R. R., ECKLUND, W. L., CARTER, D. A., GAGE, K. S., AND ETHIER, S. A. (1993). Research applications of a boundary-layer wind profiler. *Bull. Amer. Meteor. Soc.*, 74(4):567–580.

ROGERS, R. R., LEBLANC, S. G., COHN, S. A., ECKLUND, W. L., CARTER, D. A., AND WILSON, J. S. (1996). Profiler measurements of turbulence and wind shear in a snowstorm. *Beitr. Phys. Atmosph.*, 69(1):27–36.

ROTACH, M. W. (1993). Turbulence close to a rough urban surface. Part I: Reynolds stress. *Boundary-Layer Meteorol.*, 65:1–28.

ROTH, M. AND OKE, T. R. (1993). Turbulent transfer relationships over an urban surface. I: Spectral characteristics. *Quart. J. R. Met. Soc.*, 119:1071–1104.

ROTH, M., OKE, T. R., AND STEYN, D. G. (1989). Velocity and temperature spectra and cospectra in an unstable suburban atmosphere. *Boundary-Layer Meteorol.*, 47:309–320.

ROUSE, W. R., NOAD, D., AND MCCUTCHEON, J. (1973). Radiation, temperature and atmospheric emissivities in a polluted urban atmosphere at Hamilton, Ontario. *J. Appl. Meteor.*, 12:798–807.

ROUSSEEUW, P. J. AND LEROY, A. M. (1987). *Robust Regression and Outlier Detection.* Wiley, New York. 329 pp.

SATO, T. AND WOODMAN, R. F. (1982). Spectral parameter estimation of CAT radar echoes in the presence of fading clutter. *Radio Sci.*, 17(4):817–826.

SCHMIDT, H. AND SCHUMANN, U. (1989). Coherent structure of the convective boundary layer derived from large-eddy simulations. *J. Fluid Mech.*, 200:511–562.

SMITH, P. L. AND FETTER, R. W. (1989). A historical review of the development of the electromagnetic-acoustic (EMAC) probe. In *Preprints 24th Conference on Radar Meteor.*, pages 732–736, Tallahasee, Florida. Amer. Meteor. Soc.

SPANGLER, T. C. AND DIRKS, R. A. (1974). Meso-scale variations of the urban mixing height. *Boundary-Layer Meteorol.*, 6:423–441.

STRAUCH, R. G., MERRITT, D. A., MORAN, K. P., EARNSHAW, K. B., AND VAN DE KAMP, D. (1984). The Colorado wind-profiling network. *J. Atmos. Ocean. Tech.*, 1:37–49.

STULL, R. B. (1988). *An Introduction to Boundary Layer Meteorology.* Kluwer Academic Publishers, Dordrecht/Boston/London. 666 pp.

SUMMERS, P. W. (1964). *An Urban Ventilation Model Applied to Montreal.* Ph.D. Thesis in Meteorology, McGill University, Montreal. 166 pp.

TAKAHASHI, K., MASUDA, Y., MATUURA, N., KATO, S., FUKAO, S., TSUDA, T., AND SATO, T. (1988). Analysis of acoustic wave fronts in the atmosphere to profile the temperature and wind with a radio acoustic sounding system. *J. Acoust. Soc. Am.*, 84(3):1061–1066.

TAKEDA, T. AND IWASAKA, Y. (1982). *Features and Behavior of Aerosols in the Urban Atmosphere.* Water Research Institute, Nagoya University. 301 pp.

TATARSKI, V. I. (1961). *Wave Propagation in a Turbulent Medium.* McGraw-Hill, New York/Toronto/London. 285 pp.

TEUNISSEN, H. W. (1980). Structure of mean winds and turbulence in the planetary boundary layer over rural terrain. *Boundary-Layer Meteorol.*, 19:187–221.

TRAINER, M., RIDLEY, B. A., BUHR, M. P., KOK, G., WALEGA, J., HÜBLER, G., PARRISH, D. D., AND FEHSENFELD, F. C. (1995). Regional ozone and urban plumes in the southeastern United States: Birmingham, a case study. *J. Geophys. Res.*, 100(D9):18,823–18,834.

TSUDA, T., ADACHI, T., MASUDA, Y., FUKAO, S., AND KATO, S. (1994). Observations of tropospheric temperature fluctuations with the MU Radar-RASS. *J. Atmos. Ocean. Tech.*, 11:50–62.

TSUDA, T., MASUDA, Y., INUKI, H. TAKAHASHI, K., TAKAMI, T., SATO, T., FUKAO, S., AND KATO, S. (1989). High time resolution monitoring of tropospheric temperature with a Radio Acoustic Sounding System (RASS). *Pure Appl. Geophys.*, 130(2/3):497–507.

TUKEY, J. W. (1977). *Exploratory Data Analysis.* Addison-Wesley, Reading, Mass. 688 pp.

VANMARCKE, E. (1983). *Random Fields.* MIT Press, Cambridge, Mass. 382 pp.

WALLACE, P. R. (1953). Interpretation of the fluctuating echo from randomly distributed scatterers. part II. *Can. J. Phys.*, 31:995–1009.

WANNER, H. AND FILLIGER, P. (1989). Orographic influence on urban climate. *Weather and Climate*, 9:22–28.

WYNGAARD, J. C. (1992). Atmospheric turbulence. *Annu. Rev. Fluid Mech.*, 24:205–233.

YAP, D. (1969). Air pollution and vertical temperature distribution over Montreal. M.Sc. Thesis in Meteorology, McGill University, Montreal. 75 pp.

YAP, D., GUNN, K. L. S., AND EAST, C. (1969). Vertical temperature distribution over Montréal. *Naturaliste Can.*, 96(4):561–580.